

Open Research Online

The Open University's repository of research publications
and other research outputs

Observations of low mass X-ray transients in outburst

Thesis

How to cite:

Hynes, Robert Ian (1999). Observations of low mass X-ray transients in outburst. PhD thesis The Open University.

For guidance on citations see [FAQs](#).

© 1999 The Author

Version: Version of Record

Copyright and Moral Rights for the articles on this site are retained by the individual authors and/or other copyright owners. For more information on Open Research Online's data [policy](#) on reuse of materials please consult the policies page.

oro.open.ac.uk

UNRESTRICTED

Faculty of Science, The Open University

Observations of Low Mass X-ray Transients in Outburst

Robert Ian Hynes M.A. M.Sc.

Submitted for the degree of Doctor of Philosophy

September 1999

AUTHOR'S No: T1138603

DATE OF SUBMISSION: 30 SEPTEMBER 1999

DATE OF AWARD: 15 DECEMBER 1999

CONTENTS

LIST OF FIGURES	v
LIST OF TABLES	vii
ABSTRACT	viii
ACKNOWLEDGEMENTS	ix
1 INTRODUCTION	1
1.1 Low Mass X-Ray Transients	1
1.2 The Origin and Evolution of LMXBs	5
1.3 X-Ray States of LMXBs	7
1.4 Characteristics of SXT Outbursts	8
1.5 The Outburst Mechanism	10
1.6 Advective Accretion Flows	12
1.7 The Evidence for Black Holes in SXTs	17
1.8 The Multiwavelength Target-of-Opportunity Programme	20
2 REDUCTION OF DATA FROM GROUND BASED TELESCOPES	21
2.1 Preliminary Stages of CCD Data Reduction	22
2.1.1 Bias Removal	22
2.1.2 Dark Count Subtraction	24
2.1.3 Correction for Sensitivity Variations	24
2.2 JKT Photometry of XTE J2012+381	25
2.3 UKIRT Photometry of XTE J2012+381	28
2.4 AAT Spectroscopy of GRO J1655–40	28
2.5 WHT Spectroscopy of XTE J2123–058	29
2.5.1 Basic Image Processing	29
2.5.2 Spectral Extraction	33
2.5.3 Wavelength Calibration	33
2.5.4 Flux Calibration	35
2.5.5 Sources of Error	35
2.6 WHT Spectroscopy of XTE J2012+381	37
2.6.1 Basic Image Processing	37
2.6.2 Spectral Extraction	37
2.6.3 Calibration	39
3 REDUCTION OF DATA FROM <i>HST</i> /FOS	40
3.1 Introduction	40
3.2 The Pipeline Calibration Process: CALFOS	44
3.2.1 Raw Data Input	44
3.2.2 Statistical Error Calculation	44
3.2.3 Data Quality Initialisation	44
3.2.4 Conversion to Count-rates and Dead Diode Correction	44
3.2.5 GIM Correction	45
3.2.6 Paired-pulse Correction	45

3.2.7	Background Subtraction	45
3.2.8	Scattered Light Subtraction	46
3.2.9	Flatfield Correction	46
3.2.10	Sky Subtraction	46
3.2.11	Wavelength Computation	46
3.2.12	Aperture Throughput and Focus Corrections	47
3.2.13	Absolute Calibration	47
3.2.14	Correction for Time-dependent Sensitivity Variations	47
3.2.15	RAPID Mode Processing	47
3.3	Reducing Spectra from the G160L Grating	48
3.4	Reducing PRISM Spectra	53
3.5	Reducing Spectra from the High Resolution Gratings	56
3.6	Extracting RAPID Mode Light Curves	57
4	GRO J1655-40	62
4.1	Introduction	62
4.1.1	The 1996 Outburst	64
4.1.2	System Parameters	65
4.1.3	Reddening and Distance	68
4.2	X-Ray Observations	73
4.3	Emission Lines	77
4.3.1	Ultraviolet Resonance Lines	77
4.3.2	Helium and Bowen Fluorescence Lines	77
4.3.3	A Constraint on the Extreme Ultraviolet Flux	82
4.4	Characterisation of Continuum Spectra	84
4.4.1	The Steady State Black-body Disc Model	86
4.4.2	Black-body Fits	87
4.4.3	Self-absorbed Synchrotron Emission	90
4.5	Echo Mapping	92
4.5.1	Comparison of Light Curves	92
4.5.2	Cross Correlations	94
4.5.3	Fitting Transfer Functions	100
4.5.4	Maximum Entropy Echo Mapping	102
4.5.5	Interpretation of Echo Mapping	102
4.6	Multi-wavelength Observations Through X-Ray Dips	104
4.7	The Continuum Spectral Energy Distribution Reconsidered	106
4.7.1	The Optical Energy Source	106
4.7.2	Recalibration of the PRISM/RD Spectra	107
4.7.3	The Companion Star Contribution	107
4.7.4	Irradiated Disc Spectra	110
4.8	Discussion	114
4.8.1	A Decaying Warp?	114
4.8.2	Obscuration by a Disc Corona?	115
4.8.3	Long Period Oddities?	116
4.8.4	Conclusion	116

5	XTE J2123-058	117
5.1	Introduction	117
5.1.1	System Parameters	119
5.1.2	Reddening and Distance	119
5.2	The Continuum Flux Distribution and Light Curve	122
5.3	The Emission Line Spectrum	124
5.3.1	N III-C III and He II 4686 Å Emission	126
5.3.2	H I Balmer and He II Pickering Lines	127
5.4	Line Variability	127
5.5	Doppler Tomography	132
5.6	Discussion	134
5.6.1	A Neutron Star SW Sex System?	134
5.6.2	Is this Behaviour Typical of LMXBs?	135
5.6.3	The Magnetic Propeller Interpretation	136
5.6.4	The Disc Re-impact Interpretation	140
5.6.5	The Origin of XTE J2123-058	141
6	XTE J2012+381	142
6.1	Introduction	142
6.2	JKT Photometry	143
6.3	WHT Spectroscopy	146
6.4	UKIRT Photometry	148
6.5	Has the Optical Counterpart Been Correctly Identified?	148
6.6	What is the Nature of XTE J2012+381?	151
7	GRO J0422+32	152
7.1	Introduction	152
7.1.1	System Parameters	156
7.1.2	Reddening and Distance	157
7.2	The Continuum Spectrum	159
7.2.1	Interstellar Reddening	159
7.2.2	The Companion Star Contribution	159
7.2.3	The Far Ultraviolet Spectrum	162
7.2.4	Black Body Models	163
7.2.5	Simple Non-thermal Models	163
7.2.6	Model Atmosphere Spectra	164
7.2.7	Advective Models	166
7.3	Emission Lines	167
7.4	Discussion	168
8	CONCLUSIONS	172
	REFERENCES	175
	APPENDICES	187
A	THE RELATIVE FLUX CALIBRATION PROCEDURE FOR XTE J2123-058 SPECTROSCOPY	188

B	THE OPTIMAL EXTRACTION OF BLENDED SPECTRA	191
B.1	Introduction	191
B.1.1	Point Spread Function Fitting of Photometric Images	191
B.1.2	Optimal Extraction of Spectra	193
B.2	The Spatial Profile	194
B.3	Fitting Profiles	197
B.4	Cosmic Ray Rejection	200
B.5	V404 Cyg: Another Application of the Algorithm	201

LIST OF FIGURES

1.1	Roche potential of a typical binary	3
1.2	Visualisation of a typical LMXB	4
1.3	Outburst lightcurves of A 0620–00	8
1.4	The limit-cycle mechanism	10
1.5	Advective models for V404 Cyg in quiescence	13
1.6	Advective model for X-ray spectral states	15
2.1	Typical CCD layout.	23
2.2	Standard and instrumental magnitudes for Landolt field 110.	27
2.3	Spectroscopic flat fields used for XTE J2123–058.	31
2.4	Spectrum of the comparison star used for XTE J2123–058.	34
2.5	Airmasses and slit angles used for XTE J2123–058.	36
2.6	Fit to spatial profiles of XTE J2012+381	38
2.7	Spectrum of the Telluric standard for XTE J2012+381.	38
3.1	Average <i>HST</i> /G160L count rates for GRO J0422+32 and GRO J1655–40 . .	49
3.2	Background subtracted G160L count rates	52
3.3	Average PRISM/BL spectra	54
3.4	Average PRISM/RD spectra	55
3.5	G270H spectra	58
3.6	G400H spectra	59
4.1	Long term X-ray light curve of GRO J1655–40.	63
4.2	Light curves of the 1996 outburst.	66
4.3	Best fit of reddened power-law to UV data	70
4.4	Far-UV spectrum	76
4.5	<i>HST</i> line profiles of He II and Bowen blend	78
4.6	O III line profiles	79
4.7	All <i>HST</i> and AAT spectra	85
4.8	Dereddened spectra	85
4.9	Fit of disc spectrum to far-UV data	86
4.10	Blackbody fits to optical spectra	89
4.11	Synchrotron fits to optical spectra	91
4.12	<i>HST</i> and <i>RXTE</i> light curves	93
4.13	<i>HST</i> and <i>RXTE</i> light curves from 1996 June 8	95
4.14	ICFs for May 14 data	96
4.15	ICFs for June 8 data	97
4.16	Combined ICF for June 8 data	98
4.17	Best-fits to <i>HST</i> lightcurves	99
4.18	χ^2 surfaces from fitting Gaussian transfer functions to lightcurves	101
4.19	Observations of X-ray dips, 1996 June 20	105
4.20	Change in PRISM/RD calibration	107
4.21	Subtraction of companion spectrum	110
4.22	Broad-band spectrum from May 14 observation	113

5.1	<i>RXTE</i> /ASM outburst light curve of XTE J2123–058.	118
5.2	Dereddened spectra of XTE J2123–058 and GRO J0422+32	121
5.3	Continuum light curves	123
5.4	Normalised continuum light curve from July 20	124
5.5	Average spectrum	125
5.6	H I and He II lines	128
5.7	Average spectra near H α	129
5.8	Trailed spectrograms	130
5.9	Line light curves	131
5.10	Doppler tomogram of He II 4686 Å emission	133
5.11	A magnetic propeller model for He II emission	139
6.1	<i>RXTE</i> /ASM outburst light curve of XTE J2012+381.	143
6.2	Optical and infrared images of the field of XTE J2012+381	144
6.3	WHT spectra of XTE J2012+381 and the USNO star	147
6.4	Test of reality of H α emission	149
7.1	<i>CGRO</i> /BATSE and <i>R</i> band long-term lightcurves of GRO J0422+32	153
7.2	<i>HST</i> spectra	160
7.3	Dereddened PRISM/RD spectrum compared with simple models.	161
7.4	Comparison of PRISM/RD spectrum with Kurucz spectra.	165
7.5	Comparison with PRISM/RD spectrum with advective spectra.	167
7.6	Near UV spectra of A 0620–00 and GRO J0422+32	169
A.1	Calibration stages for XTE J2123–058 spectra.	189
B.1	Fit to spatial profiles of XTE J2012+381	196
B.2	Wavelength dependence of profile fit parameters	198
B.3	Examples of spatial profiles of V404 Cyg	202
B.4	Average spectra of V404 Cyg and the blended star	203
B.5	Continuum and H α light curves of V404 Cyg and the blended star	204

LIST OF TABLES

1.1	Properties of SXTs with dynamical mass estimates	16
1.2	Currently active SXT ToO programmes	19
2.1	Log of XTE J2012+381 photometry	26
2.2	Log of GRO J1655–40 spectroscopy	29
2.3	Log of XTE J2123–058 spectroscopy	30
3.1	<i>HST</i> /FOS modes used in observing GRO J0422+32 and GRO J1655–40. . .	41
3.2	Log of <i>HST</i> /FOS observations of GRO J0422+32.	42
3.3	Log of <i>HST</i> /FOS observations of GRO J1655–40.	43
4.1	Reddened power-law fits to UV spectra of GRO J1655–40	68
4.2	Log of <i>RXTE</i> observations.	74
4.3	Properties of He II and Bowen emission lines detected in May spectra. . . .	80
4.4	Parameters of black body fits	88
4.5	Parameters of synchrotron fits	92
4.6	Results from parameterised Gaussian fitting to <i>HST</i> lightcurves	101
4.7	Companion star magnitudes	108
5.1	Spectral lines detected in XTE J2123–058	126
6.1	Astrometry of XTE J2012+381	145
6.2	Optical photometry of objects near XTE J2012+381.	146
6.3	Infrared photometry of objects near XTE J2012+381	149
7.1	Emission lines detected by <i>HST</i> in GRO J0422+32	168

RESEARCH DEGREES CENTRE

LIBRARY AUTHORISATION FORM

Please return this form to the The Research Degrees Centre with the two bound copies of your thesis to be deposited with the University Library.

All students should complete Part 1. Part 2 only applies to PhD students.

Student: ROBERT IAN HYNES PI: T1138603

Degree: PHD

Thesis title: OBSERVATIONS OF LOW MASS X-RAY TRANSIENTS IN
OUTBURST

Part 1 Open University Library Authorisation [to be completed by all students]

I confirm that I am willing for my thesis to be made available to readers by the Open University Library, and that it may be photocopied, subject to the discretion of the Librarian.

Signed:  Date: 25/05/00

Part 2 British Library Authorisation [to be completed by PhD students only]

If you want a copy of your PhD thesis to be available on loan to the British Library Thesis Service as and when it is requested, you must sign a British Library Doctoral Thesis Agreement Form. Please return it to the Research Degrees Centre with this form. The British Library will publicise the details of your thesis and may request a copy on loan from the University Library. Information on the presentation of the thesis is given in the Agreement Form.

Please note the British Library have requested that theses should be printed on one side only to enable them to produce a clear microfilm. The Open University Library sends the fully bound copy of theses to the British Library.

The University has agreed that your participation in the British Library Thesis Service should be voluntary. Please tick either (a) or (b) to indicate your intentions.

[a] ☒ I am willing for the Open University to loan the British Library a copy of my thesis.
A signed Agreement Form is attached.

[b] ☐ I do not wish the Open University to loan the British Library a copy of my thesis.

Signed:  Date: 25/05/00

I must begin, of course, with a big thank you to Carole Haswell, at various times and in various places advisor, diplomat, friend, fund raiser, library, mentor, politician, teacher, travel companion and too many other things to list. As well as her advice and encouragement, without her efforts to assemble and implement the *HST* target-of-opportunity programme, I would have had far fewer puzzling results to struggle with, as well as less interesting results to get excited about.

Thanks are also due to various students, post-docs and young-at-heart lecturers at Sussex and the Open University who have brought the whole Ph.D. experience to life in vibrant technicolour. I am particularly grateful to Sinan, without whose Unix wizardry I would have been lost so many times (and who provided the \LaTeX style file used for this work), and to Dan for putting up with me as a housemate for six months while this work was being written. Also those who have provided continuity all the way from M.Sc. through D.Phil., Ph.D. and soon beyond, especially Andrew, Pierre, Luisa and Hannah. I should also thank all those at the Open University who have made my rather last-minute transition here less painful, in particular Chris Wigglesworth.

Moving on to more serious matters, I am grateful to my collaborators on the work included here: Jorge Casares, Phil Charles, Wan Chen, Rob Fender, Emilios Harlaftis, Keith Horne, Jonathan Kemp, Kieran O'Brien, Paul Roche, Chris Shrader and Cristina Zurita.

Thanks are also due to Alastair Allan, Charles Bailyn, Malcolm Coe, Rob Fender, Coel Hellier, Raj Jain, Jeff McClintock, Jerry Orosz, Miguel Serra-Ricart, Rob Robinson, Chris Shrader, Roberto Soria and Ping Zhao for obtaining or sharing data, all of which was appreciated, even if I have not included it here. I am grateful to Ann Esin for generating ADAF spectral models for GRO J0422+32.

I could not list all the people with whom I have discussed this work by e-mail, at conferences, and elsewhere, and who have not been above taking an inexperienced Ph.D. student seriously. It will have to suffice to list a few who have provided direct input: Ann Esin, Mike Garcia, Jean-Pierre Lasota, Tim Naylor, Jan van Paradijs, Danny Steeghs, Graham Wynn, Ping Zhao and two anonymous referees.

My research has been funded by a Research Studentship awarded by the Particle Physics and Astronomy Research Council, held at the University of Sussex from October 1996 to March 1999 and at the Open University since then. In addition I have been grateful for some additional funding sources: the University of Sussex PATT rolling grant funded two observing runs; the Nuffield Foundation supported a collaborative visit to St Andrews; NASA grants for the *HST* and *RXTE* projects (see below) funded attendance at conferences to present the results included here; an assortment of other visits have in some way benefited from funding provided by Tim Abbott, Jorge Casares, Phil Charles, Carole Haswell, Joe Patterson, and Rob Robinson.

The William Herschel and Jacobus Kapteyn Telescopes are operated on the island of La Palma by the Isaac Newton Group in the Spanish Observatorio del Roque de los Muchachos of the Instituto de Astrofísica de Canarias. The United Kingdom Infrared Telescope is operated by the Joint Astronomy Centre on behalf of the Particle Physics and Astronomy Research Council. The Anglo-Australian Telescope is operated by the Anglo-Australian Observatory. Thanks to PATT for allocating us time and to W. Martin and R. Padman for letting us change our minds and override our own programme on 24 hour notice to observe XTE J2123–058. Thanks also to the JKT and UKIRT service programmes for obtaining data on XTE J2012+381 and to the staff of the Isaac Newton Group for such excellent support.

Support for *HST* work was provided by NASA through grant numbers NAG5-3311, GO-4377-02-92A and GO-6017-01-94A from the Space Telescope Science Institute, which is operated by the Association of Universities for Research in Astronomy, Incorporated, under NASA contract NAS5-26555. Thanks to the staff at STScI, especially Jeff Hayes, Tony Keyes, Tony Roman, Michael Rosa and Ed Smith.

Support for *RXTE* work was provided through grant NAS5-32490. This work made use of the *RXTE* and *CGRO* Science Centers at the NASA Goddard Space Flight Center. *RXTE* Quicklook results were provided by the *RXTE*/ASM teams at MIT and at the *RXTE* SOF and GOF at GSFC. *CGRO*/BATSE Earth occultation data products were provided by the BATSE Instrument Team at the Marshall Space Flight Center via the *CGRO* Science Support Center at GSFC.

Quite an assortment of software has been used in this work, in particular, IDL (Research Systems Inc.), IRAF (National Optical Astronomy Observatories), STSDAS (STScI), some parts of the Starlink software collection, MOLLY and DOPPLER (Tom Marsh) and DOPMAP (H. C. Spruit).

This research has made use of the SIMBAD database, operated at CDS, Strasbourg, France and the NASA Astrophysics Data System Abstract Service.

My escapades around Britain and the world have been made much more enjoyable by the hospitality of many people in many places: Jorge Casares, Wan Chen, Keith Horne, Kieran O'Brien, Natasha Papousek, Rob Robinson, Tariq Shahbaz, Chris Shrader and Bill Welsh. Special thanks are due to Tim and Jackie Abbott who have introduced me to the delights of two tropical 'paradises' with unfailing hospitality.

Above all, I am grateful to Mum (without whose generosity I would be bankrupt!) and to Joy who has made my last eight months a delight, as well as spotting a frightening number of mistakes in the reference list and generally preserving my sanity while writing this.

For Dad: "I'm finally doing what you said I always should have done. I wish you were still here to see it"...

Chapter 1

INTRODUCTION

1.1 Low Mass X-Ray Transients

A widespread astrophysical problem involves the collapse of gas with angular momentum. Nature's solution to this problem is to form an accretion disc, which viscously extracts angular momentum allowing the gas to fall inwards. Accretion discs occur on a wide range of scales in the Universe from young stellar objects and interacting binary stars to active galactic nuclei, and may play a role in gamma-ray burst production. Interacting binaries represent an ideal laboratory in which to study the underlying physics because they vary on accessible timescales from milliseconds to years and they rotate; hence the system may be viewed from different orientations.

To understand the structure and behaviour of an interacting binary, it is necessary to first understand its gravitational environment. While the basic physics is very simple (effectively two point masses rotating about their common centre of mass) the combination of gravity and rotation leads to interesting effects. It is most helpful to visualise the binary in the corotating frame of reference, in which the stars appear at rest. In this frame as well as real gravitational forces from the two stars, there are fictitious centrifugal and Coriolis forces arising because the corotating frame is non-inertial. The combined effect of the gravitational and centrifugal forces can be represented by the Roche potential (Frank, King & Raine 1992):

$$\Phi_R(\mathbf{r}) = -\frac{GM_1}{|\mathbf{r} - \mathbf{r}_1|} - \frac{GM_2}{|\mathbf{r} - \mathbf{r}_2|} - \frac{1}{2}(\boldsymbol{\omega} \times \mathbf{r})^2. \quad (1.1)$$

The Coriolis force, $-2\boldsymbol{\omega} \times \mathbf{v}$ per unit mass, is velocity dependent, hence cannot be repre-

sented by a potential. A more complete mathematical treatment is given by Kopal (1959). Figure 1.1 represents the Roche potential of a typical binary with a mass ratio of $q = 0.33$, i.e. the accretor is three times as massive as the mass donor. There are several key points to note. Firstly, as well as the potential wells of the two stars, the potential drops off at large radii, due to the fictitious centrifugal force. This is a consequence of assuming corotation. There are five stationary points, the Lagrangian points. The most important for an interacting binary is L_1 , the inner Lagrangian point. This is a saddle point between the two stars and represents the easiest route for material to be transferred between them. The Roche lobe of a star is defined as the teardrop shaped equipotential surface which just touches the L_1 point. If the star grows beyond its Roche lobe material will be transferred to the other star through the L_1 point; it is an interacting binary. Because of the additional Coriolis force, the material does not fall straight toward the centre of the lobe; it has angular momentum and will instead settle into a ring; viscous interactions will then cause the ring to spread into a disc. Of the other points, L_2 and L_3 are also saddle points on the line of centres of the two stars, and L_4 and L_5 are local maxima. These latter four points represent unstable points of equilibrium¹ at which material may become trapped.

Binary stars can loosely be categorised into three groups: detached, semi-detached and contact binaries. In detached binaries, both stars are inside their Roche lobe and there is normally no exchange of material between them. The majority of binary stars are of this type. In a semi-detached binary, one star is large enough to be in contact with its Roche lobe and material is funnelled through the L_1 point into the Roche lobe of the other star, the accretor. This category includes a variety of objects: Algols (Richards & Albright 1999), in which the accretor is a normal size star, cataclysmic variables (Warner 1995) in which it is a white dwarf and X-ray binaries (Lewin, van Paradijs & van den Heuvel 1995) in which it is a black hole or neutron star. In a contact binary both stars fill or overflow their Roche lobes and they will form a bizarre dumbbell shaped object with two stellar cores within a common envelope. The classification of a given binary changes with time as the stars evolve and their radii change. Angular momentum losses may also change the binary separation. An interacting binary which is semi-detached today has likely been through detached and contact phases at different times as described in Section 1.2.

The term interacting binary most commonly conjures up images of semi-detached systems in which Roche lobe overflow occurs, but also the contact binaries represent an

¹When the Coriolis force is included L_4 and L_5 are stable equilibria for corotating particles (Frank, King & Raine 1992; Symon 1960), provided the mass ratio is extreme ($q < 0.04$ or $q > 24$.)

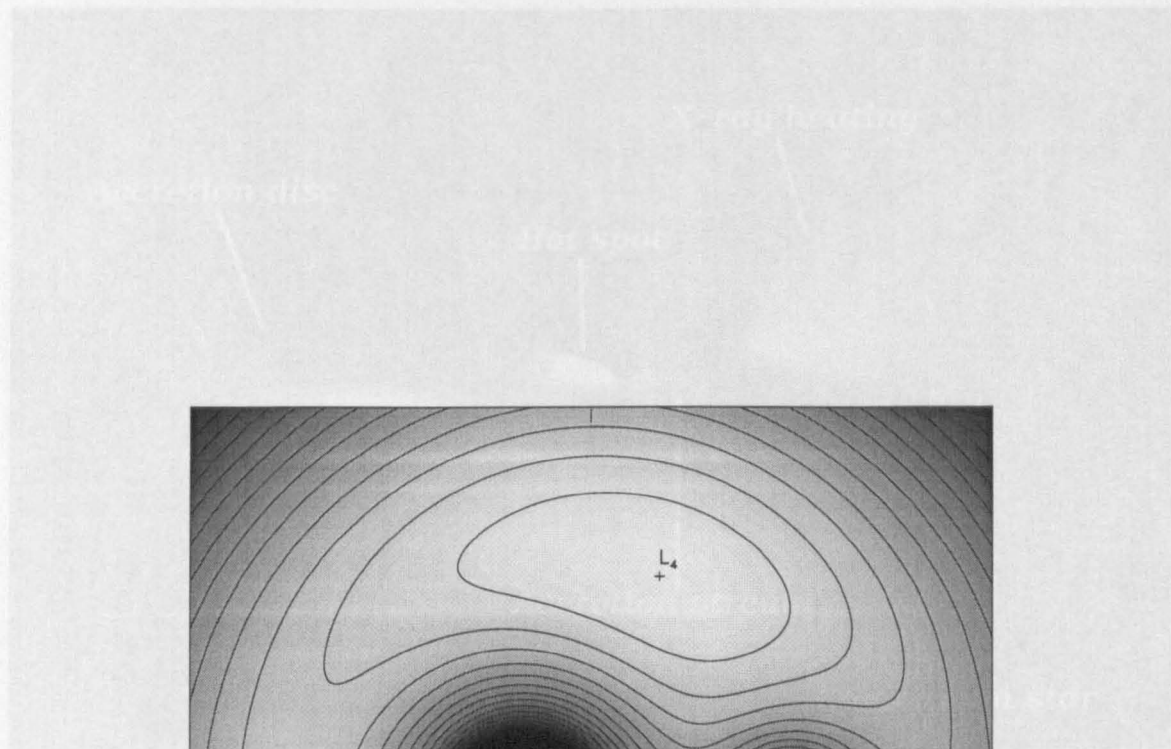


Figure 1.1: Roche potential of a typical binary, $q = 0.33$. If this were a typical interacting binary, the more massive star on the left would be the accretor and that on the right the mass donor. The potential is represented by both greyscale and equipotential contours. The Lagrangian points, stationary points on the surface, are represented by L_{1-5} .

extreme level of interaction and is now detected only in the outburst of low-mass X-ray binaries (LMXBs) and in the outburst of high-mass X-ray binaries (HMXBs).

Figure 1.1: Roche potential of a typical binary, $q = 0.33$. If this were a typical interacting binary, the more massive star on the left would be the accretor and that on the right the mass donor. The potential is represented by both greyscale and equipotential contours. The Lagrangian points, stationary points on the surface, are represented by L_{1-5} .

LMXBs are persistent, variable, X-ray sources. In the quiescent state, the X-ray emission is very low, but it increases during outbursts. The outbursts are caused by the accretion of material from the companion star onto the surface of the compact object.

LMXBs are persistent, variable, X-ray sources. In the quiescent state, the X-ray emission is very low, but it increases during outbursts. The outbursts are caused by the accretion of material from the companion star onto the surface of the compact object.

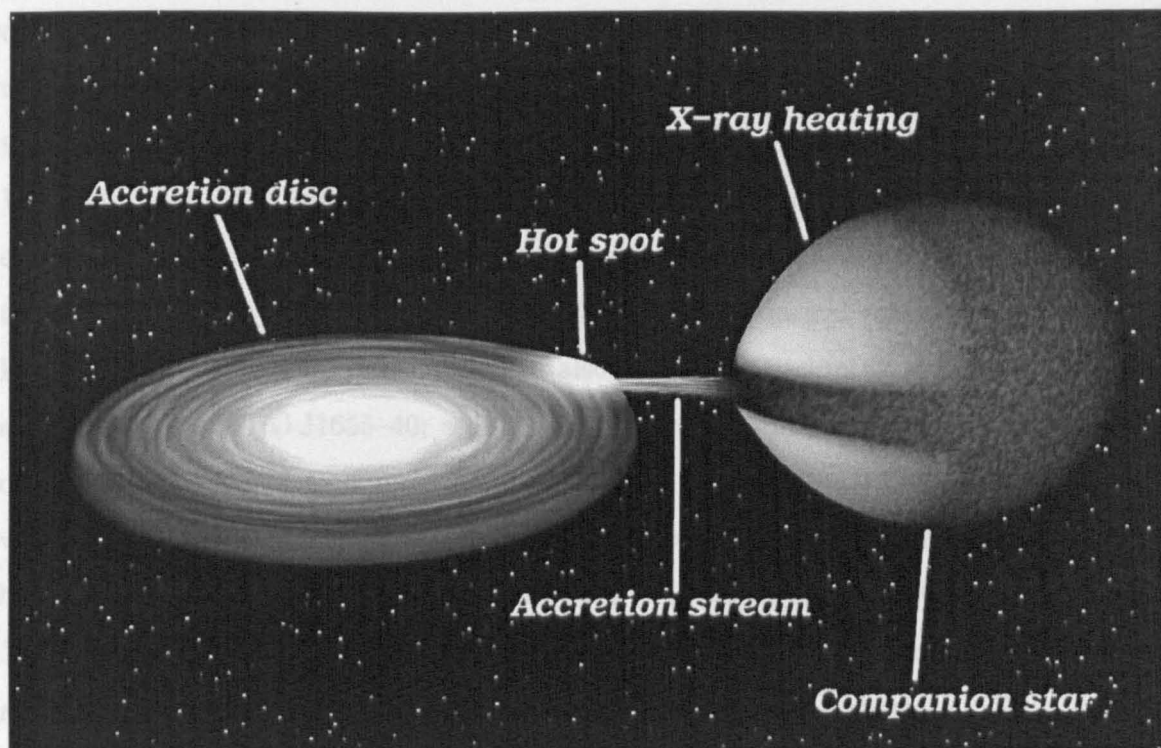


Figure 1.2: Schematic picture of an LMXB in outburst. The image was generated by the author using a custom written code for a mass ratio of 0.33. The greyscale represents logarithmically scaled black body fluxes at 5500 \AA . Realistic temperature distributions were used for the disc and star, but the strength of heating of both were set to very low values so that all parts of the system were visible. Normally the disc and heated face of the companion will be *much* brighter than the unheated regions and the latter will effectively be invisible.

extreme level of interaction and, in some detached high-mass X-ray binaries (HMXBs), interaction occurs via a strong stellar wind. This work will, however, focus upon semi-detached, lobe overflow systems, more particularly low-mass X-ray binaries (LMXBs). These contain a neutron star or black hole accreting from a low mass ($\lesssim 1 M_{\odot}$) star. The class is closely related to cataclysmic variables in which the accretor is a white dwarf; indeed the distinction can become blurred when considering supersoft X-ray sources (Kahabka & van den Heuvel 1997), now believed to have white dwarf primaries sustaining steady nuclear burning on their surface, but until recently considered to be black hole candidates.

Most known LMXBs are persistent, if variable, X-ray sources; famous examples include Sco X-1, Her X-1 and Cyg X-2. The transient systems only emit significant X-rays in

distinct outbursts, however (Tanaka & Shibazaki 1996). These outbursts are relatively rare, with recurrence times typically of decades. When they do occur, they are spectacular, with increases in X-ray flux of up to a factor of 10^8 and optical brightening of up to 10 magnitudes. The prototypical SXT, A 0620–00, stunned astronomers in 1975 by its extreme X-ray brightness, e.g. 23 times the brightness of the Crab supernova remnant in the 2–18 keV energy band (Elvis et al. 1975)², and an optical magnitude of ~ 12 (see Figure 1.3). Strong radio outbursts are also observed (Hjellming & Han 1995) and in some cases (e.g. GRO J1655–40; see Chapter 4 for more discussion) relativistic ejections occur. It is observed that most of the transient LMXBs contain black hole accretors, whereas persistent sources appear all to involve accretion onto a neutron star. It should be emphasised that these are low mass X-ray transients, in contrast to the high mass X-ray transients in which a neutron star is in an eccentric orbit around a Be star. The low mass transients are more commonly referred to as soft X-ray transients (SXTs) or X-ray novae (XRN). Neither of these are fortunate choices of name: some SXTs are actually hard X-ray sources (e.g. GRO J0422+32; see Chapter 7) and X-ray novae involve a completely different outburst mechanism to classical novae. Nonetheless, for continuity with existing literature, the term SXT will be used from henceforth.

This work describes observations of four SXTs at various stages of outburst. Two, GRO J1655–40 and GRO J0422+32, are considered strong black hole candidates; the third, XTE J2123–058 has a neutron star accretor and in the fourth, XTE J2012+381, the compact object type is unknown.

1.2 The Origin and Evolution of LMXBs

The origin of LMXBs is relatively uncertain; Verbunt (1993) and Verbunt & van den Heuvel (1995) discuss the important issues and these works provide the primary source for this section. By comparison, for CVs a fairly clear picture exists (Kolb 1996) even if details, such as angular momentum loss mechanisms, remain to be resolved.

The most likely origin of an LMXB is in a wide binary with an extreme mass ratio. The progenitor of a black hole or neutron star must be much more massive than the low-mass companion; hence the extreme mass ratio. Such a star will expand dramatically in its later phases of evolution. If the companion is too close, then it will be engulfed by the envelope of the giant star, and will spiral in and eventually merge with the giant's core. If the

²A 0620–00 remains the brightest extra-Solar X-ray source ever observed.

companion is too distant, it will not be engulfed at all, and the binary will remain wide. Formation of an LMXB thus appears to require some fine tuning, with the companion close enough to enter the giant's envelope and spiral in, but far enough out that the giant will undergo a supernova before a complete merger occurs. As the envelope of a giant is very tenuous, this case will likely leave the low-mass companion largely unchanged. Note that unlike the common envelope phase of CV evolution, because of the extreme mass ratio, the spiralling in process will probably not release enough energy to drive off the common envelope; thus the companion will still be within the envelope when the supernova occurs.

The largest difficulty with this picture is how the system can remain bound through the supernova. The compact object progenitor will lose a lot of mass very quickly and the companion will find itself essentially with the same position and velocity as before the supernova, but in orbit around a much less massive object. It may, therefore, no longer be gravitationally bound. One suggested solution involves neutron star kicks, asymmetric supernova explosions that can give a neutron star a velocity of order 100 km s^{-1} . If the direction of the kick is right it can compensate for the mass loss, but for every LMXB saved in this way, several others will be disrupted. Other solutions invoke a less massive progenitor that initially forms a white dwarf before undergoing accretion induced collapse, or a triple star system. This problem is mainly relevant to the formation of neutron star LMXBs; in the black hole case, a smaller fraction of the progenitor's mass is likely to be lost in the supernova and so the companion will remain bound in most circumstances.

After the spiral-in and supernova, the companion will be in a detached but fairly close orbit, probably eccentric. Tidal interactions between the stars will tend to circularise the orbit and synchronise the rotation of the companion with the binary orbit, so that it always presents the same face to the compact object. Orbital angular momentum losses will also occur and will cause the orbital period and separation to shrink; eventually the companion will come into contact with its Roche lobe and mass transfer will begin. Angular momentum loss will continue to shrink the binary and it is this (normally) which drives sustained mass transfer. Gravitational radiation will always lead to an angular momentum loss. Except for very close binaries, however, this will not be very effective and cannot account for inferred mass transfer rates of many systems: a stronger angular momentum loss mechanism is thus needed. The most likely candidate is magnetic braking. Rapidly rotating late type stars are expected to have strong magnetic fields. These enforce corotation of the stellar wind, allowing the latter to carry away significant rotational

angular momentum from the star. The star's rotation is, however, coupled to the orbit by tidal forces; hence the stellar wind effectively carries away orbital angular momentum. Even this process will not shrink the orbit enough for binaries with large initial separations to interact. These will only become LMXBs when the companion evolves off the main sequence and expands to fill its Roche lobe.

1.3 X-Ray States of LMXBs

A convenient description of the behaviour of LMXBs is provided by the X-ray spectral state classification. van der Klis (1994) suggested that the spectral and variability behaviour of black hole XRBs and those containing low magnetic field neutron stars can be well described in terms of three states: low, high and very high. For an update see van Paradijs (1998). Five states have now been identified based on X-ray energy spectra and variability characteristics, i.e. the power-density spectra (PDS). The states appear to be determined by the mass accretion rate; in increasing order of this quantity they are:

- **Quiescent:** The very low-luminosity state occupied by quiescent SXTs. Faintness is the main identifying feature and precludes detailed spectral or timing analysis at present.
- **Low (hard):** The energy spectrum takes a power-law form. Variability is very strong, with the PDS dominated by broad-band noise, dropping off as a power-law at higher frequencies.
- **Intermediate:** The flux is intermediate between low and high states. There are spectral and timing similarities to the very high state, however.
- **High (soft):** The energy spectrum is characterised by a two component form with a soft thermal component and hard power-law tail. Variability is extremely low, with a power-law PDS.
- **Very high:** The power-law spectral component is stronger relative to the thermal component. Variability strength is intermediate between the low and high states. The PDS shows band limited noise similar to the low state, but with the addition of strong quasi-periodic oscillations (QPOs) with frequencies of order 10 Hz.

These states are not exclusive to LMXBs. For example, the HMXB and black hole candidate Cyg X-1 alternates between the low and high states and has also exhibited an

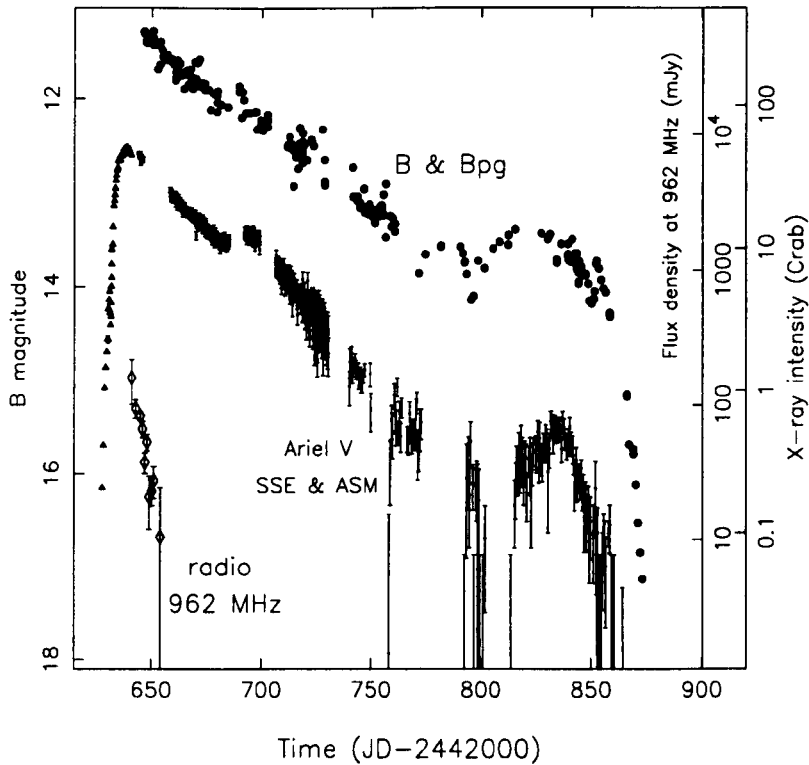


Figure 1.3: Optical, X-ray and radio outburst lightcurves of the prototypical SXT, A 0620–00. Taken from Figure 1 of Charles (1998) which was in turn simplified from Figure 4 of Kuulkers (1998a).

intermediate state (Belloni et al. 1996). The states appear to reflect the structure of the inner accretion flow, and are therefore independent of the nature of the companion star and, to some extent, the compact object.

1.4 Characteristics of SXT Outbursts

A thorough compilation of SXT lightcurves has been presented by Chen, Shrader & Livio (1997). The ‘canonical’ SXT light curve is characterised by a fast rise, exponential decay form. The optical and X-ray light curves of the prototypical SXT A 0620–00 are a good example; they are reproduced in Figure 1.3. Many other systems have shown lightcurves with similar characteristics, e.g. GRO J0422+32 (Chapter 7) and XTE J2123–058 (Chapter 5). Some other systems show the same lightcurve structure, but have linear rather than exponential decays, e.g. XTE J2012+381 (Chapter 6); see Shahbaz, Charles & King (1998) for a classification of systems into exponential or linear decay. There are other light curves which are very different to this, however. Chen, Shrader & Livio (1997) identify triangular

outbursts (with a much slower rise), outbursts with short or long plateaus, outbursts with variable decay rates and multiply peaked outbursts. A good example of the latter is GRO J1655–40 (Chapter 4).

Several common features can be identified in the fast rise, exponential decay lightcurves, as illustrated in Figure 1.3. The outburst rise is typically exponential, or at least the period of steepest rise is. Rise timescales (defined by Chen, Shrader & Livio (1997) as the e-folding time on the steepest part of the rise) are concentrated around 1–2 d. Decay timescales are longer; there is a wide spread, peaking around an e-folding time of 24 d. This is for the X-ray light curves. An optical rise has never been fully observed and decay times are up to three times longer than in X-rays. This difference in decay rates reflects spectral changes during the decay; as the disc cools, its spectrum shifts to lower energies. Even at outburst peak, most X-ray emission comes from the high-energy end of the thermal disc spectrum (its Wien tail), and consequently drops off steeply as the temperature decreases. The optical emission, however, initially comes from the low-energy Rayleigh-Jeans tail of the disc spectrum. As the disc cools, the disc spectrum shifts into the optical band slowing the apparent decay. At the very end of the outburst (or at least the brightest phase of it) the decay becomes non-exponential and X-ray and optical fluxes drop off steeply. This can be seen in A 0620–00 in Figure 1.3. An even clearer case is provided by GRO J0422+32; see Figure 7.1.

The monotonic decay is usually interrupted by one or more secondary maxima, classified as glitches, bumps and mini-outbursts. A glitch is a small step-like rise after which the decay continues as normal, but from the new, higher level; a glitch is seen after day 680 in the X-ray lightcurve in Figure 1.3. Optical and UV glitches are also present, although they can be harder to distinguish. Glitches occur within the first hundred days of the outbursts and are always the first secondary maximum to occur. Bumps also occur during the exponential decay phase, but drop off after the peak, rather than resuming the exponential decay from the bump peak. A bump is seen in Figure 1.3 peaking around day 830 in the X-ray light curve. Mini-outbursts have been less extensively studied because they occur after the steep drop-off and may have often been missed. The best example is GRO J0422+32 (Figure 7.1). They resemble short outbursts.

Optical and UV observations of SXTs in outburst (and persistent LMXBs) reveal evidence for substantial heating of the disc and companion star (van Paradijs & McClintock 1995), with hot, blue spectra (inferred temperatures of 25000 K or more) and high excita-

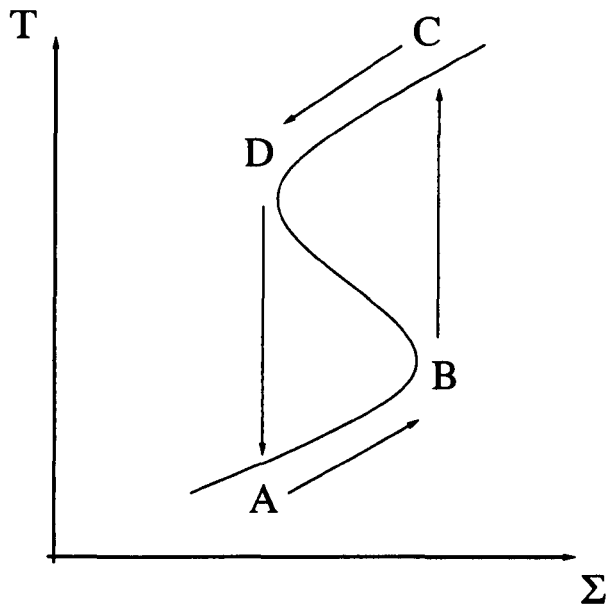


Figure 1.4: The limit-cycle disc instability mechanism. Axes are disc surface local surface density (Σ) and local effective temperature (T). The arrows indicate the limit-cycle behaviour. See text for description.

tion emission lines such as He II and C IV. LMXBs appear brighter in outburst than can be readily explained by viscous heating alone (see Section 4.7.1 for a discussion of how this problem applies in GRO J1655–40) and strong optical modulations are often seen due to viewing the strongly heated inner face of the companion star from varying angles (see Chapter 5 for examples of this modulation in XTE J2123–058.) There remain difficulties in understanding how irradiation can occur, however (Dubus et al. 1999 and references therein), as theory predicts that the disc should adopt a convex radial profile shielding the outer parts from direct irradiation. Additional factors, such as scattering of X-rays or disc warping are required to explain the observational evidence that irradiation of the outer disc does occur.

1.5 The Outburst Mechanism

The most promising models for explaining SXT outbursts invoke the thermal-viscous limit cycle instability previously developed for cataclysmic variables; the so called disc instability model (DIM). See Cannizzo (1999) and references therein for an overview of the current situation. The basic instability mechanism arises from the highly temperature sensitive opacity of disc material when hydrogen is partially ionised. This is commonly represented

by the equilibrium surface density vs. effective temperature relation shown in Figure 1.4; the S-curve. The curve shows local equilibrium disc states. Only the lower (AB) and upper (DC) branches are stable, however; these correspond to cool, low-viscosity and hot high-viscosity states respectively. The branch connecting them (BD) is thermally and viscously unstable. To appreciate this simply, it is necessary to realise that the temperature is directly related to the mass transfer rate (for a steady state disc then $T^4 \propto \dot{m}$; Frank, King & Raine 1992) since material falling inwards loses gravitational energy, hence viscously heating the disc. This does not depend on the details of the viscosity mechanism, but will be modified by non-viscous heating (e.g. X-ray irradiation.) Because of this the vertical temperature scale of Figure 1.4 is equivalent to a scale of the mass transfer rate, or $\dot{\Sigma}$. On the branch BD the effect of increasing Σ is thus to decrease $\dot{\Sigma}$; hence mass will pile up and Σ will increase further.

The behaviour of an LMXB depends on where its disc annuli lie in the $\Sigma - T$ plane, and thus on the mass transfer rate from the companion. If the mass transfer rate is low, all parts of the disc are on the lower branch and the system will be permanently quiescent. If the mass transfer rate is high, the whole disc will be on the upper branch and the system will be a persistent X-ray source. If the mass transfer rate would require some parts of the disc to lie on the unstable middle branch, however, the system may be a transient³, and annuli will follow a limit cycle (ABCD...) around its unstable equilibrium state. Consider a single disc annulus in more detail. Beginning from A, the annulus is in the cool state, with a low disc viscosity. This is insufficient to allow all the mass flow from the companion to be accreted; hence the disc surface density will increase and the annulus will move to the right along the equilibrium line AB. When it tries to pass beyond B, there will be no equilibrium state available on the lower-branch and a transition to the upper branch will occur. On this high viscosity branch, however, material is accreted faster than it is replenished by the companion and the surface density will decrease again (CD). When D is reached, the density cannot decrease any more on the upper branch and a transition back down to the lower branch occurs and the cycle begins again.

Of course different annuli will evolve independently, and will not reach the end of a branch simultaneously. The global behaviour is believed to depend on heating and cooling waves. At the beginning of an outburst, the first annulus to reach B will make the transition to the hot state. This will trigger a heating wave which will propagate through the disc so that the rest of the disc also enters the hot state. At the end of the outburst,

³See the discussion of irradiation below for a caveat to this.

the first annulus to make the transition to the cool state will trigger a cooling wave. In the standard model (a disc heated only by viscosity) the rise of the outburst corresponds to the rapid propagation of the heating wave, and the exponential decay to the slower cooling wave propagation. Some fine tuning of the radial variation in viscosity is required to produce an exponential decay.

More recently, King & Ritter (1998) have emphasised the importance of X-ray irradiation in heating the disc. This can maintain the disc in the hot state even when viscous heating would not, and hence delay the propagation of a cooling wave. In this variation of the model, the exponential decay corresponds to the purely viscous draining of the disc while it is entirely in the hot state. When irradiation is weak enough to allow a cooling front to form, the decay accelerates; this is the drop-off at the end of the exponential decay phase. If irradiation is never strong enough to suppress the cooling wave (mainly an issue for long-period systems) then the exponential decay phase does not happen and the decay is expected to be linear, as seen in XTE J2012+381 (Chapter 6).

This fusion of the DIM with irradiation has met with some success in explaining the outburst behaviour but there remain difficulties. One of the strongest is that the long recurrence time of SXT outbursts requires an extremely low quiescent viscosity. Nevertheless, significant X-ray luminosity is detected in quiescence, far more than can be consistent with such a low viscosity. An extra ingredient is needed for the inner disc regions producing X-rays; the proposed solution is that the inner disc evaporates into an advective flow.

1.6 Advective Accretion Flows

The difficulties with applying the ‘standard’ DIM to quiescent SXTs led to the application of models of advective accretion flows to SXTs (Narayan, McClintock & Yi 1996). The essential idea is that there exist stable accretion flows (for low mass transfer rates) which radiate very inefficiently and hence can advect energy into a black hole event horizon (i.e. there is bulk transport of thermal energy released by viscosity.) Physically this situation can arise in low density flows if the Coulomb coupling between ions and electrons is very weak. Viscosity is then likely to predominantly heat the ions due to their larger mass (Narayan & Yi 1995; see Quataert & Gruzinov (1999) for a critique of this assumption.) They do not radiate efficiently, however, and if they are unable to transfer energy to the electrons then the energy remains locked in the flow. The flow becomes a two temperature

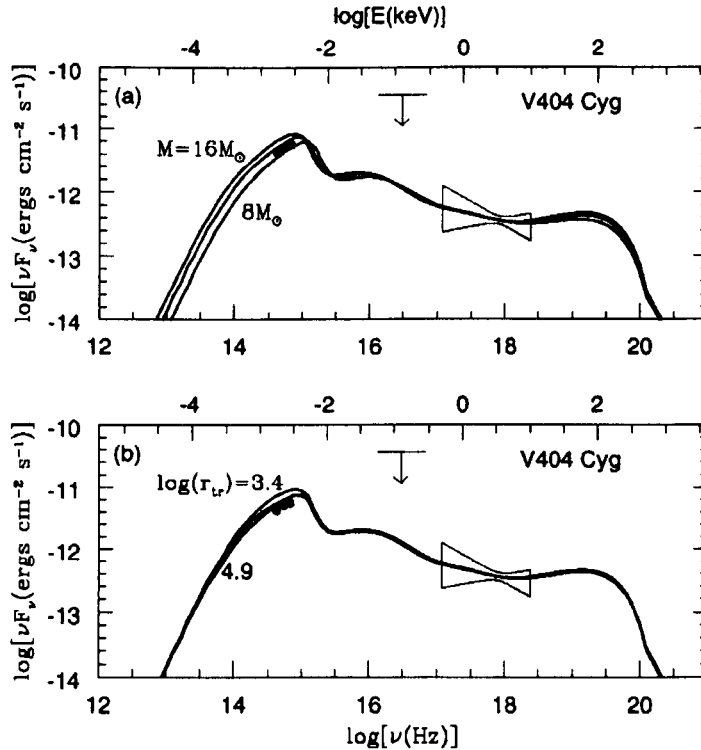


Figure 1.5: Advective model fits to the broad band spectrum of V404 Cyg in quiescence. The upper panel shows models with varying masses, the lower panel varying transition radii. Taken from Figure 4 of Narayan, Barret & McClintock (1997).

one, with hot ions ($T_i \sim 10^{12}$ K) and cooler electrons ($T_e \sim 10^{10}$ K). This model predicts low luminosity high energy emission (emitted non-thermally) from the small amount of ionic thermal energy that can ‘leak’ to the electrons via Coulomb interactions.

The global accretion flow structure suggested is that there is a conventional geometrically thin disc in the outer part of the Roche lobe. At some transition radius, this becomes evaporated (see Meyer 1999 for discussion of possible mechanisms) into a quasi-spherical, optically thin flow. In this inner low density flow, ion–electron interactions are ineffective and so the flow is advective. The models that have been most extensively applied are the Advection Dominated Accretion Flow (ADAF) models described in Narayan, McClintock & Yi (1996) and Narayan, Barret & McClintock (1997). These models initially used a self-similar solution for the structure of the ADAF, but later versions employed self-consistent global solutions. The predicted spectrum takes a multi-peak form, shown in Figure 1.5 as applied to V404 Cyg. From left to right, the first peak, in the optical, is due to self-absorbed synchrotron emission as electrons spiral around tangled magnetic fields

that are assumed to be advected with the flow. The second, soft X-ray, peak is caused by Comptonisation of the synchrotron peak. The third peak in hard X-rays is an amalgam of multiple Compton scatterings and bremsstrahlung emission. These spectral fits, albeit based on very sparse data, have been presented as evidence that the advective models are the best description of quiescent SXTs. So far published applications of the model to SXTs comprise A 0620–00 (Narayan, McClintock & Yi 1996; Narayan, Barret & McClintock 1997), V404 Cyg (Narayan, McClintock & Yi 1996; Narayan, Barret & McClintock 1997), X-ray Nova Muscae 1991 (Narayan, McClintock & Yi 1996; Esin, McClintock & Narayan 1997) and GRO J1655–40 (Hameury et al. 1997).

Although the advective models were initially developed to explain the quiescent behaviour of SXTs, the hybrid thin disc plus advective flow picture has subsequently been extended as a possible model for all of the spectral states described in Section 1.3 by Esin, McClintock & Narayan (1997). The proposed scheme is illustrated in Figure 1.6. Beginning from the quiescent state, as the mass transfer rate is increased the density of the ADAF increases resulting in enhanced Comptonisation. Gradually, Comptonisation of synchrotron photons by the hot electrons becomes the dominant process for electron cooling; this is the (smooth) transition from the quiescent to low state. The enhanced Comptonisation, not only of synchrotron photons but also soft thermal photons from the disc, will increase the cooling rate of the electrons. At the same time, the increasing density in the flow (due to the increasing mass transfer rate) will lead to stronger Coulomb coupling between ions and electrons; hence the ion cooling will also increase. This will lead to a kind of condensation, with the ADAF collapsing down into a thin disc. This is expected to occur first at the outer edge of the ADAF, causing the disc to move inwards. The period when the inner disc radius is decreasing is identified with the intermediate state. When the mass transfer rate is high enough that an ADAF cannot exist at any radius, the thin disc extends to close to the black hole and its thermal emission dominates. This is the high state. To explain the very high state requires the input of additional physics, which Esin, McClintock & Narayan (1997) admit is very speculative. The very high state exhibits a stronger power-law component in the energy spectrum and enhanced variability. Both are likely associated with the corona, so to incorporate the very high state into the model requires some way to reverse the process of condensation of the corona. It is suggested that this could occur due to direct energy dissipation in the corona, perhaps by reconnection of magnetic field loops expelled from the disc. Esin, McClintock &

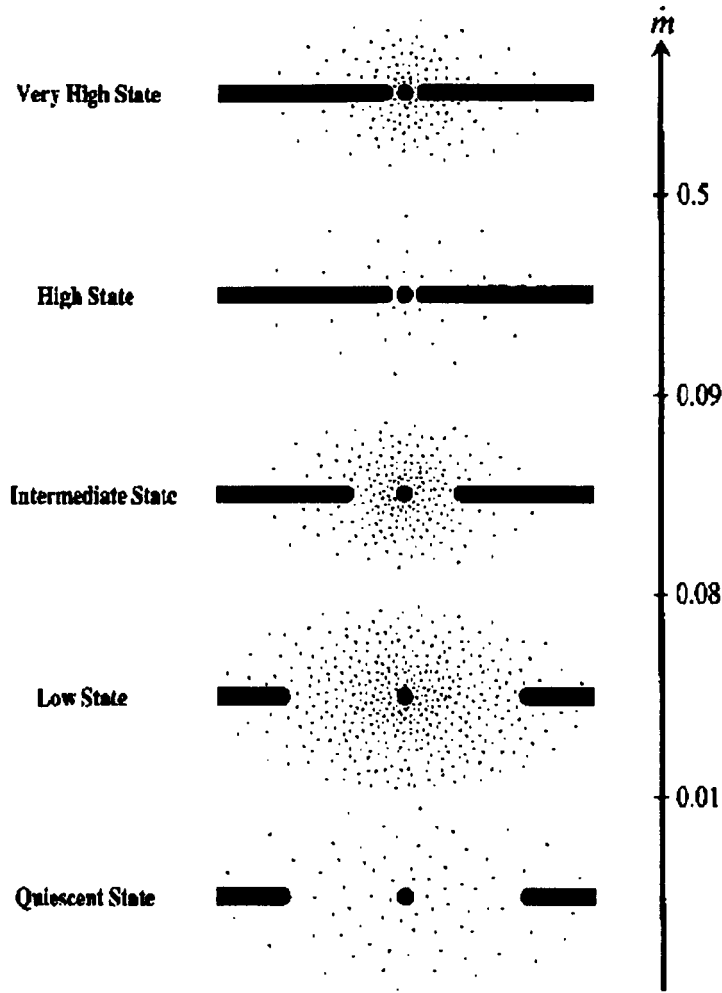


Figure 1.6: Suggested interpretation for X-ray spectral states in the context of advective models. Taken from Figure 1 of Esin, McClintock & Narayan (1997).

Narayan (1997) have demonstrated some success in modelling the spectral evolution of X-ray Nova Muscae 1991 (which was observed in all five spectral states) using this model. Życki, Done & Smith (1998) have independently used observations of the smearing of the X-ray reflection spectrum in this system to show that the inner disc radius does change in qualitative agreement with the model of Esin, McClintock & Narayan (1997) but that the retreat of the disc during decline is slower than predicted.

There remain many critics of the ADAF models in detail (many of whom would accept that advection in some form is important). The models do make a number of *ad hoc* assumptions. For example the transition radius is generally taken to be as large as possible without being inconsistent with observed $H\alpha$ emission velocities. In fact $H\alpha$ emission

Table 1.1: Properties of SXTs with dynamical mass estimates. Unless otherwise noted, data are taken from Charles (1998); see that work for full references. Updated values are from: 1. Webb et al. (1999), 2. Shahbaz et al. (1996), 3. Filippenko et al. (1999), 4. Shahbaz, Bandyopadhyay & Charles (1999b), 5. Shahbaz et al. (1999a).

Name	V_{\min}	P_{orb} (hrs)	$f(M)$ (M_{\odot})	M_x (M_{\odot})
GRO J0422+32	22.2	5.1	1.19 ± 0.02^1	$> 7.25^1$
X-ray Nova Vel 1993	20.6^2 (R)	6.9^2	3.17 ± 0.12^3	$> 3.9^3$
A 0620–00	18.3	7.8	2.91 ± 0.08	$\sim 6.4^3$
GS 2000+25	21.5	8.3	5.01 ± 0.12	10 ± 4
X-ray Nova Muscae 1991	20.5	10.4	3.01 ± 0.15	6_{-2}^{+5}
X-ray Nova Ophiuchi 1977	21.5	12.5	4.86 ± 0.13	6 ± 2
Cen X-4	18.4	15.1	0.21 ± 0.08	1.3 ± 0.6
4U 1543-47	16.6	27.0	0.22 ± 0.02	5.0 ± 2.5
GRO J1655–40	17.2	62.9	2.73 ± 0.09^5	$5.5 - 7.9^5$
V404 Cyg	18.4	155.3	6.08 ± 0.06	12 ± 2

indicates only that the thin disc extends at least this far in, and hence provides only an upper limit on the transition radius.

A major concern at present was raised by Blandford & Begelman (1999) who demonstrate that an advective flow has a positive Bernoulli constant, indicating that the flow is unbound. Consequently it may be that significant outflows occur, even in quiescence; Blandford & Begelman (1999) refer to such accretion flows as adiabatic inflow-outflow solutions (ADIOS). It is unclear how much effect this will have, if any. The positive Bernoulli constant indicates the possibility of outflows, but does not require them. If strong outflows do occur then this is likely to change the structure of the advective flow, and hence the predicted spectra, significantly.

1.7 The Evidence for Black Holes in SXTs

Evidence for the definite existence of Galactic black holes has long been sought, but until recently, there was only one strong black hole candidate, the HMXB Cyg X-1. Studies of SXTs have changed this picture and the majority of black hole candidates are now SXTs

(Charles 1998). SXTs present an especially appealing environment in which to study black holes because in quiescence it is possible to study the light from the companion star almost in isolation. By measuring the Doppler shifts of its absorption lines, one can measure its projected orbital velocity and hence constrain the mass of the object it is orbiting around. More specifically, from the orbital period and observed radial velocity semi-amplitude, one can determine the mass function, $f(M)$ (Frank, King & Raine 1992),

$$f(M) = \frac{K_2^3 P}{2\pi G} = \frac{M_1 \sin^3 i}{(1+q)^2} M_\odot. \quad (1.2)$$

While the first form of mass function is expressed in terms of directly measurable quantities, the second contains information about the stellar masses. Given a measured $f(M)$ (from the observed period and radial velocity curve),

$$M_1 = \frac{\sin^3 i}{(1+q)^2} f(M). \quad (1.3)$$

If the binary mass ratio ($q = M_2/M_1$) and inclination, i , can also be estimated then clearly a full solution is possible, including the compact object mass. Even without this, however, the mass function is useful, as $\sin^3 i \leq 1$ and $1+q > 1$; hence $M_1 > f(M)$. The mass function therefore represents an absolute lower limit to the compact object mass. Table 1.1 summarises the current state of dynamical mass determinations of SXTs.

Dynamical arguments for a black hole accretor then rely on the assumption that any compact object too massive to be a neutron star must be a black hole. Exactly what this maximum neutron star mass should be is a subject of debate. The problem arises from uncertainty about the equation of state of degenerate neutron matter. Consequently, strict upper limits must come from identifying a minimal set of constraints that must be satisfied by any plausible equation of state. The commonly accepted maximum mass is $3.2 M_\odot$ derived by Rhoades & Ruffini (1974) based on i) assuming a non-rotating neutron star, ii) requiring causality to be obeyed (i.e. requiring the speed of sound to be less than c), and iii) assuming that the equation of state is known up to a density of $\rho_0 = 4.6 \times 10^{14} \text{ g cm}^{-3}$. None of these assumptions are unassailable, as discussed by Friedman & Ipser (1987): rapidly rotating neutron stars do exist (millisecond pulsars), the causality constraint only applies in a non-dispersive medium and the value of ρ_0 chosen is somewhat optimistic. Friedman & Ipser (1987) show that relaxing the causality constraint, choosing a more conservative value for ρ_0 and considering a maximally rotating neutron star can increase the theoretical upper mass limit to as high as $\sim 14.3 M_\odot$. An even more exotic alternative has been suggested in the form of Q stars (Bahcall, Lynn & Selipsky 1990; see Miller,

Shahbaz & Nolan 1998 and references therein for a recent discussion). Q-stars have very different equations of state to neutron stars and in principal, these could have masses $> 100 M_{\odot}$. In practice, however, even a $12 M_{\odot}$ Q-star (appropriate for V404 Cyg) requires the Q-matter equation of state to be applicable at implausibly low densities (a factor of ten less than that of normal nuclear matter).

Defining an absolute and general upper limit for the mass of any compact object that is not a black hole is thus difficult. Leaving aside theoretically possible equations of state and considering actual proposed prescriptions, however, Friedman, Parker & Ipser (1986) showed that from a sample of ten suggested equations of state, the largest mass possible, allowing for maximal rotation, was $\sim 3.2 M_{\odot}$, consistent with the Rhoades-Ruffini limit. Most researchers in the field would probably accept that a compact object more massive than this must be a black hole. Observational evidence points to neutron star masses much less than this and the recent review of Thorsett & Chakrabarty (1999) showed that radio pulsars have a remarkably narrow mass-distribution, all being consistent with $1.35 \pm 0.04 M_{\odot}$.

While it is difficult to prove conclusively that a compact object is not a neutron star, a positive identification is more straightforward: the detection of Type I X-ray bursts (Lewin, van Paradijs & van den Heuvel 1995) is considered a definite signature of a neutron star. These are thermonuclear explosions (analogous to classical nova explosions) on the neutron star surface. They occur on low magnetic field neutron stars due to a thermonuclear instability associated with the ignition of helium burning in accreted material. XTE J2123–058 (discussed in Chapter 5) shows Type I bursts, hence this is a neutron star transient.

In the absence of a persuasive dynamical mass estimate there are no definite signatures of a black hole. Rather there are a number of characteristics which are shown by most dynamical black holes but by few neutron stars. The presence of several of these signatures does not prove that the compact object is a black hole, but it does at least flag an object as a black hole candidate worthy of more detailed study. Suggested black hole diagnostics include (Tanaka & Lewin 1995) a high luminosity ultrasoft spectrum, a high energy power-law tail extending to above 20 keV, the detection of both high-soft and low-hard states and the presence of large amplitude (~ 30 per cent) flickering in the low state. For example, XTE J2012+381 (Chapter 6) showed an ultrasoft spectrum with a hard power-law tail (White et al. 1998) and was thus identified as a black hole candidate by these authors.

More recently, the successes of advective models described in Section 1.6 have led to

Table 1.2: Currently active ToO programmes to observe SXTs. Only those associated with the *HST/RXTE* collaboration are listed.

Facility	PI	Waveband	Type of observations
<i>RXTE</i>	Chen	X-ray	Timing and spectroscopy
<i>HST</i>	Haswell	UV/optical	Rapid spectroscopy
WHT	Haswell	Optical	Rapid spectroscopy
AAT	Haswell	Optical	Rapid spectroscopy
NTT	Chaty	Optical/IR	Photometry and spectroscopy
UKIRT	Haswell	IR	Photometry

claims that these provide direct evidence of the lack of a hard surface to the compact objects in black hole systems. In particular, systems previously believed to harbour black holes appear to be systematically X-ray fainter in quiescence than those known to contain neutron stars (Narayan, Garcia & McClintock 1997). This is proposed to prove that in black hole systems gravitational energy is advected through the event horizon whereas in neutron star systems it cannot escape view. The sample of available data is small, however, and selection effects need to be accounted for (for example systems of similar periods should be compared.) Menou et al. (1999) reexamine the data and find that, indeed, black hole systems are fainter and that their quiescent luminosities are consistent with stellar evolution models if advection occurs. They also find, however, that although neutron star systems are brighter than those containing black hole candidates, they are still a factor of $\sim 10^3$ fainter than predicted to be by advective models, indicating that the situation is more complex than the simple comparison between objects with and without solid surfaces. Menou et al. (1999) suggest that the reason for the discrepancy is that in quiescent neutron star systems a magnetic propeller suppresses accretion at low mass transfer rates, so that material is invisibly ejected rather than accreted. The subject of magnetic propellers in SXTs will be discussed further in Section 5.6.3.

1.8 The Multiwavelength Target-of-Opportunity Programme

As SXT outbursts are widely separated in time and unpredictable, their observation is painfully difficult. At the same time, it is extremely valuable to obtain simultaneous,

multiwavelength observations. For this purpose, a multiwavelength network of target-of-opportunity (ToO) programmes has been formed, to override existing schedules when a bright SXT is discovered. The jewel in the crown of the collaboration are linked *HST* (PI Dr. Carole Haswell) and *RXTE* (PI Dr. Wan Chen) programmes. It is intended that a series of simultaneous observations will be obtained from as near to the outburst peak as possible, through the decline. The goals for this simultaneous X-ray/UV/optical programme include monitoring the evolution of the broad band spectral energy distribution, performing echo-mapping to determine the location of X-ray reprocessing locations and obtaining velocity resolved observations of strong UV resonance lines. Other override programmes are in place on WHT, AAT, UKIRT (PI Dr. Carole Haswell) and at ESO (PI Dr. Sylvain Chaty) to support these observations in the optical and near infrared.

To date, *HST* has only obtained spectroscopic observations of three SXTs in outburst. X-ray Nova Muscae 1991 was observed in 1991 under director's discretionary time (PI Panagia; Cheng et al. 1992) and GRO J0422+32 was observed under the ToO very late in outburst (Chapter 7). Neither of these observations had simultaneous coverage from other facilities. The only real test of the network as a whole has been for GRO J1655-40. A series of simultaneous *HST* and *RXTE* observations were obtained from peak through decline as planned, and AAT observations were also made near the peak. These data form the subject of Chapter 4. All three SXTs were observed using the Faint Object Spectrograph (FOS). The currently active *HST* ToO will use the newer Space Telescope Imaging Spectrograph (STIS). This will be more efficient, and has new capabilities, including a high time resolution TIMETAG mode ideal for the echo-mapping project and echelle configurations permitting high velocity resolution for all of the UV resonance lines simultaneously. It remains to be seen how this, coupled with the other facilities available to the collaboration, will advance knowledge of SXT outbursts.

Chapter 2

REDUCTION OF DATA FROM GROUND BASED TELESCOPES

In this chapter will be considered the reduction of data obtained with several ground-based telescopes on low-mass X-ray transients in outburst. These data comprise photometric observations made with the Jacobus Kapteyn Telescope (JKT) and the United Kingdom Infrared Telescope (UKIRT) and spectroscopy using the Anglo-Australian Telescope (AAT) and the William Herschel Telescope (WHT).

All of these data were obtained using charge-coupled device arrays (CCDs), or their infrared counterparts. The goal in reducing such data is to translate the two-dimensional data recorded by such an array into either one-dimensional data in the case of spectroscopy, i.e. a spectrum, or zero-dimensional data in the photometric case, i.e. a magnitude. This transformation should be performed as precisely and accurately as possible. High precision is desirable in order to minimise random errors in the data; this is often measured by the signal-to-noise ratio of a spectrum or photometric light curve. Accuracy is also important: the final results should be subject to no systematic errors or biases. While it is desirable to achieve both of these goals simultaneously, sometimes they conflict: minimising random errors may only be possible at the expense of introducing systematic errors and vice-versa. A simple example of this problem is the choice of photometric aperture. A large aperture will collect virtually all of the starlight, and hence give an unbiased estimate of the total flux from the object. It will, however, allow a large amount of sky light into the aperture and while this can be subtracted without biasing the result, the random errors in the flux from the star will be increased. A smaller aperture will reduce the

sky contamination and hence the random error. Some of the starlight will, however, fall outside the aperture. Assuming a point spread function for the stellar image, this can be approximately corrected, but the result may be subject to a systematic error due to under or overestimating the loss outside the aperture. Other examples of this trade-off between precision (low random error) and accuracy (low systematic error) will be met in this chapter.

In reducing data, then, there are sometimes choices to be made. The reduction process is to some extent determined by what is to be done with results. While this will not be a strong theme of this chapter, in which it mostly is possible to perform a general-purpose reduction, it will become important in the following chapter on *HST* data where the same data may be reduced in several different ways to yield different information.

2.1 Preliminary Stages of CCD Data Reduction

The initial steps in CCD¹ data reduction are common to most datasets, whether photometric or spectroscopic. These comprise removing the base count rate induced by the bias voltage applied to the chip, subtracting any counts due to a dark current and correcting for sensitivity variations across the chip, both on large and small scales. For those datasets for which data reduction was performed by the author, standard IRAF tasks were used, principally from the CCDRED package (Massey 1997), supplemented by custom IDL routines where necessary.

2.1.1 Bias Removal

The process of reading out a CCD involves measuring an analogue voltage and converting it into a digitised sum of counts. In order to ensure that the output from this analogue to digital conversion is always positive, a small bias voltage is applied. This results in a non-zero base level for recorded counts. This plateau level (the bias) must be removed as the first stage of data reduction.

Ideally the bias level will be uniform across the chip and constant in time, so that it is sufficient to subtract a constant from each pixel. In practice this is seldom the case and both spatial and temporal variations must be accounted for. The approach taken in

¹While the detectors used in the infrared are not CCDs, many of the same data reduction principles apply; elements of this discussion are therefore also applicable to UKIRT data reduction, considered in Section 2.3.

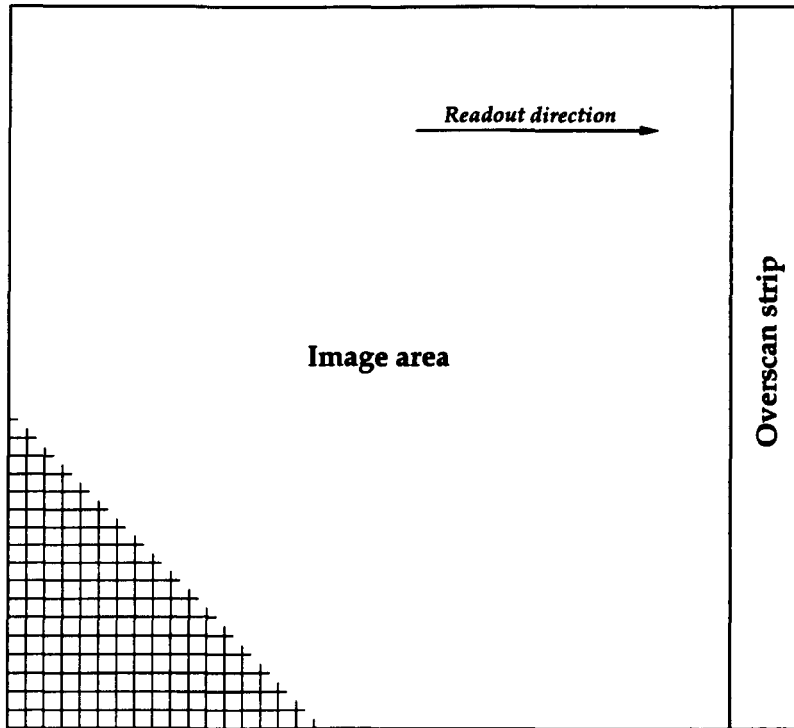


Figure 2.1: Layout of the overscan region on a typical CCD. Some detectors (e.g. the TEK4 on the JKT) may have multiple overscan regions on different sides. The size of the pixels is greatly exaggerated, and not all CCDs have a square image area.

this work is to use a combination of an overscan strip, on each image, which monitors time-dependence in the bias level, and a series of bias frames, typically taken during the day or at the beginning of the night, which measure the two-dimensional bias structure of the whole CCD.

In more detail, the overscan region will comprise of order twenty columns (see Figure 2.1). These will be averaged to estimate the bias level for each readout row. If the variation between rows is small then an average bias level may be used; otherwise the variation will be fit by a low-order polynomial or spline function. The reason for this fitting is that there will not be enough overscan columns to give a noise-free measure of the bias variation, and so if the averaged overscan region were simply subtracted as is, noise would be introduced into the image. This is an example of the trade-off between precision and accuracy inherent in data reduction: the fitted overscan region will avoid introducing unwanted noise into the image, but may not fully represent the structure present in the bias. The optimum compromise will vary from CCD to CCD. For the datasets considered, overscan correction was applied as part of the CCDPROC task in IRAF and was fitted with either a straight line or a first order spline.

The first order correction using the overscan region is applied to *all* images, including bias frames and flat-fields. After overscan correction, the bias frames ideally should be completely flat, but in practice often show a residual structure of order a few counts. To obtain the best measure of this structure a number of bias frames are averaged; 10–20 is usually adequate if no small scale structure is present. This is done using the ZEROCOMBINE task within IRAF, which in addition rejects the highest value recorded for each pixel to remove cosmic ray hits. To avoid introducing noise into images by subtraction of a noisy bias frame, a low-order surface fit to the bias variation is used. This is done using IMSURFIT within IRAF, the order of the x and y functions being increased until the residuals show negligible structure. The bias frames considered could be adequately fitted using polynomials of fifth order or less.

2.1.2 Dark Count Subtraction

The bias level of an image is independent of exposure time. CCDs are also subject to a dark current which gives an additional background count proportional to exposure time.² This dark count can in principle be measured by taking long exposures with the shutter closed. In practice it is usually negligible, and unless long periods of time are set aside to measure it, it cannot be determined well enough to be accurately subtracted, i.e. the uncertainty in the measurement is greater than the value. For this reason it is not corrected for in any of the datasets considered here.

2.1.3 Correction for Sensitivity Variations

After correction for additive effects (bias and dark count) the images should measure the recorded photons from source and sky. One must then correct for variations in sensitivity from pixel to pixel and from one part of the chip to another, and also for uneven illumination of the CCD. These corrections are done using flat fields, images of the inside of the dome, the twilight sky or a projector internal to the instrument. This is the most complex stage of the reduction process as it is necessary to correct for several effects simultaneously:

- Sensitivity variations intrinsic to the CCD between one pixel and another, typically on small spatial scales.
- Uneven illumination of the CCD due to dust, either on the CCD surface itself, on

²More properly to dark-time, which may include some additional integrating time when the shutter is closed.

the filter of a CCD camera or on the slit of a spectrograph. In photometry, this results in dust rings caused by diffraction of light by the dust particles; the size of the rings varies according to where in the optical path the dust lies. In spectroscopy a dusty slit will produce dark lines parallel to the spectrum. Dust presents a severe challenge to flat fielding as grains may move slightly according to telescope position, and may accumulate over the course of an observing run. Their behaviour is thus time-dependent.

- Uneven illumination on larger scales, for example due to vignetting in the optical path or a spectrograph with slightly non-uniform width.
- Fringing effects, caused by interference within a detecting thickness of the CCD comparable to the wavelength of light. This can be treated as a flat-fielding problem in reducing spectroscopy as a given region of the CCD receives monochromatic light, to within the spectral resolution. Photometric fringing, however, is more complex as a range of wavelengths, defined by the filter bandpass, are superposed. For a continuum spectrum, the fringing averages out. For sky lines, it may not do, resulting in a fringed emission line pattern superposed on an unfringed continuum image. Photometric fringing is not a problem in any of the datasets considered here, so will not be discussed further.

Given the complex nature of flat-fielding, and the need to tailor the method to specific datasets, further discussion of this topic will be deferred to the following sections in which individual sets of observations are considered in increasing complexity.

2.2 JKT Photometry of XTE J2012+381

Multicolour photometry of the field of XTE J2012+381 was obtained using the Jacobus Kapteyn Telescope (JKT) on 1998 June 3. The CCD camera (Telting 1999) was used with the TEK4 1024 × 1024 CCD. These data were obtained by Dr. Nic Walton through the JKT service programme. Only *V*, *R* and *I* band images showed the target. A log is given in Table 2.1.

Debiasing was performed using IRAF tasks as described above. Debaised flat fields were then combined, for each filter, using the FLATCOMBINE task. The total flat counts per pixel in each band were > 175000 electrons, so statistical noise in the flat-field frames will be < 0.25 per cent. As well as large scale non-uniformities, ~ 50 small dust rings were

Table 2.1: Log of useful JKT and UKIRT photometric observations of XTE J2012+381.

Date	Telescope	Observing period (UT)	Total exposure (s)	Band
1998 Jun 3	JKT	04:37–04:42	300	<i>I</i>
		04:44–04:52	500	<i>V</i>
		05:25–05:30	300	<i>R</i>
1998 Aug 14	UKIRT	11:17–12:37	580	<i>J</i>
		12:37–13:34	320	<i>K</i>

seen in the flat frames. These are common to all filters so arise from dust on the CCD. Initial data reduction was completed by dividing object frames by these flat-field frames; no residual dust effects were apparent.

The field is crowded so photometry used the DAOPHOT algorithms (Stetson 1987) as implemented in the DAOPHOT package within IRAF (Massey & Davis 1992; Davis 1994). This method measures the point spread function (PSF) of a set of template stars and then deblends the stars of interest assuming that they have the same PSF. It makes possible the measurement of positions and magnitudes even for very closely blended stars. The DAOPHOT algorithms are related to the method used in Section 2.6 for deblending spectra, so will be outlined in Appendix B.1 where that method is developed in detail.

Absolute flux calibration involves two stages: extinction correction and comparison with standard stars of known brightness. Both stages are potentially complicated in broad band photometry by variations in extinction and sensitivity across the filter bandpass. This means, for example, that for *V* band observations of a very red star and a very blue one, the red star will suffer less extinction than the blue one. This is because the *V* band light from the red star predominantly comes from long wavelengths (low extinction), whereas that from the blue star mainly comes from shorter wavelengths (higher extinction). Thus in principle, extinction corrections should be colour-dependent. In practice, to calibrate at this level of accuracy requires observations of standard stars of a range of colours at a range of airmasses. Only a single airmass was available for these data so it was not possible to calculate an atmospheric extinction curve specific to this night. Standard extinction coefficients, provided by Dr. Iain Steele were instead used. These are 0.15 mag. per airmass

in V , 0.09 in R and 0.05 in I .

It is also beneficial to perform a colour-dependent calibration against standard stars, if possible. This takes account of differences between the photometric system in which the standards were defined (typically a particular combination of photomultiplier and filter) and the actual system used on the telescope (determined by a CCD and a different filter.) This was possible for these data as the standards in our calibration field (stars 499, 502, 503, 506 and 507 from Landolt standard field 110; Landolt 1992) span a range in colours from $V - R = 0.335 - 1.373$. XTE J2012+381 is only slightly outside this range. As can be seen from Figure 2.2, a significant colour dependence is present, especially in the I band, reflecting differences between the photometric system used by Landolt (1992) and that of the JKT.

2.3 UKIRT Photometry of XTE J2012+381

Data from the United Kingdom Infrared Telescope (UKIRT) on XTE J2012+381 was obtained under the UKIRT Service Programme by Dr. Chris Davis and Dr. John Davies; it was offered to the author by Dr. Malcolm Coe. Data reduction was performed by him; photometry and calibration by the author. The following description of the data is adapted from his contribution to Hynes et al. (1999).

UKIRT observations were obtained on 1998 August 14. The weather was clear, winds were light and the humidity was low. The images were obtained using the IRCAM3 camera (Leggett 1999). The detector array has a size of 256×256 , with a pixel scale of 0.286 arcsec. A total of 29×20 s exposures were obtained in J and 32×10 s in K . A log is given in Table 2.1. Data reduction was performed using IRCAMDR software.

As for the JKT observations, point spread function fitting was done using DAOPHOT in IRAF. Flux calibration was performed with respect to the UKIRT standard FS4 (Casali & Hawarden 1992). The data on the standard were taken between the J and K band observations of the source. Extinction is a small effect in the infrared, so no corrections were applied for this.

2.4 AAT Spectroscopy of GRO J1655-40

Anglo-Australian telescope (AAT) spectroscopy of GRO J1655-40 was obtained on 1996 May 11-13 by Dr. Coel Hellier and Dr. Alastair Allan as part of an override programme to

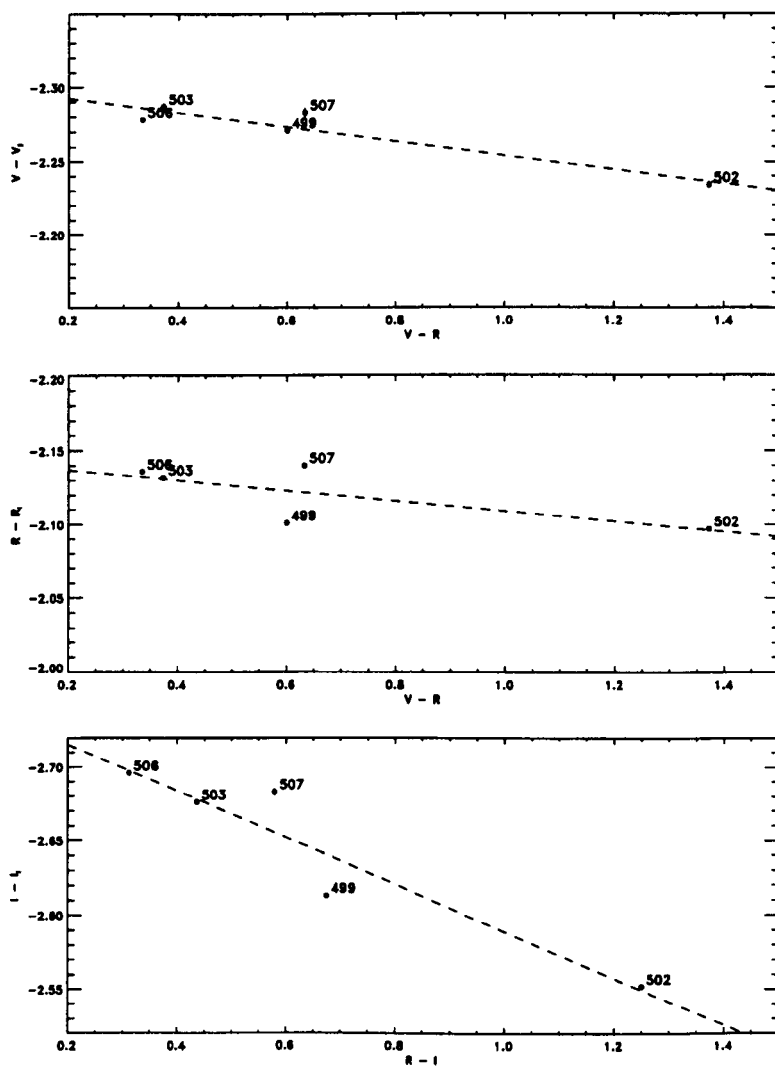


Figure 2.2: Relation between standard and instrumental magnitudes as a function of photometric colour for several stars in Landolt standard field 110. These are used to calibrate JKT photometry of XTE J2012+381.

Table 2.2: Log of AAT spectroscopic observations of GRO J1655–40.

Date	Start time (UT)	Duration (s)	Wavelength range (Å)
1996 May 11	13:34	300	4500–7495
1996 May 12	13:40	200	4498–7947
1996 May 13	13:32	500	3884–7341

perform high time resolution optical spectroscopy with simultaneous *RXTE* monitoring. In addition to the rapid spectroscopy, a longer exposure was taken each night. These were fully reduced by Dr. Emiliios Harlaftis (the principal investigator for the override) and Kieran O’Brien. The following description of the data is adapted from their account as it appeared in Hynes et al. (1998b).

The RGO spectrograph (Stathakis & Johnston 1997) was used in conjunction with the 270R grating and TEK CCD. This gave a mean reciprocal dispersion of 3.4 Å pixel^{-1} . A log of the relevant exposures is given in Table 2.2. The spectra were extracted from the raw images with the optimal extraction algorithm of Horne (1986), using suitable fits for the sky lines. The calibration used subroutines within the MOLLY spectroscopic data reduction package. Spectra were wavelength calibrated using 3rd order polynomial fits to copper-argon arc calibration spectra. The flux calibration used wavelength dependent fits to tabulated data for the flux star LTT 4364 (Hamuy et al. 1994), including Telluric line extinction effects. The final stage of the calibration used wide-slit exposures of the flux star to make an approximate correction for slit losses. This was necessary because the object frames used a narrower slit width.

2.5 WHT Spectroscopy of XTE J2123–058

XTE J2123–058 was observed with the William Herschel Telescope(WHT) on the nights of 1998 July 18–20 using the ISIS dual-beam spectrograph (Carter et al. 1993). The EEV10 4096×2048 CCD was mounted on the blue arm and the TEK2 1024×1024 CCD was on the red arm. A log of observations is given in Table 2.3.

On July 18 two spectra were obtained by Dr. Miguel Serra-Ricart. One used the R300B grating on the blue arm, the other the R158R grating on the red arm. On July 19–20, ISIS

Table 2.3: Log of WHT spectroscopic observations of XTE J2123–058. On July 20/21 each line denotes a sequence of consecutive exposures with autoguiding turned on. The position of the stars on the slit should be constant within each such sequence, but may vary slightly between them. The wavelength coverage is the maximum range of usable data from each sequence. For the blue arm observations, the choice of this range is somewhat subjective as the CCD is heavily vignetted at both ends. The unvignetted coverage on July 19–20 was $\sim 4000\text{--}6500\text{ \AA}$.

Date	Start time (UT)	Duration (s)	Number of exposures	Wavelength range (\AA)	Resolution (\AA)
1998 July 18/19	02:40	1200	1	3750–6250	2.9
	02:40	1200	1	6153–9124	3.4
1998 July 19/20	23:38	1200	16	3750–6800	2.9
1998 July 20/21	23:46	1200	5	3750–6800	4.1
	02:41	1200	6	3750–6800	4.1
	05:10	1200	1	3750–6800	4.1
	05:35	100	1	3750–6800	5.6

was used in single blue arm mode with the R300B grating. On July 18–19 an 0.7 arcsec slit was used as the seeing was 0.5–0.7 arcsec. On July 20 this was widened to 1.0 arcsec as the seeing was poorer, but still sub-arcsec. On July 19–20 the slit was aligned to pass through a second comparison star. A total of 28 1200sec exposures were obtained over the latter two nights sampling all orbital phases. On July 20 a final 100sec exposure was taken with a 4 arcsec slit for flux calibration.

2.5.1 Basic Image Processing

For data from July 18, this stage was performed by Dr. Miguel Serra-Ricart and collaborators. Data from July 19–20 was fully reduced by the author. Standard IRAF procedures were used to remove the bias level from the images, as described in Section 2.1.1. Flat-fielding was more difficult as the spectrum of the tungsten projection lamp used varies dramatically over the spectral range covered making it impossible to adequately expose the blue spectrum without saturating the red. This problem is compounded because fringing,

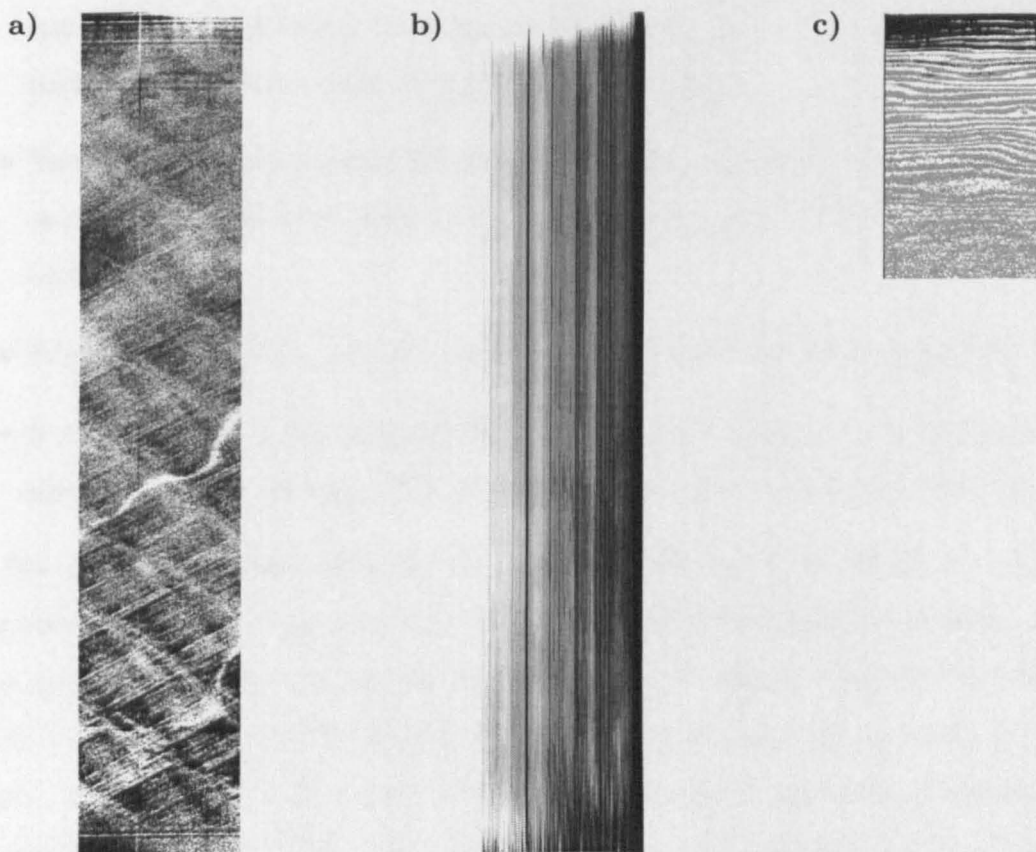


Figure 2.3: Spectroscopic flat fields from WHT/ISIS for XTE J2123–058. All images have been displayed using a histogram-equalised greyscale to emphasise the structure. a) The master flat used to correct fine scale structure in all spectra. b) A sample illumination correction image. c) A flat correction image (only the red end of the spectrum needs to be corrected.)

which is significant at the red end of the spectrum, varies over the course of the night, and hence must be corrected using contemporaneous flats. It was not, however, practical to take enough flats in between object exposures to give adequate signal-to-noise in the blue part of the spectrum for correction of pixel-to-pixel variations. These contemporaneous flats cannot therefore be used to correct all sensitivity variations.

The following structures can be identified in the flats:

- Small amplitude sensitivity variations, with very fine structure and significant diagonal pattern. One must assume that these are a property of the CCD and do

not varying dramatically with time, as the signal-to-noise ratios of the flat-fields are insufficient to correct them in time dependent fashion.

- Variations in illumination along the slit. These vary slowly in the dispersion direction and include both large scale variations and sharp dust features. These are time-dependent.
- Fringing at the red end of the spectrum only. This is also time-dependent.
- A large scale, but relatively smooth variation in the dispersion direction due to the spectrum of the flat lamp. This should not be corrected for in the object frames.

The problem was approached in three stages. The first is to remove the small scale structure of the CCD from both object frames and their contemporaneous flats. This was done using a set of flats produced at the beginning of the night of July 20 (i.e. the middle of the run) using the R600B grating in the blue; these had been obtained for another target. Nine such flats were used resulting in a signal-to-noise ratio of 100–500 in the unvignetted part of the CCD. They are also free of fringes making it easier to isolate the CCD structure. This was done using the `APFLATTEN` task within IRAF which removes both the spectral shape of the flat lamp and uneven illumination along the slit, leaving only the fine structure of the CCD. This fine structure flat is shown in Figure 2.3.

After removing this structure from the contemporaneous flat fields, the next stage was to create the illumination correction images. This was done by first using the IRAF task `APNORMALIZE` to remove the spectral shape of the projector lamp, and then smoothing the image in the dispersion direction with a 40 pixel width Gaussian. Since this is much larger than the fringing scale, fringes were very effectively removed leaving only the illumination correction image. A sample is shown in Figure 2.3.

Finally the `APNORMALIZED` flats were divided by the illumination correction image to leave only fringing structure. Since these were somewhat noisy, even in the red region, they were smoothed with a 5×2 pixel boxcar (2 pixels in the dispersion direction). The noise is significantly smaller than the fringe amplitude, so the small increase in the noise incurred by using these images will be outweighed by the benefit of removing the fringes. Since the fringes are only seen in the red spectrum, the fringe correction was only applied above 5880 Å. An example is shown in Figure 2.3.

2.5.2 Spectral Extraction

One-dimensional spectra were extracted from the images using the IRAF implementation of the optimal extraction method (Horne 1986; Marsh 1989; Massey, Valdes & Barnes 1992; see discussion in Appendix B.1). The IRAF package comprises a number of routines to perform aperture tracing, sky subtraction and the extraction of the spectra itself. It was accessed through the APALL script. In more detail, the stages are as follows.

Firstly, one must define an extraction aperture. This involves locating the centre of the spatial profile *at some wavelength*, choosing the width of the of the extraction window and identifying one or more sky regions. For these data a window of ± 16 pixels about the centre was chosen, and the sky was defined by the average of pixels -35 to -20 and +20 to +35. Within each sky window median filtering was used to ignore cosmic rays.

Then one must trace the aperture in the dispersion direction. Very rarely will the spectrum lie exactly parallel to a CCD line. Instead, some distortion will be present, so that the aperture centre is a function of column number (i.e. of wavelength). This is accounted for by tracing the aperture in both directions beginning from that defined in the previous step. Inevitably, the resulting trace of aperture centres will be noisy, so it is normal to perform a polynomial fit to the measurements. The distortion usually varies slowly, and so a low-order polynomial is generally a better choice than a cubic-spline function which can be too flexible. For the data discussed here a polynomial function of order 3–6 was found adequate; the highest orders were only used on high quality data for which the aperture trace was well defined.

The final stage is to perform an optimal extraction of the spectrum using the two-dimensional aperture defined by the previous steps. The implementation used was that within IRAF, with exploitation of the full capabilities of the method, including cosmic ray removal. Some bad pixels remained in the extracted one-dimensional spectra, particularly very low or negative values. These were obviously erroneous. As the number of spectra involved was small, these were cleaned by interpolation between adjacent good values. This was done interactively using the SPLOT task within IRAF.

2.5.3 Wavelength Calibration

Wavelength calibration of the extracted spectra requires a mapping between pixel number and wavelength. This is often very close to a linear function, but small distortions benefit from using a more flexible function provided enough information is available to constrain

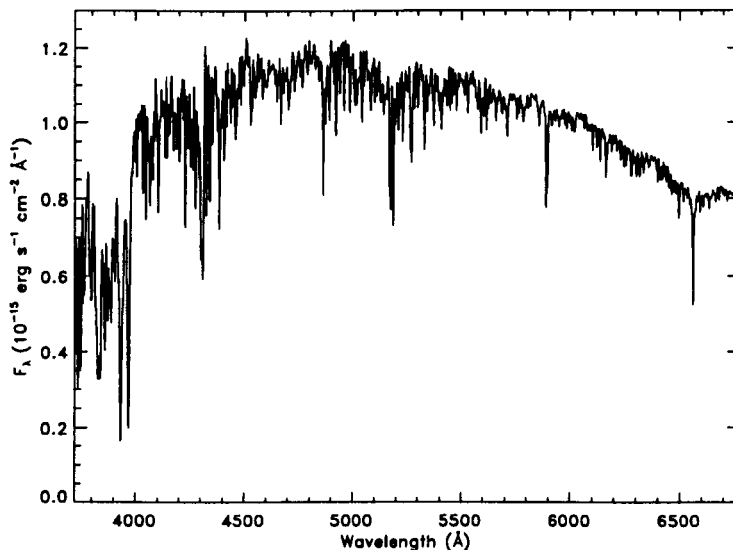


Figure 2.4: Calibrated spectrum of the slit comparison star used to calibrate spectra of XTE J2123–058. The spectral type appears to be early G.

such a function. A complication is that this mapping typically changes with time as the spectrograph flexes. This problem is unavoidable with instruments mounted on the telescope which change their orientation as the telescope moves across the sky. The ISIS spectrograph is known to be particularly susceptible to this problem (P. A. Charles 1998, priv. comm.), so accurate wavelength calibration requires careful monitoring of this time-dependence.

Wavelength calibration for these data was achieved in two stages. The primary calibration is via a series of exposures of a copper-argon arc lamp through the night. Between 90 and 105 lines were identified in each arc image using standard arc maps (Sinclair 1992; Sinclair 1995). A mapping between their wavelengths and positions was established using a 10th order cubic spline function, with RMS residuals of ~ 0.2 Å. Object spectra were wavelength calibrated using a linear interpolation in time between these spline functions.

Since a linear interpolation only represents a first-order correction for spectrograph flexure, the calibration was refined using the O [I] $\lambda 5577.37$ night sky emission line, the strongest feature in this region of the spectrum (Jenkins & Unger 1991). It is assumed that the small remaining errors due to spectrograph flexure can be approximated by a constant shift in wavelength, to be determined from the position of the O [I] line. The rms of these corrections was 0.3 Å on July 19 and 0.2 Å on July 20.

2.5.4 Flux Calibration

Flux calibration was also performed as a two-stage process. The spectrograph slit was aligned to pass through another star to serve as a comparison. From each image spectra of both stars were extracted as described above. The spectrum of XTE J2123–058 was calibrated relative to the comparison star in each case. The final, wide-slit image was used to calibrate the comparison star relative to the spectrophotometric standard Feige 110 (Oke 1990).

A complication is that the comparison star appears to be an early G star; its summed spectrum is shown in Figure 2.4. The structure seen is due to absorption lines, not noise. In fitting individual spectra of the comparison star, however, it becomes difficult to distinguish noise from the absorption lines. Fitting the continuum appropriately depends crucially on being able to make this distinction, as one should fit through the mean of noise, but fit the upper envelope of absorption lines. The solution adopted involves a number of stages, and is subtle. It is described in detail in Appendix A.

2.5.5 Sources of Error

The consistency ($\pm 0.3 \text{ \AA}$) in the positions of the O [I] 5577.37 \AA line before they are used to correct for flexure gives confidence that after this correction, the wavelength calibration should be accurate to less than this amount, so any systematic error in the wavelength calibration is significantly less than one pixel.

The accuracy of the flux calibration is less certain, however. Possible sources of error include an incorrect atmospheric extinction curve and differential slit losses

Uncertainty in the shape of the extinction curve represents a significant source of error in determining the absolute flux of the comparison star, and hence of XTE J2123–058. The wide slit observation used for absolute calibration was obtained at airmass 1.72, whereas the spectrophotometric standard Feige 110 was observed at airmass 1.25. An average extinction curve for La Palma (King 1985) was assumed in correcting for this difference. The presence of significant dust in the atmosphere at the time of the observations, however, means not only that the extinction curve may be quite different from an average one, but that the extinction may not even be a function of airmass alone, but may depend on the azimuth of the star. This uncertainty will only affect the absolute flux calibration; division by the comparison star spectra in each case should ensure that it introduces no uncertainty in the *relative* calibration of different spectra. Thus *changes* in the spectral

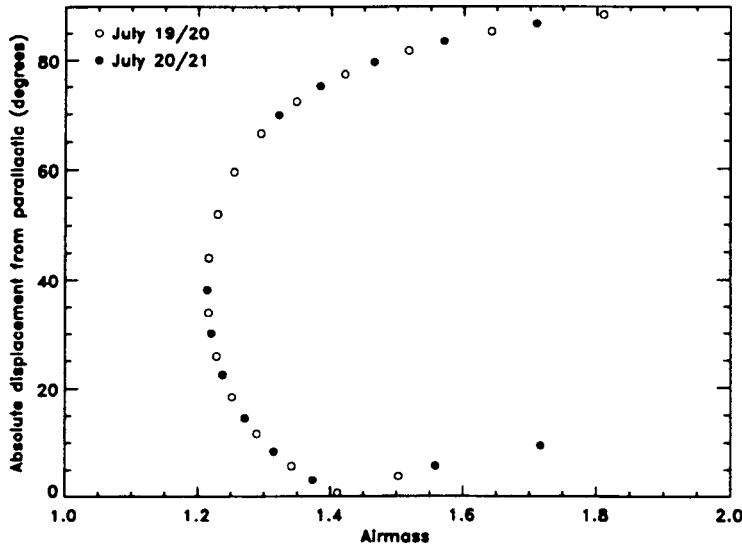


Figure 2.5: Airmasses and slit angles (relative to the parallactic angle) at which XTE J2123–058 was observed. Slit losses will vary considerably from the beginning of the nights (upper right) to the end (lower right.)

slope, for example, or a lack of them, cannot arise from uncertainties in the extinction curve.

A harder problem to rectify is wavelength dependent slit losses from the blue spectrum due to differential refraction (Filippenko 1982). This effect leads to the blue image of the star being displaced to slightly above the red image. For the observations considered, a comparison star was required on the slit so the slit was rotated to maintain constant angle on the sky, and was not aligned with the parallactic angle (i.e. perpendicular to the horizon). Autoguiding was performed with a red filter, so the position of the blue image of the stars will have moved across the slit as the airmass and slit angle (relative to parallactic) changes during the night (see Figure 2.5.) This can be clearly seen in the spectra: a very weak blue source spectrum is seen at the beginning of each night when the slit was near perpendicular to the parallactic angle. At the end of each night, the slit is nearly parallel to the parallactic angle and the blue spectrum is much stronger. In principal, the object and comparison star should be affected by this to the same degree, and so the effect should disappear in relative flux calibration. There will always be some uncertainty in aligning the slit parallel to the line of centres of the two stars, however, and this can lead to a residual time-dependent distortion of the spectra due to slit losses. This

effect is small in these spectra, but does appear to be present; its effects will be considered in more detail in Section 5.2.

2.6 WHT Spectroscopy of XTE J2012+381

XTE J2012+381 was observed with the WHT on 1998 July 20. The ISIS dual-beam spectrograph was used in single red arm mode to maximise throughput with the low-resolution R158R grating ($2.9 \text{ \AA pixel}^{-1}$) and the TEK2 CCD. A 1 arcsec slit was used giving an instrumental resolution of 5.5 \AA . This was aligned to pass through the line of centres of XTE J2012+381, USNO A1.0 star 1275.13846761 (Monet et al. 1996; hereafter the USNO star) and a third star to be used to define the point-spread function.

2.6.1 Basic Image Processing

Standard IRAF procedures were used to debias and flat-field the spectrum as described in Section 2.1. Sky subtraction was performed by fitting fourth order polynomials to the sky background with the stellar profiles masked out. The subtracted image showed no significant residuals in the sky regions.

2.6.2 Spectral Extraction

Although the seeing was good (spatial FWHM 0.9 arcsec) XTE J2012+381 was still heavily blended with the USNO star; a sample binned spatial cut is shown in Figure 2.6. The third star on the slit was therefore used as a template for the spatial profile (parameterised as a Voigt function) thereby allowing deblending of the profiles of XTE J2012+381 and the USNO star. This method is described in detail in Appendix B. It was found that the wavelength dependence of the parameters of the spatial profile could be well fitted by fourth-order polynomials with no smaller scale patterns in the residuals. The centre position of the profile varies by less than one pixel over the whole spectrum. The Gaussian core width and the Voigt damping parameter both vary by about 5 per cent. The Voigt model was found to give a very good fit over most of the profile. It does somewhat overestimate the extreme wings of the profile, so it was necessary to use the profile correction described in Appendix B. With this correction, no significant deviations between model and data can be discerned (see Figure 2.6).

2.6.3 Calibration

Wavelength calibration was achieved using a fit to a copper-neon arc spectrum (Sinclair 1995) obtained immediately before the object spectrum and checked against the night sky emission lines (Jenkins & Unger 1991).

A Telluric correction spectrum was formed by normalising the spectrum of the spectrophotometric standard BD+40 4032 (Stone 1977) observed later in the night. This has spectral type B2 III so $H\alpha$ and He I absorption lines were masked out. The correction spectrum was shifted slightly to compensate for spectrograph flexure between this exposure and that of our target. It was also rescaled to give a least-squares fit to the normalised sum of the three spectra on the slit. This was done by raising the correction spectrum to a power chosen to give the best fit. A short exposure of our target was made immediately before observing BD+40 4032 so this standard was also used to obtain absolute flux calibration. Both calibration observations used a wide slit (4 arcsec) to ensure photometric accuracy.

An important issue in deciding on the reliability of the calibration is the accuracy of the slit alignment through the centres of the three stars. Based on positions derived from the JKT photometry (Section 2.2 and Section 6.2), the slit was aligned to pass through the line of centres of the USNO star and an isolated comparison star used to define the spatial profile as a function of wavelength. This comparison star had been chosen to lie approximately along the line of centres of the two blended stars; hence the three should be co-linear. This is true to within the astrometric accuracy, i.e. the derived V , R and I positions of the red star scatter evenly to either side of the line of centres of the USNO star and comparison star. The offset of the red star from the line of centres of the other two stars should therefore be less than 0.1 arcsec, the scatter in the astrometry. The positioning of the slit was judged by eye using reflections off the slit jaws. This leads to some uncertainty in centring the stars within the slit, but as the stars are co-linear to within a fraction of the slit width, this should not affect their *relative* brightness significantly.

Chapter 3

REDUCTION OF DATA FROM *HST*/FOS

3.1 Introduction

The Faint Object Spectrograph (hereafter FOS, see Keyes et al. 1995; Keyes 1997b) was a first generation instrument of the *Hubble Space Telescope* (*HST*). It was removed together with the Goddard High Resolution Spectrograph (GHRS) by the second servicing mission in February 1997. Subsequently the Space Telescope Imaging Spectrograph (STIS) has taken over the rôles of both of these instruments.

There were two Digicon detectors: blue (BL) optimised for use in the ultraviolet and amber, or red (RD), optimised for the optical but actually more sensitive than the blue over all of its useful wavelength range. Photoelectrons from a two-dimensional photocathode were accelerated onto a linear array of 512 diodes. The Digicons were thus more akin to an array of photomultipliers than to the CCD detectors commonly employed on ground-based telescopes. Overscanning¹ was used to reduce the effect of isolated bad diodes. Since the width of the line spread function equalled that of a diode, sub-stepping² was used provide adequate sampling. With default overscanning ($\times 5$) and sub-stepping ($\times 4$) the effective number of pixels was 2064. A selection of gratings and a prism provided access to approximately 1140–8850 Å at resolving powers of up to 1300.

The FOS was used to observe GRO J0422+32 and GRO J1655–40. The dispersion modes employed are summarised in Table 3.1 and a log of *HST* observations is presented in Tables 3.2 & 3.3.

¹Obtaining multiple sub-spectra displaced by an integral number of diodes.

²Multiple sub-spectra displaced by fractions of a diode.

Table 3.1: *HST*/FOS modes used in observing GRO J0422+32 and GRO J1655–40. The PRISM modes have non-uniform dispersion and resolution: the resolution is highest in the UV.

Disperser	Detector	Wavelength Range (Å)	Reciprocal Dispersion (Å diode ⁻¹)	Resolution ($\lambda/\Delta\lambda$)
G160L	Blue(BL)	1140–2508	6.87	250
G190H	Blue(BL)	1573–2330	1.47	1300
PRISM	Blue(BL)	1500–6000	–	–
G270H	Amber(RD)	2222–3277	2.05	1300
G400H	Amber(RD)	3235–4781	3.00	1300
PRISM	Amber(RD)	1850–8950	–	–

All of the data under consideration were obtained using FOS RAPID mode (Welsh et al. 1994): a time-series of spectra with a typical sampling of a few seconds. The result is effectively a trailed spectrogram. GRO J0422+32 was too faint at the time of observation to exploit this capability. GRO J1655–40 was brighter, but to extract useful results it was still necessary to bin, either in time, resulting in averaged spectra, or in wavelength, resulting in broad-band lightcurves.

As with all of the *HST* instruments, data from supported instrument modes is provided in calibrated form after treatment by the pipeline software: CALFOS for the FOS. This is described in Section 3.2. CALFOS provides wavelengths and absolute fluxes and errors, enabling very easy examination of a dataset. As with any automatic process, however, some effects are not treated adequately by the pipeline and necessitate a manual recalibration of some or all stages of the pipeline process. In addition, some of the desired forms of extraction, for example, wavelength binned lightcurves, require a customised extraction process. To achieve this a combination of IRAF tasks, including STSDAS packages, and custom written C and IDL programs was used.

Some stages of the reduction of this data were initially carried out by Dr. Carole Haswell. In the case of GRO J0422+32, it did not prove necessary to repeat this process, beyond confirming her conclusions. Some of the text included in Sects. 3.3–3.5 is there-

Table 3.2: Log of *HST* /FOS observations of GRO J0422+32.

Date	Disperser / detector	UT Start (hh:mm)	UT End (hh:mm)	Integration time (s)	Sub-step
1994 Aug 25	PRISM/RD	21:21	21:29	365.4	4
	G270H/RD	21:34	22:03	1471.1	4
	PRISM/RD	22:56	23:03	365.4	4
	G400H/RD	23:09	23:39	1551.8	4
1994 Aug 26	PRISM/BL	00:38	00:45	365.4	4
	G160L/BL	00:51	01:14	1124.7	4
	G160L/BL	02:10	02:55	2273.2	4
	PRISM/BL	04:08	04:15	365.4	4
	PRISM/BL	15:24	15:32	365.4	4
	G160L/BL	15:38	15:45	365.4	4
	G160L/BL	16:37	17:22	2273.2	4
	G160L/BL	18:14	18:36	1120.0	4
	PRISM/BL	18:43	18:50	365.4	4
	G160L/BL	18:56	18:58	142.4	4
	G160L/BL	19:51	20:36	2273.2	4
	G160L/BL	21:27	21:57	1480.6	4
	PRISM/BL	22:01	22:08	365.4	4

Table 3.3: Log of *HST*/FOS observations of GRO J1655–40. Not shown are visits on 1996 May 20,27 when target acquisition failed.

Date	Disperser / detector	UT Start (hh:mm)	UT End (hh:mm)	Integration time (s)	Sub-step
1996 May 14	G190H/BL	00:07	00:15	365.4	4
	G160L/BL	00:20	00:47	1574.9	2
	PRISM/BL	01:42	01:48	280.0	4
	G160L/BL	01:54	02:24	1733.0	2
	G160L/BL	03:18	03:36	893.2	4
	G160L/BL	03:40	03:47	438.5	2
	PRISM/BL	03:53	03:59	308.5	4
	G270H/RD	04:56	05:10	692.9	4
	G400H/RD	06:32	06:40	379.6	4
	PRISM/RD	08:08	08:15	313.2	4
1996 Jun 8	PRISM/RD	12:49	13:06	893.2	4
	PRISM/RD	14:22	15:03	2383.2	2
	PRISM/BL	16:02	16:42	2332.2	2
	PRISM/BL	17:41	18:18	2099.9	2
1996 Jun 20	PRISM/RD	11:36	11:47	617.4	2
	PRISM/RD	12:35	12:52	963.4	2
	PRISM/RD	12:55	13:13	994.9	2
	PRISM/BL	14:12	14:51	2293.8	2
	PRISM/BL	15:53	16:34	2413.1	2
1996 Jun 30	PRISM/RD	13:02	13:15	617.4	2
	PRISM/RD	14:04	14:20	963.4	2
	PRISM/RD	14:24	14:41	994.9	2
1996 Jul 22	PRISM/RD	07:10	07:28	893.2	4
	PRISM/RD	08:43	09:26	2511.5	2

fore adapted from her descriptions written for Hynes & Haswell (1999). In the case of GRO J1655–40, a thorough rereduction was carried out by the author. Some of the latter material has previously been published in Hynes et al. (1998b) and Hynes et al. (1998c).

3.2 The Pipeline Calibration Process: CALFOS

The following summary of the steps performed by CALFOS is adapted from the *HST* Data Handbook (Keyes 1997b). For ease of comparison the same sequence is used. This summary is not exhaustive, but focuses on the steps that required modification.

3.2.1 Raw Data Input

The starting point for the calibration process is the raw data files. The .d0 files contain recorded counts per pixel. As the data were obtained in RAPID mode, this file, and all subsequent data files, is effectively a trailed spectrogram. The .q0 raw quality files contain flags to indicate where data from a given pixel may be defective. They are generated by the spacecraft and so are the most rudimentary error check; further flags will be added by later stages of processing. A number of supplemental files store further information about the observation.

3.2.2 Statistical Error Calculation

The Digicon detectors used in the FOS are free of readout noise and errors can therefore be readily derived from Poisson statistics. The error estimate on the recorded counts from a pixel is the square root of the number of counts. This error spectrum is processed through subsequent steps in parallel with the data.

3.2.3 Data Quality Initialisation

The raw data quality flags are merged with further flags from reference tables. These tables include information on problems such as dead diodes which may only become known later and so cannot be recorded by the spacecraft.

3.2.4 Conversion to Count-rates and Dead Diode Correction

This step converts recorded counts *per pixel* to the number of counts expected per second *per diode* if all diodes were reliable. It uses information from the science trailer files (.d1)

to determine the exposure time of each pixel. The number of active diodes (up to five due to overscanning) contributing to a given pixel is taken from the dead diode reference table enabling the correct count rate to be reconstructed even where one or more dead diodes are present. The corrected count rates are written out as the `.c4` files.

3.2.5 GIM Correction

As the data were all obtained after 1993 April 5, geomagnetic-induced image motion GIM was corrected onboard the spacecraft and so this step was not performed by CALFOS. A problem of similar nature was, however, encountered in some data on GRO J0422+32 in that the stellar image appeared to be poorly centred in the dispersion direction on the RD detector. This difficulty will be addressed in Section 3.4.

3.2.6 Paired-pulse Correction

There is a small but finite dead time ($\sim 10 \mu\text{s}$) after recording one count. At high count rates this may mean that some counts are missed; the detector's response becomes non-linear. The effect is negligible for these data on relatively faint objects. No correction at all is applied when the count rate is below 10 counts per second. When the count rate exceeds this (only applicable to some of the GRO J1655-40 PRISM data), but is below 52000 counts per second the correction is,

$$x = \frac{y}{1 - yt} \quad (3.1)$$

where x is the corrected count rate, y is the recorded count rate, and $t = 9.62 \times 10^{-6} \text{ s}$. A more complex correction is applied for count rates above 52000 counts per second, but this is not applicable to any of these data. Our highest count rates are below 200 s^{-1} , so the correction is less than 0.2 per cent. At the level of accuracy of our results, this effect is utterly negligible and so this correction is neglected in our customised data reduction procedures.

3.2.7 Background Subtraction

This step and the next will be discussed more fully in subsequent sections, as this is where the greatest difficulties with the CALFOS products were encountered. The goal of this step is to correct for a particle-induced dark count in the diode arrays. While the diodes do also have an intrinsic dark current, this is negligible compared to the particle-induced count

rate (Hayes & Lindler 1996). It is a function of both time and pixel number. CALFOS assumes that these two dependencies are separable, i.e. the dark count can be represented by a unique background spectrum, which is then rescaled by a scalar factor dependent on the position of the satellite within the Earth's magnetic field at the time of observation. The difficulty arises because this model underestimates the background level in many cases. This is clearly illustrated in Figure 3.1 and will be discussed fully in Section 3.3.

3.2.8 Scattered Light Subtraction

A certain amount of scattered light is present in the spectrograph, both from diffraction patterns and light scattered off imperfect optical surfaces. For red objects, this scattered light can become significant in UV exposures. Following Kinney & Bohlin (1993), this is modelled in the most simplistic way possible by subtracting the mean count rate measured from an unexposed region of the diode array. If no unexposed regions are available, then no correction is possible. Since the correction is performed after subtraction of the modelled particle induced background, it also acts as a scalar correction of residual particle induced background counts. Only if the exact shape of the background spectrum becomes important is it essential to distinguish between particle induced background counts and scattered light; this distinction will be discussed in Section 3.3.

3.2.9 Flatfield Correction

This step removes diode-to-diode sensitivity variations by *multiplying* by an *inverse* flatfield image. The correct flatfield image is dependent on both the date of observation and the aperture used. Note that at the time of data analysis, no flatfield image was available that was appropriate to the 1996 May 14 PRISM/RD data on GRO J1655–40.

3.2.10 Sky Subtraction

Sky subtraction is only performed if sky observations are made. This was not the case for these data, so this step is omitted.

3.2.11 Wavelength Computation

Vacuum wavelengths are calculated by CALFOS based on standard dispersion coefficients; no wavelength calibration images are used, and no correction is made for motion of the telescope or the Earth. For these observations, this is adequate as none of the results are

dependent on precise wavelength calibration. The calibrated wavelengths are written to the .c0 file.

3.2.12 Aperture Throughput and Focus Corrections

This correction is only applied if the AIS-CORR flux calibration method is used (see Section 3.2.13). It consists of a wavelength dependent correction to the count rates determined by the throughput of the aperture used and a further correction according to the focus value used. In the post-COSTAR era, focal corrections are unity, so have no effect on these data.

3.2.13 Absolute Calibration

Historically, two methods of flux-calibration have been used for FOS data. Both involve multiplication by an inverse sensitivity (IVS) file to convert count rates to absolute fluxes. Until 1996 March 19, the FLX-CORR (Flux Correction) method was used by the pipeline (CALFOS) reduction. This is based on a number of IVS files specific to the aperture used and range of observation dates. After this time, AIS-CORR (Average Inverse Sensitivity Correction) became the standard procedure for pipeline reduction and is recommended for rereduction of *all* non-polarimetric observations. This uses a single average IVS file (actually two files: one for pre-COSTAR observations, one for post-COSTAR; only the latter case applies to these data). Corrections are then applied based on the aperture (see preceding section) and the time of observation (see following section). Whichever method is employed, the output of this stage is written to the .c1 file (calibrated fluxes) and the .c2 file (calibrated errors).

3.2.14 Correction for Time-dependent Sensitivity Variations

This correction is only applied if the AIS-CORR flux calibration method is used; see Section 3.2.13. This correction involves interpolating between calibration observations to obtain a correction factor to the sensitivity as a function of both time and wavelength.

3.2.15 RAPID Mode Processing

This final step calculates the total flux across the detector for each RAPID group and also propagates an appropriate error. These are written to the .c3 files. It was chosen instead to analyse RAPID mode data using a customised procedure which allows more careful

background subtraction and the use of multiple bandpasses to allow the construction of lightcurves for a defined wavelength range. This is described in Section 3.6.

3.3 Reducing Spectra from the G160L Grating

The average raw G160L spectra for GRO J0422+32 and GRO J1655-40 are shown in Figure 3.1. This grating disperses the 1140–2508 Å spectrum to diodes 319–516. Zeroth order light falls on the detector at around diodes 150–166. Elsewhere in the array, the pixels monitor the background count-rate. The CALFOS estimate of the background count rate is shown, but is clearly a poor fit.

As can be seen from Figure 3.1, the G160L spectra show a strong geocoronal Ly α emission feature, with negligible source counts shortwards of this. The problem is worse for the GRO J0422+32 data because a larger aperture was used, making the line both broader and stronger. Data below 1354 Å for GRO J0422+32 and 1255 Å for GRO J1655-40 were therefore ignored. Ly α emission from the second order spectrum was also observed at 2435 Å. Pixels contaminated by this were therefore excluded: longwards of 2352 Å for GRO J0422+32 and 2418–2455 Å for GRO J1655-40.

The largest problem in accurately calibrating G160L spectra arises from the uncertain background count rate. The FOS detectors are always subject to a particle induced dark count. The count rate is dependent on the geomagnetic position of the satellite. This is modelled and subtracted by CALFOS, but as can be seen from Figure 3.1, the model underestimates the true background level. Two explanations for the discrepancy are suggested in the literature. It is documented that the CALFOS background model underestimates the dark count by up to ~ 30 per cent (Keyes et al. 1995). The model assumes that the distribution of dark count over the diode array is independent of time, and then rescales this ‘background spectrum’ according to the count rate predicted from the satellite position. If the discrepancy between model and data were purely that the background count rate were underestimated, then one could rescale the background model to fit an unexposed region and subtract this rescaled background spectrum. This was the approach taken by McClintock, Horne & Remillard (1995) in their analysis of the quiescent SXT A 0620-00.

Kinney & Bohlin (1993) propose an alternative explanation: that the extra counts are actually due to scattered red light. This is expected to make a significant contribution to the detected counts for very red objects, and so must be considered as an explanation for the background in GRO J1655-40, which is highly reddened. More recent versions of

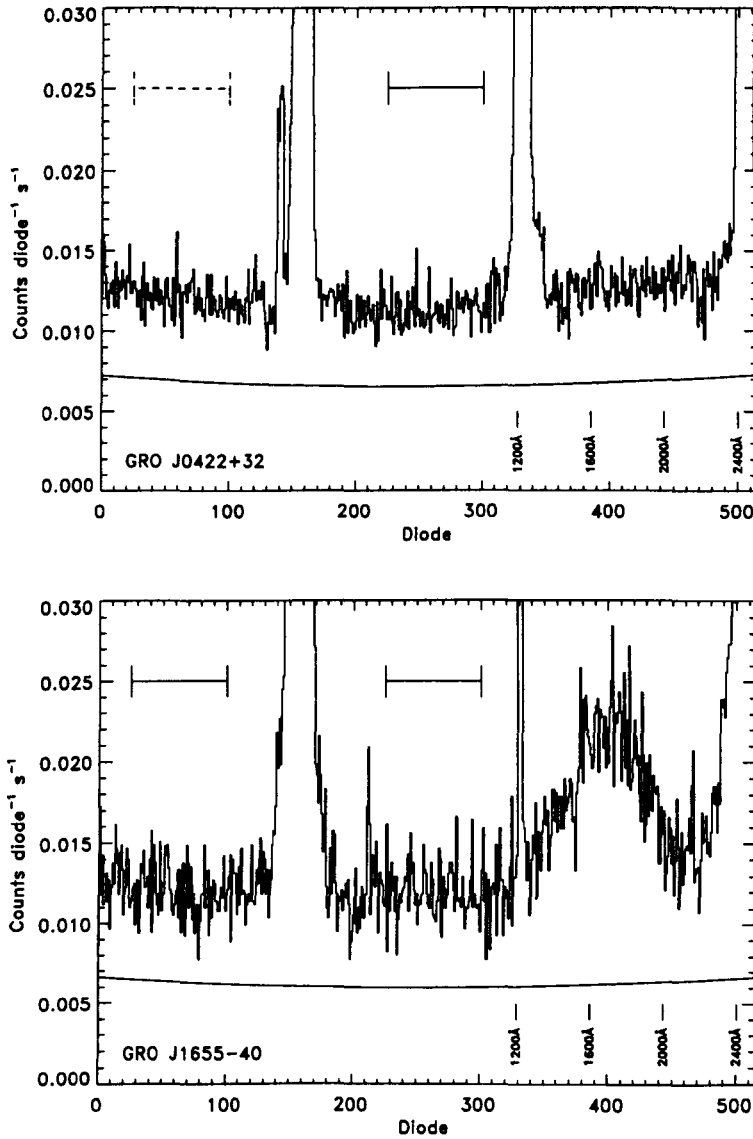


Figure 3.1: Count rates in the averaged G160L spectra of GRO J0422+32 (top) and GRO J1655-40 (bottom). The zeroth order spectrum is seen centred at diode 160. The first order spectrum runs from diodes 319–516. Geocoronal Ly α emission is clearly seen around diode 330 and the 2175 Å interstellar absorption feature around diode 462, prominent only for GRO J1655-40. The strong rise above the 2175 Å feature in GRO J1655-40 is the source spectrum; the similar looking rise in GRO J0422+32 is actually geocoronal Ly α , which is why it drops again at the extreme red end. The smooth solid line shows the model background calculated based upon the geomagnetic position. The adopted unexposed regions are indicated. They span diodes 25–100 and 225–300 respectively. Only the second region was used for GRO J0422+32.

CALFOS include a simplistic scattered light correction. This assumes that all parts of the diode array are illuminated evenly, and that all counts in unexposed regions are due to scattered light. The model then uses the difference between the data and background model in an adopted unexposed region (diodes ~ 225 –300 for the G160L/BL combination) to determine a constant scattered light contribution to be subtracted.

This disagreement is significant because the *shape* of the extra background spectrum that is assumed affects the UV continuum flux attributed to the target. This is clearly crucial in the case of GRO J0422+32 and to a lesser extent for GRO J1655–40. It is therefore necessary to examine which of these processes could be responsible for the extra background counts.

The strongest piece of evidence is that provided enough exposures are averaged, no significant difference is seen between the two objects: the average count rate in the unexposed region is the same for GRO J0422+32 and GRO J1655–40, and the CALFOS model underestimates this by the same amount. This strongly suggests that the same process applies to both objects. Since GRO J1655–40 was six magnitudes brighter than GRO J0422+32 at the time of observation, and is redder, it is unlikely that the effect of scattered red light from the source will be the same in the two cases. This is consistent with the conclusion of McClintock, Horne & Remillard (1995) who explicitly ruled out scattered optical light in their G160L observations of A 0620–00, which was two visual magnitudes brighter than the GRO J0422+32 was at the time of the observations. Other possible sources of scattered light not previously considered include UV light from the source and geocoronal emission. The former can be ruled out since GRO J0422+32 was incredibly faint, and possibly undetected, in the UV at the time of observation and it was certainly much fainter than GRO J1655–40. One would not expect to see the same background level in this case. The latter explanation would seem more plausible except that a larger aperture (‘4.3’; actually ~ 3.7 arcsec for post-COSTAR observations) was used for GRO J0422+32, so more geocoronal light will have entered the spectrograph than for GRO J1655–40. There is then no reason why the background level will be the same for GRO J0422+32 and for GRO J1655–40.

A much more likely explanation is that the extra background is particle dominated. This will then be a property of the detector (and spacecraft position), not of the aperture used and is independent of the object observed. Averaged over enough spacecraft positions, we would quite naturally expect the background to be the same for GRO J0422+32 and

GRO J1655–40.

The corrections needed for the PRISM/BL spectra (see Section 3.4), which used the same detector, but a different disperser, were of comparable size to those for G160L. This suggests that the background level is a property of the detector, independent of which disperser is used and so further supports a model based on particle events rather than scattered light.

A final test is to compare the shapes of the background spectrum with the two models. This is difficult, as in neither dataset were enough data accumulated to define the background spectrum to high accuracy. The GRO J0422+32 dataset has the highest signal-to-noise ratio in the background, so this will be used. Figure 3.2 shows the rebinned residuals after subtraction of background models. In the upper panel it is assumed that all of the background is due to particle events and a model background spectrum rescaled to fit diodes 225–300 is subtracted. In the lower panel the CALFOS background level is assumed and a constant scattered light term determined by the mean level in diodes 225–300 is then subtracted. Assuming a particle dominated background gives a mean residual count rate in diodes 1–136 of $(2.8 \pm 0.9) \times 10^{-4} \text{ s}^{-1}$, about half obtained using a uniform scattered light model: $(5.4 \pm 0.9) \times 10^{-4} \text{ s}^{-1}$. While the particle model seems to give a better estimate of the shape of the background count rate than the CALFOS scattered light model, neither model gives a mean count in the test region (diodes 1–136) within 3σ of zero. The scattered light model assumed, in particular, is oversimplistic in assuming that scattered light is uniform across the diode array. This test therefore provides at best inconclusive support for the particle background model. It indicates that if this is the correct interpretation, then the model possibly has some deficiencies in the predicted shape of the background spectrum.

In both GRO J0422+32 and GRO J1655–40 the source of background counts therefore appears to be dominated by particle events. This is the only interpretation which can adequately explain the similarity between the background spectra in the two sets of data. This disagrees with the earlier interpretation of Hynes et al. (1998b) where a scattered light model for GRO J1655–40 was adopted from considering that dataset alone. Since the source spectrum is much brighter in that case, however, the small difference in the shape of the background spectrum between the two models has minimal effect on the derived spectra and does not significantly affect the conclusions of this work.

These G160L results, and also those obtained with the PRISM/BL (Section 3.4), indi-

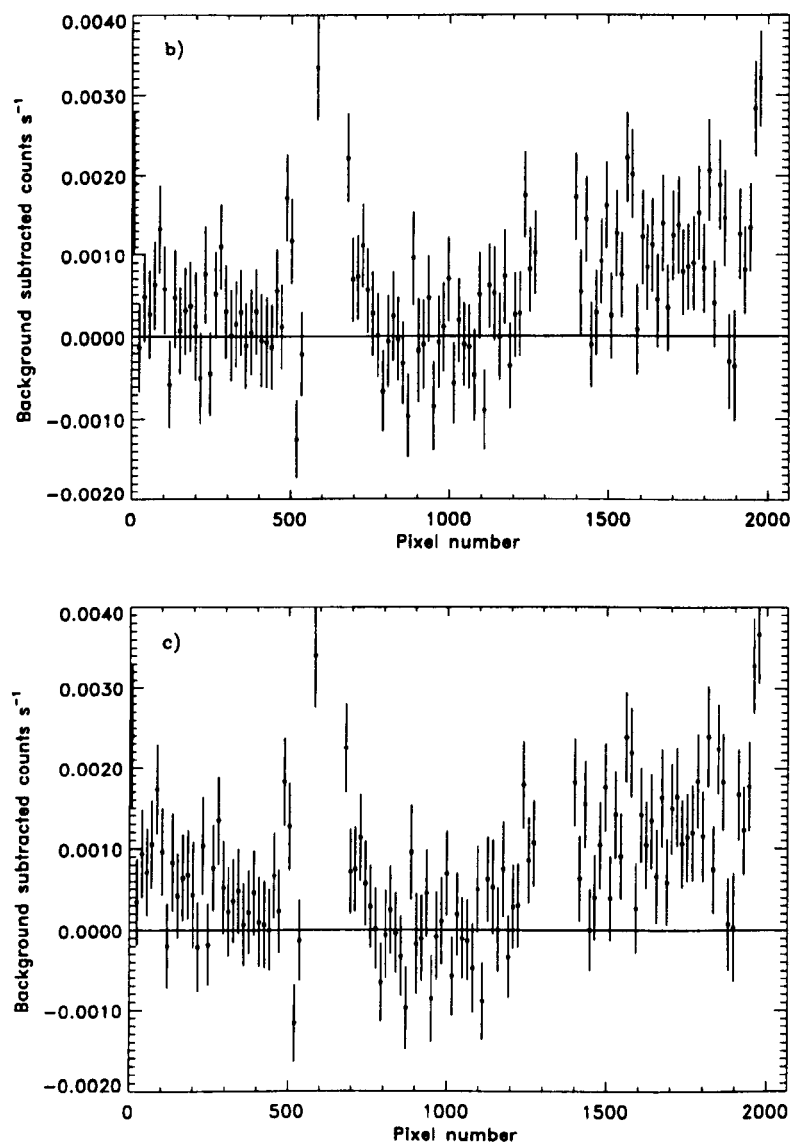


Figure 3.2: Rebinned count rates for GRO J0422+32 after subtraction assuming extra counts are due to particle events (above) and scattered light (below).

cate that the discrepancy in the background model for the BL detector is large: $\sim 60 - 100$ per cent, with mean count rate $0.010 - 0.012 \text{ cts s}^{-1} \text{ diode}^{-1}$. This disagrees with the analysis of dark data from Cycles 1 to 4 (Hayes & Lindler 1996) from which a mean BL count rate of $0.0064 \pm 0.00083 \text{ cts s}^{-1} \text{ diode}^{-1}$ was deduced.

3.4 Reducing PRISM Spectra

As for the G160L grating, the PRISM configurations leave many unexposed pixels which can be used to monitor the background count rate; typical raw PRISM/BL and PRISM/RD spectra are shown in Figs. 3.3 and 3.4 respectively. Diodes 350–500 were used as a background region for PRISM/BL and 25–225 for PRISM/RD. For PRISM/BL, the discrepancy in the CALFOS model is large, and comparable to that seen with the G160L grating: the recorded background is 63 ± 3 per cent higher for GRO J0422+32 and 57 ± 2 per cent higher for the spectrum of GRO J1655–40 shown (from 1996 June 8). In the case of PRISM/RD observations, the model is more successful, with a discrepancy of 2 ± 3 per cent for GRO J0422+32 and 16 ± 1 per cent for GRO J1655–40. For GRO J1655–40, other visits show similar excesses in the PRISM background levels.

Spectra obtained using the PRISM have a non-uniform dispersion, which becomes very low at the red end of each spectrum (232 \AA per pixel at the far end of the lowest resolution PRISM/RD spectra). Under these circumstances, a small error in centring the star in the dispersion direction can lead to a large error in the wavelength and hence flux calibration. In the GRO J0422+32 PRISM/RD spectra, there did appear to be such an offset. This was detected by Dr. Carole Haswell as a wavelength error by comparison of the position of the Mg II (2798 \AA) line with its position in the higher resolution G270H spectrum. The offset was the same for both PRISM/RD exposures, so the miscentering was probably also the same for the G270H exposure taken between them and the G400H exposure immediately after. The offset was corrected by shifting both G270H and PRISM/RD spectra by 12 pixels after flat-fielding. This also brought the $H\alpha$ and $H\beta$ emission lines in the PRISM/RD spectrum to within one pixel of their rest wavelengths. Since the PRISM/BL spectrum contains no prominent emission lines (the Mg II line is undetected), it is impossible to determine if a similar offset is present in this case. This makes the calibration of the PRISM/BL spectra less certain than PRISM/RD for GRO J0422+32. Since the BL detector is also less sensitive than the RD, model fitting focussed on the PRISM/RD spectrum. In the case of GRO J1655–40 PRISM/BL data, comparison with

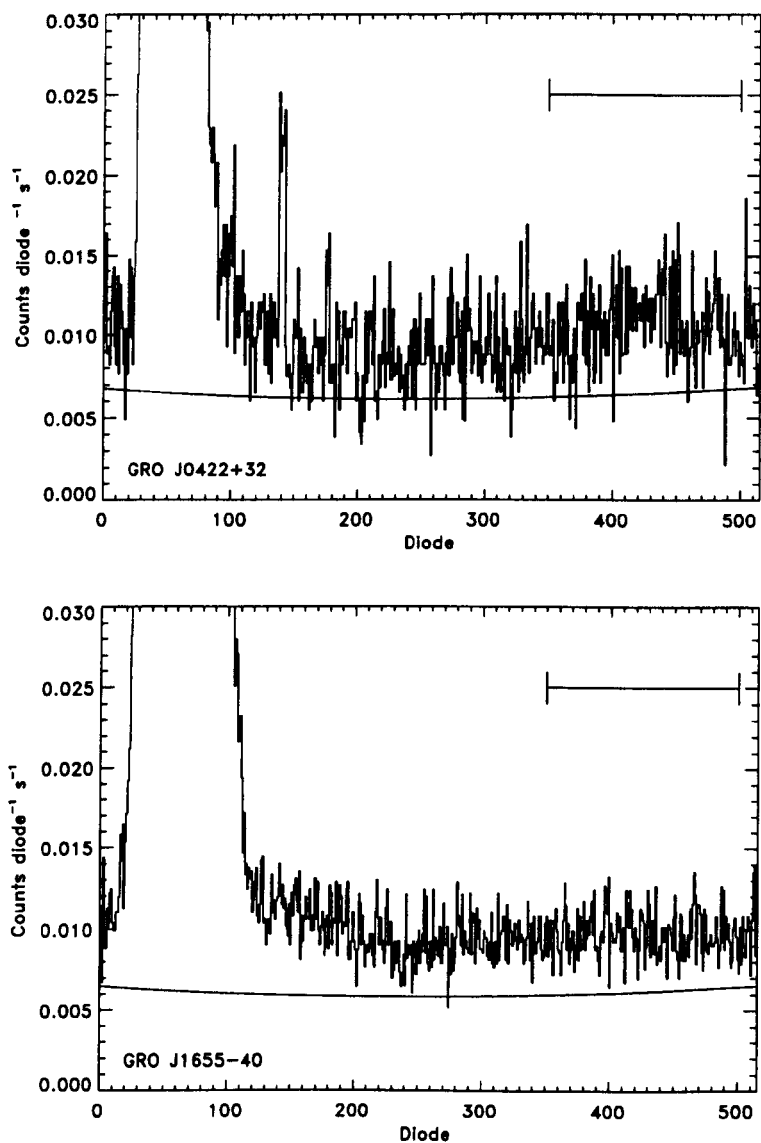


Figure 3.3: Count rates in averaged PRISM/BL spectrum of GRO J0422+32 (top) and the 1996 June 8 spectrum of GRO J1655-40 (bottom). Also shown with the smooth solid line is the model background calculated based upon the geomagnetic position. The adopted unexposed regions are indicated.

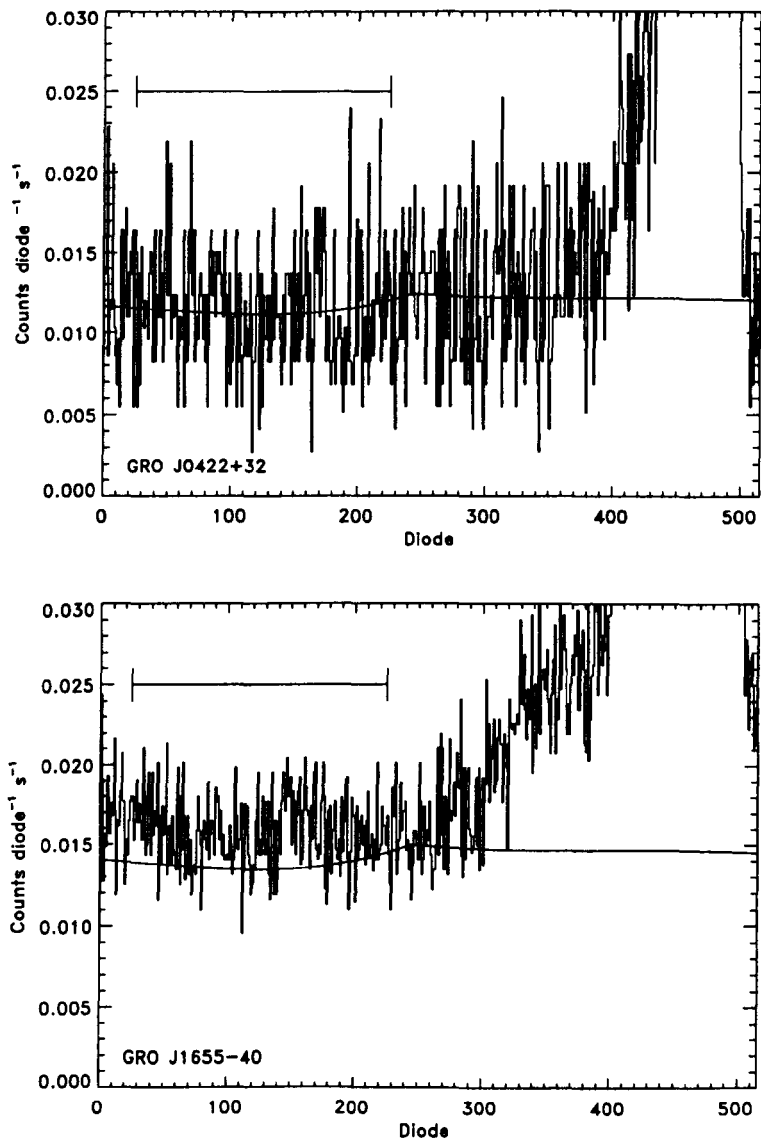


Figure 3.4: Count rates in averaged PRISM/RD spectrum of GRO J0422+32 (top) and the 1996 June 8 spectrum of GRO J1655-40 (bottom). Also shown with the smooth solid line is the model background calculated based upon the geomagnetic position. The adopted unexposed regions are indicated.

PRISM/RD allows an estimate of the point at which miscentering has a significant effect by looking for a significant difference in calibrated fluxes. This point varied from visit to visit from 2900–4500 Å. For PRISM/RD, there are no internal checks of the calibration. The spectra were compared with contemporaneous AAT observations (see Section 2.4). The flux levels are consistent to within the intrinsic variability between different nights of the AAT spectra and the shape generally agrees well up to ~ 7000 Å. A sharp drop off is seen at the longest wavelengths which is attributed to miscentering, so cut-offs are adopted on a case by case basis ranging from 7300–7650 Å.

The GRO J1655–40 PRISM/RD data from the 1996 May 14 visit (only) showed pronounced a dip from 3735.8–3991.4 Å that was not matched by features in the grating spectra. While this region is approximately 20 pixels wide (the width that would be affected by a single dead diode), it does not correspond to a known faulty diode. An alternative explanation is that this is an uncorrected flatfield defect. This is plausible as no flatfield image was available for the paired aperture PRISM/RD configuration used on this visit.

Finally it should be noted that the revised calibration files (Keyes 1997a) made a significant difference to the flux calibration for the extreme long wavelength end of the PRISM/RD spectrum, with the flux longwards of 7500 Å being increased by 20–80 per cent.

3.5 Reducing Spectra from the High Resolution Gratings

Because of the high dispersion, the count rates per pixel are relatively low and the background is generally a serious problem for the high resolution gratings. The problem is exacerbated because these gratings completely fill the diode array with the source spectrum, leaving no region to monitor the background. The single G190H exposure of GRO J1655–40 proved to be so sensitive to the background level as to be unusable and did not appear to agree with the spectrum from the G160L grating (Section 3.3). Since this was only a short exposure, it was chosen to reject this data. Comparing the G270H and G400H spectra with those from the PRISMs, for which an unexposed region was available, the CALFOS procedure seems to have subtracted the background reasonably well. This is plausible, as the results obtained with the G160L grating and PRISMs suggest that the model background works well for the red detector, but is very poor for the blue. This is probably why the G190H/BL spectrum was incorrect, whereas the G270H/RD and G400H/RD

spectra appear believable. Nonetheless, a precise recalibration cannot be attempted for any of the high resolution spectra, neither can the uncertainty in the background level be quantified, except to note that for GRO J1655–40 the background is negligible above $\sim 2600 \text{ \AA}$. The G270H and G400H spectra are therefore used primarily to search for and examine spectral lines.

Other than the uncertain background level, reduction of the spectra of GRO J1655–40 proved relatively straightforward. Two difficulties were encountered in the data on GRO J0422+32 however. Firstly, as discussed above, there was a problem with centring within the aperture for the observations made with PRISM/RD. All of the PRISM/RD observations were made as a continuous sequence, so we can expect that the error (in pixels) will be common to all. This assumption was the basis of the measurement of the shift made in Section 3.4. The derived shift of twelve pixels was thus applied to both the G270H and G400H spectra, recalibrating as discussed above. A second problem with the G400H spectrum was that diode number 114 appeared to be noisy introducing a spurious emission feature. It is clear that this is the cause because i) the feature is exactly 20 pixels wide, the range of pixels that will be affected by a single bad diode, ii) the feature lines up with the diode boundaries (at substep 4 this would only happen 25 percent of the time) and iii) diode number 114 has been reported to be intermittently noisy (Keyes 1997b), so this behaviour is not unexpected. The pixels contaminated by this spurious emission are therefore discarded as no straightforward correction exists for noisy diodes and the contaminated region only spans 15 \AA .

The final G270H and G400H spectra are shown in Figs. 3.5 & 3.6 respectively. For clarity, they have been rebinned by a factor of four so that there is approximately one pixel per resolution element (i.e. one per diode³).

3.6 Extracting RAPID Mode Light Curves

The RAPID mode PRISM/BL and PRISM/RD spectra for GRO J1655–40 can be used for rapid spectroscopy. This mode delivers a series of time resolved spectra, termed groups, from which light curves were constructed. Over most of the spectral range of the PRISMs, the spectral resolution is very poor and low signal-to-noise requires substantial binning; hence it is only possible to study continuum variations.

Count rate light curves were extracted from the .c4 files provided by STScI, performing

³Because of overscanning, data from several diodes actually contribute to a binned pixel.

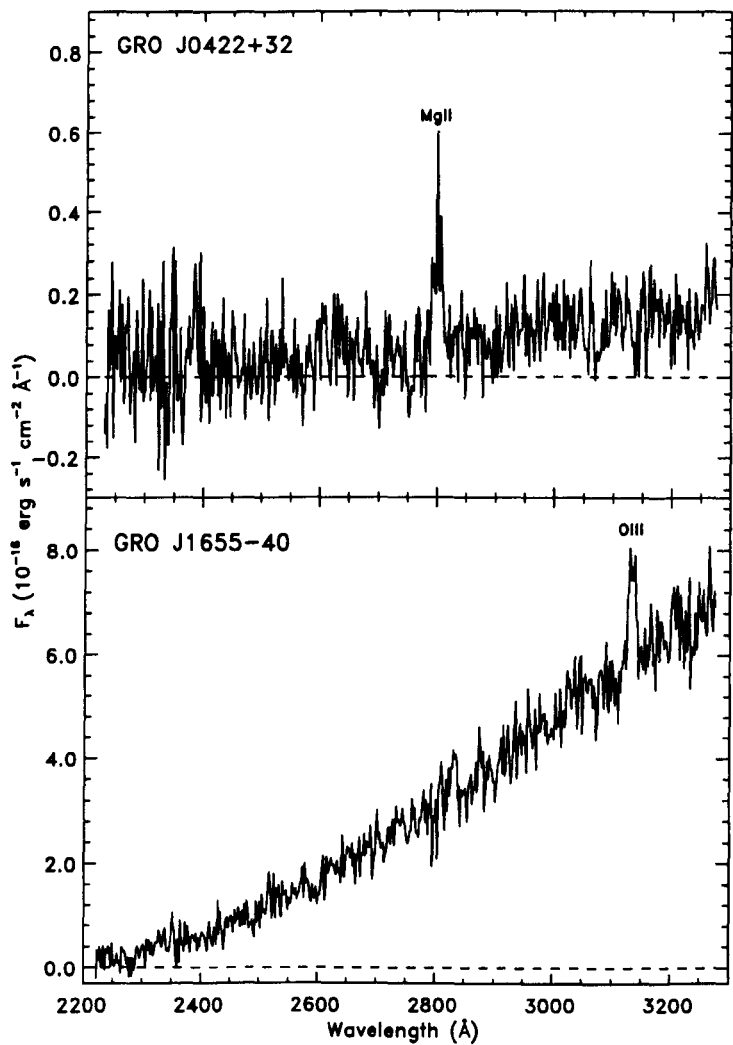


Figure 3.5: G270H spectra of GRO J0422+32 and GRO J1655-40. Prominent emission lines of Mg II 2798 Å in GRO J0422+32 and O III 3133 Å in GRO J1655-40 are marked.

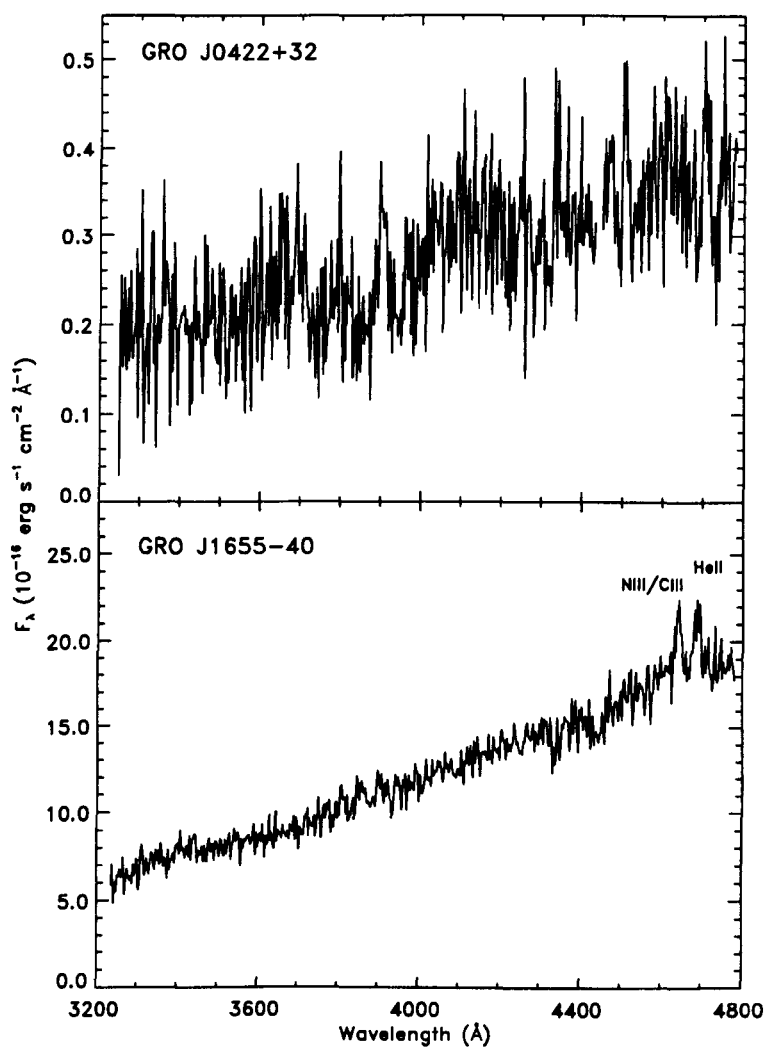


Figure 3.6: G400H spectra of GRO J0422+32 and GRO J1655-40. Prominent emission lines of the Bowen blend, N III/C III $\sim 4640 \text{ Å}$ and He II 4686 Å in GRO J1655-40 are marked. These and other possible detections will be discussed in Chapters 4 and 7.

background subtraction by hand. Some care was needed in defining errors, as the .c4 files have been corrected for bad diodes, a process which effectively changes the gain from pixel to pixel. The raw .d0 files, which simply record counts measured per pixel, were therefore used as the starting point. The Digicons have zero read-noise, so the error on the .d0 counts is simply the square root of the recorded counts (Poisson statistics) and the signal-to-noise ratio is also the square root of the number of counts. The latter is used to derive the errors in the c4 files, as the signal-to-noise ratio will be unaffected by a multiplicative correction for bad diodes. In principle this approach will break down for very low count rates, because the error, which depends on the count rate, cannot be reliably estimated from the recorded counts. With the relatively wide bandpasses adopted, count rates are high enough that this is not a problem.

The standard background models are adopted as a template for the background spectrum throughout. These are rescaled to match unexposed regions on a group-by-group basis. The total background subtracted count rate over the desired wavelength range is then integrated to obtain light curves. The background count rates for both the PRISMs and the G160L zero order light (see below) is low enough that the error in the background count rate is negligible compared to photon counting errors in the source light.

Several sets of wavelength ranges were used. Firstly, very broad bands covering all the available data, with effective bandpasses defined by the FWHM of the *count rate* spectra: 3100–4800 Å for PRISM/BL and 3800–7400 Å for PRISM/RD. Secondly, three narrower bands were used to search for wavelength dependence in the delay times and variability amplitudes: 2000–4000 Å (hereafter UV light curve), 4000–6000 Å (blue) and 6000–9000 Å (red). For the PRISM/BL combination, only UV and blue light curves could be produced.

An alternative bandpass is provided by the G160L zeroth order light curve (Horne & Eracleous 1993; Eracleous et al. 1994). This is undispersed, so no control is possible over wavelength used; the spectral response is centred at 3400 Å and has a FWHM of 1900 Å. This was only available on 1996 May 14.

A final subtlety involves the start times of the groups. As discussed by Christensen et al. (1997), FOS RAPID mode may produce groups unevenly spaced in time: the “too rapid RAPID” problem. Because of this the standard data products contain an uncertainty in the start times of individual groups of $-0.255\text{ s}/+0.125\text{ s}$. The start times were therefore recalculated by Mr. Ed Smith using the RAPID-TIMES program at STScI which reduces the *relative* uncertainty between groups to $< 1\ \mu\text{s}$. There is still an unavoidable 0.255s

uncertainty in the *absolute* start time of each exposure (i.e. the zero point of each series of groups.)

The derived group times are determined by the spacecraft clock. Since the spacecraft is moving around Earth, there is in principle a further uncertainty in the relative start times of groups due to light travel time across the spacecraft orbit. Since this is only at an altitude of 610 km, however, the maximum timing uncertainty introduced, relative to a geocentric observer, is ± 0.02 s. For these purposes, such an error is completely negligible, so no attempt is made to correct for it.

Chapter 4

GRO J1655–40

4.1 Introduction

The SXT GRO J1655–40 was discovered on 1994 July 27 when the Burst and Transient Source Experiment (BATSE) on *CGRO* first detected it in outburst. By August 1 it had reached a level of 1.1 Crab in the 20–200 keV energy band (Zhang et al. 1994; Harmon et al. 1995). This turned out to be just one of a remarkable series of outbursts that finally appeared to subside in late 1997. The full BATSE outburst history is shown in Figure 4.1. Over this period, the source was extensively observed by the various instruments on board *CGRO* (Harmon et al. 1995; Levinson & Mattox 1996; Crary et al. 1996; Kroeger et al. 1996; Zhang et al. 1997; Grove et al. 1998a; Hynes et al. 1998b; Tomsick et al. 1999b), *ROSAT* (Greiner, Predehl & Pohl 1995; Greiner 1996), *ASCA* (Zhang et al. 1997; Ueda et al. 1998), *Granat* (Zhang et al. 1997), *Mir-Kvant* (Borozdin et al. 1997) and from 1996 *RXTE* (Kuulkers et al. 1998; Méndez, Belloni & van der Klis 1998; Hynes et al. 1998b; Hynes et al. 1998c; Tomsick et al. 1999b; Sobczak et al. 1999). In spite of its complex long-term variability, snapshots of its X-ray behaviour are typical of black hole candidates. Broadband observations in 1995 July–August (Zhang et al. 1997) found the two-component spectrum typical of the high/soft state of these objects (see Section 1.3.) The power-law component extended to at least 600 keV (Kroeger et al. 1996). Ueda et al. (1998) report spectra in both high/soft and low/hard states. Sobczak et al. (1999) in 1996–7 observed a variety of spectra which they classify as the very high state during the first phase of the outburst, the high/soft state during the second phase, and the low/hard state at the very end. Both Tomsick et al. (1999b) and Sobczak et al. (1999) note the very rapid

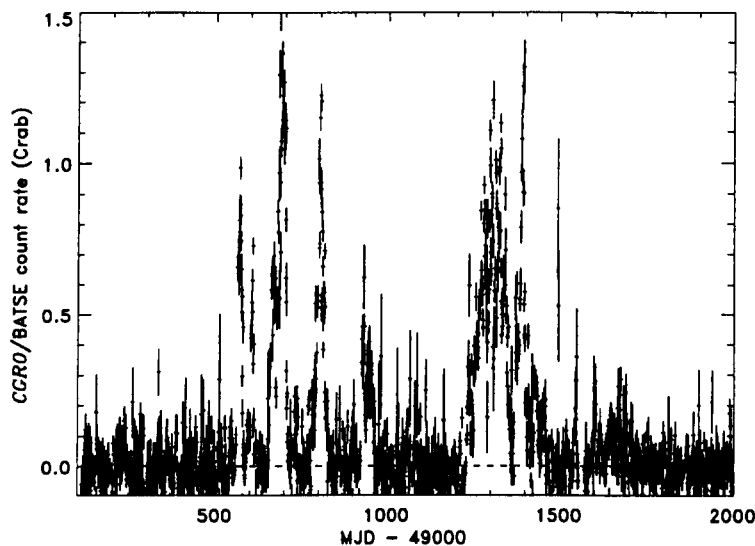


Figure 4.1: Full known outburst history of GRO J1655–40 as monitored by *CGRO*/BATSE from 1994–7. The light curve is clearly very complex and does not follow a fast rise – exponential decay pattern.

spectral changes during the very high state in 1996, with power-law component increasing by a factor of ten and softening during periods of days. Méndez, Belloni & van der Klis (1998) analyse the spectral state of GRO J1655–40 at the end of the same outburst from the perspective of rapid variability characteristics, and also find a transition from high to low state, passing briefly through the intermediate state. Two other interesting kinds of X-ray variability were seen. Kuulkers et al. (1998) showed GRO J1655–40 to be a ‘dipper’, a source showing short (~ 1 min) and very deep X-ray dips (~ 8 per cent of the out of dip flux). These dips occur at photometric phases 0.72–0.86. The spectrum during a dip can be interpreted as a heavily absorbed version of the out of dip spectrum, although a soft excess requires an unabsorbed component as well. The most obvious interpretation is that the central X-ray source is obscured by clumps or filaments of material above the plane of the accretion disc in the vicinity of the stream impact point. The other intriguing kind of hard X-ray variability was a 300 Hz quasi-periodic oscillation, seen by *RXTE* when the X-ray spectrum was hardest (Remillard et al. 1999). This has variously been interpreted as a precession of the inner disc due to relativistic frame dragging (i.e. the Lense-Thirring effect) by Cui, Zhang & Chen (1998) and as ‘diskoseismic’ g-mode (or possibly c-mode) oscillations of the inner disc by Nowak & Lehr (1998). Both of these interpretations invoke

a rapidly spinning black hole (80 per cent of maximum or more).

The X-ray source was identified with a 14–15th magnitude red object in the optical (Bailyn et al. 1995a). Unfortunately, its southern location has made optical coverage sparse at best. Optical spectra showed emission lines from H I, He I, He II and N III (Bailyn et al. 1995a; Bianchini et al. 1997). Dramatic changes were seen both in line fluxes and profiles (Bianchini et al. 1997) and these appear to correlate with *CGRO*/BATSE hard X-ray changes (Shrader et al. 1996). The orbital period was found to be 2.6 d and partial eclipses were claimed to be detected (Bailyn et al. 1995b). van der Hooft et al. (1997) modelled the optical light curve seen in mid 1995 using a model including an irradiated companion star and light curves. Phillips, Shahbaz & Podsiadlowski (1999) also invoked an irradiated companion to interpret distortions in the outburst radial velocity curve. Optical polarisation studies (Scaltriti et al. 1997; Gliozzi et al. 1998) revealed significant optical polarisation perpendicular to the axis of the radio jet (see below). This polarisation was smoothly modulated on the orbital period and is attributed to the accretion disc as the polarisation is approximately parallel to the inferred disc plane, as expected if it arises from scattering in the disc atmosphere; the smooth modulation is inconsistent with a compact jet base. The modulation has a minimum around the same time that X-ray dips occur, and may therefore arise from obscuration of the polarised region by a bulge in the disc rim.

Radio observations in 1994 (Tingay et al. 1995; Hjellming & Rupen 1995) revealed a series of radio outbursts correlated with hard X-ray outbursts, but with declining amplitude. Most remarkably, interferometry resolved expanding collimated jets similar to those seen in active galactic nuclei. The proper motions implied a jet velocity of 92 per cent of the speed of light and GRO J1655–40 was therefore identified as the second known ‘microquasar’ in the Galaxy (the first was GRS 1915+105, Mirabel & Rodríguez 1994). The jet production mechanism is essentially unknown, though there has been a great deal of theoretical effort directed in this direction. Proposed mechanisms include hydromagnetic acceleration by the accretion disc (Blandford & Payne 1982) and acceleration along field lines threading a rapidly rotating black hole (Blandford & Znajek 1977). Intriguingly, like GRO J1655–40, GRS 1915+105 is also believed to harbour a rapidly spinning black hole, suggesting that jet production may indeed be linked to black hole spin (Zhang, Cui & Chen 1997). Subsequent outbursts of GRO J1655–40 were more disappointing, with no radio detection in 1995, and only a very short-lived radio outburst in 1996 (Hunstead, Wu

& Campbell-Wilson 1997).

4.1.1 The 1996 Outburst

During the 1996 outburst period a series of simultaneous *HST* and *RXTE* visits were performed, backed up by ground based observations and *CGRO* BATSE data. These will be described in this chapter, so it is appropriate to provide more detail on this period in the history of GRO J1655–40. The observations described in this chapter have previously been presented in Hynes et al. (1998b) and Hynes et al. (1998c). In addition some material is drawn from Hynes (1998), as this updates the previous works, and other elements appear in Esin, Lasota & Hynes (1999) and O'Brien et al. (1999).

After a period of apparent quiescence from late 1995 to early 1996, GRO J1655–40 went into outburst again in late 1996 April (Remillard et al. 1996) and remained active until 1997 August. The general nature of the outburst is characterised by Figure 4.2, showing the *CGRO* BATSE (20–200 keV), *RXTE* ASM (2–12 keV) and *V* band light curves from 1996–7. Orosz et al. (1997) observed an optical rise leading the X-ray rise detected by *RXTE* by about 6 days. They suggested that this initial behaviour was consistent with the limit-cycle instability. Hameury et al. (1997) have successfully modelled both the optical and soft X-ray rise in GRO J1655–40 using a two-component model involving a conventional outer disc and an advective inner disc. In this model, the outburst is triggered by the limit cycle instability acting in the outer disc, but the 6 day soft X-ray delay is due to the need to fill up the inner disc.

The subsequent X-ray behaviour was not as expected. The soft X-ray flux (2–10 keV), as followed by the *RXTE*/ASM, remained at an approximately constant level for more than four months, though with considerable short term variability (the flaring very high state referred to above) while the hard X-ray flux (20–200 keV) as monitored by *CGRO*/BATSE was observed to rise very slowly, not reaching its peak until four months after the initial dramatic increase in the soft flux. In spite of this complex X-ray behaviour, the optical fluxes are consistent with a fast-rise, exponential decay pattern for the first part of the outburst, although they later rise again. The overall impression is that optical brightness follows soft X-ray fluxes, but is suppressed when hard X-ray emission is present. Thus during the hard X-ray rise, the optical fluxes fall, whereas during 1997, when the hard flux is very low, optical fluxes follow soft X-rays.

Radio detections of this outburst were short-lived; there certainly was not the sustained

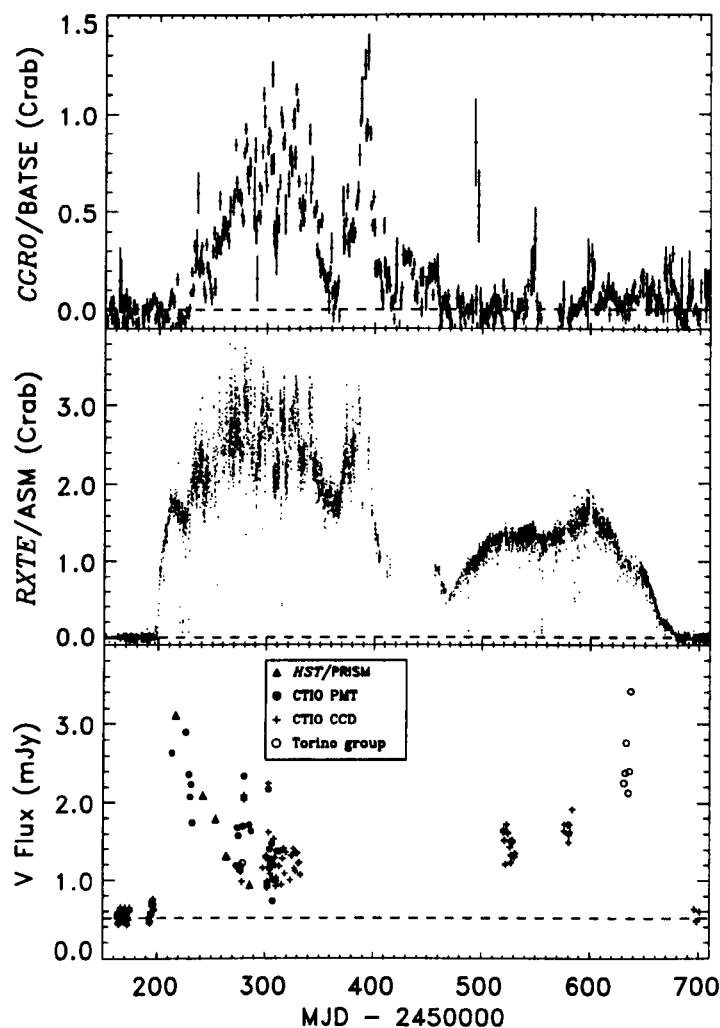


Figure 4.2: Long term light curves of the 1996 outburst. The time-axis begins at 1996 March 8. V band data comprise synthetic photometry from the *HST*/PRISM spectra, photoelectric photometry from CTIO provided by Jonathan Kemp, CCD photometry from CTIO provided by Dr. Charles Bailyn, Dr. Jerry Orosz and Raj Jain and photopolarimetric observations of the Torino group (Scaltriti et al. 1997; Gliozzi et al. 1998). The discrepant behaviour of the optical and X-ray data is clear. The first radio detection of this outburst was on day 231.6. The closest non-detection was 9 days before this, making the exact beginning of the radio flare difficult to pinpoint.

radio activity, nor the large amplitudes, of the 1994 outburst, and no jets were detected. Hjellming & Rupen (1996) report no detection above 0.5 mJy between 1996 January and May 20. On May 28, Hunstead & Campbell-Wilson (1996) detected GRO J1655–40 at a flux of 55 ± 5 mJy (843 MHz); Hjellming & Rupen (1996) also observed the source at 19 mJy (4.8 GHz). This flare decayed initially with an e-folding time 1.4 days (Hunstead, Wu & Campbell-Wilson 1997) making it much shorter lived than the activity at other wavelengths. The first detection of this flare corresponds to day 232 in Figure 4.2 and appears to coincide with the initial step-like rise in the BATSE light curve. The actual beginning of the flare could have been up to 9 days before this, however. This contrasts with the outburst of 1994 when radio flares *followed* hard X-ray outbursts. The radio flare also approximately coincides with the beginning of the very high state as classified by Sobczak et al. (1999).

4.1.2 System Parameters

The system parameters of GRO J1655–40 are the best known of any SXT due to the brightness of the companion in quiescence and the consequent small disc contamination. Several quiescent studies (Orosz & Bailyn 1997; van der Hooft et al. 1998; Shahbaz et al. 1999) have established that the system consists of an early F subgiant star in a high inclination ($\sim 70^\circ$) 2.6 d orbit around a massive compact object. The latter is almost certainly a black hole.

The companion has been classified as F3–F6 IV by Orosz & Bailyn (1997), with a best fit for F5 IV. Shahbaz et al. (1999) basically agree with this finding a best fit for F6 III with a main sequence companion ruled out. There has been a great deal of speculation about the evolutionary state of the companion star. One possibility is that it is crossing the Hertzsprung gap, a short-lived phase that occurs after it leaves the main-sequence. The case is argued by Kolb et al. (1997) and Kolb (1998). A difficulty of this model is that binary companions crossing the Hertzsprung gap are expected to drive a very high mass transfer rate, due to rapid radius expansion, and hence appear in persistently active LMXBs. It is argued that there is an even more short-lived sub-phase in which the radius temporarily shrinks and transient behaviour is possible. Regös, Tout & Wickramasinghe (1998), however, believe that this explanation is implausible. They argue that a Hertzsprung gap-crossing scenario is only possible if the companion does not fill its Roche lobe and accretion is driven by winds. They prefer a model in which the companion is

actually still on the main-sequence, but that strong mixing occurs across the core-envelope boundary, perhaps driven by convective overshooting. This still predicts a higher mass transfer rate than observed, but the discrepancy is much smaller than for a lobe-filling star crossing the Hertzsprung gap. At present this question remains unresolved.

The binary mass function has been progressively constrained to $3.16 \pm 0.15 M_{\odot}$ (Bailyn et al. 1995b), $3.24 \pm 0.09 M_{\odot}$ (Orosz & Bailyn 1997) and $2.73 \pm 0.09 M_{\odot}$ (Shahbaz et al. 1999). Only the last study used purely quiescent data. These authors claim that the larger mass functions derived by earlier studies are biased by including outburst data in the analysis. Certainly the data of Shahbaz et al. (1999) is a much better fit to a pure sine wave than that of Orosz & Bailyn (1997), which is clearly distorted.

Shahbaz et al. (1999) were also able to estimate the binary mass ratio by measuring the rotational broadening of absorption features in the companion spectrum. They measure $82.9 < v \sin i < 94.9 \text{ km s}^{-1}$ and infer $0.337 < q < 0.436$ at 95 per cent confidence. This compares favourably with the values of $0.289 < q < 0.385$ (Orosz & Bailyn 1997) and $0.24 < q < 0.42$ (van der Hooft et al. 1998), both at 3σ confidence, derived from fits to ellipsoidal modulations. This is also consistent with the value inferred by assuming that the motion of He II lines seen in outburst accurately reflects the compact object motion: $q = 0.354 \pm 0.035$ (Soria et al. 1998; Shahbaz et al. 1999).

Finally the binary inclination has been measured from ellipsoidal light curve fits performed independently by Orosz & Bailyn (1997), who obtain $69.0^{\circ} < i < 70.6^{\circ}$ (3σ) and van der Hooft et al. (1998) who estimate $63.7^{\circ} < i < 70.7^{\circ}$. The former estimate only takes account of statistical errors, whereas van der Hooft et al. (1998) perform a more thorough analysis of possible systematic effects.

In combining these quantities to estimate masses, the most recent analysis of Shahbaz et al. (1999) is followed¹, who use their own mass function (based only on quiescent data), the mass ratio derived from rotational broadening and the cautious inclination estimate of van der Hooft et al. (1998). They then derive $M_x = 5.5 - 7.9 M_{\odot}$ and $M_c = 1.7 - 3.3 M_{\odot}$, both at 95 per cent confidence. This is strong evidence for a black hole in GRO J1655-40.

¹Parts of the work presented here were performed before this study was published and assume the parameters of Orosz & Bailyn (1997), including masses of $M_x = (7.02 \pm 0.22) M_{\odot}$ and $M_c = (2.34 \pm 0.12) M_{\odot}$. These values are consistent with the constraints of Shahbaz et al. (1999).

Table 4.1: Best fits to May 14 UV observations using a power-law spectrum reddened with the Seaton (1979) Galactic average extinction curve. Various models for the subtraction of excess light from the UV spectrum are considered in order to assess the systematic uncertainty this introduces.

Background model	$E(B - V)$	α	χ^2_R
Pure scattered light,			
best estimate	1.19 ± 0.07	0.35 ± 0.16	1.10
Pure particle background,			
best estimate	1.21 ± 0.07	0.47 ± 0.17	1.10
lowest estimate	1.08 ± 0.06	0.57 ± 0.15	1.10
highest estimate	1.34 ± 0.09	0.37 ± 0.19	1.12

4.1.3 Reddening and Distance

It is important to determine the distance and interstellar reddening of GRO J1655–40 in order to calculate the absolute flux distribution for comparison with models. Fortunately both of these quantities can be well constrained: the reddening is $E(B - V) = 1.2 \pm 0.1$ and the distance is 3.2 ± 0.2 kpc.

Ultraviolet Extinction

The *HST* ultraviolet spectrum through the 2175 Å interstellar absorption feature was used to estimate the reddening. The method assumes that the observed spectra can be fit by a reddened power-law, and has previously been applied to the SXTs X-ray Nova Muscae 1991 (Cheng et al. 1992) and GRO J0422+32 (Shrader et al. 1994). While the underlying spectrum may not be an exact power-law, this should be a reasonable approximation over the restricted spectral range in which the extinction curve varies rapidly. No other assumptions about the properties of GRO J1655–40 are required, although an extinction curve must be adopted. This analysis uses the mean Galactic extinction curve of Seaton (1979). The R_V dependent curves of Cardelli, Clayton & Mathis (1989) were also considered. It was found that the fits did not constrain the value of R_V , but that if the Galactic average $R_V = 3.2$ is assumed then the results are comparable to those from the Seaton (1979) curve. The unusual extinction curve of σ Sco (Clayton & Hanson 1993), which lies 17°

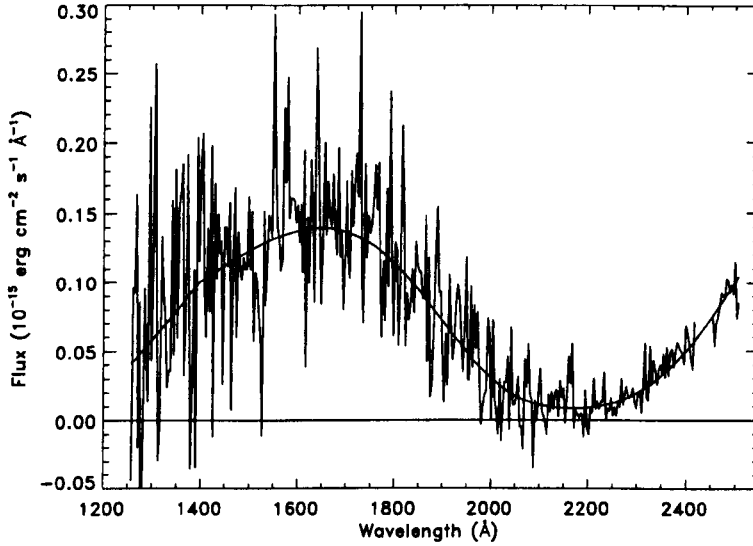


Figure 4.3: Best fitting reddened power-law to 14 May UV data assuming all the excess background to be scattered light.

from GRO J1655–40, was also tested. The fit with this curve was significantly poorer than with the Seaton (1979) curve. Adopting a Galactic average extinction curve is likely to be appropriate for GRO J1655–40. Its reddening is quite high, and absorption likely arises from a number of distinct regions. The overall extinction curve probably is an average of more diverse individual curves. In support of this argument, Krelowski & Papaj (1993) examine colour excess ratios (a measure of the extinction curve shape) as a function of distance. There is a large scatter for nearby objects, but this converges with distance. At the distance of GRO J1655–40, 3.2 kpc (see Section 4.1.3), the scatter is small.

Initial attempts to fit a reddened $f_\nu \propto \nu^{1/3}$ power-law to the whole spectrum by Horne et al. (1996) suggested a value of $E(B - V) = 1.3$. This yielded a poor fit to the 2175 Å feature however. Examining spectra dereddened using all the extinction curves listed above, and a range of extinction parameters, robustly reveals an intrinsic break around 2600 Å. Analysis of background counts and scattered light in the UV cannot explain this purely as a calibration problem. A fit of a single reddened power-law is therefore only appropriate below 2600 Å. It was decided to base a revised reddening estimate on the UV data obtained with the G160L grating only. While both the G270H and PRISMs overlap into the region below 2600 Å, this region is very sensitive to an incorrect background subtraction (more so than is the case for the G160L in the same overlap region) and so

including this data would be more likely to systematically bias the reddening estimate than to improve it.

Reddened power-law models were fitted to the average G160L spectra by χ^2 minimisation, using a robust grid-search method to locate the minimum. Errors are estimated from 1σ two-parameter confidence intervals as defined by Lampton, Margon & Bowyer (1976). The estimates are shown in Table 4.1. They are not sensitive to whether the excess light is taken to be scattered light or particle induced but they are strongly affected by the *level* subtracted. To quantify the effect of the uncertain background level, fits were performed for estimates of the maximum and minimum background level in the particle dominated case. These were estimated by fitting the background level repeatedly in 50 pixel bins and taking the highest and lowest estimates. The fit to the spectrum assuming all of the excess to be scattered light², shown in Figure 4.3, is extremely good.

Direct Optical Estimation

A direct estimate of the visual extinction, A_V , can also be obtained by considering the expected absolute magnitude of the companion star. Orosz & Bailyn (1997) obtain a best fit spectral type of F5 IV, with an acceptable range of F3–F6 IV and an effective radius of $4.85 \pm 0.08 R_\odot$. Using absolute magnitudes and radii of main sequence F3–F6 stars (Gray 1992) the magnitudes can be rescaled to the effective radius of GRO J1655–40 thereby approximating the absolute magnitude of the companion star to be $M_V = 0.7 \pm 0.5$ (allowing for uncertainty in the spectral type and radius.) Orosz & Bailyn (1997) observe a mean apparent magnitude in quiescence of $m_V = 17.12$ and estimate by fitting photospheric absorption lines that the disc contributes < 10 per cent of the visible light. Assuming a disc contribution of ~ 5 per cent gives an apparent magnitude of the companion star of 17.18 ± 0.06 . The errors in this figure are significantly less than in the estimate of the absolute magnitude. Adopting a distance of 3.2 ± 0.2 kpc (see Section 4.1.3, the difference between absolute and apparent magnitudes implies $A_V = 4.0 \pm 0.5$ hence, assuming an average extinction curve ($R_V = 3.2$), $E(B - V) = 1.25 \pm 0.17$.

Interstellar Absorption Lines

In keeping with the highly reddened nature of GRO J1655–40, a rich spectrum of interstellar features are seen in the AAT spectra. The equivalent width of the unresolved Na D

²As noted in Section 3.3, it now appears more likely that background counts are particle induced. This makes no significant difference to this result.

doublet is $2.5 \pm 0.1 \text{ \AA}$; diffuse interstellar bands (Herbig 1995) at 5778/80, 6177 and 6284 \AA can also be identified. Bianchini et al. (1997) make more precise measurements of the equivalent widths of the Na D doublet (5890 \AA) and the 6613 \AA interstellar band of 2.26 \AA and 0.27 \AA respectively. They deduce $E(B - V) = 1.30$ and 0.97 respectively.

This method should be viewed with caution however. Firstly, Baily et al. (1995a) obtained a much larger Na D equivalent width of 4.5 \AA at a time when the doublet was blended with He I emission. In spite of this they obtain a *lower* reddening of $E(B - V) = 1.15$ simply by using a different equivalent width–reddening relation. Secondly, as noted by Munari & Zwitter (1997), the Na D lines are not in general sensitive to $E(B - V) \geq 0.5$ due to saturation, so this method can underestimate the reddening; whether it does or not depends on the detailed substructure of the lines which is not usually resolved.

There may also be signs of the very broad structure (VBS) that has previously been reported in extinction curves of highly reddened objects (Krelowski, Maszkowski & Strobel 1986). This consists of very shallow dips in the extinction curve between 5000 \AA and 8000 \AA and appears as apparent weak, broad emission features centred at 5300, 5900 and 6800 \AA . VBS can possibly be identified in the AAT spectra, in particular around 6800 \AA , (see Figure 4.7).

X-Ray Absorption

The most precise measurements of the absorption column density are those obtained by fitting *ASCA* spectra. Inoue et al. (1994) derive $N_{\text{H}} = 5 \times 10^{21} \text{ cm}^{-2}$ from observations on 1994 August 23. Subsequent observations obtained $4.4 \times 10^{21} \text{ cm}^{-2}$ (Nagase et al. 1994) and $8 \times 10^{21} \text{ cm}^{-2}$ (Inoue, Nagase & Ueda 1995). Greiner, Predehl & Pohl (1995) use the *ROSAT* high-resolution imager to resolve the dust scattering halo. Modelling this they deduce $N_{\text{H}} = 7 \times 10^{22} \text{ cm}^{-2}$.

Summary

It is encouraging that direct estimates of the visual extinction, measurements of interstellar absorption lines and fitting the 2175 \AA feature all give consistent results. The *HST* value is adopted as the best estimate of the reddening: $E(B - V) = 1.2 \pm 0.1$. This can be compared with the extinction maps of the Galactic plane presented by Neckel, Klare & Sarcander (1980). GRO J1655–40 lies close to the boundary of two of their regions, one of low extinction, for which $E(B - V) \sim 0.4$ is expected at 3.2 kpc, and one of high extinction,

for which the highest extinctions measured (up to ~ 2.5 kpc) correspond to $E(B - V) = 1.3$. A value of $E(B - V) = 1.2$ is thus consistent with the position of GRO J1655-40.

Furthermore, using the gas to dust scaling of Bohlin, Savage & Drake (1978), and their estimate of the scatter in this relationship, this $E(B - V)$ value would correspond to a range of hydrogen column densities of $N_{\text{H}} = 4.6 - 10 \times 10^{21} \text{ cm}^{-2}$, in good agreement with the range of *ASCA* values observed (but not with the *ROSAT* value which far exceeds all other optical, UV and X-ray measurements).

Distance

Hjellming & Rupen (1995) estimate the distance from a kinematic model of the jets to be 3.2 ± 0.2 kpc. There is also a lower limit from observations of the 1420 MHz interstellar absorption (Tingay et al. 1995) of 3.0 kpc and an upper limit can be obtained by the method of Mirabel & Rodríguez (1994). The latter assumes that the proper motions of the two jets can be identified relative to the central source and then only involves the requirement that these proper motions are produced by material moving at no more than the speed of light. Mirabel & Rodríguez (1994) give

$$\beta \cos \theta = \frac{\mu_a - \mu_r}{\mu_a + \mu_r} \quad (4.1)$$

and

$$D = \frac{c \tan \theta}{2} \frac{\mu_a - \mu_r}{\mu_a \mu_r} \quad (4.2)$$

where $\beta = v/c$, θ is the angle of the jets to the line of sight, μ_a and μ_r are the proper motions of the approaching and receding jet respectively and D is the distance. These can be combined to give

$$D \leq \frac{c}{\sqrt{\mu_a \mu_r}}. \quad (4.3)$$

Using the proper motions of Hjellming & Rupen (1995) then yields $D \leq 3.5$ kpc.

The lower and upper limits support the distance estimate of Hjellming & Rupen (1995), 3.2 ± 0.2 kpc, which will be adopted hereafter.

4.2 X-Ray Observations

While the focus of this work is primarily on optical and ultraviolet astronomy, X-ray data from *RXTE*/PCA obtained simultaneous with the *HST* data are also relevant to the analysis. The data were reduced by Dr. Wan Chen and Dr. Chris Shrader. The following

descriptions of the data processing are adapted from their contributions to Hynes et al. (1998b) and Hynes et al. (1998c).

As part of the multi-wavelength ToO programme described in Section 1.8, GRO J1655–40 was observed with the *RXTE* Proportional Counter Array (PCA) at six separate epochs³, four of which coincided with *HST* pointings. Table 4.2 shows the observing log. The total exposure time was 40.74 ks. The PCA consists of 5 gas proportional counter modules, and provides spectral coverage over the 2–60 keV range. For a complete discussion of the *RXTE* instrumentation see Jahoda et al. (1996). Two standard PCA data modes were used, with a 12.5 ms time resolution and 256 energy channels, together with a 16 energy channel mode binned at 4 ms time resolution and two single channel, single bit modes at 62 μ s.

Spectra were constructed from the ‘standard mode’ data with 128 energy channels over the bandpass. Typical count rates were $\sim 10^4 \text{ s}^{-1}$, so statistical errors were very small. Response matrices and estimated background count spectra were constructed using the standard *RXTE* data analysis procedures. Subsequent spectral analysis then used the XSPEC package distributed by the High Energy Astrophysics Science Archive Research Center (HEASARC).

The spectrum from May 14 was compared with that presented by Sobczak et al. (1999) for May 9 and found to differ in normalisation by a factor of 3.3, with that of May 14 lower. Examination of the *RXTE*/ASM lightcurves, however, showed only a 5 per cent random variability in this period. The spectral shape was very similar, differing only in a stronger power-law tail in the later spectrum (as might be expected since the hard fluxes were rising at this point.) This discrepancy must arise from a problem in calibration⁴. It was decided to renormalise the spectrum from May 14 provided by Dr. Chris Shrader to match that of Sobczak et al. (1999). This was decided because a) this is the more recent calibration and b) fits of a multicolour black body spectrum by Sobczak et al. (1999) yield very plausible parameters; an inner disc radius of $\sim 3R_{\text{Sch}}$ and a mass transfer rate $\sim 0.1\dot{M}_{\text{Edd}}$. Similar fits to the normalisation of Dr. Chris Shrader would require a disc radius less than R_{Sch} and a mass transfer rate only a few per cent of Eddington.

Since the highest time resolution from the *HST* data is only about 2–3 s, X-ray light

³There were many other PCA pointings under independent proposals and also several public ToO observations were performed.

⁴A careful recalibration of the May 14 spectrum is needed. A quick re-extraction did yield a spectrum closer to that of Sobczak et al. (1999) (Shrader 1999 priv. comm.)

Table 4.2: Log of *RXTE* observations.

Date	Start/End	Duration
	(UT)	(ks)
May 14	00:07–00:28	1.26
	01:42–02:04	1.32
	03:24–03:40	0.96
May 20	13:55–14:33	2.28
	14:35–14:56	1.26
	15:42–16:09	1.62
	16:11–16:33	1.32
	17:24–17:46	1.32
	17:48–18:09	1.26
May 27	17:29–18:19	3.00
	19:07–19:55	2.88
June 8	12:45–13:41	3.36
	14:21–15:23	3.72
	15:57–17:02	3.90
	17:33–18:34	3.66
June 20	12:55–13:12	1.02
	14:31–14:54	1.38
	16:07–16:35	1.68
June 30	13:00–13:59	3.54

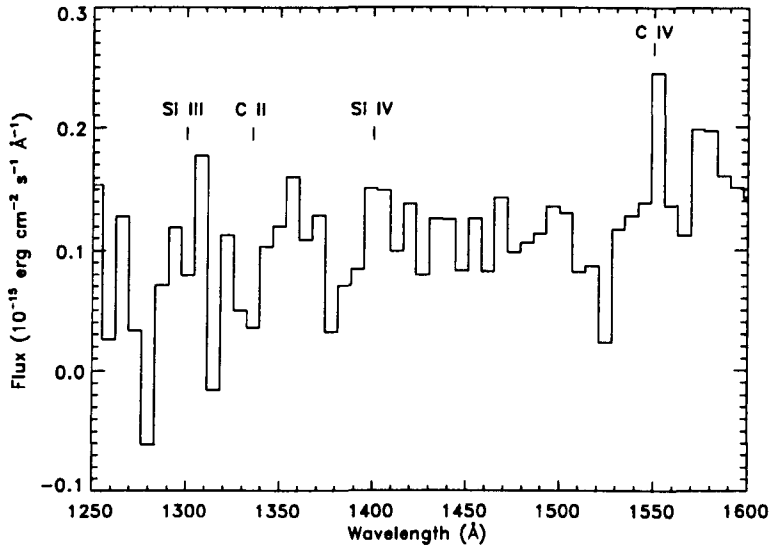


Figure 4.4: Far-UV *HST* spectrum showing possible P Cygni profiles in the UV resonance lines. The spectrum has been rebinned to one pixel per resolution element.

curves were extracted from the standard-1 mode data in 1 s time bins using the `saextrct` task in the `FTOOLS` software package. The average count rate of GRO J1655-40 during the first observing period (when the object was faintest in X-rays) was more than $2 \times 10^4 \text{ counts s}^{-1}$ of “good events” (i.e., after 80 per cent of internal background events are rejected by the anti-coincidence logic), thus no background subtraction procedure is necessary as the remaining background is $\leq 35 \text{ counts s}^{-1}$. The relative timing accuracy of the *RXTE* data is limited only by the stability of the spacecraft clock which is good to about $1 \mu\text{s}$ or less. The absolute timing accuracy, however, is also limited by uncertainties in the ground clock at the White Sands station and other complications. For these data, the absolute timing accuracy is estimated to be about $8 \mu\text{s}$ which is substantially better than that of *HST*/FOS and certainly sufficient for the applications considered here.

4.3 Emission Lines

4.3.1 Ultraviolet Resonance Lines

P Cygni profiles appear to be present in the UV resonance lines: Si III (1302 Å), Si IV (1397 Å) and C IV (1549 Å) together with possible C II (1335 Å) absorption. These are shown in Figure 4.4. Although the detection of these is marginal, their positions are

correct and the peak to trough separation of all three P Cygni profiles corresponds to velocities of order 5000 km s^{-1} ; comparable to (although somewhat higher than) those seen in dwarf novae in outburst (Shlosman & Vitello 1993 and references therein). Shlosman & Vitello (1993) model the expected disc wind profiles in the C IV 1550 Å line accounting for the non-radial outflow and solving the radiative transfer problem in detail. They find that for low inclination systems where the disc is seen through the wind, only a blue-shifted absorption component is seen. For high inclination systems, symmetric emission is seen from the wind. Only for a relatively narrow range of inclinations are ‘classical’ P Cygni profiles showing absorption and emission in similar strengths expected. This range of inclinations is around $60\text{--}70^\circ$, in good agreement with the inclination determined for GRO J1655–40 in quiescence, which adds support to this interpretation. The high noise level of the data, however, prevents distinguishing between such a disc wind and a pure radial outflow, possibly emanating in the inner regions.

4.3.2 Helium and Bowen Fluorescence Lines

The only helium line detected in the *HST* spectrum is He II Paschen α (4686 Å), illustrated in Figure 4.5. There is no detection of He II Paschen β (3203 Å) or He II Balmer α (1640 Å). In the AAT spectra, it is also possible to (marginally) detect the 5411.5 Å Pickering γ line.

There is strong emission around 4640 Å (Figure 4.5) due to the blend of three N III Bowen lines (4634, 41, 42 Å). It is possible that there is also some contribution from the non-Bowen C III lines (4647, 51, 52 Å). These lines cannot be deblended in any of the spectra presented here. Soria et al. (1998) found on 1996 June 8 that the N III lines dominate, with the C III lines much weaker. They also identify O II 4662 Å emission.

Supporting the Bowen interpretation for the 4641 Å blend are the detections of three O III Bowen lines, representing both the O1 (3133, 3444 Å) and O3 (3407 Å) cascades (see below). These are shown in Figure 4.6. Only the line at 3133 Å is unambiguously detected; this is theoretically expected to be the strongest line of the O1 channel.

The Bowen fluorescence mechanism as it applies in X-ray binaries has been well discussed from a theoretical standpoint by Deguchi (1985) and in the context of observations of Sco X-1 by Schachter, Filippenko & Kahn (1989). The essence of the mechanism is this: the He II Lyman α transition (303.783 Å) is nearly coincident with two transitions of O III. He II photons can excite these; the subsequent decays, through the O1 and O3 channels respectively, produce UV emission lines of O III. One of these decay transitions,

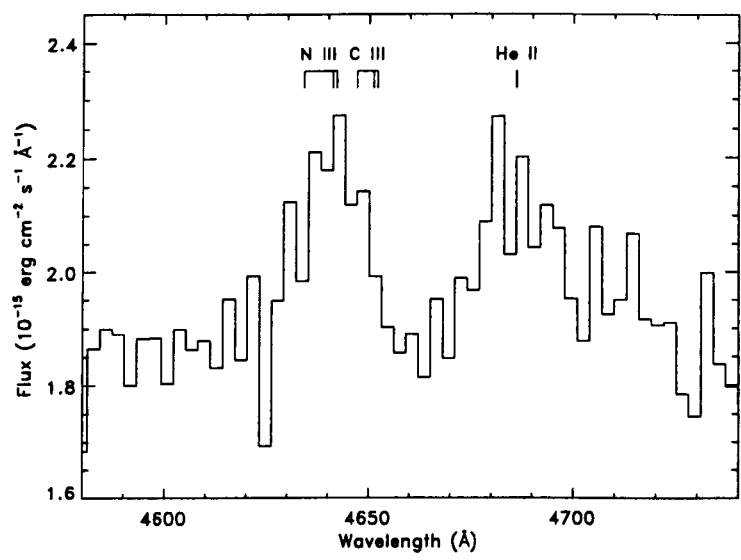


Figure 4.5: *HST* line profiles of The N III 4634, 4641, 4642 Å and He II 4686 Å emission lines. The positions of the C III 4647, 4651, 4652 Å lines are also marked. The spectrum has been rebinned to one pixel per resolution element.

Table 4.3: Properties of He II and Bowen emission lines detected in May spectra.

Line	Telescope/ date	Fitted wavelength	Line flux (10 ⁻¹⁵ erg s ⁻¹ cm ⁻²)	FWHM (Å)
O III(λ3133)	<i>HST</i> /May 14	3133.2 ± 0.7	2.9 ± 0.4	14 ± 2
O III(λ3407)	<i>HST</i> /May 14	3405.0 ± 2.6	2.6 ± 0.9	21 ± 5
O III(λ3444)	<i>HST</i> /May 14	3439.3 ± 4.3	2.3 ± 0.9	21 ± 5
N III(λλ4634, 41, 42)	AAT/May 11	4638.9 ± 0.9	7.7 ± 0.5	26 ± 2
	AAT/May 12	4637.1 ± 1.1	7.3 ± 0.8	24 ± 3
	AAT/May 13	4635.7 ± 0.9	11.0 ± 1.0	27 ± 2
	<i>HST</i> /May 14	4640.8 ± 0.8	6.3 ± 0.6	16 ± 2
He II(λ4686)	AAT/May 11	4685.0 ± 0.9	4.6 ± 0.5	18 ± 3
	AAT/May 12	4686.2 ± 1.1	2.7 ± 0.6	11 ± 3
	AAT/May 13	4681.7 ± 0.7	8.5 ± 0.9	18 ± 2
	<i>HST</i> /May 14	4686.1 ± 0.9	6.2 ± 0.6	21 ± 2

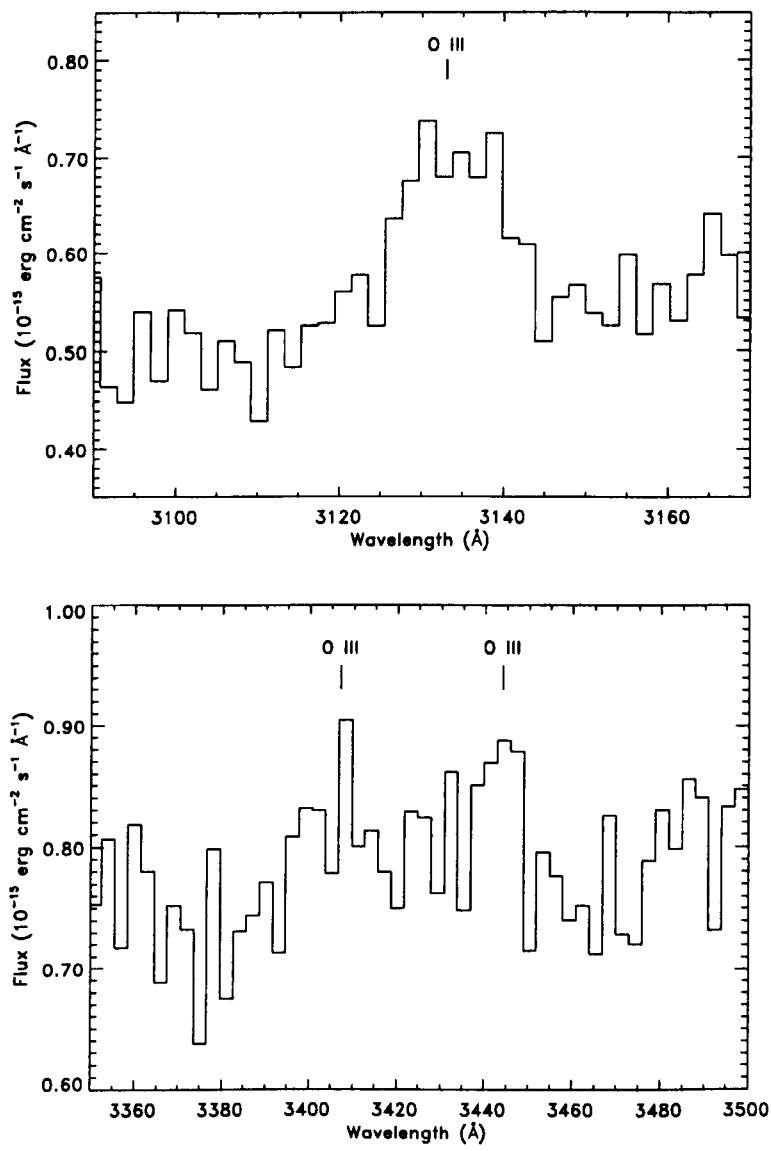


Figure 4.6: *HST* line profiles of the O III 3133 Å and possible 3407, 3444 Å emission lines. The spectra have been rebinned to one pixel per resolution element.

the O4 channel, is in turn nearly coincident with a doublet of N III. This can then be excited and decay to produce N III emission lines. Using the measured line fluxes of the principal related lines it is possible to measure the efficiency of this process, as measured by the Bowen yields.

The oxygen yield is the probability that a He II Lyman α photon will produce a cascade through the O1 channel. It is measured by

$$y_{\text{HeO1}} = k_{\text{H}} \frac{f(\lambda 3133)}{f(\lambda 4686)} \quad (4.4)$$

where $f(\lambda)$ is the *dereddened* line flux. Following Schachter, Filippenko & Kahn (1989), $k_{\text{H}} = 0.28$ is adopted. This value is dependent on the temperature of the producing region, but the uncertainty this introduces is comparable to the uncertainty in the line flux measurements and much less than that in dereddening the flux ratio. Using the Seaton (1979) extinction curve with $E(B - V) = 1.2 \pm 0.1$, gives

$$y_{\text{HeO1}} = 0.70 \pm 0.15. \quad (4.5)$$

Deguchi (1985) predicts values for this yield between 0.5 and 0.8; Schachter, Filippenko & Kahn (1989) find values ranging from 0.47–0.59 for Sco X-1. The results for GRO J1655–40 are consistent with these, but are not precise enough to further constrain the emission line region.

In an analogous way, the nitrogen yield, y_{ON} , represents the fraction of O4 photons which produce a nitrogen cascade. The situation is complicated here by two factors. Firstly the C III component cannot be deblended from the N III blend, so there is really only an upper limit on the N III flux. Secondly, to perform this calculation correctly it is necessary to know the strengths of both the O1 and O3 cascades, since both can in turn initiate an O4 cascade. The O3 lines cannot reliably be measured so this contribution cannot be quantified. If the O3 contribution is simply ignored, this will also lead to overestimating the yield. An upper limit is therefore

$$y_{\text{ON}} = k_{\text{KM}} \frac{f(\lambda\lambda 4634, 41, 42)}{f(\lambda 3133)} \quad (4.6)$$

where $k_{\text{KM}} = 8.6$, independent of physical conditions. Hence for GRO J1655–40,

$$y_{\text{ON}} \leq 3.7 \pm 0.8. \quad (4.7)$$

Again, this is in reasonable agreement with Schachter, Filippenko & Kahn (1989) who find $y_{\text{ON}} = 3.2 - 4.0$ for Sco X-1, with the same assumptions; they also note that this is an overestimate.

Clearly these measurements do not tightly constrain the location of the Bowen line emission region. They are, however, completely consistent with measurements in Sco X-1 indicating that conditions are similar.

4.3.3 A Constraint on the Extreme Ultraviolet Flux

The observed line flux of the He II 4686 Å line can also be used to place an upper limit on the EUV flux, subject to some assumptions. Photoionisation in the disc and/or companion star by 55–280 eV photons (bounded by the ionisation energy of He II and the carbon K-edge) will produce He III, which will then recombine leading to 4686 Å emission. One can estimate the EUV flux which will give the observed line emission. This is a very useful constraint, as this region of the spectrum can never be observed directly for a source with even moderate reddening. Since 4686 Å could also originate in collisional excitation (at the stream impact point for example), this will be an upper limit. It is also very dependent on the assumed geometry, both of the EUV and line emitting regions. The method has been developed in the context of cataclysmic variables, where the EUV flux is believed to originate at the boundary layer of the disc and white dwarf (Patterson & Raymond 1985; Marsh & Horne 1990). Marsh, Robinson & Wood (1994) demonstrated that it could also be applied to SXTs, with the EUV instead originating from the inner regions of the disc. Their calculation assumes that the EUV radiation is isotropic, appropriate for a point source or a corona. If it originates in the optically thick inner accretion disc then because both the companion star and the outer disc see these regions at a high inclination, and hence foreshortened, this will therefore overestimate the EUV flux incident upon them.

This inclination effect introduces a factor of $\cos \theta$ into the EUV angular flux distribution, where θ is the angle of the EUV radiation to the disc normal. It is assumed that there is no shielding by the inner part of the disc. Two extreme cases are considered: radiation intercepted by the disc only and radiation intercepted by the companion star assuming a vanishingly thin disc.

In the disc case, the fraction, α , of EUV luminosity intercepted is

$$\alpha \simeq \frac{\int_0^{H/R} \cos \theta \, d(\cos \theta)}{\int_0^1 \cos \theta \, d(\cos \theta)} \simeq \left(\frac{H}{R} \right)^2 \quad (4.8)$$

integrating over the upper half of the (symmetric) distribution and approximating $\cos \theta = \sin(\pi/2 - \theta) \sim H/R$ for small disc thicknesses.

The companion star case is modified by an additional factor of $f(\theta)$ in the denominator integral representing the fraction of azimuth subtended by the companion. The problem

can be simplified by modelling it as a circle of radius r_{eq} centred on the companion position which subtends the same solid angle at the primary as the real Roche lobe does. r_{eq} can be determined numerically as a function of the mass ratio, q . For GRO J1655–40 ($q = 2.99$), $r_{\text{eq}} = 0.286$, somewhat larger than the polar radius of 0.269. Then

$$f \simeq \frac{2\sqrt{r_{\text{eq}}^2 - \cos^2 \theta}}{2\pi} \quad (4.9)$$

and so the fraction of flux intercepted is

$$\alpha \simeq \frac{\int_0^{r_{\text{eq}}} f(\theta) \cos \theta d(\cos \theta)}{\int_0^1 \cos \theta d(\cos \theta)} \simeq \frac{2r_{\text{eq}}^3}{3\pi}. \quad (4.10)$$

The 4686 Å line luminosity is denoted by L_{4686} and the integrated 55–280 eV luminosity by L_{EUV} . A fraction α of the total number of 55–280 eV photons are intercepted by the disc or companion star and a fraction ϵ of the total number of photoionisations caused by 55–280 eV photons recombine through this channel. For Case B recombination (appropriate when the emission line region is optically thick to the ionising radiation but optically thin to the recombination lines), $\epsilon \simeq 0.2$. The ratio of luminosities will be

$$\frac{L_{\text{EUV}}}{L_{4686}} = \frac{1}{\alpha\epsilon} E_{\text{EUVE}} \left(\frac{\lambda_{4686}}{h} c \right) \quad (4.11)$$

where E_{EUVE} is an average energy of the EUV photons. The EUV flux, F_{EUV} , that would be observed is related to the total luminosity by $F_{\text{EUV}} = L_{\text{EUV}} \cos i / 2\pi d^2$, where d is the distance of the system. For optically thin recombination lines, the line emission will be isotropic. The relation between flux and luminosity then depends only on the fraction, β , of the emission line region that is seen: $F_{4686} = \beta L_{4686} / 4\pi d^2$. For a disc, only one face is visible and $\beta = 0.5$ (neglecting self-obscuration of part of the disc by a possible flared rim.) For lines originating on the companion star, β is phase and inclination dependent. The ratio of EUV to line fluxes is

$$\frac{F_{\text{EUV}}}{F_{4686}} = \frac{2 \cos i}{\beta\alpha\epsilon} E_{\text{EUVE}} \left(\frac{\lambda_{4686}}{h} c \right). \quad (4.12)$$

Observed line fluxes are in the range $(2.7\text{--}8.5) \times 10^{-15} \text{ erg s}^{-1} \text{ cm}^{-2}$. If these are produced in the disc, then they should be phase independent, and this range must be interpreted as due to stochastic variability. One should then use the line flux from May 14 to obtain the best estimate of the May 14 EUV flux. Dereddening this (assuming $E(B-V) = 1.2 \pm 0.1$) and taking $\epsilon = 0.2$, $E_{\text{EUVE}} = 100 \text{ eV}$, an EUV bandwidth of 55–280 eV, $\lambda_{4686} = 4686 \text{ Å}$ and assuming a minimum fractional disc half thickness of $H/R = 0.01$, as

was taken by Marsh, Robinson & Wood (1994), this translates into an *upper* limit on the EUV flux per unit frequency interval of $f_\nu(2.4 \times 10^{16} \text{ Hz}) \lesssim 5.9 \times 10^{-24} \text{ erg cm}^{-2} \text{ s}^{-1} \text{ Hz}^{-1}$ for the case where 4686 Å emission originates only in the disc.

Examining the four line fluxes as a function of orbital phase, however, the flux is highest at spectroscopic phase 0.19, when the heated face of the companion star is seen nearly face on, and lowest at phase 0.81, when the rear face of the companion star is visible. This suggests that the 4686 Å emission originates at least partially on the companion star and so this cannot be completely shielded by the disc. With this interpretation it is more appropriate to use the highest 4686 Å flux, when virtually all of the emission region ($\beta \sim 1$) is visible, to constrain the EUV flux to be $f_\nu(2.4 \times 10^{16} \text{ Hz}) \lesssim 2.3 \times 10^{-25} \text{ erg cm}^{-2} \text{ s}^{-1} \text{ Hz}^{-1}$. This constraint is shown in Figure 4.22 in relation to the optical/UV and X-ray data.

The latter calculation represents the more realistic limit, in the sense that if the disc did become very thin then the 4686 Å flux would not become vanishingly small; it would instead be produced on the companion star. The fundamental assumption in deriving this upper limit is that none of the EUV flux is shielded by the inner disc. This is not a secure assumption and some self-shielding of the outer disc by the inner is likely to occur (Dubus et al. 1999 and references therein.)

4.4 Characterisation of Continuum Spectra

Because the *HST* data provide broad-band, calibrated spectra from red to UV wavelengths, they are well suited for studying the shape of the optical/UV spectral energy distribution. The analysis of this is divided into two parts. The first, in this section, describes the simple characterisation of the spectrum included in Hynes et al. (1998b). The second part (Section 4.7) attempts to refine the analysis in the light of what has been learned since Hynes et al. (1998b) was submitted; the spectra in this form have been included in Esin, Lasota & Hynes (1999).

A montage of all the spectra (including those from AAT) in their original, reddened form are shown in Figure 4.7. Figure 4.8 shows the same spectra after dereddening and transforming to a $\log \nu$ – $\log F_\nu$ representation.

In view of the large uncertainty in determining the intrinsic flux distribution from such highly-reddened spectra, together with distortions from specific interstellar features (e.g. very broad structure, diffuse interstellar bands), which are largely unresolved by PRISM/RD, it was not considered appropriate to attempt to fit a detailed model for the

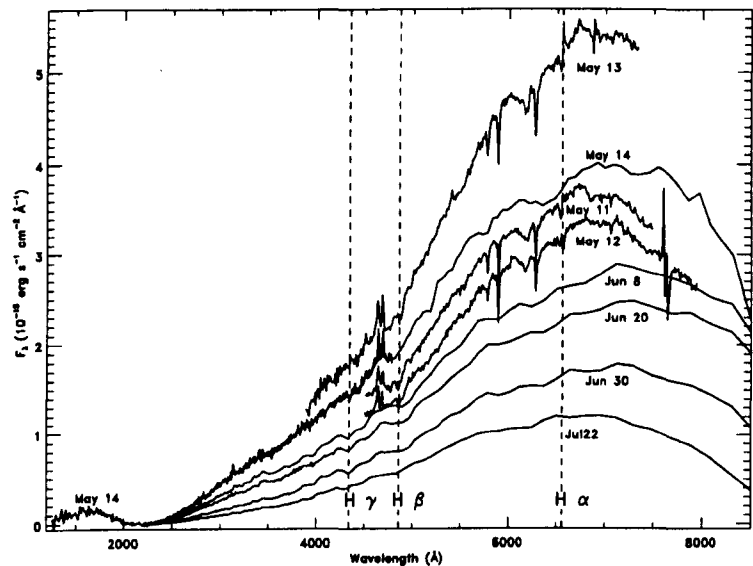


Figure 4.7: Composite spectra for all *HST* and AAT observations. Spectra have been rebinned to 10 Å for clarity. The long wavelength data has been retained for comparison here, but was truncated for subsequent analysis. See text for details. The calibration does not incorporate the changes described in Section 4.7.2.

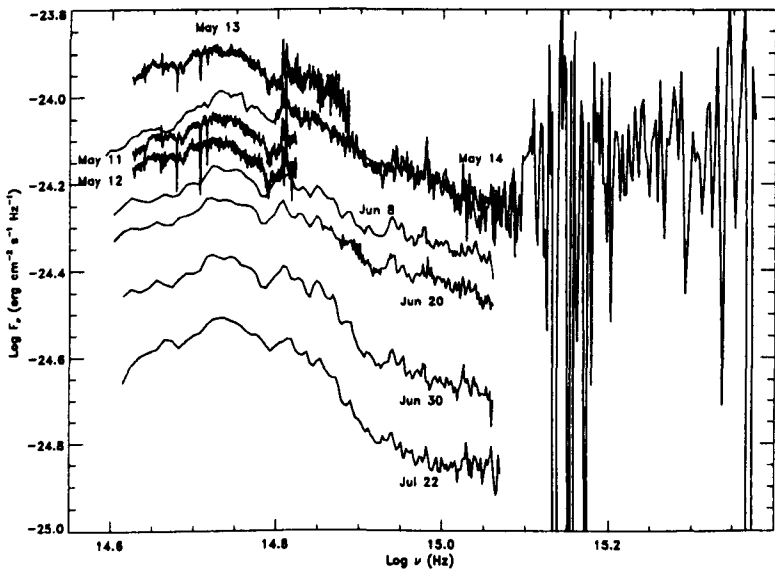


Figure 4.8: Spectra dereddened using the Seaton (1979) extinction law with $E(B - V) = 1.2$.

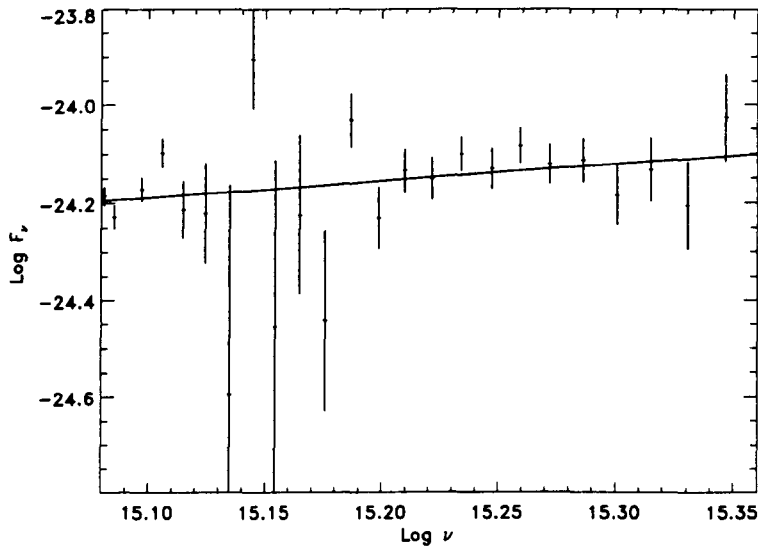


Figure 4.9: Fit of a $\nu^{1/3}$ spectrum to the rebinned G160L far-UV data to determine \dot{M} .

complete spectra, even if a suitable model could be found. Instead a simple characterisation of the observed spectra was sought and then compared with the available sources of radiation.

4.4.1 The Steady State Black-body Disc Model

The far-UV data from the first *HST* visit is suggestive of the $\nu^{1/3}$ spectrum expected from a steady state optically thick accretion disc⁵; a similar UV spectral index was found in *HST* observations of X-ray Nova Muscae 1991 (Cheng et al. 1992). While a SXT in outburst is clearly not in a steady state, it is often assumed that this will be a good approximation on the decline from outburst if the viscous timescale of the disc is shorter than the timescale of mass transfer rate variations. This interpretation will be examined more critically in Section 4.7.1. The spectrum of a steady state disc is discussed by Frank, King & Raine (1992) and Cheng et al. (1992). For frequencies, ν , such that

$$kT(R_{\text{out}}) \ll h\nu \ll kT(R_{\text{in}}) \quad (4.13)$$

⁵This spectrum is dependent on the dereddening. Although the fit to the reddened far-UV spectrum explicitly assumed a power-law form, the extinction curve was fixed giving little freedom to adjust the shape of the spectrum. That the reddened power-law then yielded a very good fit to the data with an $E(B - V)$ value consistent with other determinations indicates that the intrinsic spectrum is indeed close to a power-law.

where R_{in} and R_{out} are the radii of the inner and outer edges of the disc and h is Planck's constant, the spectrum reduces to the canonical $\nu^{1/3}$ disc spectrum:

$$f_\nu = f_0 \frac{\cos i}{d^2} (m\dot{m})^{2/3} \nu_{15}^{1/3} \int_0^\infty \frac{x^{5/3} dx}{e^x - 1} \quad (4.14)$$

where $f_0 \simeq 2.9 \times 10^{-26} \text{ erg s}^{-1} \text{ cm}^{-2} \text{ Hz}^{-1}$, i is the inclination, d is the distance in kpc, m is the compact object mass in M_\odot , \dot{m} is the mass transfer rate in $10^{-9} M_\odot \text{ yr}^{-1}$, ν_{15} is the frequency in units of 10^{15} Hz and the integral evaluates to 1.9.

This model spectrum was fitted to the far-UV data (see Figure 4.9) and, with the parameters of Section 4.1.2, a value of $\dot{M} \simeq 8 \times 10^{-7} M_\odot \text{ yr}^{-1}$ is deduced, adopting the best estimate of background counts and reddening. Allowing the full range of backgrounds and reddening values discussed earlier gives a range of $1 \times 10^{-7} M_\odot \text{ yr}^{-1} \leq \dot{M} \leq 7 \times 10^{-6} M_\odot \text{ yr}^{-1}$. This can be compared with the Eddington accretion rate of $\dot{M}_{\text{Edd}} = 1.6 \times 10^{-7} M_\odot \text{ yr}^{-1}$ (taking a compact object mass of $7 M_\odot$ and assuming an accretion efficiency of 10 per cent.) This interpretation of the far-UV spectrum thus requires a very large mass transfer rate.

The extrapolation of this spectrum into the EUV would predict $f_\nu (2.4 \times 10^{16} \text{ Hz}) \simeq 1.7 \times 10^{-24} \text{ erg s}^{-1} \text{ cm}^{-2} \text{ Hz}^{-1}$. This exceeds the constraint on the flux at this frequency (see Section 4.3.3) and suggests that either this extrapolation is invalid, or that the assumptions used in deriving the EUV constraint, for example that the inner disc does not obstruct the EUV flux, are inappropriate. This question will be returned to in Section 4.8.

4.4.2 Black-body Fits

The optical spectrum is not an extrapolation of the far-UV power-law, showing a peak in excess of the extrapolation. It is unclear whether an extrapolation is appropriate, however, as the power-law from a steady-state disc spectrum is expected to drop off at long wavelengths as the spectrum becomes dominated by the Rayleigh-Jeans tail of the edge of the disc. The simplest analysis is thus to ignore the power-law component in the optical and fit a single component to the optical peak. This characterisation thus represents an upper limit on the spectrum of the optical component. The alternative extreme, to simply extrapolate the power-law into the optical would result in approximately half the flux at the peak of the optical spectrum coming from the power-law. It would not change the position of the peak of the optical component dramatically, so this component should have roughly the same temperature and no less than half the inferred area. In this section the

Table 4.4: Properties of blackbody fits to the optical and near-UV ($\lambda \geq 2600 \text{ \AA}$) *HST* spectra.

	T(K)	A($\times 10^{23} \text{ cm}^2$)
May 14	9800	5.0
June 9	9900	3.4
June 20	9700	3.1
June 30	8900	2.9
July 22	8700	2.2

optical peak is fitted with a black body spectrum. A similar analysis using self-absorbed synchrotron spectra is presented in Section 4.4.3.

The best fitting parameters are determined by χ^2 minimisation. Since the scatter about the fit is predominantly due to intrinsic and interstellar features rather than measurement uncertainties, very large χ^2 values are obtained and applying conventional χ^2 confidence region methods leads to unrealistically small error estimates. In line with the simple characterisation approach no attempt was made to construct rigorous confidence limits. The deduced parameters are shown in Table 4.4 and the fits to the spectra in Figure 4.10. This does not give a good fit in detail, but will give an approximate estimate of the properties of a thermal model.

The derived areas in Table 4.4 can readily be compared with the available emitting area. Adopting a disc radius of 80 per cent of the effective Roche lobe radius (Eggleton 1983) and an inclination of $\sim 70^\circ$, the projected area of the disc face is $\sim 2.1 \times 10^{23} \text{ cm}^2$. In addition, radiation from the outside edge of the disc may be non-negligible since GRO J1655–40 is a high-inclination system. de Jong, van Paradijs & Augusteijn (1996) have found that for some persistent low mass X-ray binaries, the disc half-thickness, H/R can be greater than 0.2. With the inclination of GRO J1655–40 and a disc of this thickness, the projected area of the edge amounts to ~ 70 per cent of the projected area of the disc face, increasing the total area presented by the disc to $\sim 3.6 \times 10^{23} \text{ cm}^2$. The estimated radius of the companion star, $4.85 R_\odot$ (Orosz & Bailyn 1997), also corresponds to an average area $\sim 3.6 \times 10^{23} \text{ cm}^2$, comparable to that of the disc. It is therefore possible that the companion star, if X-ray heated, could also account for at least some of the optical peak. Further discussion of

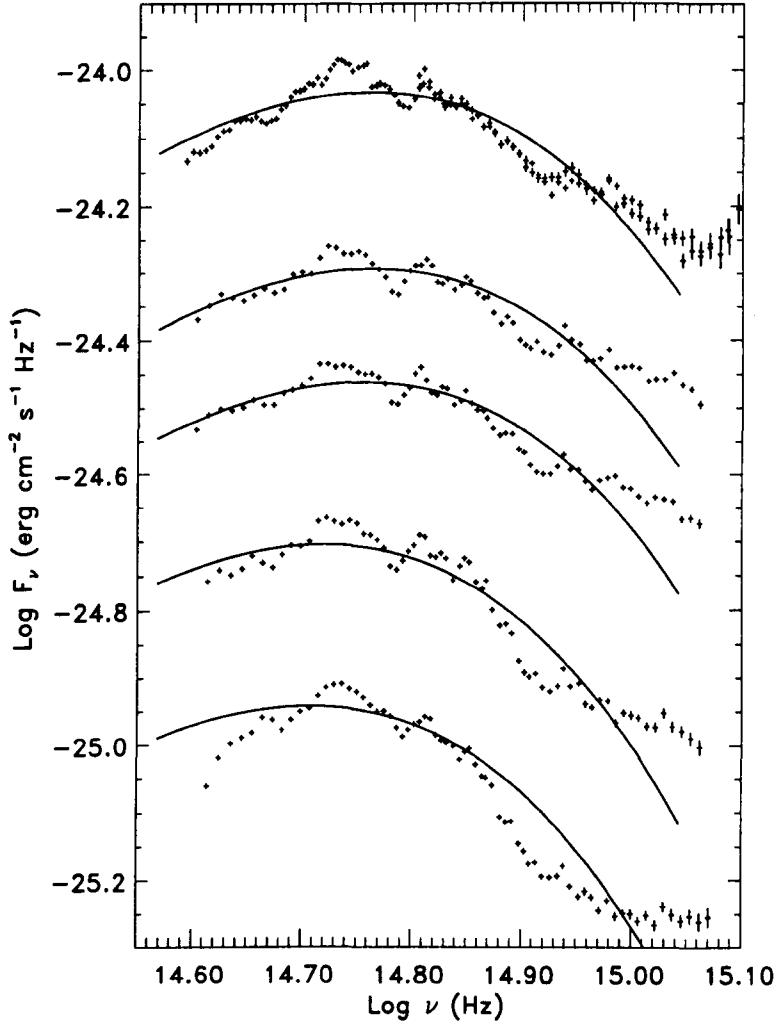


Figure 4.10: Blackbody fits to the optical excess in the *HST* spectra ($\lambda \geq 2600 \text{ \AA}$). The fits are poor in detail and are only intended to characterise the coarse properties of this component. In order to separate the successive visits clearly, a downward shift of 0.1 has been introduced in each visit relative to the one above it, i.e. the lowest visit has been shifted downwards by 0.4. The calibration does not incorporate the changes described in Section 4.7.2.

these possibilities will be deferred to Section 4.8.

4.4.3 Self-absorbed Synchrotron Emission

An alternative to thermal models was also considered, namely that the optical peak could be self-absorbed synchrotron emission. This possibility was considered following the suggestion of Dr. Rob Fender that the dropping section of the spectrum between $\log \nu \sim 14.75$

and 15.05 resembles an optically thin synchrotron spectrum. To reproduce the turnover at low frequencies would require that the synchrotron emission becomes self-absorbed below $\log \nu \sim 14.75$. This model has more parameters than the black body model, and can give a better fit to the observed spectrum, in particular for the rapid turnover at the peak.

The simplest possible model for producing this spectrum is adopted. There is a synchrotron emitting slab containing a magnetic field of uniform strength and energetic electrons. The slab has linear dimension l , electron density n_e and electron power-law energy distribution $n_e(E) = \kappa E^{-p}$. The magnetic field is B and there is equipartition of energy between the field and the particles. The expected spectrum is derived by Longair (1994) and has the functional form:

$$I_\nu = X \nu^{5/2} \left[1 - \exp(-Y \nu^{-(p+4)/2}) \right]. \quad (4.15)$$

Practically, this is fitted to the data for X , Y and p and then the underlying physical parameters are determined from these convenience parameters. The exact expressions are rather complex; $X = X(B, p)$, $Y = Y(B, p, \kappa, l)$.

The best fits with such models are shown in Figure 4.11 and the deduced parameters are given in Table 4.5. The source must be very compact to produce self-absorption in the optical. The size is actually the best constrained of the parameters as for a self-absorbed synchrotron source, the observed flux depends only on the angular size of the source and the magnetic field. With an estimate of the distance (3.2 kpc) the derived linear size then scales with only the fourth root of the assumed magnetic field.

The clearest evolution in the spectra is the overall decline in flux level; this translates mainly into a shrinking of the inferred synchrotron source. There is also a steepening of the spectrum. This may be due to a change in the electron power-law index, as modelled, or it may be due to a cut-off in the electron distribution above which inverse-Compton and synchrotron losses dominate. Such a cut-off could also contribute to the sharpness of the spectral turnover near 2600 Å.

Synchrotron emission is often considered exclusively a radio phenomenon. That this is not the case is demonstrated by the existence of optical counterparts to extragalactic radio jets. Observations of the other Galactic superluminal jet source GRS 1915+105 have revealed infrared jets, with the same position angle as the radio jets (Sams, Eckart & Sunyaev 1996) and infrared flares, initially discovered by Fender et al. (1997), have been shown to be closely correlated with radio flares but occurring up to an hour earlier (Mirabel et al. 1998). Both of these results are suggestive of infrared synchrotron emission.

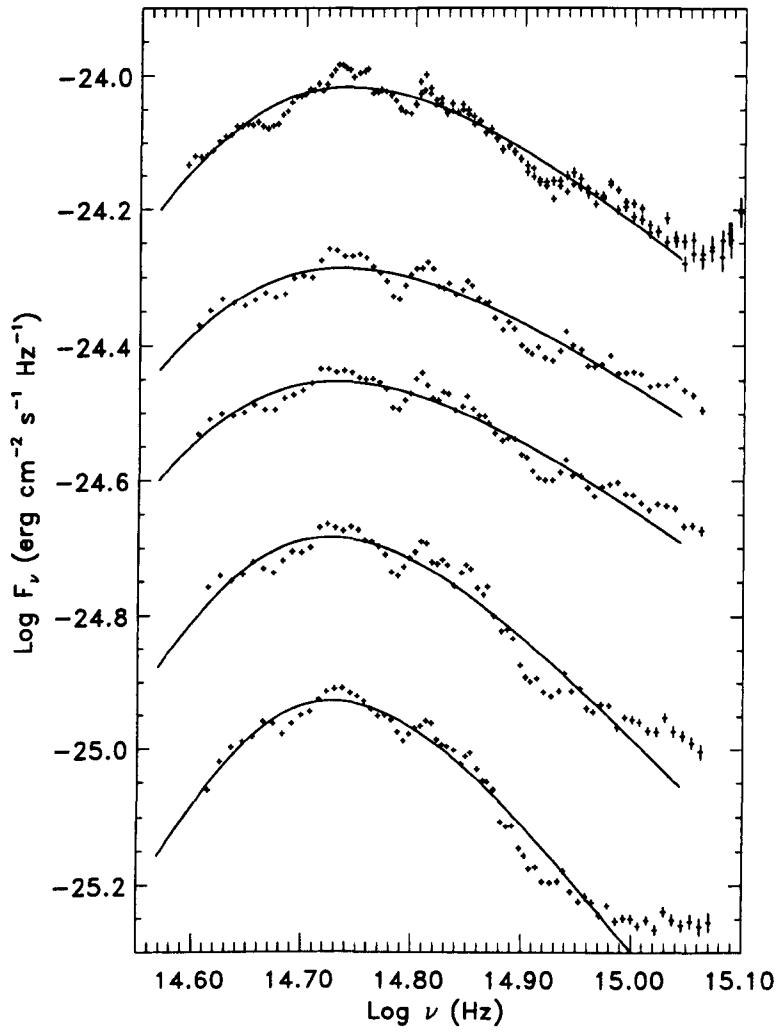


Figure 4.11: Self-absorbed synchrotron fits to the optical peak in the *HST* spectra ($\lambda \geq 2600 \text{ \AA}$). A downward shift has been introduced as in Figure 4.10 to separate the successive visits. The calibration does not incorporate the changes described in Section 4.7.2.

Table 4.5: Parameters of self-absorbed synchrotron models for *HST* optical and UV data. The Schwarzschild radius of a $7 M_{\odot}$ black hole corresponds to 2.1×10^6 cm. In each case, deduced electron energies are $\gamma \sim 50$ – 90 , estimated from the observed synchrotron frequency range of $14.6 \leq \log \nu \leq 15.0$. Electron densities are lower limits obtained by integrating the electron distribution over this energy range.

	p	l (R_{sch})	B (kG)	N_e (10^{12}cm^{-3})
May 14	3.7	97	54	7.6
June 9	3.3	80	61	8.3
June 20	3.4	76	59	8.4
June 30	4.5	70	48	7.8
July 22	5.3	60	42	7.6

It is also a feature of advective models for quiescent SXTs (discussed in Section 1.6) that the optical spectrum is produced by self-absorbed synchrotron emission.

4.5 Echo Mapping

4.5.1 Comparison of Light Curves

Figure 4.12 shows the light curves obtained in the coordinated *HST/RXTE* visits. The *RXTE* light curves exhibit variability on shorter timescales than shown; on the 1 s or less time scale, there are flickerings with RMS of 10 per cent or so.

Of the four simultaneous visits, the second, on June 8, achieved the best coordination and is most suitable for this analysis. The first visit did have some overlap but no correlation was detected between X-rays and optical (Figure 4.14.) The X-ray light curves from the third visit are contaminated by dipping structure due to transient absorption and in the fourth visit, the overlap was too small for useful analysis.

Figure 4.13 shows the correlations present in the third pair of light curves from the second visit. To illustrate wavelength dependence both UV (2000–4000 Å) and blue (4000–6000 Å) light curves are shown. While the main feature around 1200 s is present in both, the smaller correlated features are more prominent, or only present at all, in the UV light

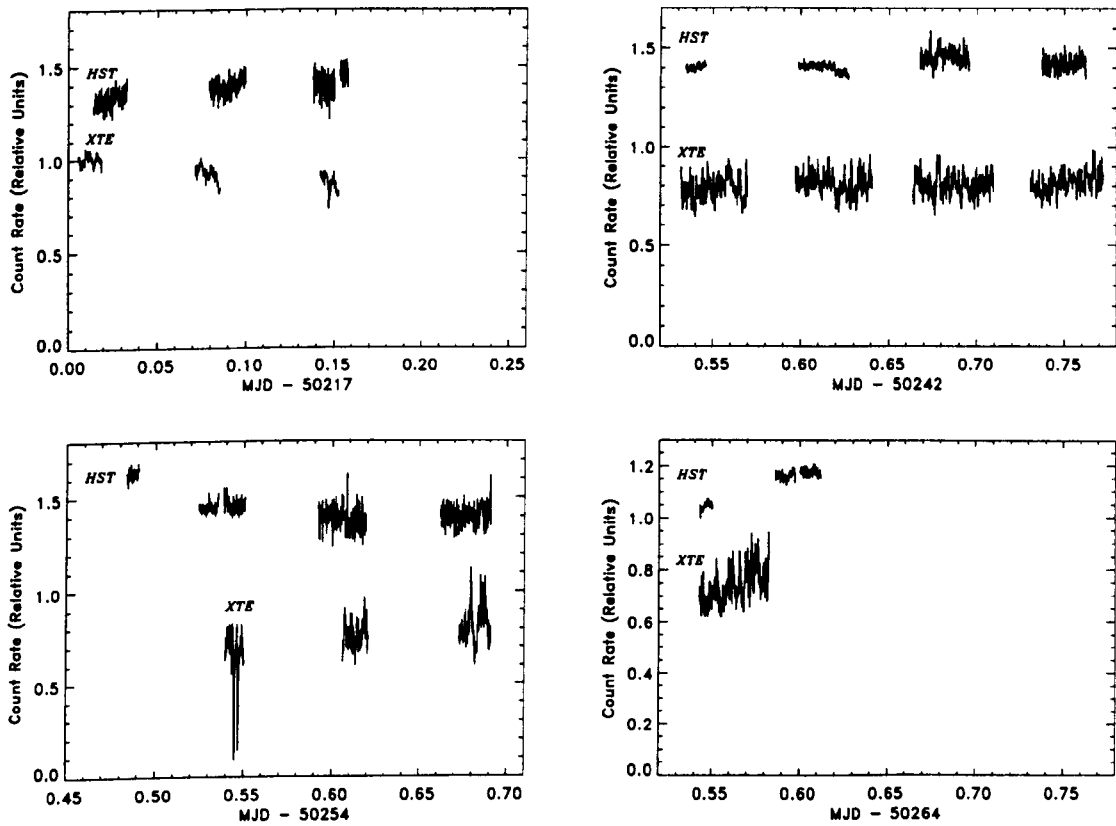


Figure 4.12: *HST* and *RXTE* light curves from simultaneous visits. The first visit *HST* light curves are derived from the G160L zero order spectrum. Other *HST* light curves use PRISM/RD or PRISM/BL. For clarity, the light curves have been rebinned to a time-resolution of ~ 10 s. The relative count rates of *RXTE* vs PRISM/RD vs. PRISM/BL vs. order zero have been rescaled but the zero point is correct. The time interval covered by each plot is the same.

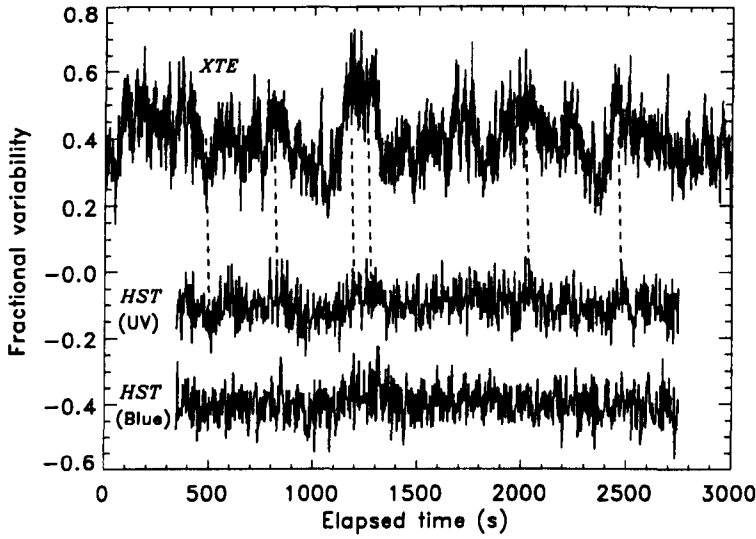


Figure 4.13: A close up of the third pair of light curves from Figure 4.12 showing correlated variability and colour dependence in the *HST* light curves. The zero point is arbitrary, but the vertical axis indicates the amplitude of variations relative to the mean count rate. The wavelengths compared are 2000–4000 Å (UV) and 4000–6000 Å (blue).

curve, suggesting that the source of variability represents a larger fraction of the total light in the ultraviolet than in the optical. There are also some features which are strong in the X-ray light curve, e.g. at 1700 s, but which do not appear in either *HST* light curve. These conclusions are borne out by a similar close comparison of the other light curves, and it is clear that the relation between X-ray and optical emission is complex. It may be, for example, that the observed X-ray variations originate from different locations, some of which can illuminate the reprocessing region and some of which cannot.

Another example of uncorrelated variability may be the apparent downward step in the second PRISM/RD light curve from the second overlapping visit. There may also be a step in the X-ray lightcurve, but the two do not match well, and the optical light curve could not be reproduced as a convolution of the X-ray light curve with a Gaussian transfer function (see Section 4.5.3). The pronounced step in the optical light curve also results in a strong auto-correlation, which leads to a very broad peak in the cross-correlation function (see Section 4.5.2). This light curve was therefore truncated just before this point to simplify the analysis in the subsequent sections.

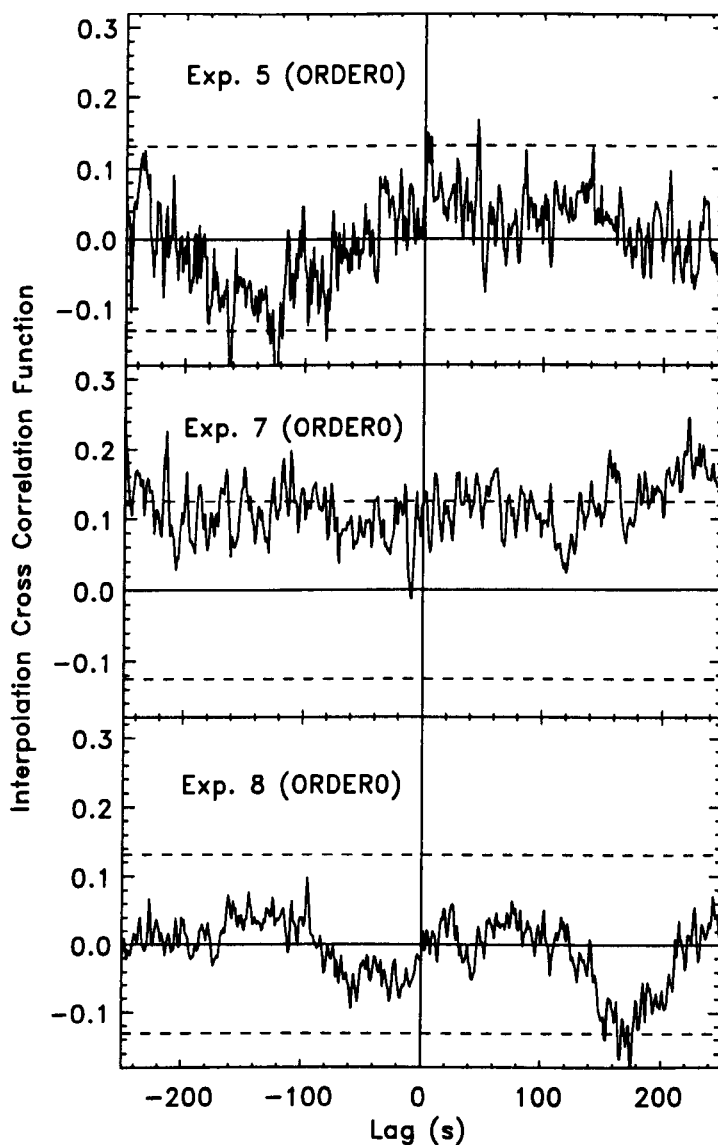


Figure 4.14: ICFs for May 14 data. Dashed lines show 3σ confidence limits expected for uncorrelated variability. No significant, repeatable peaks are seen.

4.5.2 Cross Correlations

A cross-correlation analysis is the simplest way to begin. This will identify correlations and reveal the mean lag between X-ray and optical variability. The technique is commonly used in the study of correlated variability from active galactic nuclei (AGN) where two methodologies have been developed: the Interpolation Correlation Function, ICF (Gaskell & Peterson 1987), and the Discrete Correlation Function, DCF (Edelson & Krolik 1988). White & Peterson (1994) contrasted the relative merits of the two and suggested some

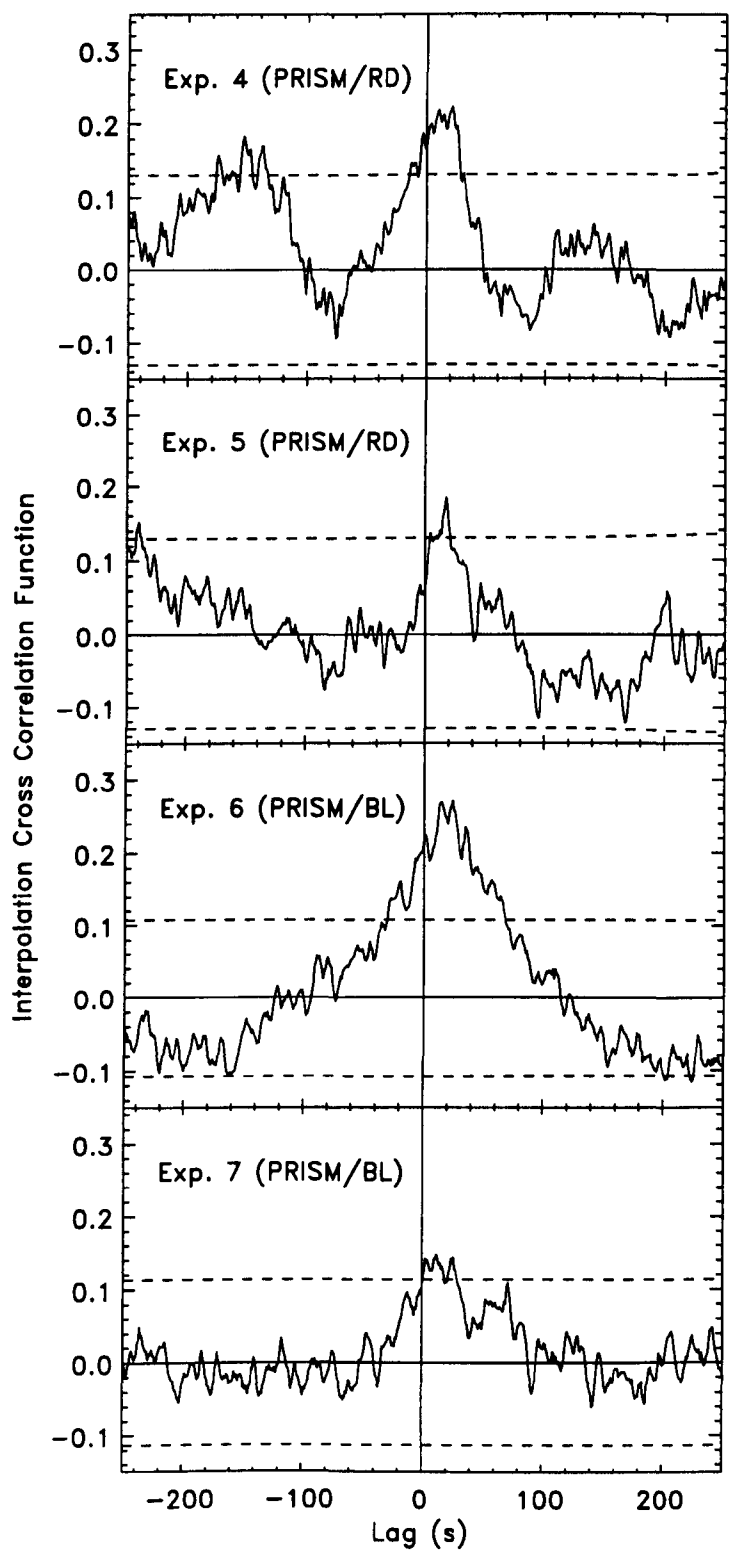


Figure 4.15: ICFs for June 8 data. Dashed lines show 3σ confidence limits expected for uncorrelated variability. All four plots show features at ~ 20 s which are significant at the 3σ level, although only Exp. 6 can be considered more than marginal at this level.

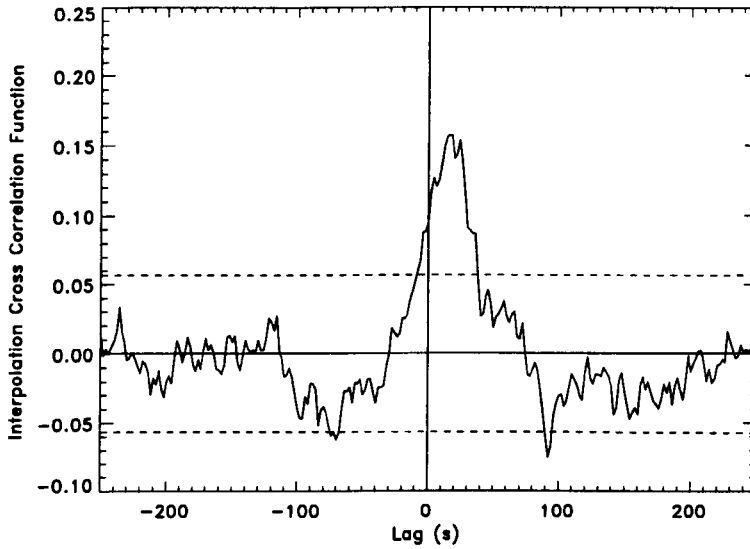


Figure 4.16: Combined ICF for June 8 using data from all four pairs of lightcurves. Dashed lines show 3σ confidence limits expected for uncorrelated variability.

improvements. Both methods have been tested on these data and no significant differences were found, so it was chosen to adopt the ICF method with one important modification. AGN line and continuum light curves are typically drawn from the same spectra, leading to identical sampling. Also for AGN the duration of a measurement is much smaller than the interval between measurements. Neither of these situations are the case for these data so modifications are required. The solution adopted is to take the *HST* data points (which have the coarser sampling and longer integration time) and interpolate the *RXTE* light curves *at several points for each HST point* in order to approximately integrate over the duration of the *HST* group. The cross-correlation function is therefore defined as follows:

$$F(\tau) = \frac{1}{N} \sum_{i=1}^N \frac{(f_{\text{opt}}(t_i) - \bar{f}_{\text{opt}})(\bar{f}_x(t'_i) - \bar{f}_x)}{\sigma_{\text{opt}}\sigma_x} \quad (4.16)$$

where

$$\bar{f}_x(t'_i) = \frac{1}{4}(f_x(t'_i - d\tau/2) + 2f_x(t'_i) + f_x(t'_i + d\tau/2)) \quad (4.17)$$

and $t'_i = t_i - \tau$ and $d\tau$ is the length of an *HST* group. The sum is over the number of points in the optical (*HST*) light curve, N . Note that $\sigma_{\text{opt}}, \sigma_x$ are the variances of the two light curves, not their average errors.

A section of the resulting ICFs from the May 14 visit, centred at zero lag, is shown in Figure 4.14. No repeated significant features are seen. Figure 4.15 shows the results

from the June 8 visit. All four ICFs show roughly coincident peaks, significant at the 3σ level. The ICF peaks occur at lags in the range 12–24 s. While other peaks are seen in individual ICFs, since they are not repeated in more than one pair of light curves, they cannot be considered significant. The data are combined to yield a single ICF in Figure 4.16. The significance of the combined peak is 8σ .

4.5.3 Fitting Transfer Functions

To characterise the distribution of time delays present between the *RXTE* and *HST* lightcurves, parameterised model transfer functions were fitted to the data⁶. In this modelling the *HST* light curve is predicted by convolving the observed *RXTE* lightcurve with a Gaussian transfer function (i.e. the time-delay distribution). The “badness-of-fit” of this model is determined by calculating the χ^2 over the data points in the *HST* lightcurve.

The model adopts the measured *RXTE* lightcurve verbatim, thus ignoring the statistical errors in the *RXTE* measurements. This is an acceptable approximation because the signal-to-noise ratio for detecting variations is much higher for the *RXTE* data than for the *HST* data.

The Gaussian transfer function

$$\psi(\tau) = \frac{\Psi}{\sqrt{2\pi}\Delta\tau} e^{\frac{1}{2}\left(\frac{\tau-\tau_0}{\Delta\tau}\right)^2} \quad (4.18)$$

has 3 parameters: the mean time delay τ_0 , the dispersion or root-mean-square time delay (hereafter rms delay) $\Delta\tau$, which is measure of the width of the Gaussian, and the strength of the response, Ψ , which is the area under the Gaussian.

Figure 4.17 shows the synthetic light curves from the Gaussian superimposed over the four *HST* lightcurves. The principal features of the *HST* lightcurves are reproduced well in the synthetic lightcurves.

Figure 4.18 shows the results of fitting the Gaussian transfer functions to the third pair of light curves. Panel (a) shows the constraints imposed by the data on the mean and rms delay. The best fit for the Gaussian fitting has $\chi_{\min}^2/779 = 1.229$. Here the 2 parameter 1σ confidence region is defined by the contour $\chi^2 = \chi_{\min}^2 + 2.3$, and the greyscale indicates

⁶The idea and initial development of this formulation were provided by Prof. Keith Horne and this work was done in collaboration with him and with Kieran O’Brien. Independent fully functional codes were developed jointly by Prof. Keith Horne and Kieran O’Brien and by this author, and yield the same results for the same data. The former code was used to generate the results presented here as it was faster. Some of the text in this section was adapted from that contributed by Prof. Keith Horne to Hynes et al. (1999).

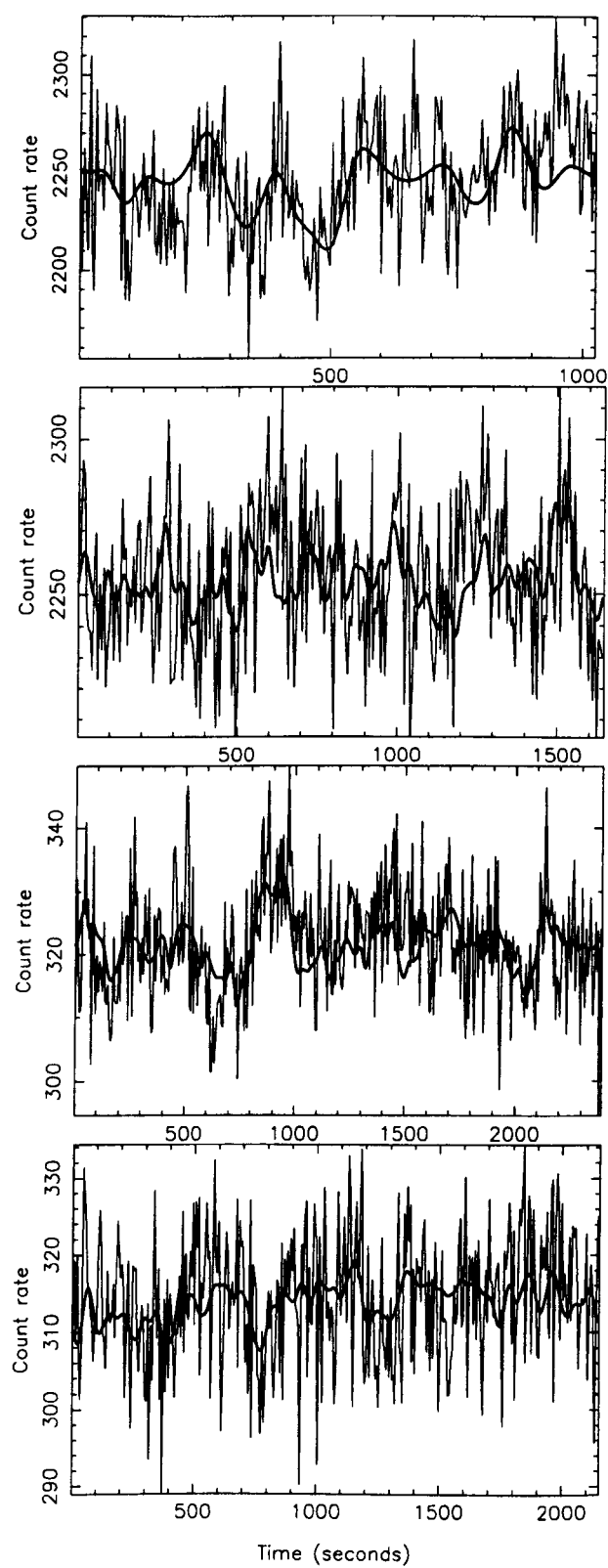


Figure 4.17: Best-fit synthetic lightcurves for all 4 data sets from Gaussian fitting, superimposed over actual *HST* lightcurves. The time axis is relative to the start of each exposure. The lightcurves have been rebinned by a factor of two for clarity. Figures provided by Kieran O’Brien.

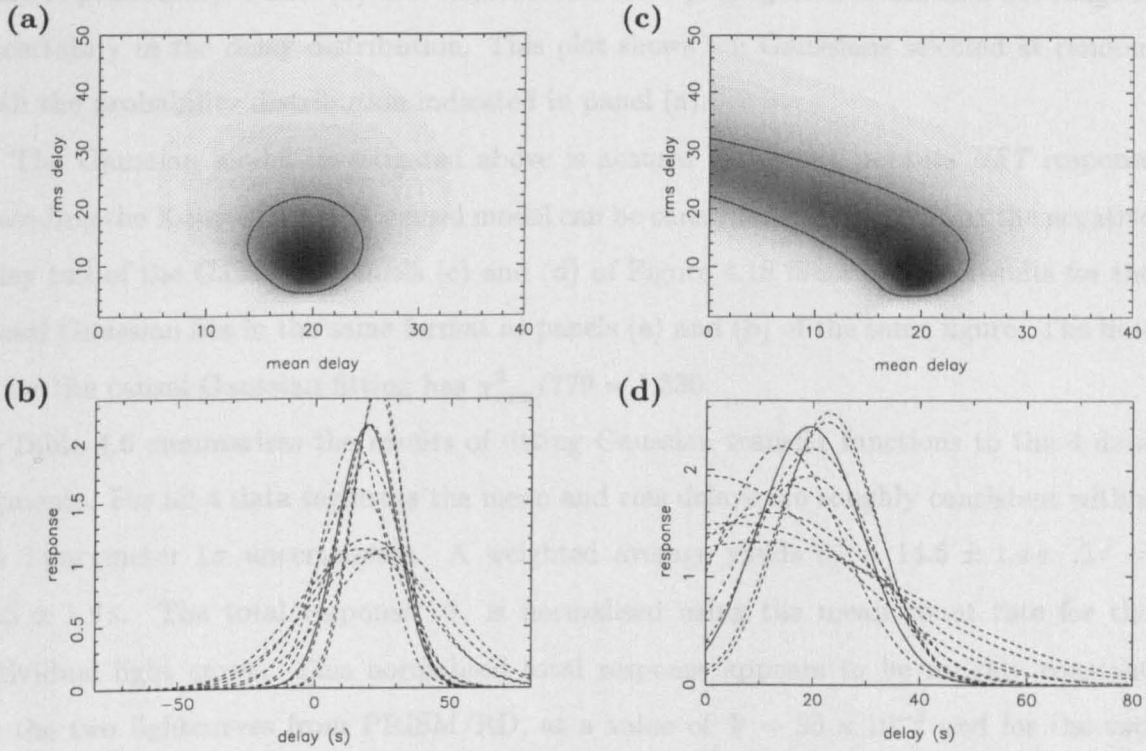


Figure 4.18: Top, acausal (left) and causal (right) χ^2 surfaces for Gaussian transfer function fitting to the *HST* lightcurve 3. Bottom, best-fit (solid line) and trial (dashed line) time-delay transfer functions to *HST* Exp. 6. The response is $\psi(\tau)$. Figures provided by Kieran O’Brien.

Table 4.6: Summary of results from parameterised Gaussian fitting to *HST* lightcurves. The rows give respectively the photometric phase, number of data points, reduced χ^2 , mean delay, rms delay and integrated response for each light curve. Uncertainties are based on 1 parameter, 1σ confidence regions. The integrated response, Ψ , has been normalised by dividing by the mean of each *HST* light curve. Fits performed by Kieran O’Brien.

	Exp. 4	Exp. 5	Exp. 6	Exp. 7
ϕ_{phot}	0.36	0.39	0.42	0.44
N	528	541	782	704
$\chi^2_{\text{min}}/(N - 3)$	1.193	1.446	1.230	1.159
τ_0 (s)	8.3 ± 4.0	$16.0^{+2.5}_{-2.2}$	19.3 ± 2.2	$13.3^{+4.7}_{-4.5}$
$\Delta \tau$ (s)	$20.0^{+6.8}_{-7.0}$	$8.6^{+2.7}_{-2.3}$	$10.8^{+3.7}_{-3.3}$	$13.5^{+7.7}_{-4.7}$
$\Psi/10^{-3}$	29 ± 1	32 ± 2	55^{+11}_{-7}	49 ± 5

relative probability. Panel (b) uses Monte Carlo error propagation to indicate the range of uncertainty in the delay distribution. This plot shows ten Gaussians selected at random with the probability distribution indicated in panel (a).

The Gaussian model investigated above is acausal because it permits *HST* response preceding the X-ray driving. A causal model can be constructed by truncating the negative delay tail of the Gaussian. Panels (c) and (d) of Figure 4.18 illustrate the results for the causal Gaussian fits in the same format as panels (a) and (b) of the same figure. The best fit for the causal Gaussian fitting has $\chi^2_{\min}/779 = 1.230$.

Table 4.6 summarises the results of fitting Gaussian transfer functions to the 4 data segments. For all 4 data segments the mean and rms delays are roughly consistent within the 1 parameter 1σ uncertainties. A weighted average yields $\overline{\tau_0} = 14.6 \pm 1.4$ s, $\overline{\Delta\tau} = 10.5 \pm 1.9$ s. The total response, Ψ , is normalised using the mean count rate for the individual light curve. This normalised total response appears to be roughly constant for the two lightcurves from PRISM/RD, at a value of $\Psi \sim 30 \times 10^{-3}$ and for the two lightcurves from PRISM/BL, at a value of $\Psi \sim 50 \times 10^{-3}$. This difference between the values of Ψ shows that the variability is stronger at short wavelengths, and suggests that the reprocessing therefore occurs in a relatively hot part of the system.

4.5.4 Maximum Entropy Echo Mapping

One of the most powerful techniques available in analysing correlated variability due to reprocessing in active galactic nuclei is the maximum entropy mapping technique (Horne 1994), widely used in the analysis of AGN light curves. This in principle makes it possible to reconstruct the transfer function without assuming any parameterised form for it. In practice, however, the maximum entropy technique still requires a *default* image to calculate entropy with reference to and the final solution will be steered towards this default image. Ideally it should have some physical significance and should be close to the true transfer function. With data of high signal-to-noise ratio, the transfer function is well constrained and a poor choice of default can be overcome. With the noisy data considered here, however, the transfer function is poorly constrained and the final result depends heavily on the default image and other control parameters put in. It was found that the maximum entropy technique could not usefully be applied to these data and that the best approach was that discussed in Section 4.5.3. Effectively this method only requires that the data constrain the first and second moments of the transfer function.

4.5.5 Interpretation of Echo Mapping

Clearly reprocessing with a mean time delay of under 25 s dominates. This is the size of lag to be expected from the accretion disc given the established system parameters discussed in Section 4.1.2. Lags of greater than 40 s are expected from the companion star at this binary phase ($\phi \sim 0.40$); together with the narrowness of the transfer function (rms delay ~ 10 s), this means that disc reprocessing must dominate over the companion star, even allowing for the maximum uncertainty in system parameters. This conclusion is supported by the colour of the induced optical variability. The response for the Gaussian fits, when normalised to the count rate for the light curves are consistent for the two PRISM/BL light curves and for the two PRISM/RD ones. The response, and hence reprocessing fraction for PRISM/BL is higher than for PRISM/RD, however, indicating that the reprocessed emission is coming from a relatively hot area of the binary, probably the accretion disc.

Why is disc reprocessing dominant? During the activity observed by van der Hooft et al. (1997), light curve analysis revealed that X-ray heating of the companion star was important; if that was the case here, echoes should be seen originating from the companion star.

One explanation favoured by Hynes et al. (1998c) and O'Brien et al. (1999) is that the X-ray absorbing material in the disc may have a significant scale height above the mid-plane so that the companion would effectively be shielded from direct X-ray illumination, thus reducing the strength of reprocessing. Another factor is the angle of incidence between the X-rays and the surface of the reprocessing region. This may affect the strength of reprocessing: firstly, at larger angles of incidence a given surface element subtends a smaller solid angle and so less X-ray energy is incident upon it; secondly, increasing the incidence angle will increase the albedo and hence result in a larger fraction of X-ray flux being reflected rather than reprocessed⁷. Both of these effects will, however, tend to make the companion relatively more effective at reprocessing than the disc, not less, and so cannot explain why larger lags are not seen.

These conclusions are borne out by detailed physical modelling of the expected transfer functions (O'Brien et al. 1999) and tight constraints can be placed on how much of the companion surface can effectively reprocess variability. Only if *most* of the companion star is shielded from irradiation will disc reprocessing dominate. The half-thickness of the

⁷de Jong, van Paradijs & Augusteijn (1996) derive disc albedos of greater than 0.9 in persistent LMXBs and suggest this is due to the high angle of incidence.

accretion disc along the line of centres must be at least $H/R \sim 0.25$ to shield the companion sufficiently. This is large, but is consistent with the modelling of the light curves of some persistent LMXBs for which values of order 0.2 have been inferred (de Jong, van Paradijs & Augusteijn 1996).

This need not mean that the assumption of a geometrically thin disc often made in modelling the disc structure is invalid, and indeed, Dubus et al. (1999) argue that inferred disc thicknesses ~ 0.2 *cannot* represent the pressure scale height of the disc as this would require temperatures $> 10^7$ K at the disc edge. Instead the thicknesses implied by this study, X-ray dips and the analysis of de Jong, van Paradijs & Augusteijn (1996), are measures of the height of X-ray absorbing material (H_{irr} in the terminology of Dubus et al. (1999).) It is likely that most of the *mass* of the disc is in a thin, central layer, but that the X-ray opaque atmosphere extends well above that layer. It is also possible, and likely, that the disc is not axisymmetric, and the shielding may come from a localised bulge, probably concentrated around the stream impact point. Excess material in some form at this disc azimuth is definitely needed to explain the phase dependence of X-ray dips (Kuulkers et al. 1998).

This conclusion (that the companion star is shielded) can be avoided if for some reason it does not effectively respond to *variability*, for example if it is irradiated indirectly via scattering from a *very* extended corona (comparable in size to the disc) or if physical conditions are such that the reprocessing of X-ray photons to optical takes a significant time (this is usually assumed to be negligible.) Both of these effects could smear out rapid optical variability to the point of being undetectable.

4.6 Multi-wavelength Observations Through X-Ray Dips

During the July 20 visit, *RXTE* observed two X-ray dips with simultaneous *HST* coverage. The light curves are shown in Figure 4.19; there is no significant optical change associated with the X-ray dips.

This non-detection of optical dips is important. In the self-absorbed synchrotron model for optical emission considered in Section 4.4.3, the requirement of optical self-absorption required a central source diameter of order 50 Schwarzschild radii, a region comparable in size to the X-ray source. The most likely site for such a compact source seemed the central accretion flow near the black hole. This would site the source of optical emission roughly coincident with the X-ray source and hence any absorbing material that causes

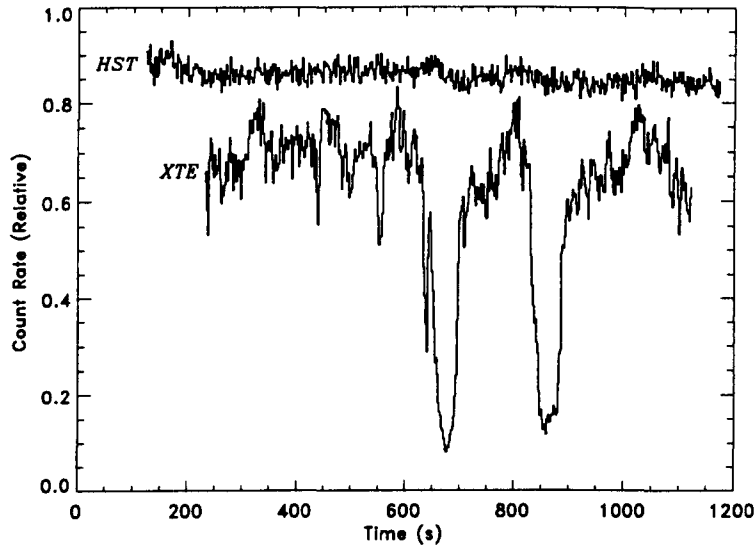


Figure 4.19: Simultaneous X-ray and optical observations through X-ray dips, 1996 June 20.

X-ray dips should also obscure the synchrotron source. The lack of optical dips argues that optical emission is not self-absorbed synchrotron.

Support for this interpretation is provided by the study of Gliozzi et al. (1998), who found significant optical polarisation, modulated on the orbital phase. The smooth modulation and the direction of polarisation are both consistent with an origin in electron scattering in the upper layers of the disc; partial eclipsing of the extended disc could very easily reproduce the observed modulation. This modulation would also be very difficult to reconcile with a compact central synchrotron source.

4.7 The Continuum Spectral Energy Distribution Reconsidered

4.7.1 The Optical Energy Source

As was discussed in the previous section, a self-absorbed synchrotron model for optical emission would predict optical dips, which are not detected, and is difficult to reconcile with a smoothly varying optical polarisation. Both of these observations instead suggest that thermal emission from the accretion disc dominates. The question remaining is what is the energy source for this emission: viscous heating or reprocessed X-rays? The echo mapping experiment indicates that at least some of the optical flux originates in X-ray reprocessing. This does not require that reprocessing should *dominate* the optical energy

budget, however. It may be a relatively small perturbation, perhaps from a localised area of the disc such as the stream impact point.

A model dominated by viscous heating of the disc has severe energy problems. Interpreting the far-UV spectrum from May 14 as the classic $\nu^{1/3}$ spectrum of a viscously heated accretion disc (Section 4.4.1) implied mass transfer rates through the UV emitting region of the disc of order five times that needed to produce an Eddington luminosity X-ray source⁸ (assuming a 10 per cent efficiency for the central X-ray source.) X-ray observations, however, indicate that the maximum X-ray luminosity in the outburst was $\sim 0.2 L_{\text{Edd}}$ (Sobczak et al. 1999). There is clearly a substantial discrepancy (a factor of ~ 25): either the efficiency of the X-ray source is very low, or substantial mass loss occurs from the inner disc. The former possibility can be discounted as the X-ray spectrum on May 14 was dominated by a thermal component from the disc, which is expected to be very efficient at converting gravitational energy to radiation⁹. While the likely detection of P Cygni profiles does imply the presence of a disc wind, a mass loss rate as severe as required to resolve the discrepancy seems very implausible.

If viscous heating cannot reproduce the observed optical spectrum, then the most likely explanation is that X-ray heating is responsible. Before testing whether such a model could adequately reproduce the broad band spectrum two refinements were applied to the *HST* spectra. Firstly, they were updated to use revised calibration files for the PRISM/RD data, as a significant change was made in the red flux calibration after the initial analysis of these data. Secondly, the quiescent contribution from the companion star was removed to isolate the spectrum of the extra light in outburst.

4.7.2 Recalibration of the PRISM/RD Spectra

After the initial spectral analysis was performed (Hynes et al. 1998b) revised *HST*/FOS calibration files became available (Keyes 1997a). The change to the PRISM/RD spectral calibration is large enough to justify correcting the spectra. This was done by calculating the ratio of the new inverse sensitivities to the old and multiplying the original calibrated spectrum by this factor. The correction function is shown in Figure 4.20, and mainly

⁸Even allowing for uncertainties in calibration and dereddening of the far-UV spectrum would require at least 60 per cent of the Eddington mass transfer rate.

⁹The efficiency does depend on the inner disc radius. Sobczak et al. (1999) estimated radii of $\sim 6.5 r_g$ on May 9–12. This is only slightly larger than expected for a Schwarzschild black hole ($6 r_g$), for which a disc efficiency of 6 per cent is expected.

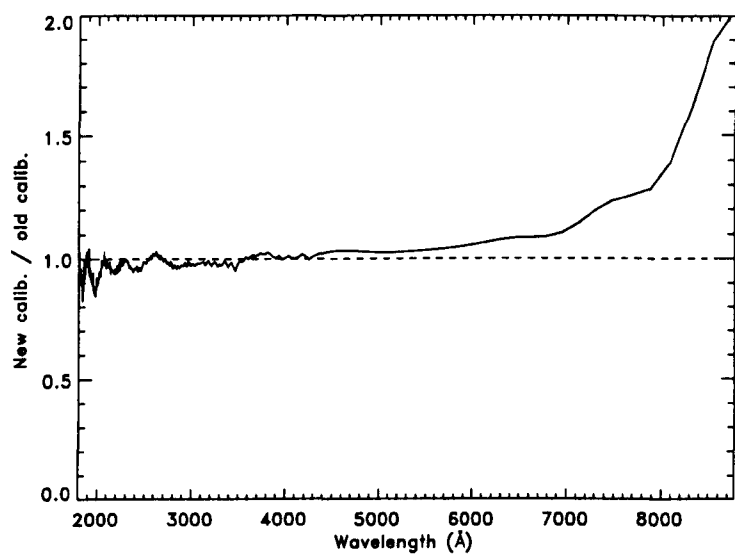


Figure 4.20: Ratio of new to original calibrations for PRISM/RD. The change is most pronounced at long wavelengths; below 7000 Å the difference is less than 10 per cent.

Table 4.7: Phases and deduced companion star magnitudes for each *HST* visit. Photometric phase zero is when the companion is at inferior conjunction.

Date	Photometric phase	Quiescent companion star magnitude (V)
May 14	0.67	17.08
June 9	0.38	17.15
June 20	0.94	17.28
June 30	0.75	16.98
July 22	0.05	17.29

affects the red spectrum.

4.7.3 The Companion Star Contribution

GRO J1655–40 is unlike most SXTs in having an F type subgiant companion. This means that even without heating, it will make a significant contribution to the optical light in outburst. This unheated contribution can be readily estimated and subtracted. The

difference spectrum between outburst and quiescence is a better diagnostic of the accretion light than the total spectrum is. As discussed in Section 4.1.2, the companion contribution is represented using the spectrum of the F5 IV star BD +630013 (Gunn & Stryker 1983). Orosz & Bailyn (1997) present quiescent *V* band light-curves and estimate that the disc contributes less than 10 per cent of this light. The orbital phase at the time of each *HST* visit was calculated from the ephemeris of Orosz & Bailyn (1997). Using these phases and the extinction solution of Section 4.1.3 *companion star V* band magnitudes can be estimated. The reddened companion star spectrum is then normalised to this level to obtain a best estimate of the quiescent companion star contribution for each *HST* visit. The phases and magnitudes are summarised in Table 4.7.

As the PRISM/RD has a non-uniform dispersion, which is very low at the red end of the spectrum, some care is needed in subtracting the companion contribution. The best approach is to produce a simulated PRISM/RD spectrum of the expected companion spectrum. First a mapping between flux and counts detected per unit wavelength is established by interpolating the inverse sensitivity function of the PRISM/RD and the dispersion (determined empirically from the pipeline wavelengths as a function of pixel number). The companion spectrum (interpolated to an arbitrary high dispersion) is thus converted to expected counts per unit wavelength. This count spectrum is then binned to the pixel sizes of the PRISM/RD (again using pipeline wavelengths) and smoothed to the instrumental resolution of 1 diode = 4 pixels (Keyes 1997a). Finally the inverse sensitivity function is used again to convert back to flux units. The result is a simulated spectrum of the companion with the same (variable) resolution and wavelength grid as the data.

Figure 4.21 shows three of the PRISM spectra (from May 14, June 20 and July 22) before and after subtracting the quiescent companion star component. This partially flattens the optical bump, but does not completely remove it, and the difference spectra are still not consistent with a $\nu^{1/3}$ viscous disc spectrum. It is possible that at least part of the reason for this is that this process underestimates the contribution from the companion because it is heated. Examining the spectra before and after subtraction, especially that from July 22, it does appear that the residual optical bump has a similar spectrum to that which was subtracted. This suggests that they are connected, and that to isolate the pure disc spectrum, a somewhat larger (and hotter) spectrum should be subtracted. Without stronger constraints on the strength of heating of the companion, however, and lacking detailed models for how this would modify the atmospheric structure, and hence

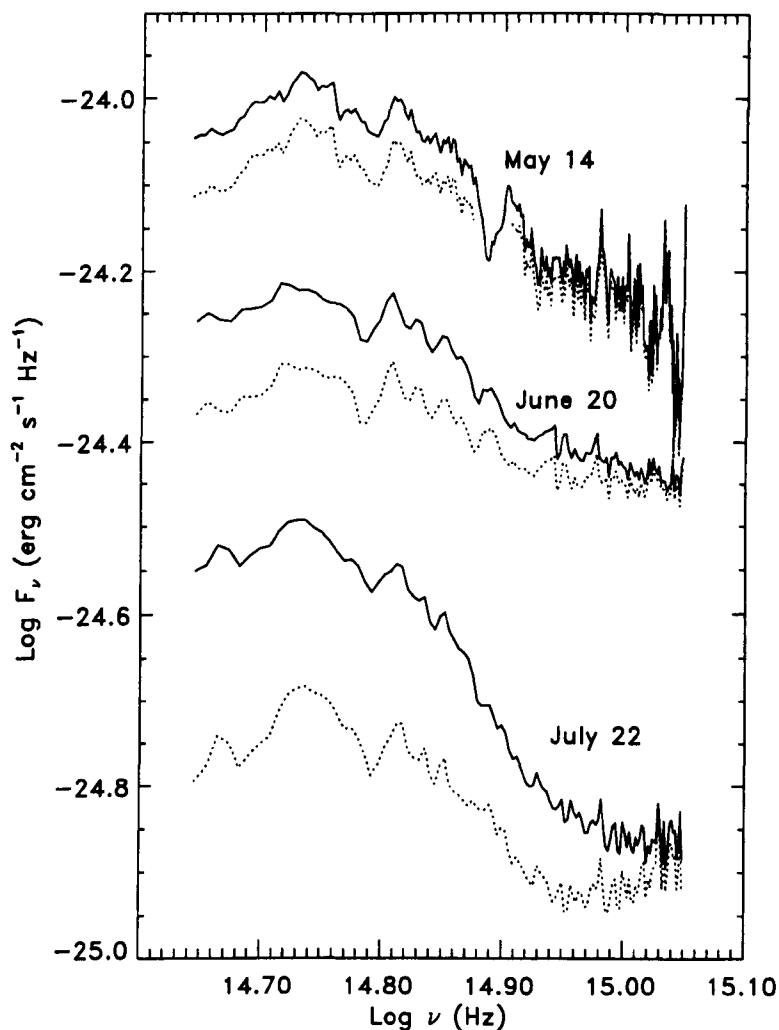


Figure 4.21: The May 14, June 20 and July 22 PRISM spectra before and after subtracting an estimate of the *quiescent* spectrum at the same orbital phase.

the emergent spectrum (in particular the size of the Balmer discontinuity), it was felt more appropriate to present a simple difference spectrum between outburst and quiescence. Note that this interpretation of the residual ‘optical bump’ contradicts the suggestion made in Section 4.5.5 that the companion is shielded from irradiation. It implies, therefore, that the alternative explanation presented there is correct; that the companion is heated but that variability is not effectively reprocessed,

4.7.4 Irradiated Disc Spectra

After recalibration of the PRISM/RD spectra and subtraction of the quiescent companion spectrum, the *HST* spectrum from May 14 is shown in Figure 4.22 together with the

simultaneous *RXTE* spectrum. The dashed line shows a simple multicolour black body disc model spectrum. The disc extends from $3R_{\text{Sch}}$ at the inner edge to 95 per cent of the effective Roche lobe radius (Eggleton 1983), with $T \propto R^{-3/4}$ throughout. No special boundary condition is applied to the inner disc edge. Theoretical prescriptions exist, e.g. Czerny, Czerny & Grindlay (1986), based on general relativistic treatments, but it was felt that uncertainty in the angular momentum of the black hole in GRO J1655–40, together with uncertainty in the physics of the inner disc region renders this level of detail inappropriate for the simple treatment used here. The mass transfer rate was taken to be the Eddington rate, assuming an efficiency of 10 per cent. This model is plotted to reiterate the point made in Section 4.7.1: that a ‘standard’ viscously heated disc model cannot simultaneously fit optical/UV and X-ray data – this model underpredicts the optical/UV flux but overpredicts EUV and X-ray fluxes. As discussed in Section 4.7.1, the most likely source of optical flux now appears to be reprocessed X-rays, in spite of the long term optical vs. X-ray anti-correlation. Figure 4.22 therefore also shows a simple model spectrum for an irradiated disc.

The model used is an extension of the black body disc spectrum. For convenience the spectrum is divided into optical/UV and X-ray segments. Irradiation is only important in determining the optical/UV spectrum. Viscous heating is represented by a viscosity temperature, the temperature at which a black body would emit a total flux equal to the viscous energy generation, $T_{\text{visc}} \propto R^{-3/4}$, which would give a $\nu^{1/3}$ form in the absence of other forms of heating. Additional flux due to X-ray reprocessing is represented by an irradiation temperature, T_{irr} , such that the effective temperature at a given point in the disc is that which would produce the same total flux as that from viscous and X-ray heating combined, i.e. $T^4 = T_{\text{visc}}^4 + T_{\text{irr}}^4$. The spectrum is then a sum of black bodies with temperatures given by this formula and areas determined by the area of an annulus at given radius. The irradiation temperature is determined using the simple parameterisation of Dubus et al. (1999)

$$T_{\text{irr}}^4 = C \frac{\dot{M} c^2}{4\pi\sigma R^2} \quad (4.19)$$

where \dot{M} is the mass transfer rate, σ is the Stefan-Boltzmann constant and R is the local disc radius. The parameter C (which is a function of radius) parameterises the efficiency of irradiation, and amalgamates uncertainty about the disc thickness, structure and X-ray albedo and the efficiency of the central engine. It can be calculated from

$$C = \eta(1 - \epsilon) \frac{H_{\text{irr}}}{R} \left(\frac{d \ln H_{\text{irr}}}{d \ln R} - 1 \right) \quad (4.20)$$

where η is the efficiency with which the central engine converts input mass into output X-rays, ϵ is the disc albedo, and H_{irr} is the height of the disc at which X-ray energy is deposited. A simple disc structure is assumed here, $H_{\text{irr}} = H_0(R/R_0)^{9/7}$ where H_0 and R_0 are the thickness and radius at the disc edge. This was proposed by Vrtilek et al. (1990) based the assumption that if the disc is heated sufficiently strongly then its vertical structure will be isothermal. It was shown by Dubus et al. (1999) that this assumption is not valid for a normal level of irradiation. Nonetheless, this simple functional form has been shown to give good agreement with broad band observations of other LMXBs (e.g. Cyg X-2, Vrtilek et al. 1990 and Sco X-1, Vrtilek et al. 1991), so it is appropriate to use it as an empirical prescription for irradiation. With this functional form and the assumption that the albedo does not vary with radius, the formulae can be rewritten as

$$T_{\text{irr}}^4 = C_0 \left(\frac{R}{R_0} \right)^{\frac{2}{7}} \frac{\dot{M} c^2}{4\pi\sigma R^2} \quad (4.21)$$

and

$$C_0 = \frac{2}{7}\eta(1 - \epsilon)\frac{H_0}{R_0} \quad (4.22)$$

where C_0 is now independent of radius; $C = C_0(R/R_0)^{2/7}$.

The X-ray spectrum is modified by including an approximate correction for spectral hardening. This arises from Comptonisation of disc photons because in the inner disc electron scattering is the dominant source of opacity (Shakura & Sunyaev 1973). The modification uses the diluted black body approximation (Shimura & Takahara 1995 and references therein) in which the local spectrum is $B(fT)/f^4$ instead of $B(T)$. f , the colour correction factor, is found to be ~ 1.7 for Galactic black hole systems at luminosities around 10 per cent of Eddington. The effect of including this simple prescription for spectral hardening is to shift the disc spectrum in a $\log \nu - \log F_\nu$ plot by $\Delta \nu = +\log f$ and $\Delta F_\nu = -\log f$ (i.e. down and to the right). As this effect only applies to the inner disc the spectrum was calculated in two parts, with the spectral hardening correction only used for the X-ray part. This renders it unnecessary to treat the radial dependence of f .

The model parameters were adjusted to give an approximate fit by eye; the purpose of this exercise is to test whether an irradiated disc can approximately reproduce the spectral energy distribution, not to derive precise model parameters. Detailed fitting of X-ray spectra is beyond the scope of this work, and has been done well by other authors, e.g. Sobczak et al. (1999). The uncertainty about the effect of heating on the companion star and the oversimplistic black body spectra also make detailed fits in the optical and UV both impossible and meaningless; as can be seen from Figure 4.22, the detailed fit in

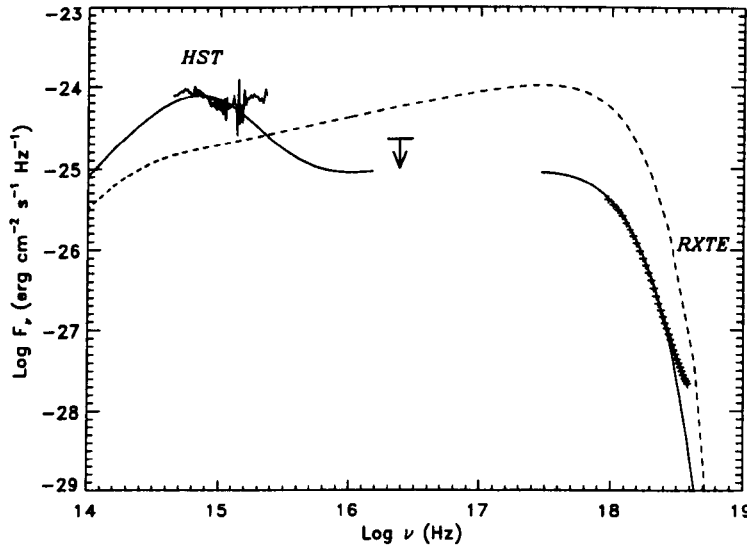


Figure 4.22: Composite broad-band spectrum for the May 14 observation. Shown are the *HST* spectra (left), the EUV constraint derived from the He II 4686 Å flux (centre; see Section 4.3.3) and the *RXTE* spectrum (right). Overlaid are simple model spectra of a viscously heated disc (dashed) and an irradiated disc (solid). The latter model is calculated in two sections to allow a simplistic treatment of X-ray spectral hardening due to Comptonisation. The fits are reasonable except in the hard X-ray and UV regions. The former is due to neglecting the power-law component. The origin of the UV spectrum is unknown.

the optical/UV is very poor. Fixed parameters were $d = 3.2$ kpc, $M_X = 7 M_\odot$, $q = 2.99$ and $i = 69.5^\circ$. The outer disc radius was again fixed at 95 per cent of the effective Roche lobe radius (Eggleton 1983). The inner disc radius was fixed at $6.5r_g$ consistent with the fitting of Sobczak et al. (1999) to data from the preceding week. The mass transfer rate was then adjusted to fit the thermal component of the X-ray spectra. A value of $1.1 \times 10^{-8} M_\odot \text{ yr}^{-1}$, corresponding to ~ 7 per cent of Eddington (assuming an efficiency of 10 per cent) was found to give good agreement. The irradiation efficiency parameter, C_0 , was then adjusted to fit the optical/UV peak with other parameters fixed; a value of 1.4×10^{-3} was used for the figure.

As can be seen in Figure 4.22, the broad band energy distribution can be approximately reproduced using this model. No power-law component has been included in the X-ray region, so the fit can be expected to deteriorate at high energies. The major failing of the model is that the upturn in the far-UV cannot be explained. It may be that using more

realistic local spectra than black bodies would improve the situation; this awaits good models for irradiated accretion disc atmospheres. It may also be that X-ray heating of the companion significantly increases its UV flux.

If this interpretation of the source of optical/UV flux is correct, then the unavoidable consequence is that in some way the irradiation efficiency, parameterised by C , must decrease dramatically during the course of the outburst. This is the only way to reconcile the optical/UV decline with the X-ray rise. Possible mechanisms for this will be discussed in the following Section.

4.8 Discussion

The most challenging result for any model of this outburst to explain is the apparent anti-correlation between optical/UV and hard X-ray behaviour. In the conventional picture of SXT outbursts driven by the limit cycle instability the fast rise–exponential decay (FRED) pattern is seen at both optical and X-ray energies (Chen, Shrader & Livio 1997). If reprocessed X-rays dominate the optical energy budget then the connection between the two is even closer and the optical/UV lightcurve should closely track the X-ray one, though with a slower decay caused by the shift of the peak of the spectrum to longer wavelengths (King & Ritter 1998). This is clearly not what GRO J1655–40 is doing: not only is a FRED pattern not seen in the X-ray lightcurve, but the optical/UV behaves in a completely different way. In other details too, this outburst differs from the canonical case. For example, the rapid rise in the soft X-ray band, and delayed, slower rise in the hard X-ray band is contrary to what was seen in X-ray Nova Muscae 1991 where the hard flux rise preceded the soft (Ebisawa et al. 1994). It would be tempting to draw an analogy with the black hole candidate GX 339–4. Motch et al. (1985) observed a hard–soft transition in this system during 1981 June in which the *soft* X-ray rise was accompanied by an apparently anti-correlated optical decline. The timescales and spectral changes involved in that transition were quite different to those in GRO J1655–40, however, and there is not an obvious connection between the two cases.

In spite of the difficulties in reconciling this anti-correlated behaviour with an irradiated disc model, this model offers the most persuasive explanation for the origin of the optical light and alternatives, such as self-absorbed synchrotron emission, are difficult to reconcile with observations. Results from the echo-mapping experiment, the lack of optical dips and the presence of smoothly modulated optical polarisation all point towards an X-ray heated

outer accretion disc. For such a model to explain the outburst evolution does, however, require a mechanism to decrease the efficiency of X-ray reprocessing rather dramatically.

4.8.1 A Decaying Warp?

One possibility has been suggested by Esin, Lasota & Hynes (1999). This is that the accretion disc is initially warped and precessing, but that X-ray irradiation of the companion star triggers enhanced mass transfer into the *plane of the disc*, which causes the warp to decrease.

It is now commonly believed that disc warping is an important effect in X-ray binaries. This is the 'standard' explanation for the 35 d superorbital period in Her X-1 and is also suggested by well established long periods in SS 433 (164 d) and LMC X-4 (30.4 d), as well as less certain periods in other systems. See Wijers & Pringle (1999) and references therein for a recent summary both of observations and models for the phenomenon. It should be noted that the inclination derived for the radio jets in GRO J1655-40 was $\sim 85^\circ$ (Hjellming & Rupen 1995), whereas the binary inclination is $\sim 70^\circ$ as discussed in Section 4.1.2. This implies that the jet axis is tilted with respect to the binary axis; a disc warp would provide a very natural explanation for this effect. Warps may be especially important to studies of irradiation. Models of the radial structure of accretion discs indicate that they should have a convex radial profile (Dubus et al. 1999 and references therein), which would shield the outer disc from direct irradiation from the vicinity of the compact object. Dubus et al. (1999) suggest that irradiation occurs in spite of this either because X-rays are scattered back down onto the disc by an extended corona, or because the disc is warped so that at a given time part of the disc can be directly irradiated, or that both effects contribute. If irradiation does depend on the disc being warped, then a decay of the warp will lead to a decay of the irradiation efficiency as required. The link between enhanced mass transfer and warp decay is more speculative, and there is no strong prediction of the decay timescale expected, other than that the observed optical decay timescale is comparable to the inferred precession periods in other systems.

van der Hooft et al. (1997) did find evidence for heating of the companion in an earlier outburst, and the apparent residual companion contribution to the spectrum after subtraction of the nominal quiescent level suggests it was significant in this outburst also. The lack of echoes at the lag corresponding to reprocessing on the companion, however, presents a problem, but not an insoluble one.

4.8.2 Obscuration by a Disc Corona?

Another possibility considered was that the irradiating X-ray flux was increasingly attenuated by a disc corona. As the optical depth of the Compton scattering corona increased, two consequences might emerge: firstly the hard X-rays, believed to be produced by Comptonisation, would increase. Secondly, the irradiation of the outer disc would decrease, as X-rays moving nearly parallel to the disc must penetrate a large optical depth of scattering material. This interpretation would predict that optical/UV and hard X-ray light curves might appear anti-correlated, exactly as observed. Indeed, a related scenario was proposed by Mineshige (1994) to explain why the onset of an optical reflare in X-ray Nova Muscae 1991 occurred simultaneously with a decrease in the Thomson optical depth deduced from X-ray spectra. There, it was suggested that evaporation of the Comptonising material allowed irradiation of the outer disc, triggering the reflare. It should be noted, however, that both the suggestion of Mineshige (1994) for X-ray Nova Muscae 1991 and that considered here depend on direct illumination of the disc through the corona. Theory suggests however (Dubus et al. 1999), that direct irradiation of the disc is impossible, and that instead the role of the corona may be to scatter X-rays back down onto the disc, hence enhancing rather than suppressing irradiation.

4.8.3 Long Period Oddities?

It has been suggested (Cannizzo 1998, priv. comm.) that the strange behaviour seen in this outburst may be a consequence of the long orbital period of this system. This will have several effects. The timescales relevant to the outer disc, in particular the viscous time, will be longer than in a short period system, leading to a longer timescale for the disc to settle into a quasi-steady state and hence possibly a continuing transfer of mass into the inner regions giving the sustained high X-ray fluxes. Detailed modelling of how the limit cycle instability would operate in such a system remains to be done, so it is not clear if this is an important effect or not. The case of V404 Cyg, with an even longer 6.5 d orbital period demonstrates, however, that ‘normal’ SXT behaviour can occur in a long period system, as this showed relatively normal lightcurves, albeit with large superposed variability.

4.8.4 Conclusion

At present, there is no compelling explanation for the behaviour of GRO J1655–40 in 1996. A decaying warp model driven by enhanced mass transfer due to X-ray heating is plausible theoretically, but there is no direct evidence that heating of the companion star does drive enhanced mass transfer. Obscuration by a Compton scattering cloud requires that direct irradiation would be possible in the absence of the cloud; theory suggests that this is not the case (Dubus et al. 1999), and that if anything, such a cloud would aid irradiation by scattering X-rays back down onto the disc. Resolution of this puzzle is likely to require better theoretical understanding of how irradiation of accretion discs really works.

Chapter 5

XTE J2123–058

5.1 Introduction

The SXT XTE J2123–058 was discovered by the All Sky Monitor (ASM) on the *RXTE* satellite at level of 100 mCrab on 1998 June 27; the detection was confirmed by the Proportional Counter Array (PCA) (Levine, Swank & Smith 1998). The *RXTE*/ASM light curve is shown in Figure 5.1. The discovery of apparent type-I X-ray bursts (Takeshima & Strohmayer 1998; Tomsick et al. 1999a) confirmed that the compact object was a neutron star and detection of twin high frequency quasiperiodic oscillations, kHz QPOs, (Homan et al. 1998; Tomsick et al. 1999a; Homan et al. 1999), as seen in other neutron star LMXBs (van der Klis 1998 and references therein) is consistent with this. Tomsick et al. (1999a) found that the X-ray spectrum could be well fitted with either a black body plus power-law model, or a Comptonised model, for the main part of the outburst. The last PCA observation, 1998 August 15, could be fitted with almost a pure power-law. It was speculated (Tomsick et al. 1999a) that this spectral change may have been due to the onset of the propeller mechanism, when the neutron star magnetosphere blocked inner disc accretion. Based on its X-ray colour-colour diagram and low-frequency power spectrum, as well as the frequency of bursts and strength of kHz QPOs, XTE J2123–058 was classified as an atoll source (Tomsick et al. 1999a; Homan et al. 1999).

The object was identified with a 17th magnitude blue star with an optical spectrum typical of SXTs in outburst (Tomsick et al. 1998a). This star is only marginally visible on a digitised UK Schmidt plate indicating substantial brightening (Tomsick et al. 1998a; Zurita, Casares & Hynes 1998). Casares et al. (1998) reported the presence of a strong

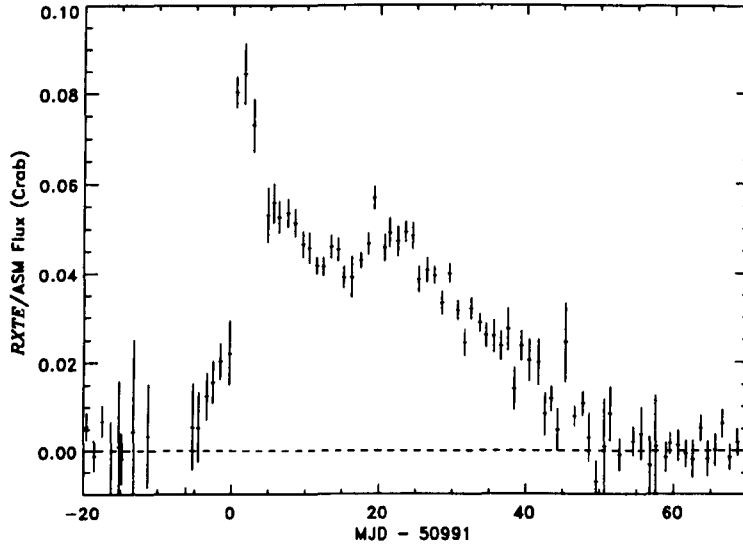


Figure 5.1: *RXTE*/ASM one-day average light curve based on quick-look results provided by the ASM/*RXTE* team. The zero point in time is chosen to coincide approximately with the first reported *RXTE* detection on 1998 June 27. WHT observations occurred around day 23.

optical modulation on a period of 1 d and attributed this to an eclipse. The orbital period was subsequently determined actually to be 6.0 hr both photometrically (Tomsick et al. 1998b; Ilovaisky & Chevalier 1998) and spectroscopically (Hynes et al. 1998a). Tomsick et al. (1998b) suggested that the 0.9-mag modulation is then due to the changing aspect of the heated companion in a high inclination system, although partial eclipses did also appear to be superimposed on this (Zurita, Casares & Hynes 1998). Ilovaisky & Chevalier (1998) reported that the light curve showed a further 0.3 mag modulation on a 7.2 d period and suggested that it is associated with disc precession. By 1998 Aug 26 XTE J2123–058 appeared to have reached optical quiescence, at a magnitude of $R \sim 21.7$ (Zurita & Casares 1998; Zurita et al. 1999).

XTE J2123–058 is an important object to study for several reasons. Firstly, neutron star SXTs are relatively rare; most neutron star LMXBs are persistently active. It is important to compare neutron star transients with the apparently more common black hole systems in order to determine how the presence or absence of a compact object hard surface affects the behaviour of the system. Such a comparison can also be used to test models for the formation and evolution of SXTs which predict different evolutionary

histories for black hole and neutron star transients (King, Kolb & Szuszkiewicz (1997) and references therein.) Secondly, XTE J2123–058 has a high orbital inclination, and possibly exhibits partial eclipses. High inclination systems provide more tools with which to determine the system geometry, and hence XTE J2123–058 can teach us things about SXTs which we cannot learn from other, lower inclination systems. Thirdly, XTE J2123–058 is at high Galactic latitude and appears to be at least 2.6 kpc above the Galactic plane (Tomsick et al. 1999a) For comparison, the mean altitude of the low-mass X-ray binary distribution (i.e. z_{rms}) is only 1 kpc (van Paradijs & White 1995). This system may be intrinsically a halo object, or may have been formed in the disc and then kicked out at high velocity when the neutron star was formed. This issue also has bearing on LMXB evolution (King & Kolb 1997).

In this chapter are presented the results of a spectrophotometric study of XTE J2123–058 using the William Herschel Telescope (WHT). The results presented here have been reported in a preliminary form in Hynes et al. (1998a) and will be presented in full in Hynes et al. (1999). The photometric study of Zurita et al. (1999) is closely related to this work and the two were performed in parallel.

5.1.1 System Parameters

Binary parameters were derived from results of fits to outburst light curves by Zurita et al. (1999). The parameters assumed are $M_1 = 1.4 M_\odot$, $M_2 = 0.3 M_\odot$, $i = 73^\circ$ and $R_{\text{disc}} = 0.75 R_{L1}$. The masses deserve comment. The light curve fits only provide a significant constraint on the mass ratio, of $q = M_2/M_1 = 4.6^{+0.5}_{-0.2}$. To obtain actual masses, one must make physical assumptions. The simplest is that the companion star is on the main sequence. The mass and spectral type are then required (via the orbital period – mean density relation; Frank, King & Raine 1992) to be $0.6 M_\odot$ and K7V respectively (Zurita et al. 1999). Combining this mass with the measured mass ratio would imply a neutron star mass of $2.8 M_\odot$. This is extremely large and far in excess of *dynamical* mass estimates for neutron stars ($< 2 M_\odot$; see Orosz & Kuulkers 1999 and references therein.) While the neutron star in XTE J2123–058 may be very massive, it seems more likely that the assumption of a main-sequence companion is invalid. Other SXTs do appear to have undermassive companions (Smith & Dhillon 1998), so this is plausible, and consistent with theoretical predictions (King, Kolb & Burderi 1996) that short period neutron star LMXBs should *only* be transient if they have evolved companions. If an evolved, undermassive

companion is accepted then there is no reason to believe the neutron star is unusual. The canonical neutron star mass of $M_1 \sim 1.4 M_\odot$ was therefore adopted; this is consistent with the most recent review of neutron star masses (Thorsett & Chakrabarty 1999).

5.1.2 Reddening and Distance

The reddening to XTE J2123–058 has been estimated both directly, by measurement of interstellar absorption lines, and indirectly, by examination of extinction maps derived from other objects. Equivalent widths for the Na D lines are 0.29 ± 0.02 and $0.30 \pm 0.02 \text{ \AA}$. Based on the strength of the D1 line and the calibration of Munari & Zwitter (1997), $E(B - V) = 0.12 \pm 0.05$; the error estimate is the estimated accuracy of the calibration as given by Munari & Zwitter (1997). This is consistent with the depth of the 4428 Å diffuse interstellar band, from which $E(B - V) < 0.23$ is obtained (Krelowski et al. 1987). Assuming $R_V = 3.1$, this implies $A_V = 0.37 \pm 0.15$, agreeing with the value of $A_V = 0.36$ quoted by Homan et al. (1999) based on dust maps in Schlegel, Finkbeiner & Davis (1998). Soria, Wu & Galloway (1999), however, estimate a somewhat lower value of $E(B - V) = 0.054$ from the reddening maps of Burstein & Heiles (1982). This author has examined these maps and agrees with this estimate at least to $\lesssim 0.06$. The source of the discrepancy is unclear; for the rest of this work $E(B - V) = 0.12 \pm 0.05$ is assumed, but it may be that the true value is lower than this.

Various distance estimates have been made, using several methods. Given a quiescent apparent magnitude and an assumed absolute magnitude of the companion star it is straightforward to derive the distance (assuming the reddening is also well constrained.) The companion absolute magnitude can, in principal, be estimated from the orbital period (see above), subject to the assumption of a main-sequence companion. Using this method, Zurita et al. (1999), who have the most comprehensive quiescent observations, derive $d \sim 7.7 \text{ kpc}$. As noted above, however, the companion of XTE J2123–058 has likely evolved off the main-sequence. For a given orbital period, this means it will be redder and fainter, and have a higher absolute magnitude; hence the distance will have been overestimated. Another assumption made is that there is negligible quiescent flux from the disc. If this is not true then the quiescent absolute magnitude of the binary will be lower than assumed; hence the distance will have been underestimated. It may be that these two effects partly cancel out, but $d \sim 7.7 \text{ kpc}$ should be regarded as a very approximate distance. Another approach is to assume that X-ray bursts do not exceed the Eddington limit. This method

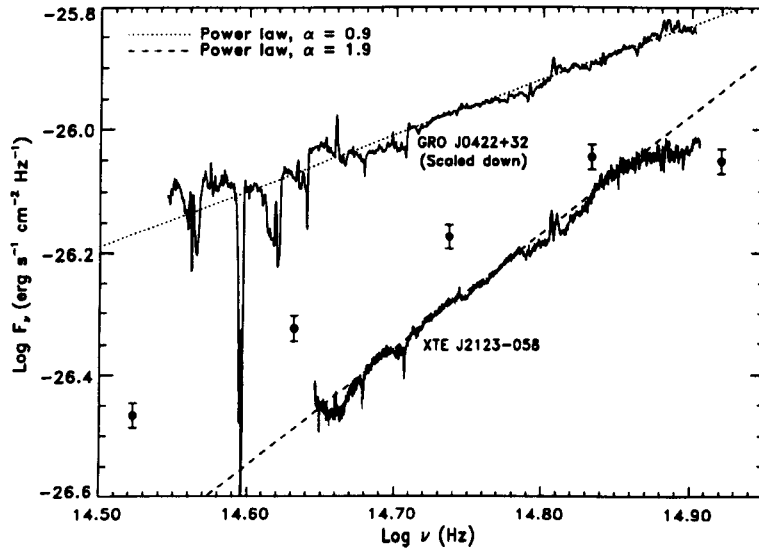


Figure 5.2: Comparison of dereddened spectral energy distributions of XTE J2123-058 (July 19-20) and GRO J0422+32. Points indicate the distribution inferred earlier in the outburst (June 30) from photometry of Tomsick et al. (1998a). Approximately fitting power-laws are also shown. The spectral energy distribution of XTE J2123-058 is clearly steeper than that of GRO J0422+32.

yields an upper limit of 14-15 kpc (Tomsick et al. 1999a; Homan et al. 1999). Other approaches involve more assumptions. Homan et al. (1999) derive $d = 10 - 15$ kpc from the empirical relationship (van Paradijs & McClintock 1994) between outburst optical brightness, orbital period and L_x/L_{Edd} . They also obtain $d = 5 - 11$ kpc from relations (Lewin, van Paradijs & Taam 1993) between average burst duration, average integrated burst flux and L_x/L_{Edd} . Finally Zurita et al. (1999) use the relation of Shahbaz, Charles & King (1998) to derive $d \sim 5.7$ kpc by using the delay of the secondary maximum in the X-ray light curve to calibrate the X-ray luminosity. There is clearly a consensus that $d = 5 - 15$ kpc, but it is difficult to be more precise than this. Fortunately, the work presented here does not depend directly on the assumed distance.

5.2 The Continuum Flux Distribution and Light Curve

The dereddened spectral energy distribution of XTE J2123-058 is shown in Figure 5.2. For comparison, the photometry of Tomsick et al. (1998a) and a spectrum of the black hole candidate GRO J0422+32 in outburst (Shrader et al. 1994) are also plotted. Dereddening

assumes $E(B - V) = 0.12$ for XTE J2123–058 (Section 5.1.2) and $E(B - V) = 0.3$ for GRO J0422+32 (Section 7.1.2). Power-laws of spectral index $\alpha = 1.9$ for XTE J2123–058 and $\alpha = 0.9$ for GRO J0422+32 (where $F_\nu \propto \nu^\alpha$) are overplotted to characterise the spectral energy distributions (SEDs) of the two objects. GRO J0422+32 is the black-hole SXT closest in orbital period to XTE J2123–058, and its SED is representative of those of short-period BHXRTs. It is clearly redder than that of XTE J2123–058 (compared to both spectroscopy and photometry), which is very close to an $\alpha = 2$ Rayleigh-Jeans spectrum. This suggests that the emission regions in XTE J2123–058 are hotter than in GRO J0422+32, although the possibility of errors in extinction correction, discussed in Section 2.5.5 weaken this conclusion.

Figure 5.3 shows light curves for three ‘continuum’ bins at 4500, 5300 and 6100 Å. The light curves have very similar shapes, with no significant differences in profile or amplitude within this wavelength range. The light curve morphology is discussed by Zurita et al. (1999); it is mainly due to the changing aspect of the heated companion star. This is the dominant light source at maximum light, near phase 0.5. At minimum light (phase 0.0) the heated face is obscured and only the accretion disc is visible. At all phases the unilluminated parts of the companion star are expected to contribute negligible flux as the outburst amplitude is ~ 5 magnitudes.

There is no strong dependence of the modulation amplitude on wavelength. The light curves do show small systematic distortions; it is likely that this is due to wavelength dependent differential slit losses between XTE J2123–058 and the comparison star. This complicates the interpretation of lightcurves at different wavelengths. The effect is less noticeable on July 20 when a wider slit was used, so these data are most suitable for searching for real wavelength dependence. The data from July 20 comprised two sequences of spectra. Within each sequence the source position on the slit was maintained by an autoguider. To first order, the effect of the distortion appears to be to shift the two sequences relative to each other, due to different positioning of the source on the slit in each sequence. This is most pronounced at the blue end of the spectrum. Allowing an arbitrary shift of each sequence is sufficient to bring them into alignment, with no significant dependence of the shape of the lightcurve on wavelength. This is shown in Figure 5.4 where lightcurves at 4150 Å, 5175 Å and 6425 Å normalised in this way are compared. The two sequences each sample nearly the full amplitude of the orbital modulation, and show no dependence of this amplitude on wavelength. This is expected if the emission regions are

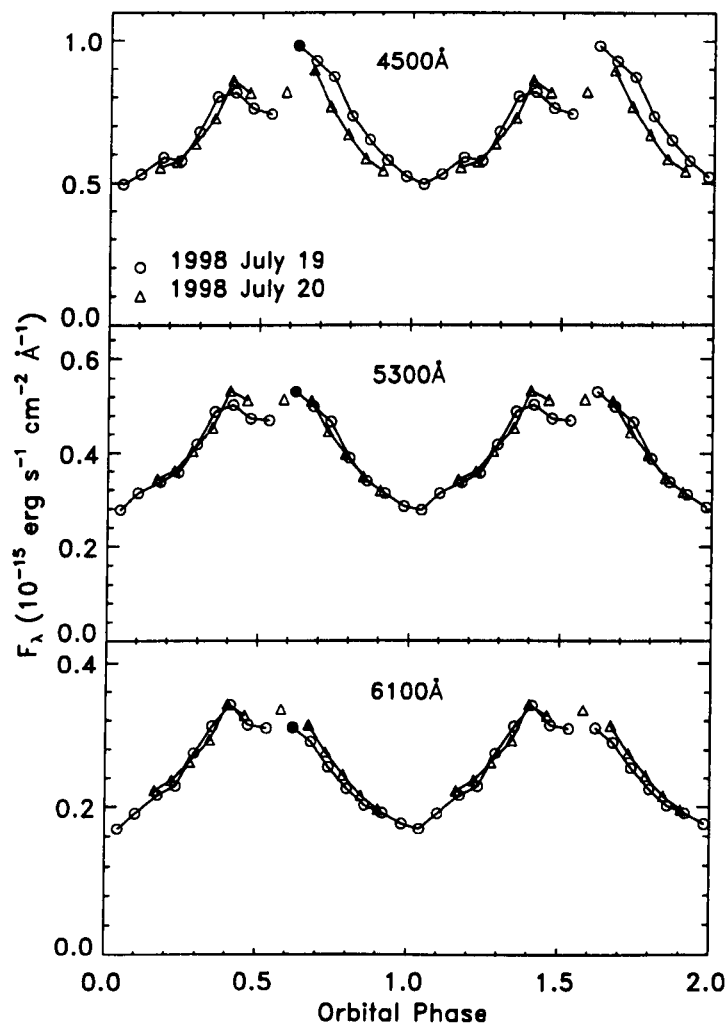


Figure 5.3: Continuum light curves of XTE J2123-058 at several wavelengths. Joined points indicate continuous sequences from Table 2.3. Solid points indicate the first observation of each night; each observing night ran approximately from phase 0.6–1.6. Apparent inconsistencies between the two nights, and differences between different wavelengths are likely due to calibration errors.

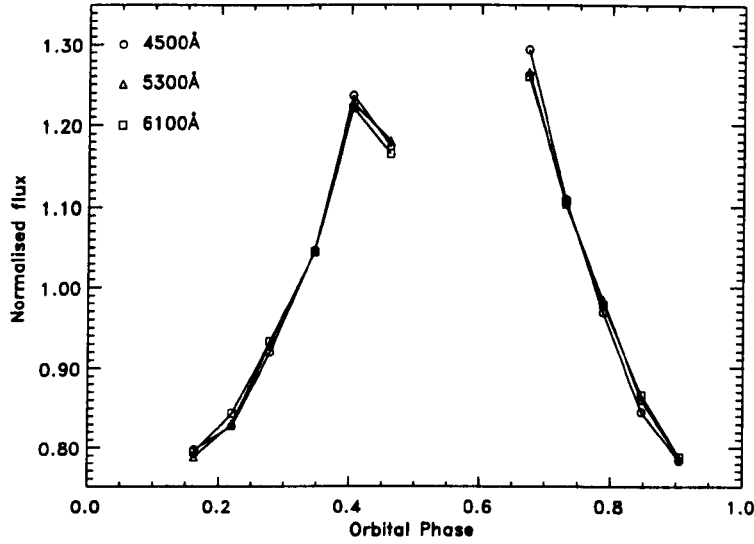


Figure 5.4: Normalised continuum light curve of XTE J2123–058 from July 20 at several wavelengths. Joined points indicate continuous sequences from Table 2.3. Each such sequence has been normalised by dividing by its mean. After this, no significant differences in the shape of the light curve remain between the three wavelengths.

sufficiently hot that only the $F_\nu \propto \nu^2$ Rayleigh-Jeans part of the spectrum is seen. This interpretation is consistent with the very steep SED shown in Figure 5.2.

5.3 The Emission Line Spectrum

At first glance, XTE J2123–058 presents a nearly featureless spectrum, with only the Bowen blend (N III/C III 4640 Å) and He II 4686 Å prominent. A number of weaker emission lines are also present, however, the Balmer lines present complex profiles and weak interstellar absorption features are seen. The interstellar lines were discussed in Section 5.1.2; emission lines are described here.

The average spectrum from July 19–21 shown in the Figure 5.5 is derived from a straight sum of count rates before slit loss and extinction corrections. As the slit losses in particular are strongly dependent on wavelength and time, this improves the signal-to-noise ratio dramatically compared to averaging calibrated spectra, but means that relative fluxes of widely separated lines may be subject to systematic errors. For example, the average blue-end spectrum is predominantly determined from the phase range ~ 0.0 – 0.5 when slit losses were minimised, whereas the red-end spectrum is closer to a uniformly

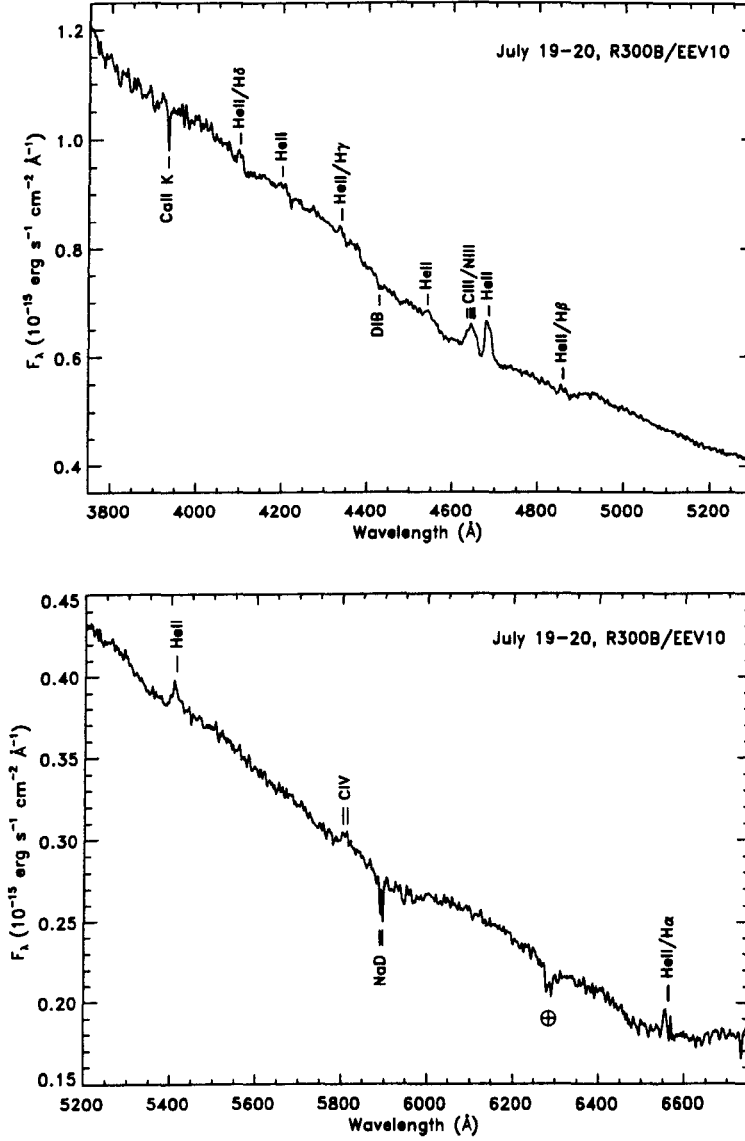


Figure 5.5: Average spectrum of XTE J2123–058. All identified absorption or emission lines are marked.

weighted average. Such problems do not apply to the spectral energy distribution which was derived by taking an average of calibrated spectra resampled onto a uniform phase grid.

5.3.1 N III-C III and He II 4686 \AA Emission

The equivalent widths of the N III/C III Bowen blend and He II 4686 \AA line imply an average N III/C III-He II ratio of 0.97 ± 0.02 , thoroughly consistent with the ratios observed in other Galactic LMXBs (typically $\sim 0.5 - 1.5$; Motch & Pakull 1989). In particular, this ratio is

Table 5.1: Spectral lines detected in XTE J2123–058. No equivalent widths are calculated for Balmer lines due to the complex nature of the line profiles, and for higher order He II lines due to the difficulty of setting a meaningful continuum level. Errors in equivalent widths are statistical errors in the average spectrum and do not account for intrinsic variability.

Identification	Wavelength (Å)	Equivalent width (Å)
Ca II K (IS)	3933.7	$+0.30 \pm 0.04$
He II 4–12/H δ	4100.0, 4107.7	
He II 4–11	4199.8	
He II 4–10/H γ	4338.7, 4340.5	
DIB (IS)	4428	$+0.24 \pm 0.05$
He II 4–9	4541.6	
N III/C III	4640	-1.98 ± 0.03
He II 3–4	4685.7	-1.92 ± 0.03
He II 4–8/H β	4859.3, 4861.3	
He II 4–7	5411.5	-0.74 ± 0.05
C IV	5801.5, 5812.1	-0.39 ± 0.06
Na I D (IS)	5890.0, 5895.9	$+0.59 \pm 0.03$
He II 4–6/H α	6560.1, 6562.5	

significantly higher than seen in LMXBs in low-metallicity environments (e.g. < 0.12 for LMC X-2 and < 0.20 for 4U 2127+11 in the low-metallicity globular cluster M15; Motch & Pakull 1989). This suggests that XTE J2123–058 originates in the Galactic population; see Section 5.6.5 for further discussion. Note that as these two lines are very close, this ratio is not affected by the uncertainty in line flux calibration described above.

5.3.2 H I Balmer and He II Pickering Lines

Balmer lines exhibit a complex profile with broad absorption and a structured emission core. This broad absorption plus core emission line structure is common in SXTs in outburst. Balmer line profiles in GRO J0422+32 (Shrader et al. 1994; Callanan et al. 1995) look very similar, showing a double-peaked core surrounded by broad absorption.

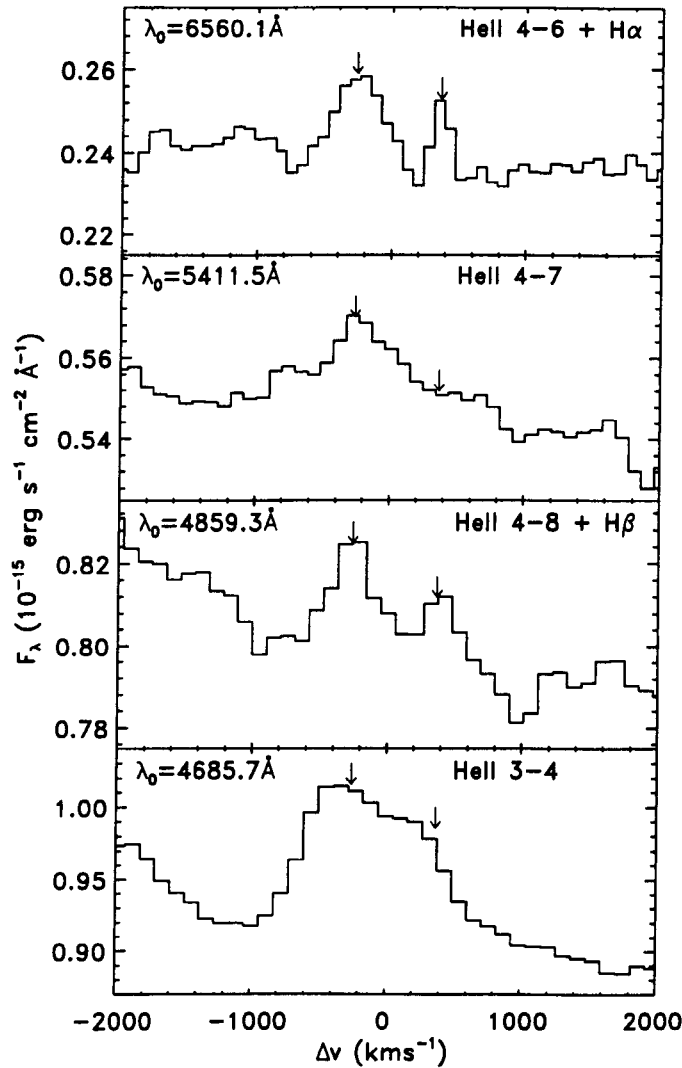


Figure 5.6: Upper three panels: Selected He II Pickering lines and coincident H I Balmer lines. The horizontal axis is velocity with respect to the rest velocity of the He II line in the panel. The arrows mark the two prominent emission components and are drawn at the same velocities in each plot. The left-hand peak is clearly a He II feature, the right hand one is probably due to Balmer lines as it only appears where Balmer lines are present. The spectrum has been dereddened assuming $E(B - V) = 0.12$ and the vertical flux scale is the same in each plot. Emission line fluxes can therefore be directly compared. The rest wavelength of the Balmer lines corresponds to velocities of $+100 \text{ km s}^{-1}$ for H α and $+130 \text{ km s}^{-1}$ for H β . The lower panel shows He II 4686 \AA on the same velocity scale for comparison. It is clearly broader than the Pickering lines, especially on the red wing, but the peak velocity is similar.

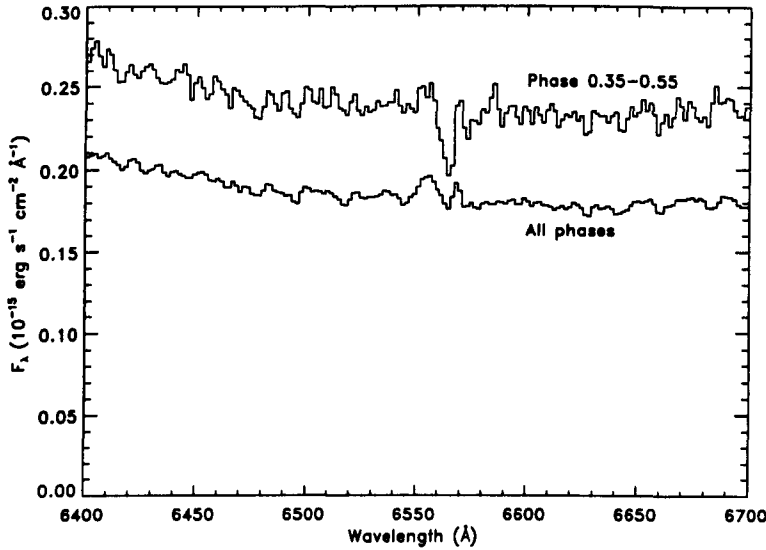


Figure 5.7: Average spectra near $H\alpha$ (lower) together with average of just phases 0.35–0.55 (upper). Real absorption can clearly be seen in the upper spectrum.

GRO J1655–40, too, exhibits this pattern (Soria et al. 1998).

The interpretation of the profiles is complicated by the presence of coincident He II Pickering lines ($n = 4-5, 6, 7 \dots$ transitions) within 2 \AA of each Balmer line. The cores are compared in Figure 5.6. $H\alpha$ and $H\beta$ are shown, together with the He II 4–6, 4–7 and 4–8 lines (Pickering $\beta-\delta$). The He II 4686 \AA line is also shown for comparison. Higher order lines show similar behaviour, at lower resolution and signal-to-noise. The two peaks marked are clearly present in both $H\alpha$ and $H\beta$, and can also be identified in $H\gamma$ and $H\delta$. The blue peak is also seen in He II 5411 \AA (4–7), but the red peak apparently is not. Peak 4686 \AA emission also coincides with the blue peak. The blue peak, however, appears weaker in flux in He II 5411 \AA than in $H\alpha$ or $H\beta$, suggesting that it contains Balmer emission as well¹. A suggested decomposition of the line profile is that the blue peak contains He II emission, and possibly also some Balmer emission. The red peak is pure Balmer emission. The broad absorption also appears to be a Balmer feature.

There is a further complication. As will be described in more detail in Section 5.4, $H\alpha$, and possibly also $H\beta$ are subject to transient absorption, strongest in the phase range 0.35–0.55. The average $H\alpha$ line profile in this phase range is shown in Figure 5.7. As the absorption component clearly lies between the two peaks, it may be that weaker absorption at all phases is partly responsible for the apparent separation of the two peaks.

¹As noted above there may be systematic errors in comparing widely separated lines. The difference

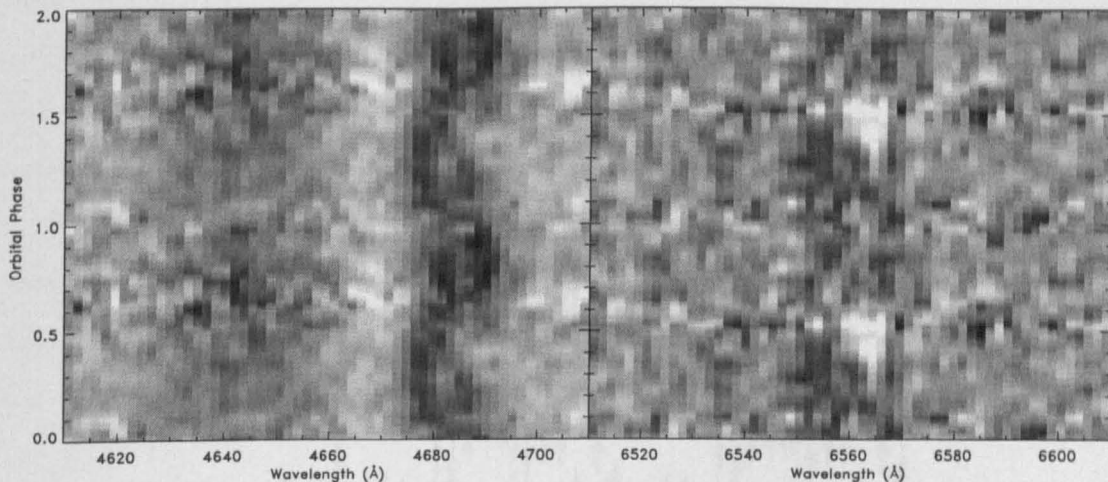


Figure 5.8: Trailed spectrograms of XTE J2123–058. The left hand panel shows behaviour of C III/N III and He II emission. The right hand panel shows blended He II 6560 Å and H α behaviour. Note the phase 0.5 H α absorption component; the white spot in the right hand panel.

5.4 Line Variability

Emission lines show significant changes over an orbital cycle, with differences in behaviour between different lines. N III/C III 4640 Å (Bowen blend) shows a flux modulation. He II 4686 Å emission is modulated in flux and also shows complex changes in line position and structure. He II 6560 Å and H α are blended and, in addition probably to showing flux and wavelength modulations, are subject to a transient absorption feature strongest around phase 0.5. The changes are illustrated with trailed spectrograms in Figure 5.8 and with integrated light curves in Figure 5.9.

The Bowen blend light curve appears similar to the continuum light curves shown in Figure 5.3. Bowen emission may therefore originate on the heated face of the companion star, with the modulation arising from the varying visibility of the heated region.

He II light curves show a double peaked structure with a strong peak near phase 0.75 and a weaker one near 0.25. The complex line behaviour seen in the spectrogram indicates multiple emission sites; simple interpretation of the integrated light curve is therefore difficult as it is an average of different light curves of several regions.

H α emission is blended with He II 6560 Å, and as discussed in Section 5.3 also comprises here is not large and *may* be an artifact of this effect.

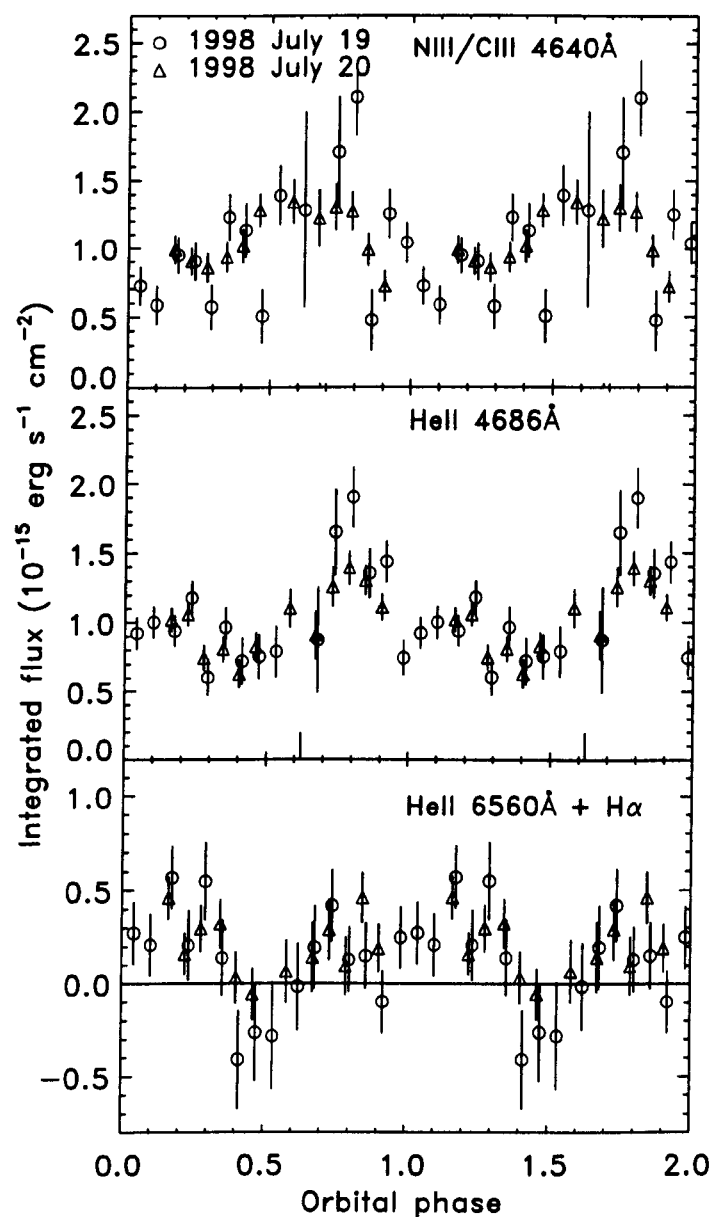


Figure 5.9: The absorption dip in the He II 6560 Å/H α light curve is real absorption below the continuum, not simply obscuration of the emission component.

several components. The most striking is the transient absorption component seen near phase 0.5. This can be clearly seen in the light curve and the spectrogram. The light curve is deceptive as it also reflects changes in the emission flux; it suggests that the feature is centred at phase 0.5 but, as can be seen from the spectrogram, this is not really the case. This shows that the feature begins quite sharp and red, around phase 0.3 and then becomes progressively more extended to the blue, fading out by phase 0.6. Whilst it is sometimes difficult to distinguish an absorption component from an absence of emission, that is not a problem here; the absorption definitely extends below the continuum as can clearly be seen in Figure 5.7.

5.5 Doppler Tomography

The maximum-entropy Doppler tomography technique of Marsh & Horne (1988), as implemented in DOPPLER, was used to identify He II 4686 Å emission sites in velocity space. The results are shown in Figure 5.10. Both the back-projection method implemented in MOLLY and the alternative maximum-entropy implementation of Spruit (1998) give similar results.

Maximum entropy Doppler tomography measured entropy with respect to a uniform default image. As the observations have low resolution, both spectral and in phase, care was taken to account for this in the image reconstruction. A velocity resolution of 180 km s^{-1} was chosen to match the highest resolution in the dataset. As each observation spanned 0.06 in phase, phase smearing was also explicitly accounted for by dividing each exposure into three spanning the exposure duration. A range of images were reconstructed with a reduced χ^2 between 0.7 and 1.2 in steps of 0.1. Convergence proved very slow, with 16000 iterations needed to reach $\chi_R^2 = 1.0$ and 48000 for $\chi_R^2 = 0.7$. It was found that a lower target χ_R^2 sharpened the image significantly, without noticeably increasing the noise, so the image with $\chi_R^2 = 0.7$ was adopted.

There is a difficulty in that one of the fundamental assumptions of Doppler tomography, that all of the line flux is always visible at *some* velocity, is clearly violated, as the integrated line flux is not constant. This is accounted for by normalising the spectra (dividing by a smooth fit to the He II 4686 Å light curve in Figure 5.9.) The structure of the derived tomogram without normalisation of the line profiles is very similar, so these results do not appear to be sensitive to this difficulty.

Doppler tomography also requires knowledge of the systemic velocity of the binary.

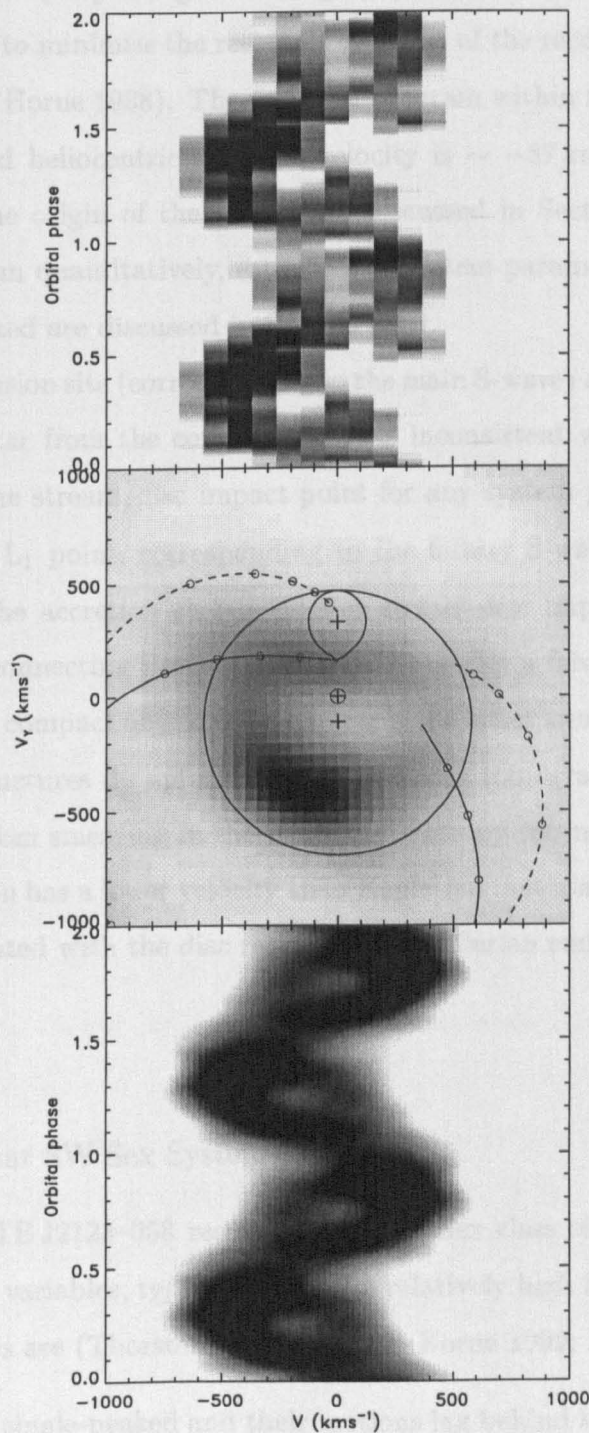


Figure 5.10: Doppler tomogram of He II 4686 Å emission in XTE J2123-058. The upper panel shows the observed trailed spectra, normalised to constant total line flux. The middle panel shows the tomogram itself, and the lower panel shows the ideal trailed spectrogram reconstructed from the tomogram.

With no *a priori* knowledge of this, it is necessary to estimate it from the He II 4686 Å line itself. This is done by repeating the tomography analysis for different assumed mean velocities and seeking to minimise the residuals of the fit of the reconstructed spectrogram to the data (Marsh & Horne 1988). The OPTGAM program within DOPPLER performs this fitting. The measured heliocentric systemic velocity is $\sim -87 \text{ km s}^{-1}$; the implications of this velocity for the origin of the binary are discussed in Section 5.6.5. In order to interpret the tomogram quantitatively, estimates of system parameters are also required. The parameters adopted are discussed in Section 5.1.1.

The dominant emission site (corresponding to the main S-wave) appears on the opposite side of the neutron star from the companion. It is inconsistent with the heated face of the companion and the stream/disc impact point for any system parameters. There is a fainter spot near the L_1 point, corresponding to the fainter S-wave, which is consistent with emission from the accretion stream and/or stream-disc impact point. There also appears to be a loop connecting these two spots and possibly a fainter ring approximately concentric around the compact object. It is unclear if the latter two features are real or are artefacts. Similar structures do appear in backprojected tomograms implying that they do not simply arise from smearing in the maximum entropy reconstruction. It is notable that nearly all emission has a lower velocity than Keplerian material at the disc edge could have, and so if associated with the disc requires sub-Keplerian emission.

5.6 Discussion

5.6.1 A Neutron Star SW Sex System?

In several respects XTE J2123–058 resembles the SW Sex class of cataclysmic variables. These are all novalike variables, typically seen at a relatively high inclination. Their main defining characteristics are (Thorstensen et al. 1991; Horne 1999; Hellier 1999):

1. Balmer lines are single-peaked and their motions lag behind that of the white dwarf. In a Doppler map emission is typically (though not always) concentrated in the lower-left quadrant at velocities lower than any part of the disc. A high velocity component is detectable with velocity semi-amplitude $\sim 1000 \text{ km s}^{-1}$. This has the same phasing as the low velocity component; and their separate identity is vigorously debated.
2. Transient absorption lines which are strongest near phase 0.5 or slightly earlier. These are moderately blue shifted.

3. Continuum eclipses have a V-shaped profile implying a flatter temperature distribution than expected theoretically. Balmer line eclipses are shallow and occur earlier than continuum eclipses. Red shifted emission remains visible at mid-eclipse.

On the first two points XTE J2123–058 shows striking similarities to the SW Sex systems. Anomalous emission line behaviour is most clearly seen in He II 4686 Å in this higher excitation system. This line appears, on average, single peaked. The emission is concentrated in the lower-left quadrant at sub-Keplerian velocities. A high velocity component is not detected, but cannot be ruled out without higher quality data. Transient absorption is seen in the Balmer lines before and around phase 0.5. It begins slightly redshifted and moves to the blue. As XTE J2123–058 does not strongly eclipse, it is impossible to comment on the third point.

Various models have been proposed for the SW Sex phenomenon. Honeycutt, Schlegel & Kaitchuck (1986) proposed a bipolar wind for SW Sex itself; see Murray & Chiang (1996) for a recent version of this model. Williams (1989) suggested that the single-peaked emission lines indicate that accretion actually occurs onto the poles of a magnetised primary, i.e. that SW Sex systems are intermediate polars. The stream overflow model was originally suggested by Shafter, Hessman & Zhang (1988); in this model the SW Sex behaviour is a result of the accretion stream spilling over the disc and reimpacting closer to the primary. For a recent exposition see Hellier (1999). A variation of stream overflow is the magnetic propeller model for SW Sex systems (Horne 1999) in which the overflowing material does not reimpact the disc, but instead is accelerated by the tangled magnetic fields of the disc and ejected from the binary. Finally, the observation that many SW Sex systems show negative superhumps prompted the suggestion (Patterson 1999) that a tilted, retrogradely precessing accretion disc, the favoured model for negative superhumps, may be a factor in the SW Sex phenomenon, possibly explaining *why* the stream overflows the disc.

5.6.2 Is this Behaviour Typical of LMXBs?

The only other SXT for which outburst Doppler tomography of adequate quality is available is the black hole candidate GRO J0422+32 (Casares et al. 1995a). Using ephemerides determined subsequently (Harlaftis et al. 1999), emission in this object appears to originate from the accretion stream/disc impact point. These data were obtained in the December 1993 mini-outburst, ~ 500 d after the peak of the primary outburst.

Data on other short-period neutron star LMXBs in an active state, however, suggests a similar behaviour to that seen here. 4U 2129+47 shows a very similar blue spectrum to XTE J2123–058 (Thorstensen & Charles 1982). Clear variations in the He II 4686 Å radial velocity are seen with maximum radial velocity around phase 0.7–0.8 and semi-amplitude $216 \pm 70 \text{ km s}^{-1}$. Spectroscopy of EXO 0748–676 (Crampton et al. 1986) also reveals radial velocity modulations in the He II 4686 Å line. The radial velocity curve measured from the line base shows maximum velocity at phase 0.76 ± 0.16 with semi-amplitude $210 \pm 92 \text{ km s}^{-1}$. For comparison, a similar radial velocity curve fit to the He II lines of XTE J2123–058 (Hynes et al. 1998a) yielded maximum velocity close to phase 0.75 with semi-amplitude $\sim 180 \text{ km s}^{-1}$. In 2A 1822–371, He II modulations are seen with maximum light at phase 0.75, maximum radial velocity at phase 1.0 and velocity semi-amplitude 300 km s^{-1} (Mason et al. 1982). Augusteijn et al. (1998) studied 4U 1636–536 and 4U 1735–44 and found the two systems similar to each other. Both show He II modulations with semi-amplitude 140–190 km s^{-1} with maximum radial velocities measured at phases 0.87–1.04²

It therefore appears that the behaviour that seen in XTE J2123–058 is at least typical of short period neutron star LMXBs. There are insufficient data to decide if this is also true for long period or black hole systems.

5.6.3 The Magnetic Propeller Interpretation

It is possible to explain fully the behaviour of the He II 4686 Å line in terms of the magnetic propeller model. This model also provides a possible mechanism for explaining the transient Balmer absorption, although the observed absorption kinematics are harder to reconcile with this interpretation.

The essence of magnetic propeller models is that in the presence of a rapidly rotating magnetic field, accreting diamagnetic material may be accelerated tangentially, leading to it being ejected from the system. It is easy to see how such a scenario may arise due to a rapidly spinning, magnetised compact object. This mechanism has been invoked to explain the unusual behaviour of the cataclysmic variable AE Aqr in terms of a magnetic field anchored to a spinning white dwarf (Wynn, King & Horne 1997; Eracleous & Horne 1996). It is also likely that magnetic propellers driven by neutron star magnetic fields exist, as proposed by Illarionov & Sunyaev (1975). These may be very important in

²These phases have shifted by 0.5 with respect to those quoted by the authors as they define phase 0 as photometric *maximum*.

suppressing accretion in neutron star SXTs in quiescence; see Menou et al. (1999) and references therein for a discussion of this situation. There is an important difference of scale, however; spin periods of white dwarfs are $\gtrsim 30$ s; spin periods of neutron stars in LMXBs are typically of order milliseconds. For XTE J2123–058, $P_{\text{spin}} = 3.92$ ms was suggested by Tomsick et al. (1999a). For such rapid rotation an important factor is the light-cylinder, defined by the radius at which the magnetic field must rotate at the speed of light to remain synchronised with the compact object spin. Outside of this radius, the magnetic field will be unable to keep up and become wound up, and the propeller will be less effective, though may still produce some acceleration (Wynn, King & Horne 1997; Wynn 1999, priv. comm.). For a ~ 4 ms spin period in XTE J2123–058, the light cylinder is at ~ 0.0003 of the disc radius; for comparison, the closest approach of a ballistic stream is ~ 0.2 of the disc radius. A *neutron star* propeller therefore appears unlikely to strongly affect the stream overflow material, although simulations are needed to test this. An alternative mechanism was suggested by Horne (1999) for SW Sex systems, in which a magnetic propeller can arise from the magnetic fields of the disc itself. This has problems, in that it should very efficiently remove angular momentum from the disc (Wynn & King 1999, priv. comm.), but this could perhaps be overcome if only a small fraction of material passes through the propeller. This mechanism allows much lower angular velocities for the field and hence a larger light cylinder; it may be the only large scale propeller mechanism possible in a neutron star system.

To construct a simple model of a magnetic propeller in XTE J2123–058, the parameterisation used by Wynn, King & Horne (1997) to describe AE Aqr is adopted. The magnetic field is modelled as a dipole with angular velocity ω_f . While such a field may be a reasonable representation of that of a compact star (white dwarf or neutron star), it is clearly a gross simplification of that of a disc-anchored propeller. In the latter case the net effect would probably arise from a mixture of unstable field structures of varying strengths and anchored at a range of radii. As it is unclear what form such structures should take, however, a dipole approximation is used for simplicity and consistency with existing work on magnetic propellers. The acceleration mechanism assumes that the flow breaks up into diamagnetic blobs of varying size and density. The field can only partially penetrate the blobs, and hence they are accelerated, but not locked to the field lines. The magnetic acceleration on a blob is given by $g_{\text{mag}} = -k[v - v_f]_{\perp}$ where v is the stream velocity, v_f is the field velocity and the velocity difference is resolved in the plane per-

pendicular to the field. The parameter k parameterises ignorance of the magnetic field strength and blob size and density and, following Wynn & King (1995), the functional dependence $k = k_0(r/r_0)^{-2}$, is adopted, where $r_0 = 10^{10}$ cm. Different blob sizes and densities will lead to a spread of values of k_0 and hence different trajectories. The uncertainty in the angular velocity of the magnetic field is unimportant provided it is high enough that $v_f \gg v$ at all points along the stream trajectory, and low enough that all regions of interest are within the light cylinder. For XTE J2123–058, this corresponds to a field period of approximately $500 \gg P_{\text{spin}} \gg 10$ s. Within this regime varying P_{spin} has the same effect as varying k_0 , and the trajectory is effectively a function of a single parameter. This simple case is adopted for the model with $P_{\text{spin}} = 50$ s. This corresponds to a field anchored at radius ~ 0.03 of the disc radius. Obviously, in reality the field structure is more extended and chaotic.

As most of the accretion likely proceeds through the disc in this system, it is assumed that the propeller mechanism acts only on overspill from the stream-disc impact point. The model therefore calculates a trajectory which is purely ballistic until it reaches the disc edge and is subject to a propeller force thereafter. Quantitatively, this makes little difference to the results compared to allowing the magnetic force to act everywhere on the stream.

The parameter k_0 is adjusted to find a trajectory which passes through the central emission on the tomogram. This is shown in the upper panel of Figure 5.11 together with two bracketting trajectories to show the dependence on k_0 . For the model to be plausible, an explanation for why one particular place on the trajectory is bright is required. Such an explanation is offered by Horne (1999), where it is pointed out that there is a point outside the binary at which trajectories for different values of k intersect. At this point, faster moving blobs cross the path of slower blobs and shocks can be expected. This can be seen in the lower panel of Figure 5.11. The region where the trajectories collide is identified with the shock region in which emission is expected.

To make a quantitative comparison of the data with this model, the brightest emission spot of the tomogram is transformed into real space. Such a conversion is not in general possible, but can be performed if parameters and a velocity field are assumed, provided that the velocity–space mapping is one–one or many–one. That is true in this case if only emission from the first loop around the binary (in velocity space) is considered. A grid of points is constructed in velocity space defined by uniform steps in k_0 and t , and those

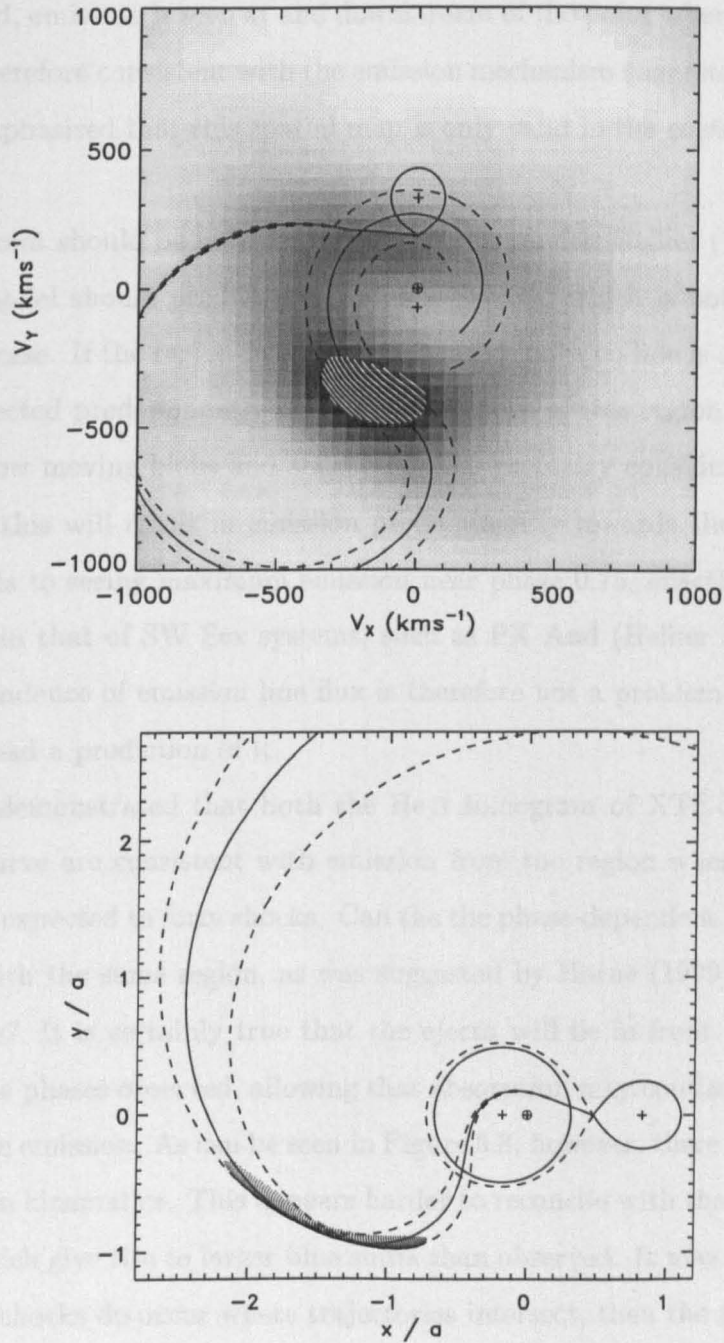


Figure 5.11: A magnetic propeller model for He II emission; see text for details of the model. The upper panel shows the tomogram with three model trajectories corresponding to different values of k_0 . The white shading indicates the region of strongest emission. In the lower panel, the same trajectories are shown in real space; units are the binary separation. The region of strongest emission in the tomogram maps to the shaded area, assuming the propeller velocity field. It is striking that this emission is coincident with the location where the stream trajectories intersect in real space.

for which the tomogram intensity is above a certain value are selected. These points are shown spatially in the lower panel of Figure 5.11. Subject to the assumptions made about the velocity field, emission is seen at and downstream of the point where trajectories cross. The data are therefore consistent with the emission mechanism suggested by Horne (1999). It should be emphasised that this spatial map is only valid in the context of the propeller model.

One other point should be noted in defence of this model. Hellier (1999) suggests that the propeller model should predict a continuous S-wave, which is not seen. This is not necessarily the case. If the region in which accelerated blobs collide is optically thick then emission is expected predominantly from the inner edge of this region where fast moving blobs impact slow moving blobs and shock. For the geometry considered, as can be seen in Figure 5.11, this will result in emission predominantly towards the top of the figure. This corresponds to seeing maximum emission near phase 0.75, exactly as is observed in these data and in that of SW Sex systems, such as PX And (Hellier & Robinson 1994). The phase dependence of emission line flux is therefore not a problem with the propeller model, but instead a prediction of it.

It has been demonstrated that both the He II tomogram of XTE J2123–058 and the line-flux light curve are consistent with emission from the region where material ejected by a propeller is expected to form shocks. Can the the phase-dependent Balmer absorption be associated with the same region, as was suggested by Horne (1999) in the context of SW Sex systems? It is certainly true that the ejecta will lie in front of the disc and/or companion at the phases observed, allowing that absorption may continue to occur further downstream than emission. As can be seen in Figure 5.8, however, there is also information on the absorption kinematics. This appears harder to reconcile with the ballistic velocities of the ejecta, which give rise to larger blue shifts than observed. It may be that this is not a problem, as if shocks do occur where trajectories intersect, then the motion of material downstream is likely to be sub-ballistic and some material may fall back towards the disc.

5.6.4 The Disc Re-impact Interpretation

The most popular alternative explanation for the SW Sex phenomenon is the accretion stream overflow and re-impact model. This was originally suggested by Shafter, Hessman & Zhang (1988). For a recent exposition, see Hellier (1999).

In the current form of this model the overflowing stream is divided into two regions.

The initial part of the stream produces transient absorption when seen against the brighter background of the disc. The later part, where the overflow re-impacts the disc, is seen in emission giving rise to the high velocity component. To reproduce observations, this model requires a number of refinements.

In its simplest form, the overflow stream should produce absorption at all phases; it always obscures some of the disc. This problem is overcome by invoking a strongly flared disc so that the overflow stream is only visible near phase 0.5. There are several limitations of the model in explaining the XTE J2123–058 data. Firstly, an absorption depth of 15 per cent of the continuum flux is seen. At this phase, at least 40 per cent of the continuum flux actually comes from the companion star, so absorption of 25 per cent of the disc light is required to achieve the observed depth, and hence at least 25 per cent of the disc has to be covered by the obscuring material. It is easy to visualise this in the context of the propeller model in which absorption is achieved with a broad fan of material outside of the binary: this could easily cover the whole disc without losing the phase dependence of the absorption. To produce transient deep absorption using material above the disc is harder. A further limitation is that it is unclear that an overflow stream above an X-ray binary disc, and hence subject to strong ultraviolet and X-ray irradiation, could survive without becoming sufficiently ionised that it could no longer produce strong $H\alpha$ absorption. In the propeller model, this absorption is produced in the less hostile region outside of the binary where significant recombination is more plausible.

The re-impact model requires that the strong emission in the lower-left quadrant be produced by overlap of weaker emission from the high-velocity component (the re-impact point) and the disc. To produce emission at the low velocities observed, however, requires the ‘disc’ component to be sub-Keplerian by a significant amount. A sub-Keplerian ring *may* be present in XTE J2123–058, but it is not clear that this is a real feature. There is no evidence for a high velocity component, but given the data quality, this is also inconclusive. The problem of apparently sub-Keplerian emission is not peculiar to XTE J2123–058, but common to the SW Sex CVs as well. A further difficulty is that in this model, the transient absorption is required to suppress bright spots in the trailed spectrogram predicted at phases 0.1 and 0.6. This absorption is not seen in He II, and indeed He II absorption is not expected without a very hot stellar atmosphere.

In conclusion, the overflow/re-impact model has a number of deficiencies when applied to XTE J2123–058; the propeller model appears to provide a better explanation

for the observed phenomena. The latter does itself have some difficulties, however, and both theoretical work, and higher quality observations are required to fully explain this phenomenon.

5.6.5 The Origin of XTE J2123–058

The question of the origin of XTE J2123–058 was raised in Section 5.1: is it intrinsically a halo object or was it kicked out of the Galactic plane? The strongest evidence is provided by the ratio of N III/C III to He II emission. This is absolutely typical of Galactic LMXBs and is inconsistent with known halo objects. In principal, the systemic velocity is also an important clue. For this object to have reached its present location it must have received a kick when the neutron star was formed, and hence it should now have a large peculiar velocity ($150\text{--}400\text{ km s}^{-1}$, Homan et al. 1999). The measured *radial component* of velocity is -87 km s^{-1} . Since this is a projection of the full velocity this is not inconsistent with the predictions of Homan et al. (1999), which could also be lowered if the source distance is less than the 10 kpc value assumed by those authors. Systemic velocities inferred from emission lines can be unreliable, however and a definitive measurement of the systemic velocity must await a study based on photospheric absorption lines of the companion star.

Chapter 6

XTE J2012+381

6.1 Introduction

The transient X-ray source XTE J2012+381 was discovered by the *RXTE* All Sky Monitor (ASM) on 1998 May 24 (Remillard, Levine & Wood 1998) rising from a level of 23 mCrab at first detection to a peak of 210 mCrab approximately 7 d later. Its ASM light curve is shown in Figure 6.1. *ASCA* observations (White et al. 1998) revealed the ultrasoft spectrum plus hard power-law tail signature of a black hole candidate, and from the absorption column-density due to neutral hydrogen ($N_{\text{H}} = (1.29 \pm 0.03) \times 10^{22} \text{ cm}^{-2}$) an interstellar extinction of $A_V \sim 7$ was estimated.

Based on the initial ASM position, a variable optical counterpart at around 15th magnitude was suggested (Wagner et al. 1998). This was not consistent with the subsequent *RXTE* Proportional Counter Array (PCA) position (Marshall & Strohmayer 1998) and the apparent variability was likely an artifact due to the extreme colour of this object ($V - R = 3.4$) and a mismatch of bandpasses between the observations compared (Garcia et al. 1998b). A radio counterpart was suggested by Hjellming, Rupen & Mioduszewski (1998a) and shown to be variable (and hence not a background radio galaxy) by Pooley (1998). It was found to be close to an 18th magnitude star (Castro-Tirado & Gorosabel 1998; Garcia et al. 1998a), identified in the USNO A1.0 catalogue by number 1275.13846761 (Monet et al. 1996; hereafter the USNO star). Spectroscopy of this star showed a nearly featureless spectrum with Balmer and Na D absorption, and no apparent emission lines; an extinction of $A_V = 2.3$ was estimated (Garcia et al. 1998a), in disagreement with that derived from absorption by neutral hydrogen. In view of this discrepancy,

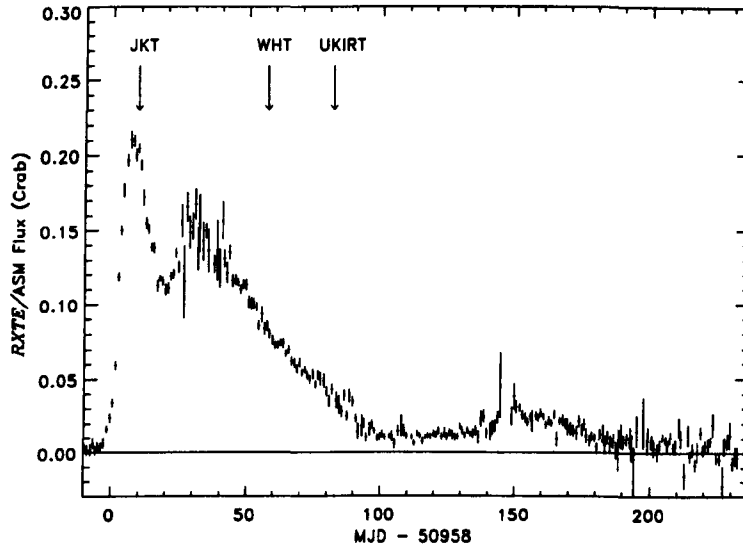


Figure 6.1: *RXTE*/ASM one-day average light curve based on quick-look results provided by the ASM/*RXTE* team. The zero point in time is chosen to coincide approximately with the first reported *RXTE* detection on MJD 50957.6. Times of JKT, WHT and UKIRT observations are marked. Note that the system has not returned to its quiescent level, and that a mini-outburst occurs around day 145.

and the absence of emission lines in the spectrum, the present author examined service observations obtained with the Jacobus Kapteyn Telescope (JKT) on La Palma closely. These showed the presence of a faint red companion star 1.1 arcsec away from the USNO star (Hynes, Roche & Walton 1998), and closely coincident with the revised position of the radio source (Hjellming, Rupen & Mioduszewski 1998b). Infrared images confirmed the presence of this second star (Callanan et al. 1998) which is now believed to be the true optical counterpart of XTE J2012+381 (Hynes et al. 1999).

In this chapter, these JKT observations are described together with optical spectroscopy and further infrared imaging. The identification of the faint red star with the X-ray source is examined and the nature of object is considered. This work has previously been published as Hynes, Roche & Walton (1998) and Hynes et al. (1999).

6.2 JKT Photometry

Multicolour photometry of the field of XTE J2012+381 was taken on 1998 June 3 through the JKT service programme and is described in Section 2.2. The timing of the observation

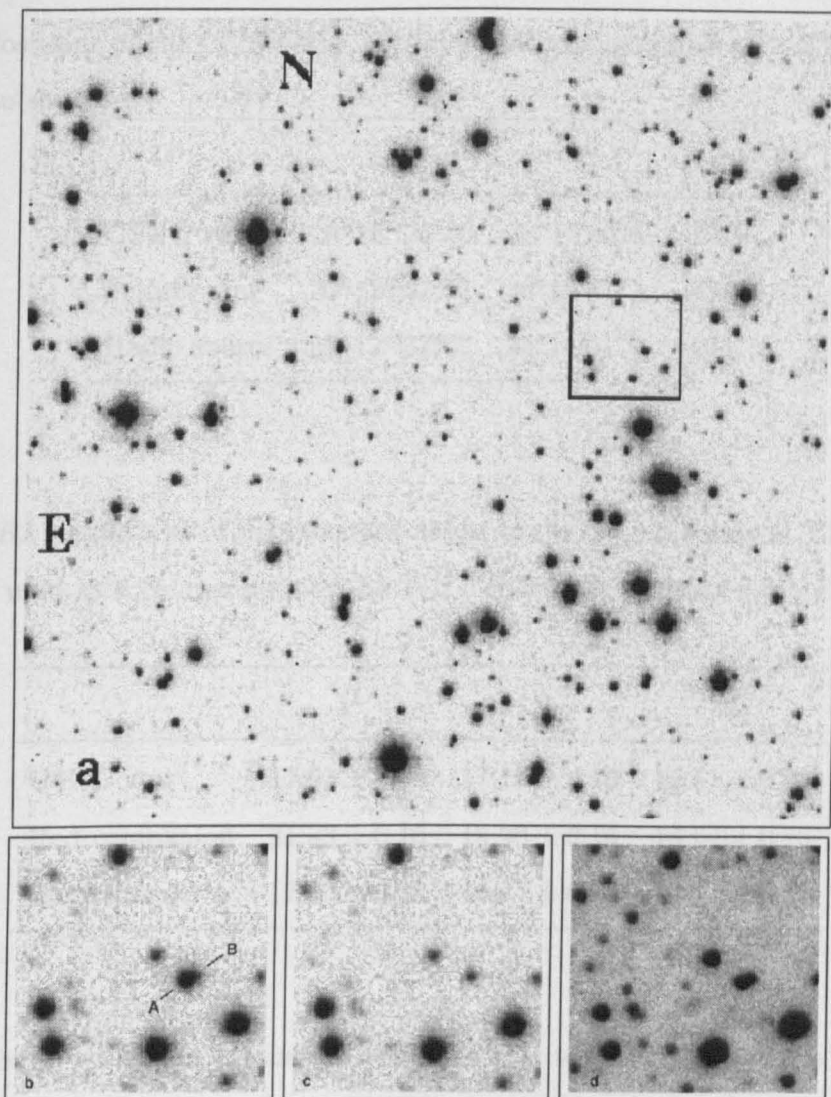


Figure 6.2: a) *V* band finding chart for XTE J2012+381 (4 arcmin square). The boxed area is blown up as b–d. b,c) Expanded *I* band JKT image before and after subtraction of the USNO star (A) from 1998 June 3. The fainter star (B) is just detectable before subtraction and clearly remains after. d) *K* band image from 1998 August 14.

is indicated in Figure 6.1.

The *V* band image of the field is shown in Figure 6.2a. As the field is crowded, the DAOPHOT task was used to deblend point spread functions as described in Section 2.2. *I* band images before and after subtraction of the PSF of the USNO star are shown in Figure 6.2b and 6.2c. A residual stellar image is clearly present after subtraction. Its offset relative to the USNO star was measured using *V*, *R* and *I* images; the results are consistent to 0.1 arcsec. Hence the position of the star was determined (Table 6.1). The position of the radio source (Hjellming, Rupen & Mioduszewski 1998b) is consistent with

Table 6.1: Positions of the USNO star, the faint red star identified with XTE J2012+381, and the radio source.

	α	δ	Error
USNO star	20 ^h 12 ^m 37 ^s .80	38°11′00″.6	0″.25
Fainter star	20 ^h 12 ^m 37 ^s .71	38°11′01″.1	0″.35
Radio source	20 ^h 12 ^m 37 ^s .67	38°11′01″.2	0″.4

Table 6.2: *VRI* magnitudes of the two stars closest to the radio position of XTE J2012+381 and the star used as a comparison for the WHT spectrum (Section 6.3.) JKT data from 1998 June 3.

	<i>V</i>	<i>R</i>	<i>I</i>
USNO star	17.91 ± 0.05	17.15 ± 0.05	16.51 ± 0.05
Red companion	21.33 ± 0.10	19.90 ± 0.15	18.64 ± 0.10
Comparison	17.69 ± 0.05	16.84 ± 0.05	16.12 ± 0.05

the fainter star to within uncertainties, but is difficult to reconcile with the USNO star.

The fainter star could only be distinguished in *V*, *R* and *I* band images and its magnitudes (Table 6.2) indicate that it is very red, with $V - R = 1.4 \pm 0.2$. The only quantitative estimate of the interstellar reddening comes from White et al. (1998) who estimate a column density $N_{\text{H}} = (1.29 \pm 0.03) \times 10^{22} \text{ cm}^{-2}$. Gas-to-dust scalings are at best approximate and different authors disagree significantly. Using the relations of Ryter, Cesarsky & Audouze (1975), Bohlin, Savage & Drake (1978) and Predehl & Schmitt (1995) implies $E(B - V) = 1.9, 2.2$ and 2.4 respectively, so this range is adopted as a reasonable estimate of reddening. Assuming the extinction curve of Cardelli, Clayton & Mathis (1989) then implies $1.4 < E(V - R) < 1.8$ and hence an intrinsic colour of $-0.6 < V - R < 0.2$.

6.3 WHT Spectroscopy

Both the USNO star and the fainter object were observed with the WHT on 1998 July 20, when the X-ray source had faded to approximately half its peak brightness. The observations are described in Section 2.6. The timing is indicated in Figure 6.1.

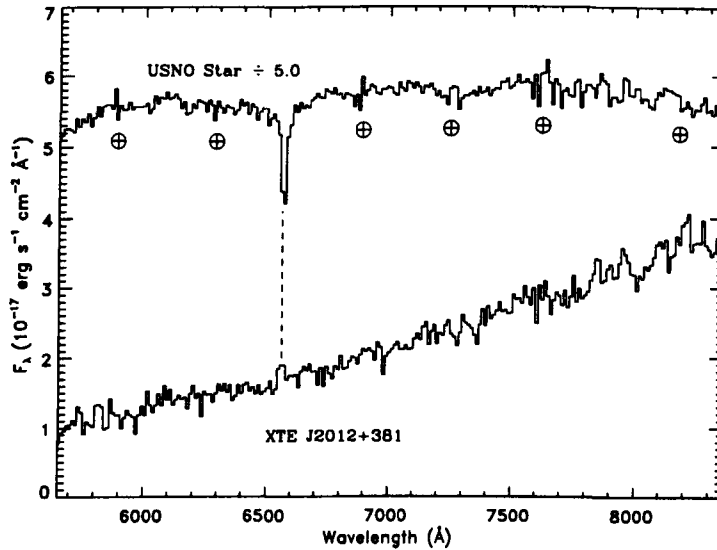


Figure 6.3: WHT spectra of the USNO star (spectral type F) and the faint red companion believed to be the optical counterpart of XTE J2012+381. Both have been binned $\times 4$ in wavelength for clarity. Atmospheric absorption features have been corrected for in both spectra. The approximate locations of the strongest features are marked \oplus to indicate where residuals from this correction may distort the spectrum. The only prominent line in either spectrum is $H\alpha$: absorption in the brighter star and weak emission in the companion.

The final calibrated spectra of both stars are shown in Figure 6.3, binned $\times 4$ in wavelength. As can be seen, the Telluric corrections are good, though slight distortion of the spectrum remains, e.g. near 7250 \AA . The only prominent non-atmospheric feature in either spectrum is $H\alpha$, in absorption in the USNO star (believed to be an early F-type star, Garcia et al. 1998a), with an equivalent width of $(6.5 \pm 0.3) \text{ \AA}$, and apparent weak emission in its red companion, equivalent width $(-6.6 \pm 1.5) \text{ \AA}$. The errors in equivalent width are statistical errors derived from the residuals of a low-order fit to the surrounding continuum. Assuming these errors are correct, the detection of $H\alpha$ is significant at the 3σ level.

The emission feature appears roughly square, with full width $40 \text{ \AA} \sim 1800 \text{ km s}^{-1}$. It is broader than the absorption in the USNO star ($\text{FWHM} \sim 10 \text{ \AA}$) and so does not look like a simple reflection of the absorption line due to an error in deblending (see Figure 6.4). It is also much wider than the night sky $H\alpha$ emission. The extraction process was also repeated without the correction to the profile wings (see Section 2.6 and Appendix B).

While this noticeably degrades the profile fit, it does not affect the $H\alpha$ emission feature.

As a final test, the derived spatial profile (including profile correction) was used to synthesise a new fake image in which the spectrum of the fainter star was left unchanged, but the $H\alpha$ line profile of the USNO star was used as a template to add artificial absorption lines (of the same strength and width) at 6100, 6425 and 6725 Å. The extraction process was then repeated on this fake image without allowing the profile correction to the line wings, i.e. using a model for the spatial profile which is known to be inadequate. This was done as a check that a combination of misfitting the spatial profile and a strong absorption line does not produce spurious emission. No emission features are seen in the spectrum of the fainter star at the position of the fake absorption lines. After subtraction of a low-order fit to the continuum, the total residual counts in 15 pixel (44 Å) bins centred on each of the line positions were measured. From the noise in the surrounding continuum, the error on the total counts from such a bin is estimated at 130 counts. At 6100, 6425 and 6725 Å respectively counts of 150, 76 and -180 were measured, a distribution (mean 14, rms 140) consistent with zero. For the bin centred on $H\alpha$, however, 550 counts are measured, significantly larger than the estimated error.

It is concluded that the $H\alpha$ emission is unlikely to be an artifact of the de-blending process but represents real emission from the faint star, detected with 3σ confidence.

6.4 UKIRT Photometry

UKIRT observations were obtained on 1998 August 14 and are described in Section 2.3. The timing is indicated in Figure 6.1.

The J and K magnitudes for the two stars are summarised in Table 6.3 together with the magnitude equivalent to the sum of their fluxes. Error estimates are derived from a combination of the consistency of standard measurements at different times (as an indicator of the reliability of the calibration) and statistical errors determined by DAOPHOT.

6.5 Has the Optical Counterpart Been Correctly Identified?

As discussed in Section 6.2, the positional coincidence of the faint red star with the radio counterpart is impressive, with a discrepancy of only 0.5 arcsec, which is consistent to within quoted uncertainties in the radio and USNO A1.0 coordinates. Given that

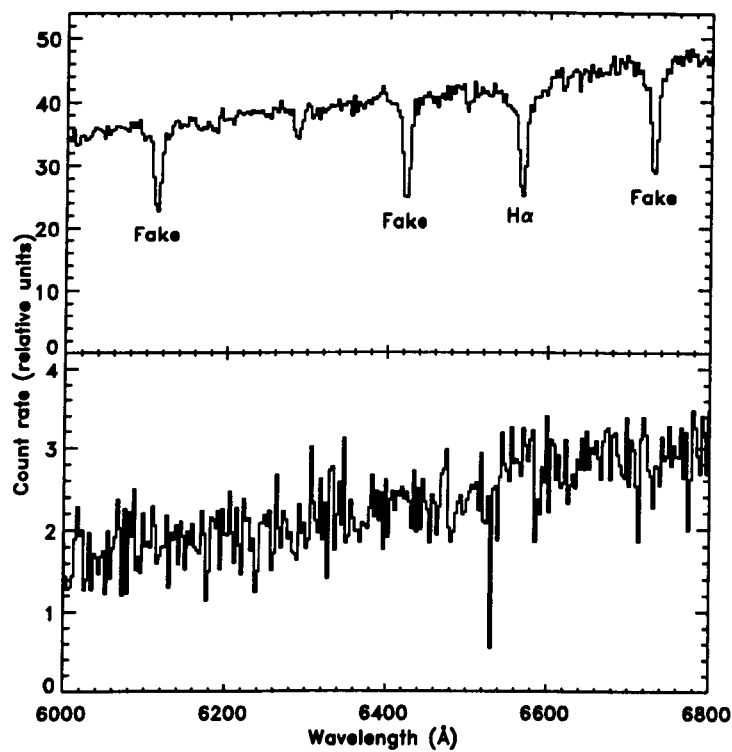


Figure 6.4: Extracted modified spectrum of the USNO star (above) and of the fainter star (below) near $H\alpha$. The true $H\alpha$ line in the USNO star spectrum is marked and also appears to be present (with a different profile) in the spectrum of the other object. Also marked are three fake absorption lines with the same strength and profile added to the two dimensional image before extraction. These do not have counterparts in the spectrum of the fainter star suggesting that the apparent emission in the latter is not an artifact due to crosstalk between the spectra during extraction.

Table 6.3: J and K magnitudes of the two stars closest to the radio position of XTE J2012+381. UKIRT data from 1998 August 14.

	J	K
USNO star	15.50 ± 0.03	15.00 ± 0.03
Red companion	17.26 ± 0.04	16.11 ± 0.04
Combined	15.30 ± 0.03	14.67 ± 0.03

this is a crowded field, however, it is appropriate to ask if other evidence supports this identification?

The intrinsic optical colour ($-0.6 < V - R < 0.2$) is certainly consistent with other SXTs; van Paradijs & McClintock (1995) find $(B - V)_0$ in the range approximately -0.4 to $+0.4$; $V - R$ colours are similar. The optical emission is likely dominated by a hot accretion disc. This colour would also be consistent with an early type star. Another characteristic of some, but not all SXTs is $H\alpha$ emission¹. This was very strong, for example, in V404 Cyg (Casares et al. 1991; Wagner et al. 1991), but weak in XTE J2123-058 (Section 5). As discussed in Section 6.3 this has probably been detected, but the evidence is inconclusive. The proposed optical counterpart certainly does not show $H\alpha$ absorption characteristic of an early type star.

A different approach is to test whether the optical counterpart had faded between the JKT and WHT observations. To do this, a model bandpass based on filter transmission, CCD response and the extinction curve for the same airmass as the JKT observations was formed. This was applied to the WHT spectra of the three stars on the slit to produce synthetic R band magnitudes for comparison with the photometry: $R = 17.23$ for the USNO star, $R = 20.23$ for the faint optical counterpart to the X-ray source and $R = 16.89$ for the isolated comparison star. The spectra do not quite cover the full R bandpass, but the loss is a very small amount at both short and long wavelengths. The effect of this, together with errors in the model bandpass, is estimated to introduce an uncertainty of no more than 0.05 magnitude when combined with the colour differences between the stars. The JKT and WHT observations of the USNO star and the slit comparison star are then approximately consistent, with perhaps a small systematic calibration error of less than 0.10 magnitudes. The much larger difference in the magnitudes for the proposed counterpart (0.33 magnitudes fainter at the second observation) then suggests that it has indeed faded optically between days 9 and 53.

The infrared counterpart also appears fainter than earlier in outburst. Callanan et al. (1998) estimated $J = 15.0 \pm 0.1$, $K = 14.3 \pm 0.1$ near the peak of outburst for the two blended stars. The comparable combined magnitudes from the later UKIRT observation are given in Table 6.3. These magnitudes are significantly different from those of Callanan et al. (1998). To produce this difference by fading of the fainter star would require a decline of 1.2 magnitudes in J and 1.0 magnitudes in K between days 9 and 82.

¹A more ubiquitous signature of an SXT spectrum would be $\text{He II } 4686 \text{ \AA}$ emission; this requires bluer observations than were practical for XTE J2012+381.

In summary, the optical counterpart to XTE J2012+381 does appear to have been correctly identified, having a typical colour for an SXT, showing possible weak $H\alpha$ emission and fading between observations. While none of these points is individually conclusive, in combination they strongly support the identification.

6.6 What is the Nature of XTE J2012+381?

The X-ray light curve of XTE J2012+381 (Figure 6.1) shows many similarities to those of other SXTs (Chen, Shrader & Livio 1997), but there are some important differences. The secondary maximum peaks around day 29, only 22 days after the first peak. This is earlier in the outburst than in most systems (45–75 days, Chen, Livio & Gehrels 1993), but is not unprecedented (Shahbaz, Charles & King 1998). The decline from secondary maximum is clearly linear. In the paradigm of King & Ritter (1998), this would imply that the disc is too large to be held in a high state by X-ray irradiation. A large disc would then imply a long orbital period. Such an interpretation is supported by observations of other SXTs (Shahbaz, Charles & King 1998), in which extended linear decays are only seen in long-period systems. A long orbital period in turn implies that XTE J2012+381 probably contains an evolved companion, similar to V404 Cyg. There are differences in the optical spectrum: for example, V404 Cyg showed very strong emission lines of hydrogen, helium and other species (Casares et al. 1991; Wagner et al. 1991), whereas XTE J2012+381 shows at most weak $H\alpha$ emission. This may not be significant; V404 Cyg was unusual in this respect, and most SXTs show little or no hydrogen emission during outburst. Another long period system, GRO J1655–40, has been seen in outburst both with $H\alpha$ emission (Bailyn et al. 1995a) and without (Section 4; Hynes et al. 1998b).

More puzzling is the apparent plateau in the X-ray brightness after day 95 at a level of ~ 12 mCrab. In this period, the flux is gradually rising and culminates in a mini-outburst around day 145, approximately 120 days after the secondary maximum. This is an intriguing timescale as both GRO J1655–40 (Harmon et al. 1995; Zhang et al. 1997) and GRO J0422+32 (Augusteijn, Kuulkers & Shaham 1993; Chevalier & Ilovaisky 1995) have also shown mini-outbursts separated by ~ 120 days. The lightcurves of these three systems are otherwise very different, and it is not clear that their mini-outbursts are caused by the same mechanism; see Chen, Shrader & Livio (1997) for a discussion of the models proposed for SXT rebrightenings.

Chapter 7

GRO J0422+32

7.1 Introduction

The hard X-ray transient GRO J0422+32 was discovered by *CGRO*/BATSE on 1992 August 5 (Paciesas et al. 1992) at a flux of 0.2 Crab. It rapidly rose to a level of 3 Crab, before beginning a gradual decline over subsequent months (Callanan et al. 1995). The BATSE light curve is shown in Figure 7.1. Extensive X-ray observations were carried out by the various satellites that were active at the time: *CGRO* (Callanan et al. 1995; van Dijk et al. 1995; Levinson & Mattox 1996; Grove et al. 1998a; Grove et al. 1998b; van der Hooft et al. 1999), *Granat* (Roques et al. 1994; Denis et al. 1994; Vikhlinin et al. 1995), *Mir-Kvant* (Sunyaev et al. 1993; Döbereiner et al. 1994) and *ROSAT* (Pietsch et al. 1993). Gamma ray emission was detected out to 600 keV by *CGRO*/OSSE (Grove et al. 1998a) and *Granat*/SIGMA (Roques et al. 1994) and above 1 MeV by *CGRO*/COMPTEL (van Dijk et al. 1995). The X-ray spectrum was very hard, being fitted by an exponentially-truncated power-law (Grove et al. 1998a), or Comptonised disc model (Sunyaev et al. 1993; Roques et al. 1994). There was no sign of the ultrasoft spectral component usually (but not always) seen in SXTs in outburst; instead the spectrum was similar to the black hole candidate Cyg X-1 in its *low state* (Sunyaev et al. 1993). The results of several X-ray timing analyses are summarised by van der Hooft et al. (1999). The power-density spectrum was observed to take a broken power-law form, flat below the break frequency (varying between 0.04–0.08 Hz) and decreasing above it. A low-frequency QPO was seen with frequency ranging from 0.03–0.31 Hz. Both the broken power-law and the low-frequency QPO are typical of black hole candidates in the low state (see Section

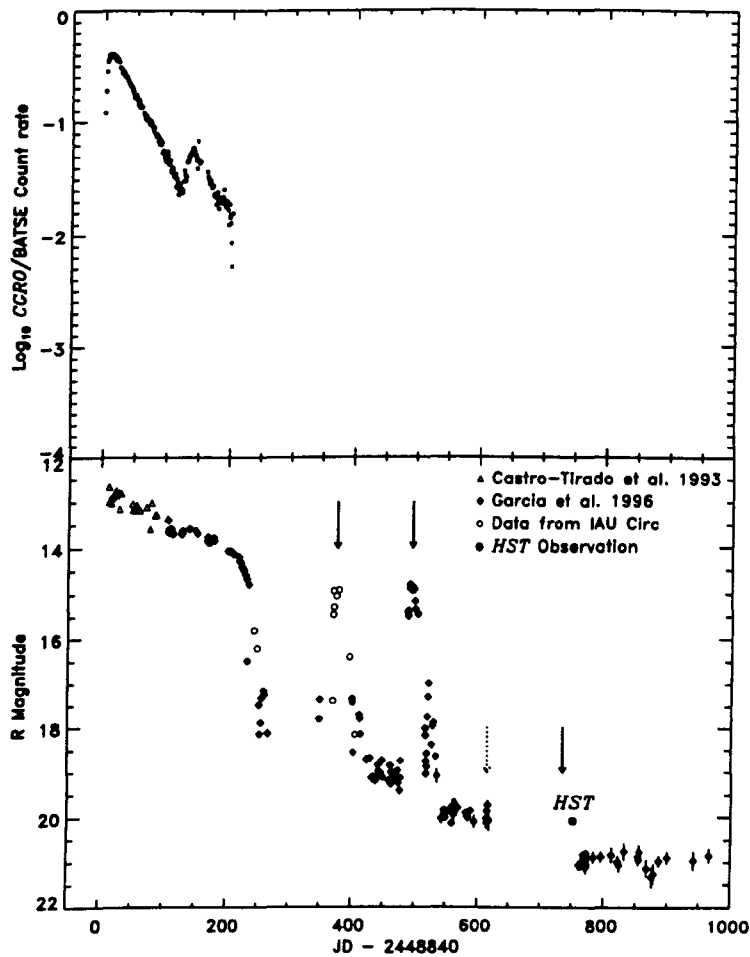


Figure 7.1: *CGRO*/BATSE (above) and *R* band (below) lightcurves of the outburst, adapted from Figure 1 of Garcia et al. (1996). Vertical arrows indicate observed or extrapolated times of mini-outburst. The *HST* measurement clearly lies significantly above the subsequent photometry, and is consistent with the expected time of a mini-outburst. Where no *CGRO*/BATSE data is shown, the source was undetected.

1.3.) The outburst thus appears to have been different to most SXTs in that the source remained in the low-state throughout. Intriguingly, it was also found that hard X-ray variability lagged soft by up to 1 s. If this lag is due to the finite time for hard X-rays to escape from a Comptonising corona via multiple scatterings, it implies this region is very extended.

The X-ray source was identified with a 13th magnitude optical nova (Castro-Tirado et al. 1993), which showed a similar decline to the X-ray source (see Figure 7.1.) There was also a lot of variability about the mean decay, with stochastic flashes on timescales of

tens of milliseconds (Bartolini et al. 1994) and random flickering on timescales up to days (Bartolini et al. 1994; Shrader et al. 1994; Chevalier & Ilovaisky 1995). In addition, Kato, Mineshige & Hirata (1995) found a modulation with a period of 5.18 hr, suggesting that it was a superhump modulation as seen in cataclysmic variables. This was supported by the discovery of a further period at 5.10 hr (Chevalier & Ilovaisky 1995; Kato, Mineshige & Hirata 1995), which is now known to be the orbital period.

The optical spectrum exhibited a blue continuum, becoming progressively redder as the outburst proceeded, evolving rapidly from $F_\nu \propto \nu^{+0.6}$ initially to $F_\nu \propto \nu^{-0.1}$ for most of the outburst (Shrader et al. 1994; King, Harrison & McNamara 1996). *IUE* observations showed a flatter, non-evolving continuum, with the same spectral index as the optical data late in outburst (Shrader et al. 1994). The optical spectrum showed strong Balmer and He II emission, with weaker lines of He I, C III, N III, O III and possibly C IV also present (Shrader et al. 1994; Callanan et al. 1995). He II 4686 Å was definitely double-peaked. Balmer lines were probably double too, although the blue component may have been at least partially associated with He II Pickering lines as is suspected for XTE J2123–058 (Section 5.6). The latter possibility is supported by the detection of the He II 5411 Å Pickering line. The Balmer lines were, in addition, situated in a very broad ($\pm 3000 \text{ km s}^{-1}$) absorption trough. These are probably absorption features of the rapidly rotating, optically thick inner disc. The same structure was clearly seen in H β in XTE J2123–058 (Section 5.6). The ultraviolet spectrum of GRO J0422+32 showed emission from N V, C IV, He II and possibly N IV and Si IV/O IV (Shrader et al. 1994).

Radio observations with the Very Large Array showed a slow power-law decay with significant superposed variability on timescales of days (Shrader et al. 1994). An initially flat spectrum became steeper later in the outburst. The combination of fading and steepening was interpreted as due to a self-absorbed synchrotron component that became smaller and more optically thick with time. A mid-infrared detection at $10.8 \mu\text{m}$ was also reported (van Paradijs et al. 1994) and interpreted as due to free-free emission from a strong X-ray driven wind.

The later stages of the outburst were characterised by several remarkable mini-outbursts, shown in Figure 7.1. Two were well studied, 1993 August (Castro-Tirado, Ortiz & Gallego 1997; Shrader et al. 1997) and 1993 December (Casares et al. 1995a). As discussed in Section 7.4, there may have been others after this. The mini-outburst recurrence time appears regular (i.e. main-outburst decay to first mini-outburst time equals first mini-outburst to

second mini-outburst time), about 120 d. The mini-outburst structure is also repeated with remarkable precision – examine Figure 2b of Chevalier & Ilovaisky (1995), or better compare the larger plots of Figure 3 of Castro-Tirado, Ortiz & Gallego (1997) for 1993 August with Figure 1 of Casares et al. (1995a). Both showed a ‘long’ outburst of ~ 40 d, followed by a deep dip, followed by a shorter, weaker outburst of ~ 15 d. Furthermore, *RXTE*/ASM data have revealed that this 120 d mini-outburst cycle continues in quiescence (Iyudin & Haberl 1997a; Iyudin & Haberl 1997b) with the same pattern of long outburst–dip–short outburst seen in X-rays (Iyudin 1999, priv. comm.) This behaviour has a parallel amongst CVs in the SU UMa type system EG Cnc (Patterson et al. 1998), which showed a similar series of mini-outbursts superposed on a gradual decline, albeit with a much shorter recurrence time of 7 d. The optical spectrum of GRO J0422+32 in mini-outburst appears to have been similar to that in outburst (Casares et al. 1995b; Shrader et al. 1997), though Castro-Tirado, Ortiz & Gallego (1997) found their 4400–7000 Å spectrum to be featureless. Casares et al. (1995a) performed Doppler tomography of He II 4686 Å, H α and H β . The interpretation of this was uncertain at the time as the system ephemeris was not known. In hindsight, it appears that the He II emission originates from the stream-impact point (Casares 1998, priv. comm.). The Balmer emission is more extended and appears to be a combination of disc emission in a ring, with a bright spot on the companion star. Several models have been put forward to explain the mini-outbursts, or echoes as they are sometimes called. Augusteijn, Kuulkers & Shaham (1993) suggest that an X-ray outburst heats the companion, triggering a burst of enhanced mass transfer. There is then a delay as this material diffuses in towards the compact object; when it arrives, there is another X-ray outburst, starting the cycle over again. Chen, Livio & Gehrels (1993) also propose a model based on X-ray heating of the companion star. Patterson et al. (1998) argue that the presence of apparently the same phenomenon in a CV indicates that the mini-outburst mechanism does not depend on strong heating of the companion. Instead they favour the pure disc instability model of Kuulkers, Howell & van Paradijs (1996) in which the cooling wave which shuts off the main outburst is reflected as a heating wave, triggering the subsequent mini-outburst. The observation of Casares et al. (1995a) of a bright stream impact point during mini-outburst does, however, favour an enhanced mass transfer model.

As part of the ongoing Target-of-Opportunity programme described in Section 1.8 GRO J0422+32 was observed with the *Hubble Space Telescope*. The ToO was triggered

to observe the 1993 August mini-outburst; the observations were delayed, however, and actually took place two years after the initial outburst. The system was nonetheless still active at this point, being two magnitudes above quiescence in the V band, and appears to have been in either an otherwise unreported mini-outburst, or an extended plateau or standstill. These results were published in Hynes & Haswell (1999).

7.1.1 System Parameters

There have been many studies of GRO J0422+32 in quiescence seeking to measure system parameters (Chevalier & Ilovaisky 1995; Orosz & Bailyn 1995; Casares et al. 1995b; Filippenko, Matheson & Ho 1995; Chevalier & Ilovaisky 1996; Beekman et al. 1997; Harlaftis et al. 1999; Webb et al. 1999). The orbital period is now known to be very short, 5.1 hr (Chevalier & Ilovaisky 1995) and the orbital inclination is thought to be low. The binary is commonly believed to consist of a black hole with a main sequence M-type companion.

Opinions differ on the exact companion spectral type. Most authors (Casares et al. 1995b; Filippenko, Matheson & Ho 1995; Harlaftis et al. 1999) favour M2. Chevalier & Ilovaisky (1995) argue that the presence of M2 features (TiO bands) in the spectrum is due to starspots and that the narrow lines in the spectrum instead favour an M0 classification. This explanation is plausible since an isolated M star with a 5.1 hr rotation period would be expected to be extremely magnetically active and have starspots. Webb et al. (1999), find that a better fit to the TiO features is obtained with an M4–M5 spectral type (their observations are still consistent with an M0 classification if these features actually originate from starspots, although this would require a very high proportion of the surface to be covered by the spots; Webb 1999, priv. comm.) It should also be noted that Martin et al. (1995) estimate a range of M0–M5 from the well known orbital period–mean density relation (Frank, King & Raine 1992), assuming a main sequence companion and 5.1 hr period. In hindsight, this logic can be reversed: spectroscopic classifications indicate that a range M0–M5 is indeed correct, so the orbital period implies that the companion is close to the main sequence. Realistically, the companion spectral type can be constrained to no better than M0V–M5V at present. For the remainder of this work, M2V will be assumed.

Similar uncertainties are present for the stellar masses. The mass function is now well determined ($f(M) = 1.13 \pm 0.09 M_{\odot}$, Harlaftis et al. 1999; $1.191 \pm 0.021 M_{\odot}$, Webb et al. 1999). Harlaftis et al. (1999) have measured the rotational broadening of the companion

star to be $v \sin i = 90_{-27}^{+22} \text{ km s}^{-1}$ which, combined with the radial velocity semi-amplitude of Webb et al. (1999), $K_C = 378.2 \pm 6.7 \text{ km s}^{-1}$, implies a mass ratio of $1/q = 9.02_{-2.68}^{+2.20}$ (or $q = 0.111_{-0.027}^{+0.033}$ in the more conventional terminology). This is consistent with the direct estimate of Filippenko, Matheson & Ho (1995) of $q = 0.1093 \pm 0.0086$ determined from the radial velocity semi-amplitude of the wings of $\text{H}\alpha$ emission¹. So far so good. Using these parameters implies a primary mass of $M_X = (1.47_{-0.06}^{+0.07}) \sin^{-3} i M_\odot$. The big uncertainty remaining is in the orbital inclination, which is essentially unknown, although likely low. The inferred masses are very sensitive to the inclination: for $i \sim 45^\circ$, $M_X \sim 4.2 M_\odot$, whereas for $i \sim 30^\circ$, $M_X \sim 11.8 M_\odot$. Most attempts to derive the inclination look for ellipsoidal modulations due to the changing aspect of the distorted companion. There are problems in applying this method to GRO J0422+32. Firstly because the inclination is quite low, the modulation will be of small amplitude. Secondly, GRO J0422+32 is faint in quiescence ($R \sim 21$). Thirdly, studies of other systems (e.g. Haswell 1996) show that the light curves often change from one epoch to another, indicating that the ellipsoidal modulation is contaminated by other sources of variability; possible mechanisms include variable tidal heating of a slowly precessing, eccentric accretion disc, variability at the stream impact hot spot and star spots on the companion. In GRO J0422+32, ellipsoidal studies have mainly been carried out in the I band, where disc contamination is expected to be small. Casares et al. (1995b) derived $i = 41^\circ \pm 6^\circ$ for $q = 0.1$, and claim a firm lower limit of $i = 30^\circ \pm 6^\circ$. Callanan et al. (1996) obtain $i < 45^\circ$ with 99 per cent confidence. Beekman et al. (1997) analyse existing and new R , R_C , I and HK light curves. The strongest constraint comes from I . Assuming the mass ratio to be around 0.1 as discussed above, this implies a 90 per cent confidence region of $10^\circ < i < 25^\circ$. Finally Webb et al. (1999) place an upper limit of $i < 30^\circ \pm 3^\circ$. None of the light curves presented is of sufficiently high quality to be confident that no distortions are present²; the best is probably the I band compilation of Beekman et al. (1997). Clearly the inclination, and hence the masses, remains uncertain. An upper limit of $i < 45^\circ$ seems acceptable, implying $M_X > 4.2 M_\odot$, but the more stringent constraints of Beekman et al. (1997); Webb et al. (1999) are persuasive, implying a higher mass still.

If the current understanding of companion stars of CVs and LMXBs is correct an upper

¹The authors do emphasise that the latter radial velocity curve does not have the correct phasing so may not reflect the motion of the compact object.

²Contrast the situation for GRO J1655–40: Orosz & Bailyn (1997) present beautiful BVR ellipsoidal light curves for this system.

limit can also be estimated for the mass. The spectral type of the companion is believed to be M0 or later. It can then conservatively be expected to have a mass of less than $0.7 M_{\odot}$ (Kolb & Baraffe 1999; Kolb 1999, priv. comm.) If a 3σ limit on the mass ratio, $1/q < 15.6$, is assumed then $M_X < 10.9 M_{\odot}$ is required. It is therefore likely that the compact object mass is in the range $4\text{--}11 M_{\odot}$ and the case for a black hole primary in GRO J0422+32 is strong.

7.1.2 Reddening and Distance

It is important to determine the interstellar reddening in order to study the *relative* spectral energy distribution – the shape of the spectrum. To study the *absolute* spectral energy distribution and luminosity, the distance to the source is also needed. Various measurements of interstellar reddening have been made, spanning a range of $E(B - V) = 0.2 - 0.4$. The distance has been estimated to be from 1–3 kpc.

Shrader et al. (1994) compare three methods. Based on the equivalent width of the 5780 Å interstellar feature they deduce $E(B - V) = 0.2 \pm 0.1$. Their fits of power-laws to the *optical* continuum using the Cardelli, Clayton & Mathis (1989) extinction law implies $E(B - V) = 0.23 \pm 0.02$. Finally good fits to the 2175 Å interstellar feature in *IUE* data³ with reddened power-laws (using the Seaton 1979 extinction curve) require $E(B - V) = 0.40 \pm 0.06$. Of these methods the first and last should be reliable. The second seems very dependent on the assumed intrinsic spectrum, but nevertheless does give sensible results. Callanan et al. (1995) measure equivalent widths of 1.2 ± 0.2 Å for the Na D lines and 0.5 ± 0.1 Å for the 5780/5788/5797 Å group. Using the relations of Barbon et al. (1990) and Herbig (1975) they deduce $E(B - V) = 0.3 \pm 0.1$. Harlaftis & Charles (1993) also study interstellar features and suggest $E(B - V) = 0.2$ based on 4428 Å and 6613 Å features. Chevalier & Ilovaisky (1995) adopt a different approach by examining 12 stars in the field surrounding GRO J0422+32 and find that their colour-colour diagram needs to be dereddened by $E(B - V) = 0.40 \pm 0.07$ in order to match the unreddened main sequence. This method assumes that all these stars, and GRO J0422+32, are subject to the same reddening; it would be appropriate if all are above the main plane of extinction. Shrader et al. (1997) fit absorbed power-laws to *ASCA* spectra from the 1993 August mini-outburst to obtain $N_H \simeq 1.6 \times 10^{21} \text{ cm}^{-2}$. Using the dust-to-gas scaling of Predehl & Schmitt (1995) this corresponds to $E(B - V) = 0.29$. Finally Castro-Tirado et al. (1993)

³Due to the low signal-to-noise ratio and uncertain background level of the G160L spectrum, an independent *HST* measurement of the 2175 Å feature is impossible.

also claim to find $E(B - V) = 0.3 \pm 0.1$ but do not state their method. Based on the spread in measured values $E(B - V) = 0.3 \pm 0.1$ is adopted for the remainder of this work. This is the same range as was chosen by Beekman et al. (1997) and Harlaftis et al. (1999).

Two approaches have been adopted to determine the distance of the system. One is to measure the strength of interstellar absorption features and assume a standard dependence on distance. Shrader et al. (1994) thus estimate a distance of 2.4 ± 0.4 kpc using the Na D lines. Callanan et al. (1995), using this method, estimate a distance of 1–2 kpc, but note that GRO J0422+32 is at a relatively high Galactic latitude and that beyond 1 kpc, the line of sight is largely out of the Galactic plane, so will not be strongly absorbed. They argue, therefore, that any method based on interstellar absorption lines can only provide a lower limit of 1 kpc. Other estimates all rely on assuming a spectral type, reddening and quiescent magnitude (with the disc contribution subtracted). Early attempts (Castro-Tirado et al. 1993; Shrader et al. 1994) are based on guesses about the quiescent magnitude and companion spectral type and can be discounted. Chevalier & Ilovaisky (1995) assume an M0V companion and $E(B - V) = 0.4$, to derive a distance 1.7 kpc. Webb et al. (1999) use their quiescent magnitude, spectral type estimate and reddening to derive $d = 1.39 \pm 0.15$ kpc. Neither of these estimates, however, takes adequate account of the uncertainty in spectral type. Webb et al. (1999) assume an absolute magnitude of $M_I = 9.86$ based on the M4V star GL 213 (Kirkpatrick et al. 1993). From the same source, an M2V star, GL 411, has $M_I = 8.32$, increasing the distance estimate to 2.8 kpc. In conclusion, the distance is almost certainly greater than 1 kpc, and probably less than 3 kpc. Where an estimate was needed, the value of 2.4 kpc favoured by Shrader et al. (1994) has been adopted, although this choice is somewhat arbitrary.

7.2 The Continuum Spectrum

The *HST*/PRISM/RD spectrum described in Section 3.4 gives broad-band, flux calibrated spectral coverage and is ideal for examining the spectral energy distribution. These data (together with the G160L spectrum in the far-UV) are shown in Figure 7.2. In order to compare the observed data with models for the accretion spectrum, however, it is necessary to correct first for interstellar reddening and then remove the contribution from the companion star. As can be seen in Figure 7.2, the latter is important only in the red.

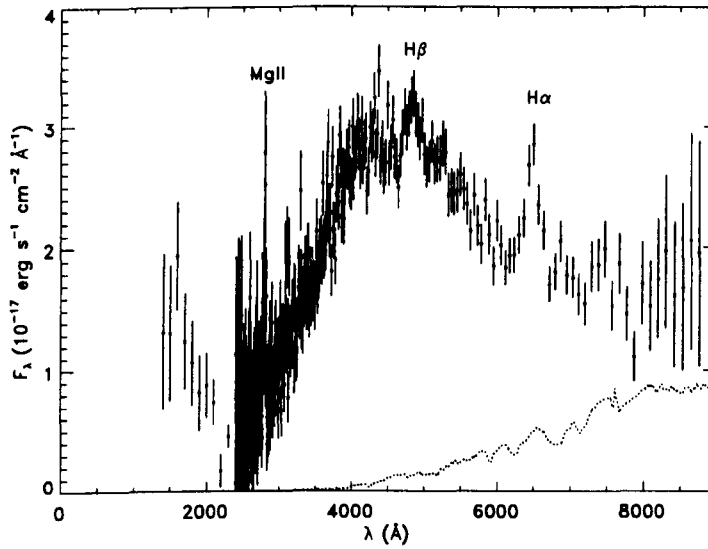


Figure 7.2: G160L and PRISM/RD spectra. The G160L spectrum has been averaged into 100 Å bins. Also shown dotted is an estimate of the spectrum of the companion star (see Section 7.2.2), reddened by $E(B - V) = 0.3$.

7.2.1 Interstellar Reddening

To correct spectra for interstellar reddening, the Galactic average extinction curve of Seaton (1979) is used assuming $E(B - V) = 0.3 \pm 0.1$ as discussed above. Since the only UV determination lies at the extreme end of the spread of estimates, however, it may be that the extinction curve actually diverges from the Galactic average giving an extra uncertainty in dereddened UV spectra.

7.2.2 The Companion Star Contribution

Since GRO J0422+32 was near quiescence when observed by *HST*, the spectrum of the companion star can be expected to be a significant fraction of the total at longer wavelengths. Unfortunately, the long wavelength resolution of the PRISM/RD spectrum is too low (e.g. ~ 330 Å at 7000 Å) to detect spectral features from the companion, so an independent analysis of veiling cannot be used to estimate how strong the contribution is. Instead it is necessary to adopt results from the literature.

Following the discussion in Section 7.1.1, the spectrum of the companion is represented by using the M2V star GL49 (Gunn & Stryker 1983) as a template. Casares et al. (1995b) give an *R* band (quiescent) magnitude of 20.96 ± 0.10 and estimate the fraction of the light

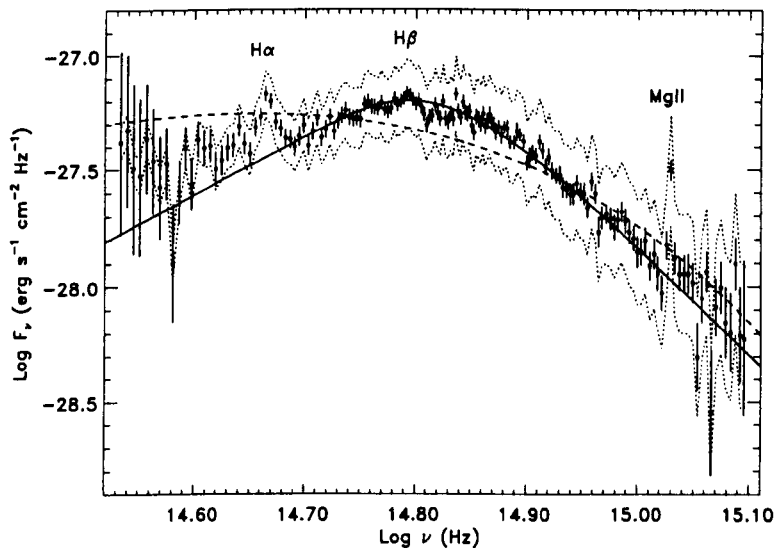


Figure 7.3: Dereddened *HST*/PRISM/RD spectrum with the companion contribution subtracted. Points with error bars correspond to the $E(B - V) = 0.3$ solution; the effect of instead assuming $E(B - V) = 0.2$ or 0.4 is indicated by dotted lines. The data below 4000 \AA ($\log \nu > 14.88$) have been averaged into 25 \AA bins for clarity. The large error bars at low frequencies are systematic and arise from assuming a ± 1 pixel uncertainty in the miscentering correction. The best fitting black body (dashed) and self-absorbed synchrotron (solid) spectra are overplotted.

due to the companion to be 52 ± 8 per cent in the $6700\text{--}7500 \text{ \AA}$ range. Their results are consistent with those of Filippenko, Matheson & Ho (1995) who estimate 40–70 per cent at 6300 \AA . The measurements of Casares et al. (1995b) imply an R band magnitude for the companion star alone of 21.68 ± 0.11^4 ; the spectrum of GL49 is normalised accordingly. The resulting spectrum, reddened by $E(B - V) = 0.3$, is shown in Figure 7.2.

As the PRISM/RD has a non-uniform dispersion, which is very low at the red end of the spectrum, some care is needed in subtracting the companion contribution. The best approach is to produce a simulated PRISM/RD spectrum of the expected companion spectrum. The method used was described in Section 4.7.3. This simulated companion spectrum can readily be subtracted from the observed PRISM/RD spectrum to obtain an estimate of the spectrum of the accretion flow shown in Figure 7.3.

Subsequent to the publication of this work (Hynes & Haswell 1999) the author became

⁴The ellipsoidal modulation is ~ 0.06 magnitudes and is neglected as it is smaller than the error in the derived average companion magnitude.

aware of two more recent studies. Harlaftis et al. (1999) reanalysed the Keck data of Filippenko, Matheson & Ho (1995) to derive a companion contribution of 61 ± 4 per cent at red wavelengths, which is just about consistent with the result of Casares et al. (1995b). Webb et al. (1999), however, not only find a smaller companion contribution of 38 ± 2 per cent in the range 6950–8400 Å, but comparing *I* band images of the system with those of Casares et al. (1995b) find that the system had faded by 0.22 magnitudes in *I* (much larger than the ellipsoidal modulation amplitude ~ 0.06 mag.) These results together imply a significantly fainter companion than determined by Casares et al. (1995b). Either one study was in error, the comparison was invalid (it is not explicitly stated that the same *I* filter was used for both observations) or the companion star itself is variable (not implausible, as it is probably highly active). The brightness of the companion *at the time of the HST observations* is therefore not well known and hence the red spectrum of the accretion flow is also uncertain.

7.2.3 The Far Ultraviolet Spectrum

The far-UV spectrum obtained with the G160L grating (Section 3.3) is something of a special case. Its interpretation is clearly problematic owing to the large background. Weak source emission does, however, appear to be present. This can be seen particularly clearly in Figure 3.2 where significant residual counts are present beyond pixel 1400, *after background subtraction*. As discussed in Section 3.3, there are uncertainties both in the shape and normalisation of the background. The source spectrum does, however, appear to be present for both background models considered and clearly exceeds any residual background in the unexposed regions. The far-UV source counts thus appear to be real. The calibrated spectrum, assuming this to be the case, is shown in Figure 7.2.

The deduced far-UV flux can usefully be compared with that measured for A 0620–00 and selected quiescent dwarf novae as tabulated by McClintock, Horne & Remillard (1995). These authors present 1650–1950 Å fluxes, dereddened and normalised to what would be seen at a distance of 1 kpc. For a range of extinctions $E(B - V) = 0.2 - 0.4$, the average flux from GRO J0422+32 over 1650–1950 Å is in the range $f_\lambda = (0.4 - 1.9) \times 10^{-16} \text{ erg s}^{-1} \text{ cm}^{-2} \text{ Å}^{-1}$. Normalised to a distance of 1 kpc (assuming a distance of 2.4 kpc), $f_\lambda = (3 - 11) \times 10^{-16} \text{ erg s}^{-1} \text{ cm}^{-2} \text{ Å}^{-1}$. Uncertainties both in the *shape* of the background spectrum and its normalisation will further increase this range and the results do not conclusively rule out zero flux in the far-UV. Comparing this with the far-UV flux

tabulation of McClintock, Horne & Remillard (1995), this measurement is comparable to observations of dwarf novae, but is ten times greater than in A 0620–00. This may be because GRO J0422+32 was not completely quiescent at the time of observation, but since the detection is marginal, the disagreement may not be significant. The deduced far-UV spectrum is strongly dependent on the exact form and level of background spectrum adopted. While the data suggest a sharp upturn in the UV, the reliability of this is far from certain (Figure 7.2).

7.2.4 Black Body Models

The simplest way to characterise the spectrum of the accretion flow is a black body fit. The best fitting black body spectrum (in the χ^2 sense) is shown by the dashed line in Figure 7.3. This has $T \sim 7600$ K and a reduced χ^2 of 3.6 after masking out emission lines. This is not a very good fit and allowing for a ± 0.1 uncertainty in $E(B - V)$ does not resolve this. The observed spectrum is sharper peaked than a black body and tends to a power-law form at short wavelengths. Adopting a temperature distribution in a disc instead of a single temperature black body can produce a power-law at short wavelengths, but will always produce a broader spectrum than a single temperature model.

7.2.5 Simple Non-thermal Models

A more promising explanation for the observed spectrum is that it is non-thermal in origin: self-absorbed synchrotron emission. Such a mechanism can readily produce a spectrum with a sharper peak than a black body and, as illustrated in Figure 7.3, can fit the spectrum rather well. The spectrum plotted is based on a free-fit of a synchrotron emitting slab model described in Section 4.4.3. The reduced χ^2 of the synchrotron fit was 1.35. The best-fit parameters were $l \sim 40$ km, $n_e \sim 10^{20} \text{ cm}^{-3}$, $p \sim 10$, $B \sim 20$ kG (assuming a distance of 2.4 kpc; Shrader et al. 1994). The electrons contributing to the observed spectrum have energies 40–80 MeV. This is clearly an oversimplistic model for the actual source of the emission and these parameters are unlikely to have great significance, but it does indicate that the observations can be interpreted as due to a self-absorbed synchrotron source. This fit is intended to demonstrate that even a very simple synchrotron emitting model can fit the accretion spectrum well. More realistic models of self-absorbed synchrotron emission in X-ray binaries invoke thermal electron distributions, but over the limited spectral range covered, a power-law model leads to a reasonable approximation to the expected spectrum.

There are two more sophisticated models that could lead to such a spectrum. The first is that the accretion disc extends inwards close to the compact object but has a magnetically dominated corona above it. Such a model was considered by di Matteo, Celotti & Fabian (1997) in the context of both active galactic nuclei and Galactic black hole candidates. In their model there are at any time a number of localised active coronal regions in which electrons are energised by magnetic reconnection (a possible mechanism for this is described by Haswell, Tajima & Sakai (1992)) and subsequently cool emitting cyclo-synchrotron radiation which becomes self-absorbed below some critical frequency. These models predict that for Solar mass black holes, the critical frequency, and hence the peak of the spectrum, should lie in the extreme UV, i.e. at higher frequencies than observed. These data were obtained when GRO J0422+32 was in a much lower state than was considered by di Matteo, Celotti & Fabian (1997), however, and this could move the peak to lower energies. An alternative set of models, which have seen much discussion recently, are the so called advective accretion flows described in Section 1.6. The models predict that the optical and UV accretion light should be dominated by self-absorbed synchrotron emission from this advective inner region. Since these data were obtained at a very low luminosity, shortly before GRO J0422+32 reached its quiescent state, such models are plausible and are considered further in Section 7.2.7..

7.2.6 Model Atmosphere Spectra

There are obviously more sophisticated models for the thermal spectrum of an accretion disc than black bodies and these should also be considered. Such model atmosphere spectra can be significantly different, but tend to differ in the form of edges or structure into the spectrum, in particular a Balmer jump in emission or absorption. A simple example is illustrated in Figure 7.4, in which are shown two Kurucz *stellar* model atmosphere spectra (Kurucz 1993), taken from the SYNPHOT database in IRAF/STSDAS. These were calculated for $T = 7500$ K (close to the best fitting black body), Solar abundances and $\log g = 0.5$ and 4.0 . These clearly provide a worse fit than a black body, as stars of this temperature show strong Balmer continuum absorption. Such a Balmer drop is clearly not present in the *HST* spectra.⁵

Of course an accretion disc atmosphere is not the same as that of a star. $\log g$ may fall

⁵It is true that a more rigorous approach would sum specific intensities over a temperature distribution in the disc, rather than using angle averaged fluxes appropriate for a whole star but this would not resolve the fundamental problem of a strong Balmer drop in spectra of the requisite temperature.

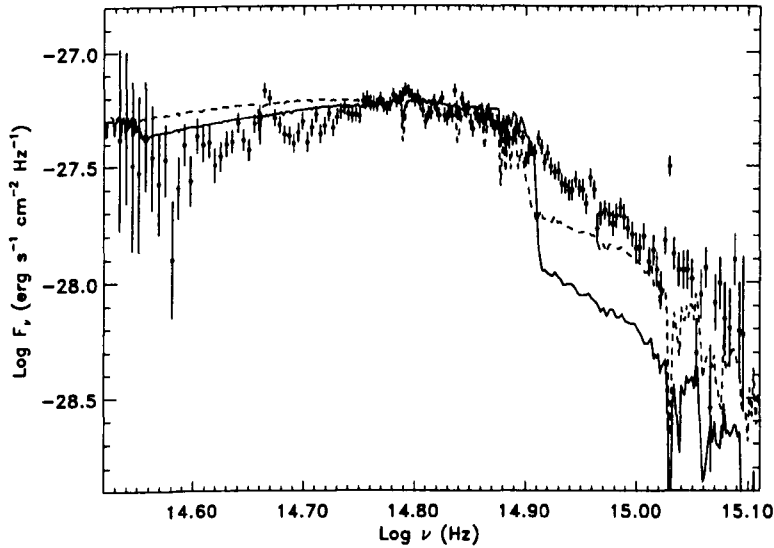


Figure 7.4: Comparison of PRISM/RD spectrum with Kurucz stellar atmosphere spectra. Both correspond to $T_{\text{eff}} = 7500$ K and Solar abundances. The solid line is for $\log g = 0.5$, the dashed line is $\log g = 4.0$. The normalisation is approximate and intended for illustrative purposes only.

outside the range considered by stellar models and the vertical temperature stratification will be different (and is essentially unknown). The reason the latter is complicated is that a star is (relatively) simple: energy is released at the centre and diffuses outwards. In an accretion disc, viscous energy may be released at all altitudes (including the atmosphere) or may be concentrated on the midplane; this is not known. Further, the disc may be heated by X-ray and ultraviolet photons from above, further increasing the uncertainty about the temperature stratification. Consequently, model atmosphere calculations for accretion discs are still in their infancy and typically consider only the simplest physical conditions. For example, Wade & Hubeny (1998) consider mid- and far-UV spectra of CVs, neglecting irradiation and winds. As GRO J0422+32 was observed at very low luminosity, the difficulty in treating X-ray irradiation is unlikely to be relevant and current models of CV spectra may be applicable. These models can broadly be divided into two categories: hot, optically thick disc models being applied to luminous CVs and cooler, optically thin discs appropriate to quiescent CVs. Since GRO J0422+32 was observed in an intermediate state, either might be applicable. Optically thick models (e.g. Wade & Hubeny 1998) are being applied in the ultraviolet and this author is not aware of published optical spectra

from similar models. It is likely, however, that they would suffer from the same problem as stellar models – a strong Balmer drop in absorption – as the models of Wade & Hubeny (1998) show an extremely strong Lyman drop in the far-UV. Simple optically thin models have been considered by Still, Horne & Hubeny (1998). Continuum emission is dominated, however, by the Balmer and Paschen edges in emission, which are no more consistent with the *HST* spectrum of GRO J0422+32 than optically thick models which predict Balmer absorption.

One could argue that the Balmer drop from an optically thick region could be filled in by optically thin Balmer continuum emission (which is expected to some extent, as Balmer emission lines are seen), but to produce an essentially smooth spectrum would then require very fine tuning of the two components. This cannot be completely ruled out, however. In view of the uncertainties in modelling accretion disc atmospheres, neither can the possibility that the combination of vertical stratification, gravity and optical thickness in the emission region conspire to avoid a Balmer edge in emission or absorption.

7.2.7 Advective Models

In Figure 7.5 is shown the results of a fit of a current generation advective model to the *HST* spectrum, kindly performed by Dr. Ann Esin. The model is that described by Narayan, Barret & McClintock (1997) and Esin, McClintock & Narayan (1997) with the addition of the electron energy equation from Quataert & Narayan (1999). Note that other than choosing a mass transfer rate, the absolute flux has not been arbitrarily scaled to fit the data (unlike the previous figures). Instead, monochromatic luminosities predicted by the model (for a given mass transfer rate) are converted to fluxes assuming a distance of 2.4 kpc as discussed in Section 7.1.2.

The model parameters assumed are a viscosity coefficient of $\alpha = 0.25$, a ratio of gas to total pressure of $\beta = 0.5$, mass transfer rate $\dot{M} = 1.7 \times 10^{-4} \dot{M}_{\text{Edd}}$ and an outer disc radius $R_{\text{out}} = 10^{4.9} R_{\text{Sch}}$. The transition from a thin disc to an advective flow occurs at $10^{4.5} R_{\text{Sch}}$. Two fits are performed for $M_X = 3 M_{\odot}$, and $M_X = 4 M_{\odot}$ to illustrate the dependence on compact object mass.

As can be seen, the fit to the ultraviolet spectrum is very good, at least to within the uncertainty in ultraviolet extinction. The absolute flux predicted is also in good agreement, in the sense that \dot{M} can be chosen to fit simultaneously the absolute flux and (at least approximately) the frequency at which the spectrum turns over. The model does

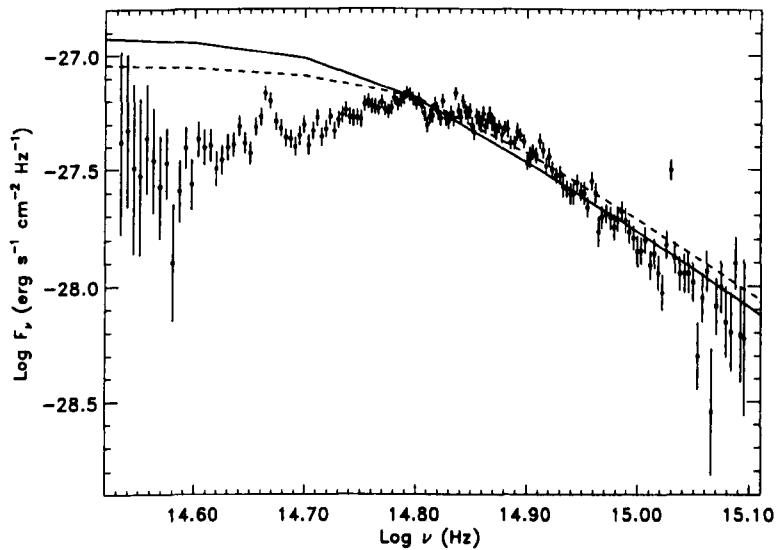


Figure 7.5: Comparison with PRISM/RD spectrum with advective model spectra. Solid line corresponds to $M_X = 4 M_\odot$; dashed line is $M_X = 3 M_\odot$. The other parameters are described in the text.

significantly overpredict flux at low frequencies. This cannot readily be explained by uncertainties in the data processing, as the two dominant sources of uncertainty in the red, miscentering of the target (see Section 3.4) and companion subtraction (see Section 7.2.2) are both only serious redwards of $H\alpha$, whereas the models diverge from the data at $\log \nu \sim 14.8$, or $\lambda \sim 4800 \text{ \AA}$. This is a weakness of the models (at least in their present form) although the self-absorbed synchrotron emission redwards of the peak is sensitive to the uncertain temperature distribution of the advective flow (Esin & Menou, 1998, priv. comm.) Possible outflows (Blandford & Begelman 1999) further increase these uncertainties. These model fits also favour low masses ($\lesssim 3 M_\odot$). Increasing the mass tends to move the synchrotron peak to the red; this could be compensated by increasing the mass transfer rate somewhat. Both effects would increase the luminosity, so to reconcile a larger mass with the data would require a larger distance than 2.4 kpc. If the distance is actually less than 2.4 kpc, as suggested by Webb et al. (1999) then the problem becomes worse.

7.3 Emission Lines

A number of emission lines were detected by *HST*. In the optical, there is unresolved $H\alpha$ and barely resolved $H\beta$ emission in the PRISM/RD spectrum. The only emission lines

Table 7.1: Dereddened fluxes and full width half maxima of detected emission lines. The detection of the Fe II blend is too marginal to reliably quantify. The measured width of H α is comparable to the width of the line spread function (LSF), so is not meaningful. The fit to H β was very poor.

	Line flux (erg s ⁻¹ cm ⁻²)	Line FWHM (Å)	LSF FWHM (Å)
Fe II (2586–2631)	–	–	–
Mg II (2796,2803))	$2.8 \pm 0.4 \times 10^{-15}$	18.5 ± 2.4	2
H β	$3.4 \pm 0.6 \times 10^{-15}$	240 ± 50	120
H α	$3.8 \pm 0.7 \times 10^{-15}$	(200 ± 30)	270

detected in the ultraviolet were Fe II (2586–2631 Å) and Mg II (2796,2803 Å), which are also seen to be prominent in A 0620–00 and Cen X-4 in quiescence (McClintock, Horne & Remillard 1995; McClintock & Remillard 1999). The deduced line parameters are given in Table 7.1. The Mg II line is well resolved by the G270H grating and has a FWHM (18.5 ± 2.4 Å) significantly larger than the separation of the two components. Neglecting the latter contribution to broadening, the FWHM in velocity space is 2000 ± 300 km s⁻¹, comparable to that observed in A 0620–00 (2500 ± 220 km s⁻¹, McClintock & Remillard 1999). Emission is detectable to velocities of ~ 1500 km s⁻¹ (i.e. FWZI ~ 3000 km s⁻¹.) This is similar to the quiescent H α and H β lines observed by Orosz & Bailyn (1995), for which this author estimates FWHM 1500 km s⁻¹ and 1800 km s⁻¹ respectively, with FWZI ~ 3000 km s⁻¹ in both cases.

Assuming the mass ratio of Webb et al. (1999), then at the circularisation radius in the disc one would expect $v_\phi \sin i \sim 660 M_X^{1/2} \sin i$ km s⁻¹. The observed velocities of the Mg II emission (and the quiescent H α emission) therefore suggest emission from a disc extending to, or somewhat inside, the circularisation radius.

7.4 Discussion

As the observations described here occurred so late in outburst, they can provide a very valuable illustration of the state of an SXT as it relaxes back to the quiescent state.

The *HST* observation is shown in the context of the *R* band outburst lightcurve in

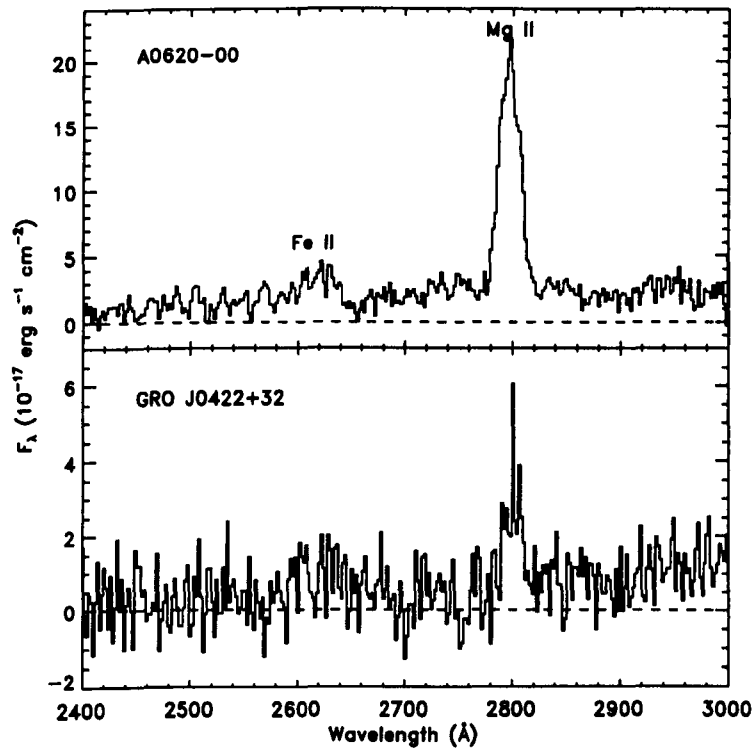


Figure 7.6: Near UV spectra of A 0620-00 (*HST*/STIS data from McClintock & Remillard 1999) and GRO J0422+32. The spectra are strikingly similar, both showing strong Mg II emission and weaker Fe II emission. A 0620-00 data kindly provided by Dr. Jeff McClintock.

Figure 7.1. Approximate magnitudes can be calculated from the PRISM/RD spectrum: $U = 20.75 \pm 0.04$, $B = 20.84 \pm 0.03$, $V = 20.42 \pm 0.04$, $R = 20.08 \pm 0.04$. On 1994 September 5, approximately 10 days after the *HST* observations, Zhao et al. (1994a) measured magnitudes of $V = 22.39 \pm 0.27$, $R = 21.06 \pm 0.10$. The system remained at this level and this is representative of its subsequent quiescent state ($V = 22.24 \pm 0.14$, $R = 20.97 \pm 0.10$, Casares et al. 1995b.) At the time of the observations described here, GRO J0422+32 was thus brighter by one magnitude in the R band and two magnitudes in V . This is a significant difference, both in flux and in colour, and it is very unlikely that the *HST* calibration could be this much in error; the error estimates above include statistical errors, the documented 3-4 per cent photometric accuracy of the FOS (Keyes 1997a) and allow for a miscentering uncertainty ± 1 pixel.

Clearly GRO J0422+32 was not completely quiescent at the time of the observations. Two possible interpretations of the (incomplete) lightcurve are suggested. The first is that

this was the final stage of a last, previously undetected, mini-outburst. If this is the case, then this mini-outburst occurred approximately 240 days after the last recorded one, consistent with the mini-outburst recurrence time of 120 days. An alternative interpretation, suggested by Dr. Ping Zhao is that after the last observations around day 600, when Zhao et al. (1994b) measured $R = 20.03 \pm 0.11$, $V = 20.67 \pm 0.22$, the system remained on a plateau, finally dropping to quiescence just after the *HST* observations. This is plausible, as both R and V band magnitudes around day 600 are similar to values deduced from the PRISM/RD spectrum. The mini-outburst interpretation is in a sense simpler, as it involves only the extrapolation of the previous outburst behaviour – uniformly separated mini-outbursts superposed on a uniform decline. Invoking a plateau, while not unprecedented in other systems (e.g. XTE J2012+381, Figure 6.1), would require a new kind of behaviour for GRO J0422+32.

At this time, GRO J0422+32 was obviously very close to quiescence, and this is seen in its spectrum; Balmer line and Mg II emission are both characteristic of *quiescent* SXTs, and Mg II was not seen in outburst either in GRO J0422+32 (Shrader et al. 1994) or in GRO J1655–40 (Section 3.5). This suggests that the state of the system is close to that in quiescence and supports the interpretation of the continuum spectrum as non-thermal emission from an advective accretion flow, with a somewhat higher \dot{M} than in quiescence. The existence of advective flows, even in fully quiescent SXTs, is by no means proven. A more traditional view of an SXT shortly before quiescence would be that a cooling wave has propagated a long way through the disc, so that the outer disc is cool and optically thin, the low state of the disc instability model, whilst the inner disc remains hot and optically thick. As noted in Section 7.2.6, this interpretation of the spectra is not ruled out, provided that Balmer continuum emission from the outer disc has exactly the right strength to fill in Balmer continuum absorption from the optically thick part of the disc. A final possibility is that a disc is present but that continuum emission originates as synchrotron emission from a corona above the disc, rather than from the disc surface. It should be noted that none of the models discussed can adequately account for the apparent far-UV upturn. It is therefore unfortunate that the reality of this effect cannot be conclusively proven as it would provide important constraints on the system structure at this time.

Discrimination between the possibilities discussed is not possible with this data set. The situation would be greatly improved by:

1. Higher spectral resolution (and signal-to-noise) in the red spectrum. This would permit direct measurement of the fraction of light from the companion, resulting in a more accurate red spectrum of the accretion flow.
2. Several epochs of data near quiescence. Then, spectral *evolution* studies would be possible. Advective models, for example, make definite predictions of how the brightness and peak frequency of the synchrotron peak should change as \dot{M} decreases.

Chapter 8

CONCLUSIONS

To a large extent, the original goals of this work were defined by the state of the literature when the *HST* target-of-opportunity (ToO) proposal was first written by Dr. Carole Haswell, and by the questions raised by the earlier observations of X-ray Nova Muscae 1991 under director's discretionary time (PI Panagia; Cheng et al. 1992). At that time the issue of advection had yet to be raised for SXTs and although X-ray irradiation had been considered (e.g. Tuchman, Mineshige & Wheeler 1990; Mineshige, Tuchman & Wheeler 1990), it was not treated as a dominant effect. Rather, the 'standard' disc instability model, as developed for CVs was applied and Cannizzo, Chen & Livio (1995), for example, briefly discuss irradiation, but assume that it does not affect the outburst evolution and, in particular, the propagation of heating and cooling fronts. Cheng et al. (1992) interpreted the *HST* optical/UV spectral energy distribution of X-ray Nova Muscae 1991 in terms of a viscously heated black-body disc spectrum with no correction for X-ray heating. A major concern of that study was to look for a signature of an inward propagating cooling wave in the evolution of the spectral energy distribution. This was expected to produce a turn down in the spectrum at long wavelengths (beyond the peak of the Planck spectrum of the coolest region inside the cooling front.) No such cooling wave signature was seen in X-ray Nova Muscae 1991, and a major theme of subsequent *HST* ToOs has been to search for this more carefully in other systems. To date, this improved test has not been possible; GRO J0422+32 was observed very late in outburst, and neither it, nor GRO J1655-40, showed the characteristic black body disc spectrum.

In hindsight, it is not at all clear that the cooling wave signature predicted is appro-

priate, as there has in the last decade been an increasing appreciation of the importance of X-ray irradiation in outbursting SXTs. The viscously heated black body disc spectrum used by Cheng et al. (1992) is not applicable to a strongly irradiated disc. Further, King & Ritter (1998) have examined the outburst evolution expected in the presence of strong X-ray heating and in their model, the cooling wave cannot propagate at all for most of the outburst, although this picture has not gone unchallenged (see Wheeler 1999 and Cannizzo 1999 for a recent discussion.) This thesis has found evidence for X-ray irradiation in GRO J1655–40 (Chapter 4) and XTE J2123–058 (Chapter 5) reinforcing the importance of the effect. The strongest case is presented by the echo-mapping experiment performed by *HST* and *RXTE* which revealed clear evidence for X-ray reprocessing in the disc of GRO J1655–40. The presence of several Bowen fluorescence lines of O III and N III in this system also indicates significant EUV irradiation of the emission regions. If the decaying warp model of Esin, Lasota & Hynes (1999) for the X-ray vs. optical anti-correlation is correct then substantial heating of the companion star is also required, as suggested by other authors (see discussion in Section 4.8.) The continuum (and possibly N III/C III) lightcurves in XTE J2123–058 also indicate strong companion star heating, and the extremely blue spectral energy distribution and the presence of high excitation emission lines (e.g. C IV) in this system reveal high temperatures and excitation levels probably energised by X-ray heating and photoionisation. While no direct evidence of heating is available for XTE J2012+381 (Chapter 6), the pronouncedly linear decay of its X-ray outburst is consistent with the model of King & Ritter (1998) for an X-ray heated disc in a long period system.

Another effect not considered by earlier studies such as Cannizzo, Chen & Livio (1995) is the possibility of advection dominated accretion flows. If these represent the correct model for a quiescent SXT, then any interpretation of the outburst rise and late decline must take advection into account. Hameury et al. (1997), for example, present a model for the rise of the 1996 outburst of GRO J1655–40 in which the presence of an advective flow modifies the disc instability model and dictates the rise behaviour. The observations of GRO J0422+32 late in outburst described in Chapter 7 appear to support some kind of non-thermally emitting accretion flow. There are some discrepancies when compared with current spectral predictions of advective flows, but other predictions of the models are borne out by the data (for example the spectral slope in the near-UV and the wavelength of peak emission for a given luminosity.) The comparison is, however, on uncertain ground

until it is clear what difference, if any, will be made by allowing for the positive Bernoulli constant of the advective accretion flows and possible consequent outflows (Blandford & Begelman 1999). The possible detection of P Cygni profiles in GRO J1655–40 (Chapter 4) indicates outflows likely do occur when the systems are luminous. Their significance in low-luminosity states remains an open question.

The parallels between the behaviour of He II and Balmer lines seen in XTE J2123–058 and the SW Sex phenomenon are an unexpected development (Chapter 5). These likely indicate that the accretion stream overflows the disc. The author's preferred interpretation, in terms of a magnetic propeller, requires that this overflow stream is then ejected from the system. It may be that this effect is relatively minor, albeit very visible, and does not modify the outburst evolution. It may be that a *disc-anchored* propeller is required to explain this behaviour, since the compact object is a rapidly rotating neutron star. If this is the case then there could be important consequences for the outburst evolution; ejection by a disc anchored propeller will remove significant angular momentum from the disc (Wynn & King 1999, priv. comm.) which is likely to influence outburst evolution.

In conclusion, the interpretation of SXT outbursts now appears more complex than it did when this project was conceived. Strong X-ray irradiation of disc and companion star, significant energy advection in the inner accretion flow at low luminosities, outflows and removal of angular momentum by a magnetic propeller could all influence the outburst evolution. Further, and more comprehensive, observations of SXTs in outburst will be required to untangle the multiplicity of contributing factors.

REFERENCES

- Augusteijn T., Kuulkers E., Shaham J., 1993, *A&A*, 279, L13
- Augusteijn T., van der Hooft F., de Jong J. A., van Kerkwijk M. H., van Paradijs J., 1998, *A&A*, 332, 561
- Bahcall S., Lynn B. W., Selipsky S. B., 1990, *ApJ*, 362, 251
- Bailyn C. D., Orosz J. A., Girard T. M., Joglee S., Valle M. Della, Begam M. C., Fruchter A. S., Gonzalez R., Ianna P. A., Layden A. C., Martins D. H., Smith M., 1995a, *Nat*, 374, 701
- Bailyn C. D., Orosz J. A., McClintock J. E., Remillard R. A., 1995b, *Nat*, 378, 157
- Barbon R., Benetti S., Rosino L., Capellaro E., Turatto M., 1990, *A&A*, 237, 79
- Bartolini C., Guarnieri A., Piccioni A., Beskin G. M., Neizvestny S. I., 1994, *ApJS*, 92, 455
- Beekman G., Shahbaz T., Naylor T., Charles P. A., Wagner R. M., Martini P., 1997, *MNRAS*, 290, 303
- Belloni T., Méndez M., van der Klis M., Hasinger G., Lewin W. H. G., van Paradijs J., 1996, *ApJ*, 472, L107
- Bianchini A., Valle M. Della, Masetti N., Margoni R., 1997, *A&A*, 321, 477
- Blandford R. D., Begelman M. C., 1999, *MNRAS*, 303, L1
- Blandford R. D., Payne D. G., 1982, *MNRAS*, 199, 883
- Blandford R. D., Znajek R. L., 1977, *MNRAS*, 179, 433
- Bohlin R. C., Savage B. D., Drake J. F., 1978, *ApJ*, 224, 132
- Borozdin K. N., Alexandrovich N. L., Arefeiv V. A., Gilfanov M. R., Revnivtsev M., Sunyaev R. A., Trudolyubov S. P., 1997, in Matsuoka M., Kawai N., eds, *All-Sky X-Ray Observations in the Next Decade*, Riken, p. 49
- Burstein D., Heiles C., 1982, *AJ*, 87, 1165
- Callanan P., McCarthy J., Garcia M., McClintock J., 1998, *IAU Circ*, 6933
- Callanan P. J., Garcia M. R., McClintock J. E., Zhao P., Remillard R. A., Bailyn C. D., Orosz J. A., Harmon A. B., Paciesas W. S., 1995, *ApJ*, 441, 786
- Callanan P. J., Garcia M. R., McClintock J. E., Zhao P., Remillard R. A., Haberl F., 1996, *ApJ*, 461, 351
- Cannizzo J. K., 1999, in Mineshige S., Wheeler J. C., eds, *Disk Instabilities in Close Binary Systems*, Universal Academy Press, p. 177

- Cannizzo J. K., Chen W., Livio M., 1995, *ApJ*, 454, 880
- Cardelli J. A., Clayton G. C., Mathis J. S., 1989, *ApJ*, 345, 245
- Carter D., Benn C. R., Rutten R. G. M., Breare J. M., Rudd P. J., King D. L., Clegg R. E. S., Dhillon V. S., Arribas S., Rasilla J. -L., Garcia A., Jenkins C. R., Charles P. A., 1993, *William Herschel Telescope: ISIS User's Manual*, ING
- Casali M. M., Hawarden T. G., 1992, *JCMT-UKIRT Newsletter*, 3, 33
- Casares J., Charles P. A., Jones D. H. P., Rutten R. G. M., Callanan P. J., 1991, *MNRAS*, 250, 712
- Casares J., Marsh T. R., Charles P. A., Martin A. C., Martín E. L., Harlaftis E. T., Pavlenko E. P., Wagner R. M., 1995a, *MNRAS*, 274, 565
- Casares J., Martin A. C., Charles P. A., Martín E. L., Rebolo R., Harlaftis E. T., Castro-Tirado A. J., 1995b, *MNRAS*, 276, L35
- Casares J., Serra-Ricart M., Zurita C., Gomez A., Alcade D., Charles P., 1998, *IAU Circ*, 6971
- Castro-Tirado A., Gorosabel J., 1998, *IAU Circ*, 6931
- Castro-Tirado A. J., Ortiz J. L., Gallego J., 1997, *A&A*, 322, 507
- Castro-Tirado A. J., Pavlenko E. P., Shlyapnikov A. A., Brandt S., Lund N., Ortiz J. L., 1993, *A&A*, 276, L37
- Charles P. A., 1998, in Abramowicz M. A., Bjornsson G., Pringle J. E., eds, *Theory of Black Hole Accretion Disks*, Cambridge University Press, p. 1
- Chen W., Livio M., Gehrels N., 1993, *ApJ*, 408, L5
- Chen W., Shrader C. R., Livio M., 1997, *ApJ*, 491, 312
- Cheng F. H., Horne K., Panagia N., Shrader C. R., Gilmozzi R., Paresce F., Lund N., 1992, *ApJ*, 397, 664
- Chevalier C., Ilovaisky S. A., 1995, *A&A*, 297, 103
- Chevalier C., Ilovaisky S. A., 1996, *A&A*, 312, 105
- Christensen J. A., Welsh W. F., Evans I. N., Reinhart M., Hayes J. J., 1997, *Timing of the FOS in RAPID Mode – “Too Rapid RAPID”*, CAL/FOS ISR 150, STScI
- Clayton G. C., Hanson M. M., 1993, *AJ*, 105, 1880
- Crampton D., Stauffer J., Hutchings J. B., Cowley A. P., Ianna P., 1986, *ApJ*, 306, 599
- Crary D. J., Kouveliotou C., van Paradijs J., van der Hooft F., van der Klis M., Rubin B. C., Scott D. M., Finger M. H., Harmon B. A., 1996, *ApJ*, 463, L79
- Cui W., Zhang S. N., Chen W., 1998, *ApJ*, 492, L53

- Czerny B., Czerny M., Grindlay J. E., 1986, *ApJ*, 311, 241
- Davis L. E., 1994, *A Reference Guide to the IRAF/DAOPHOT Package*, NOAO
- de Jong J. A., van Paradijs J., Augusteijn T., 1996, *A&A*, 314, 484
- Deguchi S., 1985, *ApJ*, 291, 492
- Denis M., Olive J. -F., Mandrou P., Roques J. P., Ballet J., Goldwurm A., Laurent Ph., Cordier B., Vikhlinin A., Churazov E., Gilfanov M., Sunyaev R., Dyachkov A., Khavenson N., Kremnev R., Kovtunenkov V., 1994, *ApJS*, 92, 459
- di Matteo T., Celotti A., Fabian A. C., 1997, *MNRAS*, 291, 805
- Döbereiner S., Maisack M., Englhauser J., Pietsch W., Reppin C., Trümper J., Kendziorra E., Kretschmar P., Kunz M., Staubert R., Efremov V., Kaniovsky A., Kusnetzov A., Sunyaev R., 1994, *A&A*, 287, 105
- Dubus G., Lasota J. -P., Hameury J. -M., Charles P., 1999, *MNRAS*, 303, 139
- Ebisawa K., Ogawa M., Aoki T., Dotani T., Takizawa M., Tanaka Y., Yoshida K., Miyamoto S., Iga S., Hayashida K., Kitamoto S., Terada K., 1994, *PASJ*, 46, 375
- Edelson R. A., Krolik J. H., 1988, *ApJ*, 333, 646
- Eggleton P. P., 1983, *ApJ*, 268, 368
- Elvis M., Page C. G., Pounds K. A., Ricketts M. J., Turner M. J. L., 1975, *Nat*, 257, 656
- Eracleous M., Horne K., 1996, *ApJ*, 471, 427
- Eracleous M., Horne K., Robinson E. L., Zhang E. H., Marsh T. R., Wood J. H., 1994, *ApJ*, 433, 313
- Esin A. A., Lasota J. P., Hynes R. I., 1999, *A&A*, submitted
- Esin A. A., McClintock J. E., Narayan R., 1997, *ApJ*, 489, 865
- Fender R. P., Pooley G. G., Brocksopp C., Newell S. J., 1997, *MNRAS*, 290, L65
- Filippenko A. V., 1982, *PASP*, 94, 715
- Filippenko A. V., Leonard D. C., Matheson T., Li W., Moran E. C., Reiss A. G., 1999, *PASP*, 111, 969
- Filippenko A. V., Matheson T., Ho L. C., 1995, *ApJ*, 455, 614
- Frank J., King A. R., Raine D. J., 1992, *Accretion Power in Astrophysics*, 2nd edition, Cambridge University Press
- Friedman J. L., Ipser J. R., 1987, *ApJ*, 314, 594
- Friedman J. L., Parker L., Ipser J. R., 1986, *ApJ*, 304, 115
- Garcia M. R., Callanan P. J., McClintock J. E., Zhao P., 1996, *ApJ*, 460, 932
- Garcia M. R., McClintock J. E., Barton E., Callanan P., 1998a, *IAU Circ*, 6931

- Garcia M. R., McClintock J. E., Berlind P., Barton E., Callanan P., 1998b, IAU Circ, 6922
- Gaskell C. M., Peterson B. M., 1987, ApJS, 65, 1
- Gliozzi M., Bodo G., Ghisellini G., Scaltriti F., Trussoni E., 1998, A&A, 337, L39
- Gray D. F., 1992, The Observation and Analysis of Stellar Photospheres, 2nd edition, Cambridge University Press
- Greiner J., 1996, A&AS, 120, 239
- Greiner J., Predehl P., Pohl M., 1995, A&A, 297, L67
- Grove J. E., Johnson W. N., Kroeger R. A., McNaron-Brown K., Skibo J. G., Philips B. F., 1998a, ApJ, 500, 899
- Grove J. E., Strickman M. S., Matz S. M., Hua X. -M., Kazanas D., Titarchuk L., 1998b, ApJ, 502, 45
- Gunn J. E., Stryker L. L., 1983, ApJS, 52, 121
- Hameury J.-M., Lasota J.-P., McClintock J. E., Narayan R., 1997, ApJ, 489, 234
- Hamuy M., Suntzeff N. B., Heathcote S. R., Walker A. R., Gigoux P., Phillips M. M., 1994, PASP, 106, 566
- Harlaftis E., Collier S., Horne K., Filippenko A. V., 1999, A&A, 341, 491
- Harlaftis E. T., Charles P. A., 1993, IAU Circ, 5728
- Harmon B. A., Wilson C. A., Zhang S. N., Paciesas W. S., Fishman G. J., Hjellming R. M., Rupen M. P., Scott D. M., Briggs M. S., Rubin B. C., 1995, Nat, 374, 703
- Haswell C. A., 1996, in E. P. J. van den Heuvel J. van Paradijs, ed, Compact Stars in Binaries, IAU Symp. 165, Kluwer, p. 351
- Haswell C. A., Tajima T., Sakai J. -I., 1992, ApJ, 401, 495
- Hayes J. E., Lindler D. J., 1996, The FOS Dark Count-rate, CAL/FOS ISR 146, STScI
- Hellier C., 1999, in Charles P. A., King A. R., O'Donoghue D., eds, The Warner Symposium on Cataclysmic Variables, New Astronomy Reviews
- Hellier C., Robinson E. L., 1994, ApJ, 431, L107
- Herbig G. H., 1975, ApJ, 196, 129
- Herbig G. H., 1995, ARA&A, 33, 19
- Hjellming R. M., Han X., 1995, in Lewin W. H. G., van Paradijs J., van den Heuvel E. P. J., eds, X-Ray Binaries, Cambridge University Press, p. 308
- Hjellming R. M., Rupen M. P., 1995, Nat, 375, 464
- Hjellming R. M., Rupen M. P., 1996, IAU Circ, 6411

- Hjellming R. M., Rupen M. P., Mioduszewski A. J., 1998a, IAU Circ, 6924
- Hjellming R. M., Rupen M. P., Mioduszewski A. J., 1998b, IAU Circ, 6932
- Homan J., Méndez M., Wijnands R., van der Klis M., van Paradijs J., 1999, ApJ, 513, 119
- Homan J., van der Klis M., van Paradijs J., Mendez M., 1998, IAU Circ, 6971
- Honeycutt R. K., Schlegel E. M., Kaitchuck R. H., 1986, ApJ, 302, 388
- Horne K., 1986, PASP, 98, 609
- Horne K., 1994, in Gondhalekar P. M., Horne K., Peterson B. M., eds, Reverberation Mapping of the Broad-line Region in Active Galactic Nuclei, ASP, p. 23
- Horne K., 1999, in Hellier C., Mukai K., eds, Annapolis Workshop on Magnetic Cateclismic Variables, ASP, p. 349
- Horne K., Eracleous M., 1993, A Rough Photometric Calibration for FOS, BLUE, G160L, ORDER0, CAL/FOS ISR 091, STScI
- Horne K., Harlaftis E. T., Baptista R., Hellier C., Allan A., Johnston H., Patterson J., Kemp J., Haswell C., Chen W., 1996, IAU Circ, 6406
- Hunstead R., Campbell-Wilson D., 1996, IAU Circ, 6410
- Hunstead R., Wu K., Campbell-Wilson D., 1997, in Wickramasinghe D. T., Bicknell G. V., Ferrario L., eds, Accretion Phenomena and Related Outflows, IAU Coll. 163, ASP, p. 63
- Hynes R. I., 1998, New Astronomy Reviews, 42, 605
- Hynes R. I., Charles P. A., Haswell C. A., Casares J., Serra-Ricart M., Zurita C., 1998a, IAU Circ, 6976
- Hynes R. I. et al. , 1999, MNRAS, in preparation
- Hynes R. I., Haswell C. A., 1999, MNRAS, 303, 101
- Hynes R. I., Haswell C. A., Shrader C. R., Chen W., Horne K., Harlaftis E. T., O'Brien K., Hellier C., Fender R. P., 1998b, MNRAS, 300, 64
- Hynes R. I., O'Brien K., Horne K., Chen W., Haswell C. A., 1998c, MNRAS, 299, L37
- Hynes R. I., Roche P., Charles P. A., Coe M. J., 1999, MNRAS, 305, L49
- Hynes R. I., Roche P., Walton N., 1998, IAU Circ, 6927
- Illarionov A. F., Sunyaev R. A., 1975, A&A, 39, 185
- Ilovaisky S. A., Chevalier C., 1998, IAU Circ, 6975
- Inoue H., Nagase F., Ishida M., Sonobe T., Ueda Y., 1994, IAU Circ, 6063
- Inoue H., Nagase F., Ueda Y., 1995, IAU Circ, 6210

- Iyudin A., Haberl F., 1997a, IAU Circ, 6605
- Iyudin A., Haberl F., 1997b, IAU Circ, 6738
- Jahoda K., Swank J. H., Giles A. B., Stark M. J., Strohmayer T., Zhang W., Morgan E. H., 1996, in Siegmund O. H., Gummin M. A., eds, EUV, X-Ray, and Gamma-Ray Instrumentation for Astronomy VII, Proc. SPIE Vol. 2808, p. 59
- Jenkins C. R., Unger S. W., 1991, The Night-sky Spectrum from La Palma, La Palma Technical Note 82, RGO
- Kahabka P., van den Heuvel E. P. J., 1997, ARA&A, 35, 69
- Kato T., Mineshige S., Hirata R., 1995, PASJ, 47, 31
- Keyes C. D., 1997a, in Casertano S. et al. , eds, Proc. 1997 *HST* Calibration Workshop, STScI, p. 420
- Keyes C. D., ed, 1997b, *HST* Data Handbook Vol. II, STScI
- Keyes C. D., Koratker A. P., Dahlem M., Hayes J., Christensen J., Martin S., 1995, Faint Object Spectrograph Instrument Handbook, STScI
- King A. R., Kolb U., 1997, ApJ, 481, 918
- King A. R., Kolb U., Burderi L., 1996, ApJ, 464, L127
- King A. R., Kolb U., Szuszkiewicz E., 1997, ApJ, 488, 89
- King A. R., Ritter H., 1998, MNRAS, 293, L42
- King D. L., 1985, Atmospheric Extinction at the Roque de Los Muchachos Observatory, La Palma, La Palma Technical Note 31, RGO
- King I. R., 1971, PASP, 83, 199
- King N. L., Harrison T. E., McNamara B. J., 1996, AJ, 111, 1675
- Kinney A. L., Bohlin R. C., 1993, Background Due to Scattered Light, CAL/FOS ISR 103, STScI
- Kirkpatrick J. D., Kelly D. M., Rieke G. H., Liebert J., Allard F., Wehrse R., 1993, ApJ, 402, 643
- Kolb U., 1996, in Evans A., Wood J. H., eds, Cataclysmic Variables and Related Objects, IAU Coll. 158, Kluwer, p. 433
- Kolb U., 1998, MNRAS, 297, 419
- Kolb U., Baraffe I., 1999, in Charles P. A., King A. R., O'Donoghue D., eds, The Warner Symposium on Cataclysmic Variables, New Astronomy Reviews
- Kolb U., King A. R., Ritter H., Frank J., 1997, ApJ, 485, L33
- Kopal Z., 1959, Close Binary Systems, Chapman and Hall

- Krelowski J., Maszkowski R., Strobel A., 1986, *A&A*, 166, 271
- Krelowski J., Papaj J., 1993, *PASP*, 105, 1209
- Krelowski J., Walker G. A. H., Grieve G. R., Hill G. M., 1987, *ApJ*, 316, 449
- Kroeger R. A., Strickman M. S., Grove J. E., Kaaret P., Ford E., Harmon B. A., McConnell M., 1996, *A&AS*, 120, 117
- Kurucz R. L., 1993, Kurucz CD-ROM No. 13, ATLAS9 Stellar Atmosphere Programs and 2 km/s Grid
- Kuulkers E., 1998, *New Astronomy Reviews*, 42, 1
- Kuulkers E., Howell S. B., van Paradijs J., 1996, *ApJ*, 462, L87
- Kuulkers E., Wijnands R., Belloni T., Mendez M., van der Klis M., van Paradijs J., 1998, *ApJ*, 494, 753
- Lampton M., Margon B., Bowyer S., 1976, *ApJ*, 208, 177
- Landolt A. U., 1992, *AJ*, 104, 340
- Leggett S. K., 1999, *IRCAM/TUFTI Manual*, JAC
(<http://www.jach.hawaii.edu/UKIRT.new/instruments/ircam/ircam3.html>)
- Levine A., Swank J., Smith E., 1998, *IAU Circ*, 6955
- Levinson A., Mattox J. R., 1996, *ApJ*, 462, L67
- Lewin W. H. G., van Paradijs J., Taam R. E., 1993, *Space Sci. Rev.*, 62, 223
- Lewin W. H. G., van Paradijs J., van den Heuvel E. P. J., eds, 1995, *X-Ray Binaries*, Cambridge University Press
- Longair M. S., 1994, *High Energy Astrophysics*, Vol. 1, 2nd edition, Cambridge University Press
- Marsh T. R., 1989, *PASP*, 101, 1032
- Marsh T. R., Horne K., 1988, *MNRAS*, 235, 269
- Marsh T. R., Horne K., 1990, *ApJ*, 349, 593
- Marsh T. R., Robinson E. L., Wood J. H., 1994, *MNRAS*, 266, 137
- Marshall F. E., Strohmayer T., 1998, *IAU Circ*, 6922
- Martin A. C., Charles P. A., Wagner R. M., Casares J., Henden A. A., Pavlenko E. P., 1995, *MNRAS*, 274, 559
- Mason K. O., Murdin P. G., Tuohy I. R., Seitzer P., Branduardi-Raymont G., 1982, *MNRAS*, 200, 793
- Massey P., 1997, *A User's Guide to CCD Reductions with IRAF*, NOAO
- Massey P., Davis L. E., 1992, *A User's Guide to Stellar CCD Photometry with IRAF*,

NOAO

- Massey P., Valdes F., Barnes J., 1992, A User's Guide to Reducing Slit Spectra with IRAF, NOAO
- McClintock J. E., Horne K., Remillard R. A., 1995, ApJ, 442, 358
- McClintock J. E., Remillard R. A., 1999, ApJ, submitted
- Méndez M., Belloni T., van der Klis M., 1998, ApJ, 499, L187
- Menou K., Esin A. A., Narayan R., Garcia M. R., Lasota J. -P., McClintock J. E., 1999, ApJ, 520, 276
- Meyer F., 1999, in Mineshige S., Wheeler J. C., eds, Disk Instabilities in Close Binary Systems, Universal Academy Press, p. 209
- Miller J. C., Shahbaz T., Nolan L. A., 1998, MNRAS, 294, L25
- Mineshige S., 1994, ApJ, 431, L99
- Mineshige S., Tuchman Y., Wheeler J. C., 1990, ApJ, 359, 176
- Mirabel I. F., Dhawan V., Chaty S., Rodríguez L. F., Marti J., Robinson C. R., Swank J., Geballe T. R., 1998, A&A, 330, L9
- Mirabel I. F., Rodríguez L. F., 1994, Nat, 371, 46
- Monet D. et al. , 1996, USNO-A1.0. A Catalog of Astrometric Standards, Technical Report, USNO
- Motch C., Ilovaisky S. A., Chevalier C., Angebault P., 1985, Space Sci. Rev., 40, 219
- Motch C., Pakull M. W., 1989, A&A, 214, L1
- Munari U., Zwitter T., 1997, A&A, 318, 269
- Murray N., Chiang J., 1996, Nat, 382, 789
- Nagase F., Inoue H., Kotani T., Ueda Y., 1994, IAU Circ, 6094
- Narayan R., Barret D., McClintock J. E., 1997, ApJ, 482, 448
- Narayan R., Garcia M. R., McClintock J. E., 1997, ApJ, 478, L79
- Narayan R., McClintock J. E., Yi I., 1996, ApJ, 457, 821
- Narayan R., Yi I., 1995, ApJ, 452, 710
- Neckel Th., Klare G., Sarcander M., 1980, A&AS, 42, 251
- Nowak M. A., Lehr D. E., 1998, in Abramowicz M. A., Bjornsson G., Pringle J. E., eds, Theory of Black Hole Accretion Disks, Cambridge University Press, p. 233
- O'Brien K. et al. , 1999, MNRAS, in preparation
- Oke J. B., 1990, AJ, 99, 1621
- Orosz J. A., Bailyn C. D., 1995, ApJ, 446, L59

- Orosz J. A., Bailyn C. D., 1997, *ApJ*, 477, 876
- Orosz J. A., Kuulkers E., 1999, *MNRAS*, 305, 132
- Orosz J. A., Remillard R. A., Bailyn C. D., McClintock J. E., 1997, *ApJ*, 478, L83
- Paciesas W. S., Briggs M. S., Harmon B. A., Wilson R. B., Finger M. H., 1992, *IAU Circ*, 5580
- Patterson J., 1999, in Mineshige S., Wheeler J. C., eds, *Disk Instabilities in Close Binary Systems*, Universal Academy Press, p. 61
- Patterson J., Kemp J., Skillman D. R., Harvey D. A., Shafter A. W., Vanmunster T., Jensen L., Fried R., Kiyota S., Thorstensen J. R., Taylor C. J., 1998, *PASP*, 110, 1290
- Patterson J., Raymond J. C., 1985, *ApJ*, 292, 550
- Phillips S. N., Shahbaz T., Podsiadlowski Ph., 1999, *MNRAS*, 304, 839
- Pietsch W., Haberl F., Gehrels N., Petre R., 1993, *A&A*, 273, L11
- Pooley G. G., 1998, *IAU Circ*, 6926
- Predehl P., Schmitt J. H. M. M., 1995, *A&A*, 293, 889
- Press W. H., Teukolsky S. A., Vetterling W. T., Flannery B. P., 1992, *Numerical Recipes in C: The Art of Scientific Computing*, 2nd edition, Cambridge University Press
- Quataert E., Gruzinov A., 1999, *ApJ*, 520, 248
- Quataert E., Narayan R., 1999, *ApJ*, 516, 399
- Regös E., Tout C., Wickramasinghe D., 1998, *ApJ*, 509, 362
- Remillard R., Bradt H., Cui W., Levine A., Morgan E., Shirey B., Smith D., 1996, *IAU Circ*, 6393
- Remillard R., Levine A., Wood A., 1998, *IAU Circ*, 6920
- Remillard R. A., Morgan E. H., McClintock J. E., Bailyn C. D., Orosz J. A., 1999, *ApJ*, 522, 397
- Rhoades C. E., Ruffini R., 1974, *Phys. Rev. Lett.*, 32, 324
- Richards M. T., Albright G. E., 1999, *ApJS*, 123, 537
- Roques J. P., Bouchet L., Jourdain E., Mandrou P., Goldwurm A., Ballet J., Claret A., Lebrun F., Finoguenov A., Churazov E., Gilfanov M., Sunyaev R., Novikov B., Chulkov I., Kuleshova N., Tserenin I., 1994, *ApJS*, 92, 451
- Ryter C., Cesarsky C. J., Audouze J., 1975, *ApJ*, 198, 103
- Sams B. J., Eckart A., Sunyaev R., 1996, *Nat*, 382, 47
- Scaltriti F., Bodo G., Ghisellini G., Gliozzi M., Trussoni E., 1997, *A&A*, 325, L29
- Schachter J., Filippenko A. V., Kahn S. M., 1989, *ApJ*, 340, 1049

- Schlegel D. J., Finkbeiner D. P., Davis M., 1998, *ApJ*, 500, 525
- Seaton M. J., 1979, *MNRAS*, 187, 73P
- Shafter A. W., Hessman F. V., Zhang E. -H., 1988, *ApJ*, 327, 248
- Shahbaz T., Bandyopadhyay R. M., Charles P. A., 1999, *A&A*, 346, 82
- Shahbaz T., Charles P. A., King A. R., 1998, *MNRAS*, 301, 382
- Shahbaz T., van der Hooft F., Casares J., Charles P. A., van Paradijs J., 1999, *MNRAS*, 306, 89
- Shahbaz T., van der Hooft F., Charles P. A., Casares J., van Paradijs J., 1996, *MNRAS*, 282, L47
- Shakura N. I., Sunyaev R. A., 1973, *A&A*, 24, 337
- Shimura T., Takahara F., 1995, *ApJ*, 445, 780
- Shlosman I., Vitello P., 1993, *ApJ*, 409, 372
- Shrader C. R., Wagner R. M., Charles P. A., Harlaftis E. T., Naylor T., 1997, *ApJ*, 487, 858
- Shrader C. R., Wagner R. M., Hjellming R. M., Han X. H., Starrfield S. G., 1994, *ApJ*, 434, 698
- Shrader C. R., Wagner R. M., Hjellming R. M., Starrfield S. G., 1996, *A&AS*, 120, 261
- Sinclair J. E., 1992, Maps of Standard Arc-lamps for the WHT ISIS, La Palma Technical Note 84, RGO
- Sinclair J. E., 1995, More Maps of Wavelength Calibration Lamps for the WHT ISIS, La Palma Technical Note 98, RGO
- Smith D. A., Dhillon V. S., 1998, *MNRAS*, 301, 767
- Sobczak G. J., McClintock J. E., Remillard R. A., Bailyn C. D., Orosz J. A., 1999, *ApJ*, 520, 776
- Soria R., Wickramasinghe D. T., Hunstead R. W., Wu K., 1998, *ApJ*, 495, L95
- Soria R., Wu K., Galloway D., 1999, *MNRAS*, 309, 528
- Spruit H. C., 1998, *astro-ph/9806141*
- Stathakis R. A., Johnston H. M., 1997, The RGO Spectrograph Manual, AAO
- Stetson P. B., 1987, *PASP*, 99, 191
- Still M. D., Horne K., Hubeny I., 1998, in Holt S. S., Kallman T. R., eds, *Accretion Processes in Astrophysical Systems: Some Like it Hot!*, American Institute of Physics, p. 133
- Stone R. P. S., 1977, *ApJ*, 218, 767

- Sunyaev R. A., Kaniovsky A. S., Borozdin K. N., Efremov V. V., Aref'ev V. A., Melioransky A. S., Skinner G. K., Pan H. C., Kendziorra E., Maisack M., Döbereiner S., Pietsch W., 1993, *A&A*, 280, L1
- Symon K. R., 1960, *Mechanics*, 2nd edition, Addison-Wesley
- Takeshima T., Strohmayer T. E., 1998, *IAU Circ*, 6958
- Tanaka Y., Lewin W. H. G., 1995, in Lewin W. H. G., van Paradijs J., van den Heuvel E. P. J., eds, *X-Ray Binaries*, Cambridge University Press, p. 126
- Tanaka Y., Shibazaki N., 1996, *ARA&A*, 34, 607
- Telting J., 1999, *Observers Guide to the JKT and JAG-CCD Camera*, ING
- Thorsett S. E., Chakrabarty D., 1999, *ApJ*, 512, 288
- Thorstensen J. R., Charles P. A., 1982, *ApJ*, 253, 756
- Thorstensen J. R., Ringwald F. A., Wade R. A., Schmidt G. D., Norsworthy J. E., 1991, *ApJ*, 102, 272
- Tingay S. J. et al. , 1995, *Nat*, 374, 141
- Tomsick J. A., Halpern J. P., Kemp J., Kaaret P., 1999a, *ApJ*, 521, 341
- Tomsick J. A., Halpern J. P., Leighly K. M., Perlman E., 1998a, *IAU Circ*, 6957
- Tomsick J. A., Kaaret P., Kroeger R. A., Remillard R. A., 1999b, *ApJ*, 512, 892
- Tomsick J. A., Kemp J., Halpern J. P., Hurley-Keller D., 1998b, *IAU Circ*, 6972
- Tuchman Y., Mineshige S., Wheeler J. C., 1990, *ApJ*, 359, 164
- Ueda Y., Inoue H., Tanaka Y., Ebisawa K., Nagase F., Kotani T., Gehrels N., 1998, *ApJ*, 492, 782
- Urry M., Reichert G., 1988, *NASA IUE Newsletter*, 34, 96
- van der Hooft F., Groot P. J., Shahbaz T., Augusteijn T., Casares J., Dieters S., Greenhill J., Hill K., Scheers L. H. A., Naber R. M., de Jong J. A., Charles P. A., van Paradijs J., 1997, *A&A*, 286, L43
- van der Hooft F., Heemskerk M. H. M., Alberts F., van Paradijs J., 1998, *A&A*, 329, 538
- van der Hooft F., Kouveliotou C., van Paradijs J., Paciesas W. S., Lewin W. H. G., van der Klis M., Crary D. J., Finger M. H., Harmon B. A., Zhang S. N., 1999, *ApJ*, 513, 477
- van der Klis M., 1994, *ApJS*, 92, 511
- van der Klis M., 1998, in Buccheri R., van Paradijs J., Alpar M. A., eds, *The Many Faces of Neutron Stars*, Kluwer, p. 337
- van Dijk R., Bennett K., Collmar W., Diehl R., Hermesen W., Lichti G. G., McConnell M., Ryan J., Schoenfelder V., Strong A., van Paradijs J., Winkler C., 1995, *A&A*, 296,

L33

- van Paradijs J., 1998, in Buccheri R., van Paradijs J., Alpar M. A., eds, *The Many Faces of Neutron Stars*, Kluwer, p. 279
- van Paradijs J., McClintock J. E., 1994, *A&A*, 290, 133
- van Paradijs J., McClintock J. E., 1995, in Lewin W. H. G., van Paradijs J., van den Heuvel E. P. J., eds, *X-Ray Binaries*, Cambridge University Press, p. 58
- van Paradijs J., Telesco C. M., Kouveliotou C., Fishman G. J., 1994, *ApJ*, 429, L19
- van Paradijs J., White N., 1995, *ApJ*, 447, L33
- Verbunt F., 1993, *ARA&A*, 31, 93
- Verbunt F., van den Heuvel E. P. J., 1995, in Lewin W. H. G., van Paradijs J., van den Heuvel E. P. J., eds, *X-Ray Binaries*, Cambridge University Press, p. 457
- Vikhlinin A., Churazov E., Gilfanov M., Sunyaev R., Finoguenov A., Dyachkov A., Kremnev R., Sukhanov K., Ballet J., Goldwurm A., Cordier B., Claret A., Denis M., Olive J. -F., Roques J. P., Mandrou P., 1995, *ApJ*, 441, 779
- Vrtilek S. D., Penninx W., Raymond J. C., Verbunt F., Hertz P., Wood K., Lewin W. H. G., Mitsuda K., 1991, *ApJ*, 376, 278
- Vrtilek S. D., Raymond J. C., Garcia M. R., Verbunt F., Hasinger G., Kürster M., 1990, *A&A*, 235, 162
- Wade R. A., Hubeny I., 1998, *ApJ*, 509, 350
- Wagner R. M., Bertram R., Starrfield S. G., Howell S. B., Kreidl T. J., Bus S. J., Cassatella A., Fried R., 1991, *ApJ*, 378, 293
- Wagner R. M., Starrfield S., Shrader C., Howell S. B., Skiff B., Koehn B., 1998, *IAU Circ.*, 6920
- Warner B., 1995, *Cataclysmic Variable Stars*, Cambridge University Press
- Webb N. A., Naylor T., Ioannou Z., Charles P. A., Shahbaz T., 1999, *MNRAS*, in preparation
- Welsh W. F., Chance D., Keyes T., Reinhart M., 1994, *High Speed Spectroscopy Using the FOS in Rapid Mode*, CAL/FOS ISR 124, STScI
- Wheeler J. C., 1999, in Mineshige S., Wheeler J. C., eds, *Disk Instabilities in Close Binary Systems*, Universal Academy Press, p. 31
- White N. E., Ueda Y., Dotani T., Nagase F., 1998, *IAU Circ.*, 6927
- White R. J., Peterson B. M., 1994, *PASP*, 106, 879
- Wijers R. A. M. J., Pringle J. E., 1999, *MNRAS*, 308, 207

- Williams R. E., 1989, *AJ*, 97, 1752
- Wynn G. A., King A. R., 1995, *MNRAS*, 275, 9
- Wynn G. A., King A. R., Horne K., 1997, *MNRAS*, 286, 436
- Zhang S. N., Cui W., Chen W., 1997, *ApJ*, 482, L155
- Zhang S. N., Mirabel I. F., Harmon B. A., Kroeger R. A., Rodríguez L. F., Hjellming R. M., Rupen M. P., 1997, in Dermer C. D., Strickmann M. S., Kurfess J. D., eds, *Proc. 4th Compton Symposium*, AIP, p. 141
- Zhang S. N., Wilson C. A., Harmon B. A., Fishman G. J., Wilson R. B., Paciesas W. S., Scott M., Rubin B. C., 1994, *IAU Circ*, 6046
- Zhao P., Callanan P., Garcia M., McClintock J., 1994a, *IAU Circ*, 6072
- Zhao P., Callanan P., Garcia M., McClintock J., 1994b, *IAU Circ*, 5929
- Zurita C., Casares J., 1998, *IAU Circ*, 7000
- Zurita C., Casares J., Hynes R. I., 1998, *IAU Circ*, 6993
- Zurita C., Casares J., Shahbaz T., Charles P. A., Hynes R. I., Shugarov S., Goransky V., Pavlenko E. P., Kuznetsova Y., 1999, *MNRAS*, submitted
- Życki P. T., Done C., Smith D. A., 1998, *ApJ*, 496, L25

APPENDIX A

THE RELATIVE FLUX CALIBRATION PROCEDURE FOR XTE J2123–058 SPECTROSCOPY

In this appendix is outlined the procedure used to perform relative flux calibration of WHT/ISIS spectroscopy of XTE J2123–058 (Section 2.5.4). Assume that after optimal extraction and wavelength calibration, there are n count rate spectra of the object, $x_i(\lambda)$ and comparison star, $c_i(\lambda)$. Spectrum n is a reference wide slit observation. Henceforth, all quantities can be assumed to be functions of wavelength, and this will not be explicitly indicated. The procedure is as follows. Several stages are illustrated in Figure A.1.

1. First sum the counts from the comparison star spectra to produce a high signal-to-noise count rate spectrum. The purpose of this is to define the line spectrum,

$$c_{\text{sum}} = \sum c_i. \quad (\text{A.1})$$

2. Next flux calibrate *all* of the comparison spectra in the usual way to produce X_i , C_i and C_{sum} . Of these, only X_n and C_n are correctly flux calibrated; the other C_i are subject to slit losses. Since it is a sum over a range of extinctions, C_{sum} will further have been inappropriately corrected for extinction. Neither of these difficulties affect the results, as it is assumed that the comparison star spectrum is constant.
3. Then divide *all* of the comparison star spectra by C_{sum} ; provided all are treated the same, it does not matter what they are divided by. The choice of C_{sum} arises because i) it gives the highest signal-to-noise description of the line spectrum, ii) it has a similar flux distribution to the individual spectra. After division by this, there

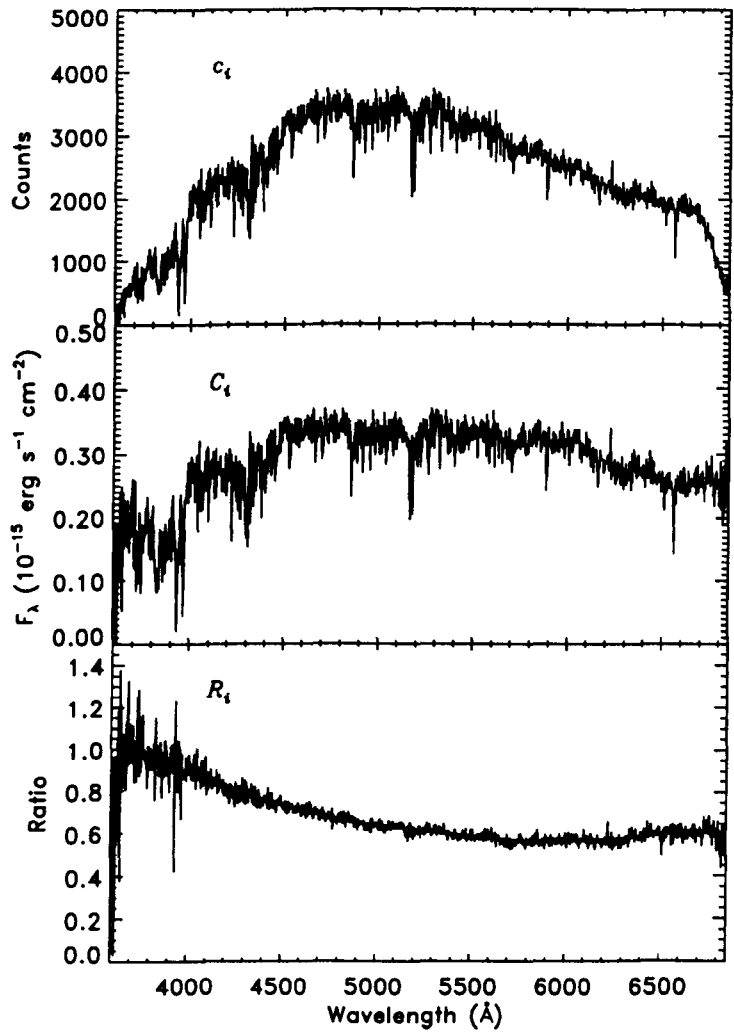


Figure A.1: Stages of comparison star processing for calibration of spectra of XTE J2123-058. Upper panel shows the count rate spectrum, centre panel is approximately flux calibrated, lower panel is a ratio spectrum formed by division by a calibrated sum of all comparison star spectra. The fit to this (R'_i) is plotted over this.

are, therefore, a series of slowly varying and approximately flat ratio spectra,

$$R_i = C_i / C_{\text{sum}}. \quad (\text{A.2})$$

These can then be fitted with a low-order cubic spline function, R'_i , so that we do not propagate noise.

4. From an individual observed approximately calibrated spectrum, C_i , the correctly calibrated spectrum can now be recovered as

$$C'_i = \frac{R'_n}{R'_i} C_i. \quad (\text{A.3})$$

5. As the object spectra are expected to be subject to the same slit losses, transparency variations, etc. as the simultaneous comparison, the same transformation can finally be applied to them:

$$X'_i = \frac{R'_n}{R'_i} X_i. \quad (\text{A.4})$$

These X'_i are the true, corrected spectra of the object, subject to the assumptions that i) the object suffers the same slit losses as the on-slit comparison and ii) the wide slit comparison spectrum, C_n is correctly calibrated. The advantage of this procedure is that the correction R'_n/R'_i is a slowly varying, noise-free function which nevertheless encapsulates all the information required about changing wavelength dependent slit losses and transparency variations.

APPENDIX B

THE OPTIMAL EXTRACTION OF BLENDED SPECTRA

B.1 Introduction

A common situation in observational astronomy is to seek accurate photometric or spectroscopic information about stars within crowded fields, i.e. where the nearest neighbour stars are blended with the stars of interest. This is a particularly common situation for X-ray binaries, most of which are faint Galactic plane objects. A solution to the photometric problem has long been available in various implementations of Stetson's DAOPHOT program (Stetson 1987). For crowded field spectroscopy, however, no widely available solution exists. A possible approach to the problem is described in this Appendix and has much in common with DAOPHOT. The spectroscopic solution also seeks to be *optimal*, in the sense that it should yield the highest signal-to-noise spectra available from the data. It thus derives from optimal extraction methods developed for unblended spectra (Horne 1986; Marsh 1989). The method is described in the context of the WHT observations of XTE J2012+381 described in Sections 2.6 and 6.3. Another application, to more recent quiescent data on V404 Cyg, is provided in Section B.5 to illustrate the reliability of the method. The implementation uses IDL routines operating on FITS images.

B.1.1 Point Spread Function Fitting of Photometric Images

An approach to crowded field photometry was presented by Stetson (1987), in the form of the DAOPHOT program. This has since become the standard tool for this problem. It was used, in its IRAF implementation, in Section 2.2. DAOPHOT attempts to model the

image as a superposition of a slowly varying sky background and a number of stellar point spread functions (PSFs).

The sky background is determined for each star by measuring the mode of the count rate within an annulus centred on the star. This is an estimate of the most likely background count rate at the star position, *including non-sky effects such as other stars, diffuse emission nebulae, etc.* There is a flaw in this method, as discussed by Stetson: while the background estimate should include other undetected stars, it should, ideally, exclude detected stars, which will be explicitly fitted later. In principal, a better approach should be to simultaneously fit a smoothly varying function to the background and PSFs to the detected stars. In practice however, this appears to increase the random scatter in the derived photometry in return for no detectable difference in the mean derived results. This implies that the systematic error introduced by including detected stars on the modal sky estimate is negligible.

The approach to modelling stellar profiles is a semi-analytical one. It is possible to model PSFs using a purely analytical function, for example a bivariate Gaussian. The disadvantage is that such a function will never be a perfect fit to the true PSF. One can add additional free parameters, but this will increase the computation time and the sensitivity to noise. Alternatively, one can construct a purely empirical function by interpolation of data. This approach works on well sampled data, but interpolation performs very unreliably on undersampled data. Under good conditions, a PSF will typically be undersampled in the core, but well sampled in the wings. Fortunately the core of stellar images is well understood (King 1971), taking a seeing-dominated Gaussian form; it is mainly in the wings, which are well sampled, where deviations from Gaussian form occur. DAOPHOT exploits this by initially fitting a Gaussian function to the core. An analytic function such as this can readily be integrated to match undersampled data. The residuals to the Gaussian fit will be most pronounced in the wings of the profile where instrumental distortions become important. These are accounted for by constructing an interpolated correction function. This hybrid fitting procedure exploits the advantages of both the analytic and empirical methods, and the same strategy will be adopted in modelling the spatial profiles of spectra.

After construction of an average PSF from one or more template stars is complete, one can proceed to fitting the model PSF to the image. For computational efficiency this process is divided up. A critical separation is defined such that two stars separated

by greater than this can be fitted independently. Detected stars are then divided into mutually exclusive groups such that a group contains all stars that are within the critical separation of another star in the group. Each group is then fitted in turn using an iterative, linearised least-squares method to obtain the final stellar magnitudes and positions. This is weighted based on an estimate of the error in each pixel value and the distance from the profile centre; the latter term is included to reduce the sensitivity to pixels moving in and out of the fitting region as the profile centre is adjusted. The weights are also dynamically adjusted to give lowest weight to points with large residuals; this reduces the sensitivity to cosmic rays and bad pixels.

B.1.2 Optimal Extraction of Spectra

Just as photometric stellar images are smeared out by the point spread function, stellar spectra are also spatially extended. To extract a spectrum from a two-dimensional image thus requires summing over a finite range of pixels. For bright, isolated objects this is not a problem; one could simply sum over an arbitrarily wide spatial range of pixels to include the majority of recorded counts at a given wavelength. For fainter objects, this summation is compromised by the background sky counts; at some point these become comparable to those from the star and the Poisson noise in the sky level degrades the extracted spectrum. Integrating over only the core of the spatial profile minimises the noise from the sky, but also discards the counts recorded in the profile wings. While the information in the wings is less valuable than that in the core (because of the extra noise from the sky counts), it is still information and could be used to refine the spectrum estimate obtained from the profile core. The key is that the information in the wings is less valuable than that in the core: this suggests that in extracting the spectrum a lower weight should be given to the wings than to the core, rather than simply throwing them away. This is the essence of the optimal extraction method: to sum over the whole spatial profile, but to use variable weights to maximise the quality of the derived spectrum.

To derive the optimal weighting scheme requires stating the problem more formally; this discussion follows that of Horne (1986). For a given pixel step in wavelength, it is assumed that a model exists for the spatial profile as a function of the spatial pixel number i ; this model is denoted by $P_{i\lambda}$. Various models are possible and are discussed in Section B.2. The optimal extraction scheme is independent of the profile model adopted. It is also assumed that a model exists for the sky background to be subtracted; this can

be determined, for example, by fitting a polynomial to each column (i.e. approximately constant wavelength) with the spectra masked out. The weighting scheme to be optimised is denoted by $W_{i\lambda}$ and finally the recorded sky subtracted count rate is $D_{i\lambda}$. For any pixel, the flux can be estimated from $D_{i\lambda}/P_{i\lambda}$. Each spatial pixel gives an independent estimate of the flux (provided errors are not spatially autocorrelated, for example as a result of resampling the image). The 'optimal' estimate of the flux can then be formed from a weighted average of these single pixel spectrum estimates:

$$F_\lambda = \frac{\sum_i W_{i\lambda} D_{i\lambda} / P_{i\lambda}}{\sum_i W_{i\lambda}}. \quad (\text{B.1})$$

The optimal set of weights, $W_{i\lambda}$, can be defined as those that minimise the variance of F_λ . The derivation of the appropriate weights is discussed in more detail in Section B.3, where the method is generalised to the extraction of multiple profiles.

B.2 The Spatial Profile

The first step in deblending spatial profiles is to define how the profile of a single star should look. Several methods have been proposed for this. Horne (1986) normalises the observed count rates for each column, then fits a low order polynomial to each line of the data. This has the advantage of making no *a priori* assumptions about the spatial profile, but is inappropriate for spectrum deblending because his spatial profile is only defined in pixel steps; it cannot easily be transferred to another star which samples the spatial profile differently. In principle, one could interpolate between pixels, but this is dangerous when the spatial profile is undersampled, as is often the case (even where the seeing is poor enough that the spatial profile would become oversampled, it is common to bin to reduce readout noise). Horne's method is also only appropriate for spectra with small distortion, i.e. nearly parallel to CCD columns. Marsh (1989) describes an extension of this empirical approach which works even for very distorted spectra. His method also produces well sampled spatial profiles which can be transferred to another star on the slit, taking advantage of the fact that strong distortion of the spectrum will lead to different columns sampling the spatial profile differently. This would be the method of choice for distorted, blended profiles. In the case of the WHT data on XTE J2012+381, however, the distortion is very slight so this method will not work; even by combining columns, the spatial profile is not well sampled.

For XTE J2012+381 it is therefore necessary to fall back on an alternative methodology,

bearing in mind that for some blended spectra the more general method of Marsh (1989) will work. The alternative is simpler to visualise, since it involves fitting a analytical profile in the spatial direction rather than a general function in the dispersion direction. This method has been successfully applied to *IUE* (Urry & Reichert 1988) data using a Gaussian profile,

$$G(x) = \frac{1}{\sigma\sqrt{2\pi}} \exp\left(-\frac{(x-x_0)^2}{2\sigma^2}\right) \quad (\text{B.2})$$

where x is the spatial coordinate and σ is the Gaussian width. As noted above, a Gaussian model will often give a good fit to the seeing dominated cores of spatial profiles. It will generally underpredict the extended wings present due to instrumental imperfections, however. An effective refinement to this is to use a Voigt profile, a convolution of a Gaussian profile with a dispersion profile:

$$F(x) = \frac{1}{4\pi^2} \frac{\gamma}{(x-x_0)^2 + (\gamma/4\pi)^2} \quad (\text{B.3})$$

where γ is the damping constant of the dispersion profile (Gray 1992). Defining $u = (x-x_0)/\sigma$ and $a = \gamma/4\pi\sigma$, the Voigt function can be written (Gray 1992) as

$$V(u, a) = \frac{1}{\sqrt{\pi}\sigma} \frac{a}{\pi} \int_{-\infty}^{\infty} \frac{\exp(-u_1^2)}{(u-u_1)^2 + a^2} du_1. \quad (\text{B.4})$$

This function provides the desired Gaussian cores, but also gives an independently variable extension in the wings. It was found that these provided a very good fit to the WHT spatial profiles. The resulting systematic residuals to the fit are very small; a numerical correction method similar to that used by DAOPHOT can be used to refine the fit even more. In the case of the data on XTE J2012+381, the resulting semi-analytical profiles fit the data with no detectable systematic error; see Figure B.1.

The first step is to perform an unconstrained fit to each row of the data, with the centre, Gaussian width, Voigt damping parameter and normalisation as free parameters. A downhill simplex (amoeba) algorithm is used to obtain the best-fit parameters (Press et al. 1992). No attempt is made to reject bad pixels or cosmic rays at this stage, as these will show up as anomalous parameter values. Of these parameter values, it is the profile centre, width and damping that define the normalised profile. All of these parameters can be expected to vary smoothly in wavelength, so after obtaining fitted values, a low order polynomial in wavelength is fitted to each parameter, rejecting anomalous values that may have been affected by cosmic rays. A fourth order polynomial was found to be adequate for XTE J2012+381; Figure B.2 shows both raw fitted values and the polynomial fits for the Gaussian width and Voigt damping parameter; the variation in the profile centre is

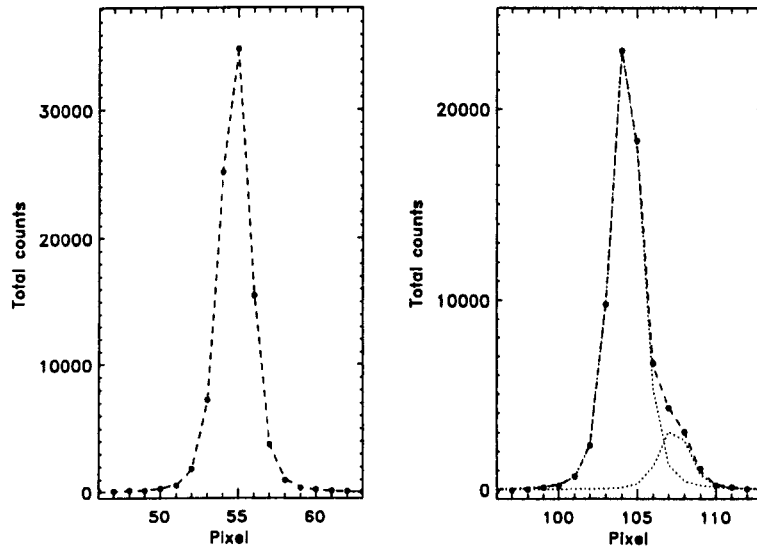


Figure B.1: Fit to spatial profiles in the red part of the WHT spectrum of XTE J2012+381. Data is shown by points, the model profile is dashed and the dotted lines indicate the Deblended components. Both data and fits have been summed over 20 pixels in the dispersion direction to reduce noise and illustrate the quality of fit achieved. On the left is the fit to the spatial profile of the template star. On the right is the two-profile fit to the stars of interest. This figure duplicates Figure 2.6 for convenience.

tiny. These polynomial fits, together with the normalisation such that $\sum_i P_i = 1$ define the spatial profile as a function of wavelength.

If, as in this case, the difference in brightness of the two stars is very large then it becomes crucial that the wing of the brighter star be very well fitted to avoid contamination of the fainter star. This is achieved using a numerical correction to the (Voigt) model profile. As anticipated, the error involved in assuming a Voigt profile is only important in the extreme wings of the profile: the core is very well fitted indeed. It is therefore possible to define a numerical correction factor (observed profile divided by model) at the sampled points and then interpolate this to obtain a general correction function for any pixel sampling. Since this involved the extreme wings of the line, where signal-to-noise will be poor, it was found that such a correction could not be defined meaningfully as a function of wavelength; instead a single, averaged, wavelength independent correction is determined. A symmetric profile is also assumed. This is a valid assumption for the WHT spectra; hence the correction is simply a function of distance from the profile centre.

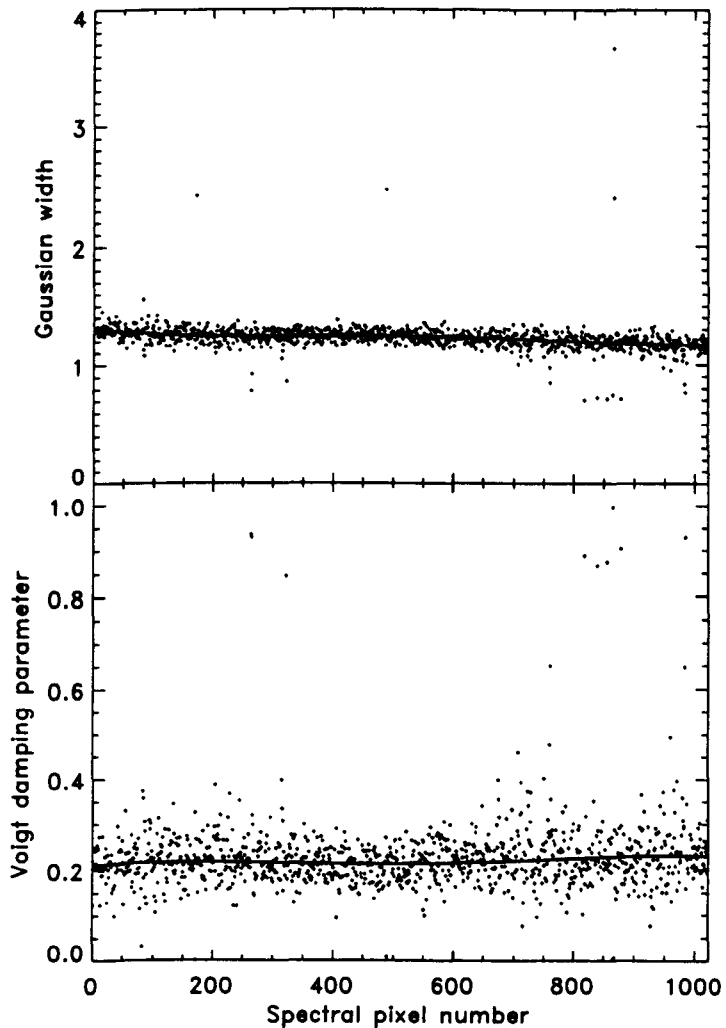


Figure B.2: Wavelength dependence of the Voigt profile fitting parameters, the Gaussian width and the Voigt damping parameter. Points mark fits to individual pixels in the dispersion direction, with no binning. The solid lines are low-order polynomial fits to the parameters.

Given higher quality data, an asymmetric, wavelength dependent function could readily be used.

Assuming that there are no changes in focus along the slit (or at least the restricted part of it which is used) and that the separation between stellar images (in pixels) is independent of wavelength, the only additional information required to define the profiles of the blended stars is the separation of each from the template star. For spectra with minimal distortion, this is easy to obtain by performing an initial fit to the average of several rows of data, leaving the centres of the two blended profiles as free parameters.

Distorted spectra would require that the distortion (known from the fits to the template profile) be removed by resampling the data for this initial fit only.

B.3 Fitting Profiles

Assuming that the fit to the spatial profile for the template star is satisfactory, the centre position and normalised profile as a function of wavelength are known, and the spectral extraction itself can be performed. The discussion begins with the simple case of fitting a single profile, before generalising to two (or more) profiles. This is a particularly easy case, since the centre and shape of the model profile are known, and it is only required to normalise it to fit the data. This first part of this discussion is adapted from Horne (1986) and Marsh (1989) and elaborates on Section B.1.2. For a given row parallel to the slit, let P_i ¹ be the normalised profile as a function of spatial pixel i , such that $\sum_i P_i = 1$. Denote the sky subtracted count rate by D_i and its variance by V_i . An unbiased estimate of the total count rate across the whole profile can be formed using a single pixel value by $F_i = D_i/P_i$, since P_i is normalised. A better estimate will be to form a weighted average of such estimates:

$$F = \frac{\sum_i W_i D_i / P_i}{\sum_i W_i}. \quad (\text{B.5})$$

The simplest weighting scheme is $W_i = P_i$, which reduces to a simple sum across the full defined aperture. The optimal weighting scheme is that which minimises the variance of F . This can be achieved by weights inversely proportional to the variances of the individual pixel estimates of $F_i = D_i/P_i$. Since $\sigma_{F_i} = \sigma_{D_i}/P_i$,

$$W_i = \frac{1}{\sigma_{F_i}^2} = \frac{P_i^2}{\sigma_{D_i}^2} = \frac{P_i^2}{V_i}. \quad (\text{B.6})$$

The optimal extraction scheme is then:

$$F = \frac{\sum_i P_i D_i / V_i}{\sum_i P_i^2 / V_i}. \quad (\text{B.7})$$

Horne (1986) notes the equivalence between this weighted average method and fitting a known profile to data of variance V_i . This equivalence will be the key to approaching blended spectra. In seeking a fit of a model to data, it is common to measure the badness of fit of the model using the χ^2 statistic; in this case defined by

$$\chi^2 = \sum_i \frac{(D_i - F P_i)^2}{V_i}. \quad (\text{B.8})$$

¹The λ subscript will be dropped from here onwards for simplicity.

An optimal solution is then one which minimises χ^2 with respect to F . In this simple case, the necessary expression for optimal F can be derived analytically by requiring

$$\frac{d}{dF}\chi^2 = \sum_i \frac{-2P_i D_i + 2F P_i^2}{V_i} = 0 \quad (\text{B.9})$$

$$\Rightarrow F = \frac{\sum_i P_i D_i / V_i}{\sum_i P_i^2 / V_i}. \quad (\text{B.10})$$

This is the same result as was obtained by considering an optimally weighted summation. Unlike that method, however, this approach is readily generalised to deblending multiple profiles. Consider profiles P_{ij} ($j = 1 \dots N$) to be fitted yielding N spectra F_j . The badness of fit statistic is then

$$\chi^2 = \sum_i \frac{(D_i - \sum_j F_j P_{ij})^2}{V_i} \quad (\text{B.11})$$

and the optimal solution requires

$$\frac{\partial}{\partial F_j} \chi^2 = 0 \quad (\text{B.12})$$

for all j . In general, these N constraints will yield N simultaneous equations with N unknowns: $F_1 \dots F_N$. This can be solved as a straightforward problem in linear algebra. Consider the two-profile case applicable to the XTE J2012+381 data. For convenience write $F_1 \equiv f$, $F_2 \equiv g$, $P_{i1} \equiv p_i$ and $P_{i2} \equiv q_i$. Then

$$\begin{aligned} \chi^2 &= \sum_i \frac{(D_i - f p_i - g q_i)^2}{V_i} \\ &= \sum_i \frac{D_i^2 + f^2 p_i^2 + g^2 q_i^2 - 2f p_i D_i - 2g q_i D_i + 2f g p_i q_i}{V_i} \end{aligned} \quad (\text{B.13})$$

and so

$$\frac{\partial}{\partial f} \chi^2 = 0 \Rightarrow \sum_i \frac{2f p_i^2 - 2p_i D_i + 2g p_i q_i}{V_i} = 0 \quad (\text{B.14})$$

$$\frac{\partial}{\partial g} \chi^2 = 0 \Rightarrow \sum_i \frac{2g q_i^2 - 2q_i D_i + 2f p_i q_i}{V_i} = 0. \quad (\text{B.15})$$

These equations appear more complex than they are, since f and g are independent of i and are the only quantities that are not known or assumed *a priori*. Define the following statistics:

$$\begin{aligned} A &= \sum_i p_i^2 / V_i \\ B &= \sum_i q_i^2 / V_i \\ C &= \sum_i p_i q_i / V_i \end{aligned}$$

$$\begin{aligned}
 D &= \sum_i p_i D_i / V_i \\
 E &= \sum_i q_i D_i / V_i.
 \end{aligned}
 \tag{B.16}$$

The two equations then take the form

$$\begin{aligned}
 Af - D + Cg &= 0 \\
 Bg - E + Cf &= 0
 \end{aligned}
 \tag{B.17}$$

with solution

$$\begin{aligned}
 f &= \frac{D/C - E/B}{A/C - C/B} \\
 g &= \frac{E/C - D/A}{B/C - C/A}.
 \end{aligned}
 \tag{B.18}$$

B.4 Cosmic Ray Rejection

One of the great strengths of optimal extraction algorithms is that the spatial profile is known. A cosmic ray or bad pixel, even when it lies on top of the spectrum, will have a different spatial profile, and hence can be recognised and rejected. This means that instead of removing cosmic rays from the extracted one-dimensional spectra, and rejecting a whole pixel step in wavelength, they can be removed from the two-dimensional spectra, retaining the information in the uncontaminated pixels. While this process is easy to do by eye, it proves difficult to train a computer to recognise cosmic rays automatically, especially when multiple profiles are being fit. Given a first approximation to the profile, bad values can be rejected by an iterative sigma-clipping algorithm (Horne 1986). The strategies used in this work to obtain the crucial first approximation are described here.

Beginning with the simplest case of recognising contamination of a single profile, the method relies on the fundamental equation of Horne's method: $F_i = D_i/P_i$ (see Section B.3). From this equation, the integrated flux across the profile can be estimated from a single pixel value; each pixel gives an independent estimate of the integrated flux. A contaminated pixel will then give an anomalous estimate. If this estimate is severely wrong, as is often the case with cosmic rays, then a straight average may be very much in error, leading to subsequent rejection of good data. A better method is to take the median value as the first estimate for the integrated flux. This then gives a first approximation to the fitted profile which forms the basis for subsequent refinement with iterative sigma-clipping.

Where two independently fitted profiles are involved more care is needed. The only case considered here is that one star is brighter than the other at all wavelengths in the

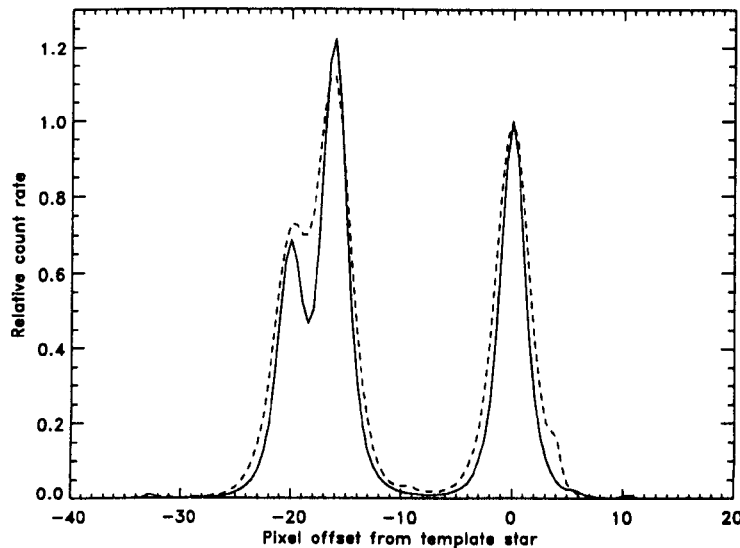


Figure B.3: Best (solid) and worst (dashed) average spatial profiles of V404 Cyg from 1999 July 7/8. Peaks are from left to right, the blended companion star, V404 Cyg and the profile template star. The profiles have been scaled such that the peak flux from the template star is unity.

spectrum (true for all data included here.) For the brightest star, a profile region is selected from the midpoint between the two stars to an arbitrary cutoff on the other side. Within this region, the profile of the brighter star is expected to dominate, so the median ratio method described above for single stars can be applied. This gives an approximate normalisation for the brighter stellar profile, which can then be subtracted. The median ratio method is then applied to the remaining profile of the fainter star to estimate a normalisation for this. With an approximate normalisation for both profiles, iterative sigma-clipping can be used to refine the list of rejected pixels.

B.5 V404 Cyg: Another Application of the Algorithm

Another X-ray binary for which this deblending method is appropriate is V404 Cyg, as this has a fainter companion star 1.5 arcsec away. There is no physical association between the two. Observations were obtained of V404 Cyg in quiescence using WHT/ISIS on 1999 July 6–8 under a programme not directly contributing to this work; a summary of preliminary results is presented to illustrate the power of the deblending method.

The instrumental configuration was optimised to minimise readout noise, hence allow-

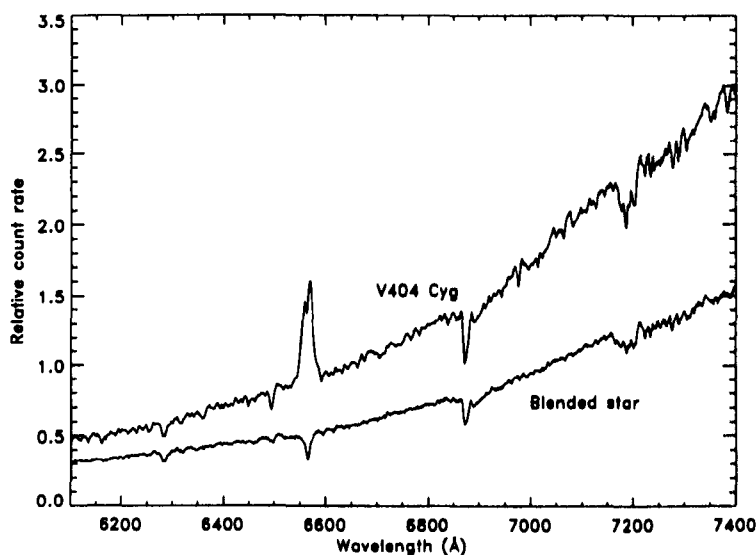


Figure B.4: Deblended spectra of V404 Cyg and the blended star. All the spectra from 1999 July 7/8 have been averaged. The deblending algorithm has clearly separated the spectra cleanly. Note the contrast between H α emission in V404 Cyg and absorption in the blended star, and also the smoothness of the (noisier) continuum in the blended star.

ing a relatively fast cycle time (in comparison to previous spectroscopy of this object), with 180 s exposures. The R316R grating was used with the TEK4 CCD and a 4 arcsec slit was used to minimise slit losses. Images were de-biased and flat-fielded with IRAF in the way described in Chapter 2. It should be emphasised that both the reduction, and especially the application of this extraction method are preliminary; hence several anomalies can be seen in the figures. The results can be improved by some fine-tuning of extraction parameters and checking by hand for unrejected cosmic rays and incorrectly fitted profiles. Even so, the present treatment illustrates what can be achieved. Figure B.3 shows two examples of averaged (in wavelength) spatial cuts with respect to the centre of the template star. The images with the best and worst seeing from the night of July 7/8 were chosen. The fainter star is clearly blended with V404 Cyg even in the best image (seeing ~ 0.4 arcsec.)

The optimal deblending algorithm was applied with two simplifications. Because the goal of this project was to obtain the highest time-resolution practical, the signal-to-noise ratio of individual frames was not high. Because of this, it was necessary to perform initial profile fitting in 51 pixel bins in the dispersion direction (giving 20 bins along the spec-

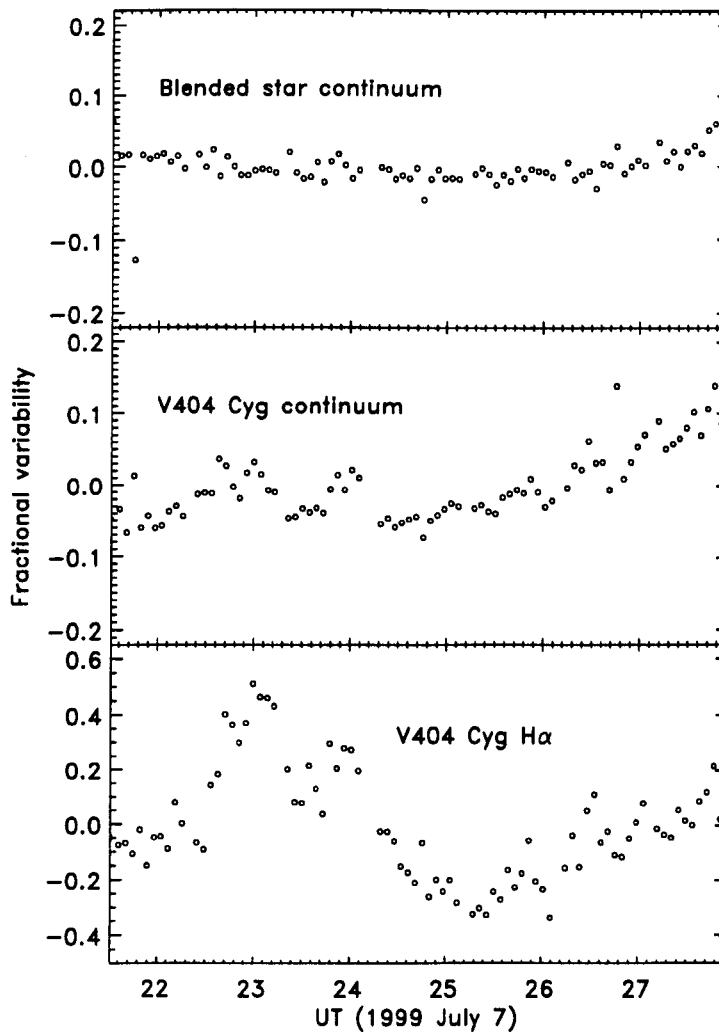


Figure B.5: Continuum light curves of V404 Cyg and its blended companion, and H α emission light curve of V404 Cyg. Note that the vertical range of the H α plot is much larger than for the continuum light curves.

trum). It was also not possible to form a profile correction for the wings. Since, however, the difference in brightness of the two stars is less extreme than for XTE J2012+381, a pure Voigt function is adequate.

Figure B.4 shows the average extracted spectra of the two blended stars from July 7/8. The spectra appear to have been separated very cleanly, with no obvious crosstalk between the two. H α is clearly in emission in V404 Cyg and absorption in the blended star. There is also a lot of structure in the spectrum of V404 Cyg (e.g. 6600–6900 Å) which is not present in the spectrum of the blended star which appears largely featureless. As V404 Cyg is brighter, the signal-to-noise ratio of its spectrum should be higher and hence

these features must be real; they likely arise from the late-type companion star which dominates in quiescence. The blended star, in contrast, appears to be of early spectral type².

Figure B.5 shows light curves of continuum from both stars and $H\alpha$ emission from V404 Cyg for the night of July 7/8. Spectra were normalised relative to the template star to approximately remove variable slit loss and transparency effects. Large variations are seen in $H\alpha$ and smaller correlated variations in the continuum of V404 Cyg. The light curve of the blended star is largely smooth, though not flat indicating that there are calibration issues remaining to be resolved; simultaneous JKT photometry was obtained for this purpose. In particular, the light curve of the blended star shows little or no contamination from the large flare occurring at the beginning of the night in V404 Cyg.

²To the author's knowledge, no spectrum of this star has previously been isolated.